ABSTRACT

Title of Thesis:	HOTSPOT REMEDIATION USING GERMANIUM SELF COOLING TECHNOLOGY
	Horacio Cesar Nochetto, Masters Of Science, 2011
Thesis Directed By:	Professor Avram Bar-Cohen, Department of Mechanical Engineering

Localized thermoelectric "self cooling" in semiconductor materials is among the most promising approaches for the remediation of on-chip hot spots resulting from the shrinking feature sizes and faster switching speeds of nanoelectronic components. Self cooling in a germanium chip is investigated, using 3-dimensional, thermal-electric, coupled numerical simulations, for a range of systems and geometric parameters. The results suggest that localized cooling, associated with the introduction of an electric current on the back surface of a germanium chip, can effectively reduce the hot spot temperature rise on the active side of the chip. It was found that self cooling in a 100µm thick chip could provide between 3.9ºC and 4.5ºC hotspot temperature reduction. When using a germanium layer above an electrically insulated silicon layer, self-cooling was found to yield an additional 1ºC to 2º C temperature reduction. A streamlined

computational tool is developed to facilitate the identification of optimal cooling parameters.

HOTSPOT REMEDIATION USING GERMANIUM SELF COOLING TECHNOLOGY

By

Horacio Cesar Nochetto

Thesis submitted to the Faculty of the Graduate School of the
University of Maryland, College Park, in partial fulfillment
of the requirements for the degree of
Masters of Science
2011

Advisory Committee:
Professor Dr. Avram Bar-Cohen, Chair
Assistant Professor Patrick McCluskey
Assistant Professor Bao Yang

© Copyright by
Horacio Cesar Nochetto
2011

Acknowledgements

I would like to thank everyone who has helped me achieve my academic accomplishments, for without them, this would not be possible.

I would first like to thank my advisor Dr. Avram Bar-Cohen, who through his mentorship, I have learned much about electronic cooling. His advice and leadership throughout my tenure as a graduate student has made this thesis possible. I would also like to thank Dr. Peng Wang who has helped me execute with great precision and accuracy the entirety of the presented work. All my teachers at University of Maryland have been influential in inspiration to continue engineering, even when the work load became unbearable.

I am also thankful for the help and distraction from the stresses of graduate school of my lab mates: Juan Cevallos, Viatcheslav Litvinovitch, Michael Manno, Emil Rahim, Pooja Rao, Frank Robinson, and Jessica Sheehan.

I would like to thank my parents; Ricardo and Cristina, who have been supportive through all my endeavors and have provided me the confidence, determination, and discipline to accomplish the obstacles that are placed in front of me.

Lastly, I would like to thank my girlfriend Terri Auth, who has given me much love, support, and happiness all throughout undergraduate and graduate school.

Table of Contents

Acknowledgements ii
Table of Contents iii
List of Tables vi
List of Figures vii
Chapter 1: Introduction 1
1.1 Motivation 1
1.2 Hotspot Cooling Methods 4
1.2.1 Passive Techniques 4
1.2.2 Active Techniques 5
1.3 Scope of Work 10
Chapter 2: The Thermoelectric Cooler 13
2.1 Main Thermoelectric Effects 14
2.1.1 The Reversible Effects 14
2.1.2 The Irreversible Effects 18
2.1.3 Summary of Thermoelectric Cooler (TEC) Effects 20
2.2 A Detailed analysis of the Peltier Effect 20
2.2.1 Solid State Physics of the Peltier Effect 21
2.2.2 Peltier Effect of Conventional Thermoelectric Cooler 24
2.2.3 Summary of Detailed Peltier Effect Analysis 26
2.3 Thermoelectric Cooler Net Effects 26
2.3.1 Net Cooling Power 27
2.3.2 Conventional Thermoelectric Cooler Cooling Tends 29
2.3.3 Summary of the Conventional Thermoelectric Coolers 31
2.4 Thermoelectric Cooler Metrics 31
2.4.1 Power and Coefficient of Performance (COP) 32
2.4.2 Maximum Hot and Cold Junction temperature Difference (ΔT_{Max}) 33
2.4.3 Figure of Merits 33
2.4.4 Summary of Conventional Thermoelectric Cooler Metrics 35
2.5 Thermoelectric Materials and Current Devices 35
2.5.1 Common Materials 35
2.5.2 Thin Film Thermoelectric Coolers (TFTEC) 37
2.5.3 Bulk Miniaturized Thermoelectric Coolers 41
2.5.4 Self Thermoelectric Cooler 43
2.5.5 Summary of Thermoelectric Materials and Current Devices 44
Chapter 3: Performance of Germanium Self Cooling Device 45
3.1 Self Cooling Device 49
3.1.1 Self Cooling Geometry 50
3.1.2 Material Properties 52
3.1.3 Boundary Conditions 54
3.2 Numerical Results under Constant Voltage Operation 58
3.2.1 Cooling Metrics 60
3.2.2 Mesh Convergence 63
3.2.3 Typical Temperature Distributions 66
3.2.4 Function of Current 68

3.2.5 Function of Cooler Size 71
3.2.6 Function of Die thickness 75
3.3 Performance Band of Germanium Self Cooling Device 83
Chapter 4: Germanium Self Cooling Meta Model 90
4.1 Meta-Model 92
4.1.1 Constant Current Self Cooler 93
4.1.2 Material Properties 95
4.1.3 Analytical Solution 96
4.2 Allocation Factor Surfaces 102
4.2.1 Surface Intersection Method 103
4.2.2 Curve Fit 109
4.2.3 Surface Fit 111
4.3 Meta-Model Discrepancy 118
4.3.1 Plane Intersection Discrepancy 120
4.3.2 Total Discrepancy 124
Chapter 5: Germanium and Silicon Bi-Layer Self Cooling 129
5.1 Bi-layer Self Cooling Device 132
5.1.1 Geometry 133
5.1.2 Material Properties 135
5.1.3 Boundary Conditions 135
5.2 Bi-Layer Numerical Results 137
5.2.1 Bi-Layer Cooling Metrics 141
5.2.2 Mesh Convergence 144
5.2.3 Typical Bi-layer Temperature Distributions 147
5.2.4 Function of Current 149
5.2.5 Function of Cooler Size 152
5.2.6 Function of Germanium Percentage 157
5.2.7 Function of Die Thickness 163
5.2.8 Thermal Contact Resistances 167
Chapter 6: Conclusions and Future Work 170
6.1.1 Germanium Self Cooler Performance: 171
6.1.2 Germanium Self Cooler Meta-Model: 171
6.1.3 Bi-Layer Self Cooler: 172
6.2 Future Work 173
6.2.1 Experimental Validation: 173
6.2.2 Bi-layer Comparisons 174
Appendices Introduction 175
Appendix A FEM Phases 177
A .1.1 Preprocessing Phase 178
A .1.2 General Conductance Matrix 183
A .1.3 Solution Phase 184
Appendix B The Thermal-Electrical Model 188
B.1 Underlying Phenomenon 188
B .1.1 Heat Diffusion 188
B .1.2 Continuity of Electric Charge 189
B.2 Coupling of Thermal and Electric Effects 190

B .2.1 Finite Element Formulation 193
B.3 Summary of Thermal-Electrical Model 194
Appendix C ANSYS 12.0 Thermal and Electrical Validation 196
C.1 Thermal Model Validation 198
C .1.1 Analytical solution 199
C .1.2 Numerical solution 200
C .1.3 Analytical and Numerical comparison 202
C.2 Electrical Model Validation 203
C .2.1 Analytical solution 204
C .2.2 Numerical solution 205
C .2.3 Analytical and Numerical comparison 207
C.3 Thermal-Electrical Model with Joule Heating 208
C .3.1 Analytical solution 209
C .3.2 Numerical solution 211
C .3.3 Analytical and Numerical comparison 214
C.4 Thermal-Electrical Model with Joule Heating and the Peltier Effect 216
C .4.1 Analytical Solution 217
C .4.2 Numerical Solution 218
C .4.3 Analytical and Numerical Comparison 222
C.5 Thermal and Electrical Model Validation Summary 224
Bibliography 226

List of Tables

Table 1: TFTEC Cooling Performance 39
Table 2: Semenyuk's Bulk Miniaturized Thermoelectric Properties trends 41
Table 3: Constant Voltage Germanium Self Cooling Device Dimensions 51
Table 4: Germanium Self Cooling Device Material Properties 54
Table 5: Non-Thermoelectric Boundary Conditions 55
Table 6: Germanium Self Cooling Device Dimensions 95
Table 7: Meta-Model Material Properties 95
Table 8: Meta-Model, Non-thermoelectric Boundary conditions 97
Table 9: Bi-Layer Self Cooling Device Dimensions 134
Table 10: Bi-Layer Self Cooling Device Material Properties 135
Table 11: Bi-Layer Non-Thermoelectric Boundary Conditions 136
Table 12: Residential Wall Material Properties, Geometry, and Boundaries Conditions 198
Table 13: Residential Wall, Analytical and Numerical Results Comparison 202
Table 14: Electrical Circuit Properties 204
Table 15: Electrical Model Circuit, Unknowns 204
Table 16: Electrical Model Circuit, Analytical and Numerical Comparison 207
Table 17: Infinite Slab Example Properties 209
Table 18: Infinite Slab, Temperature Comparison 214
Table 19: Infinite Slab, Voltage Comparison 215
Table 20: One Leg Thermoelectric Cooler (TEC) Properties 217
Table 21: One Leg Thermoelectric Cooler (TEC) Metrics 217

List of Figures

Figure 1: ITRS predictions of feature size, chip size and transistor density for high performance microprocessor chips (2)........ 1
Figure 2: A typical heat flux map (8)........ 3
Figure 3: Temperature map corresponding to Figure 2 (8)........ 3
Figure 4: A 2 Leg Conventional Thermoelectric Cooler........ 7
Figure 5: SEM photograph of silicon micro coolers (17)........ 8
Figure 6: Side view of Silicon Self Cooler (19)........ 9
Figure 7: Top view of Silicon Self cooler (19)........ 9
Figure 8: The Seebeck effect (2)........ 15
Figure 9: The Peltier Effect (2)........ 16
Figure 10: Joule Heating........ 18
Figure 11: Fourier Law (9)........ 20
Figure 12: Simplified Conventional Thermoelectric (TEC) Cooler (4)........ 22
Figure 13: Conventional Two leg Thermoelectric Cooler (TEC)........ 23
Figure 14: Zone 1 (right) and Zone 2 (right) demonstrating Peltier Cooling........ 25
Figure 15: Zone 3 (left) and Zone 4 (right) demonstrating Peltier Heating........ 25
Figure 16: Conventional Thermoelectric Cooler (TEC) with Net Cooling Power Location demonstrated........ 27
Figure 17: TEC cooling as a function of current........ 29
Figure 18: TEC cooling as a function of leg height........ 30
Figure 19: Chowdhury et al Thermoelectric Cooler (TEC) Package........ 39
Figure 20: SEM photograph of silicon micro coolers (17)........ 42
Figure 21: Side view of Silicon Self Cooler (19)........ 43
Figure 22: Top view of Silicon Self cooler (19)........ 43
Figure 23: Germanium Self Cooling Device........ 51
Figure 24: Germanium Self Cooling Device, Left is Top View, Right is bottom heating map (not to scale)........ 51
Figure 25: N-type Germanium Electrical Resistivity and Seebeck as a function of arsenic doping concentration (20) (46)........ 52
Figure 26: N-type Germanium Power factor as a function of arsenic doping concentration (20)........ 53
Figure 27: Wang and Bar-Cohen's Temperature reduction as a function of doping concentration (20)........ 54
Figure 28: Constant Voltage Germanium Self Cooling Device Boundary Condition Locations........ 55
Figure 29: Typical Quarter Current plot of Constant Voltage Self Cooler, Zoomed view of Cooler on right........ 58
Figure 30: High Order Brick Element Shape Used for Constant Voltage Self Cooler..... 64
Figure 31: Typical Mesh plot of Constant Voltage Self Cooler, Zoomed view of Cooler on right........ 64
Figure 32: Hotspot Temperature Mesh convergence for 100µm Die, 400µm Cooler, and I=1.05A........ 64
Figure 33: Cooler Temperature Mesh convergence for 100µm Die, 400µm Cooler, and I=1.05A........ 65

Figure 34: Mesh convergence Time for 100µm Die, 400µm Cooler, and I=1.05A 65
Figure 35: Power Convergence for 100µm Die, 400µm Cooler, and I=1.05A................ 66
Figure 36: Constant Voltage Self Cooler, Temperature Along the bottom of the die, for the 100µm Die and 400µm Cooler (Quarter model).. 67
Figure 37: Constant Voltage Self Cooler, Hotspot and Cooler Temperature for 100µm Die and 400µm Cooler... 68
Figure 38: Constant Voltage Self Cooler, Power for 100µm Die and 400µm Cooler...... 70
Figure 39: Constant Voltage Self Cooler, Thermal Impact Factor for 100µm Die and 400µm Cooler 71
Figure 40: Constant Voltage Self Cooler, Hotspot Temperature Reduction for 100µm die 72
Figure 41: Constant Voltage Self Cooler, Cooler Temperature Reduction for 100µm die 72
Figure 42: Constant Voltage Self Cooler, Maximum Temperature Reductions for each Cooler Width for 100µm die.. 73
Figure 43: Constant Voltage Self Cooler, Hotspot Cooling Effectiveness for 100µm die74
Figure 44: Constant Voltage Self Cooler, Power at Maximum Hotspot Temperature Reduction for 100µm die 74
Figure 45: Constant Voltage Self Cooler, Thermal Impact Factor at Maximum Hotspot Temperature Reduction for 100µm die.. 75
Figure 46: Constant Voltage Self Cooler, Hotspot Temperature Reduction 76
Figure 47: Constant Voltage Self Cooler, Cooler Temperature Reduction...................... 76
Figure 48: Constant Voltage Self Cooler, Maximum Hotspot Temperature Reduction... 77
Figure 49: Constant Voltage Self Cooler, Maximum Hotspot Temperature Reduction over large die thickness range.. 78
Figure 50: Constant Voltage Self Cooler, Hotspot Cooling Effectiveness...................... 79
Figure 51: Constant Voltage Self Cooler, Maximum Hotspot Cooling effectiveness...... 79
Figure 52: Constant Voltage Self Cooler, Maximum Hotspot Cooling effectiveness...... 80
Figure 53: Constant Voltage Self Cooler, Power... 81
Figure 54: Constant Voltage Self Cooler, Thermal Impact Factor.................................. 81
Figure 55: Constant Voltage Self Cooler, Power at Maximum $\Delta T_{Hotspot}$......................... 82
Figure 56: Constant Voltage Self Cooler, Thermal Impact Factor at Maximum $\Delta T_{Hotspot}$82
Figure 57: Hotspot off, Constant Current Self Cooler, Electric Potential Plot, 100µm die 630µm wide Cooler and 1.06A.. 84
Figure 58: Hotspot off, Constant Voltage Self Cooler, Electric Potential Plot, 100µm die 400µm wide Cooler and 1.05A.. 84
Figure 59: Hotspot off, Constant Current Self Cooler, Current Density Vector Sum Plot, 100µm die 630µm wide Cooler and 1.06A.. 85
Figure 60: Hotspot off, Constant Voltage Self Cooler, Current Density Vector Sum Plot, 100µm die 400µm wide Cooler and 1.05A.. 85
Figure 61: Hotspot off, Constant Current Self Cooler, Temperature Plot, 100µm die 630µm wide Cooler and 1.06A.. 86
Figure 62: Hotspot off, Constant Voltage Self Cooler, Temperature Plot, 100µm die 400µm wide Cooler and 1.05A.. 86
Figure 63: Minimum Hotspot Temperature Band 87
Figure 64: Maximum Hotspot Temperature Reduction Band 87

Figure 65: Maximum Hotspot Cooling Effectiveness Band 88
Figure 66: Cooler Width Band at Maximum Hotspot Temperature Reduction............... 89
Figure 67: Germanium Self Cooling Device 94
Figure 68: Germanium Self Cooling Device, Left is Top View, Right is bottom heating map (not to scale).. 94
Figure 69: Meta Model, Boundary Condition Location 97
Figure 70: Hotspot Temperature summation integer study; 300μm die, 500μm Cooler size, I=0.. 101
Figure 71: Cooler Temperature summation integer study; 300μm die, 500μm Cooler size, I=0 101
Figure 72: Cooler Discrepancy Plane for 300μm die, 1015μm Cooler Width, I=3.35A 104
Figure 73: Hotspot Discrepancy Plane for 300μm die, 1015μm Cooler Width, I=3.35A 105
Figure 74: Cooler Discrepancy Equation Accuracy for 300μm die, 1015μm Cooler Width, I=3.35A 105
Figure 75: Hotspot Discrepancy Equation Accuracy for 300μm die, 1015μm Cooler Width, I=3.35A 106
Figure 76: Alpha as a function of Cooler size for each die thickness............................ 108
Figure 77: Beta as a function of Cooler size for each die thickness 109
Figure 78: Linear Curve Fit Alpha... 110
Figure 79: Power Fit Beta 110
Figure 80: Alpha Allocation Factor Surface 113
Figure 81: Alpha value Surface Fit Discrepancy from Curve Fit 114
Figure 82: Beta Allocation Factor Surface 116
Figure 83: Beta value Surface Fit Discrepancy from Curve Fit 117
Figure 84: Beta Surface Problems 118
Figure 85: Temperature Plane Intersection discrepancy for 100μm die 121
Figure 86: Temperature Plane Intersection discrepancy at optimum Cooler sizes......... 121
Figure 87: Temperature Reduction Plane Intersection discrepancy for 100μm die 122
Figure 88: Temperature Reduction Plane Intersection discrepancy at optimum Cooler sizes... 123
Figure 89: Hotspot Cooling effectiveness Plane Intersection discrepancy for 100μm die 123
Figure 90: Hotspot Cooling effectiveness Plane Intersection discrepancy at optimum Cooler sizes.. 124
Figure 91: Total Temperature Discrepancy for 100μm die thickness 125
Figure 92: Total Temperature Discrepancy at Optimum Cooler sizes 125
Figure 93: Total Temperature Reduction Discrepancy for the 100μm die thickness 126
Figure 94: Total Temperature Reduction Discrepancy at Optimum Cooler sizes.......... 127
Figure 95: Total Hotspot Cooling Effectiveness Discrepancy for the 100μm die thickness 128
Figure 96: Total Hotspot Cooling Effectiveness Discrepancy at Optimum Cooler sizes128
Figure 97: Bi-Layer Self Cooling Device 133
Figure 98: Bi-Layer Self Cooling Device, Left is Top View, Right is bottom heating map (not to scale)... 134
Figure 99: Bi-Layer Self Cooling Device Boundary Condition Locations 136

Figure 100: High Order Brick Element Shape Used for Bi-Layer Self Cooler 145
Figure 101: Typical Mesh plot of for Bi-Layer Self Cooler, Zoomed view of Cooler on right 145
Figure 102: Hotspot Temperature Mesh convergence for 500μm Die, 85% Germanium, 1400μm Cooler, and I=4.6A 146
Figure 103: Cooler Temperature Mesh convergence for 500μm Die, 85% Germanium, 1400μm Cooler, and I=4.6A 146
Figure 104: Mesh convergence Time for 500μm Die, 85% Germanium, 1400μm Cooler, and I=4.6A 147
Figure 105: Mesh convergence Time for 500μm Die, 85% Germanium, 1400μm Cooler, and I=4.6A 147
Figure 106: Bi-layer Self Cooler, Temperature Along the bottom of the die, 100μm Die, 90% Germanium, 350μm Cooler (Quarter model) 148
Figure 107: Bi-Layer Self Cooler, Hotspot and Cooler Temperature for 100μm Die, 90% Germanium, 350μm Cooler 149
Figure 108: Bi-Layer Self Cooler, Power for 100μm Die, 90% Germanium, and 350μm Cooler 151
Figure 109: Bi-Layer Self Cooler, Thermal Impact Factor for 100μm Die, 90% Germanium, 350μm Cooler 152
Figure 110: Bi-Layer Self Cooler, Maximum Temperature Reductions for each Cooler Width for 100μm die, and 90% Germanium 154
Figure 111: Bi-Layer Self Cooler, Hotspot Cooling Effectiveness for 100μm die and 90% Germanium case 155
Figure 112: Bi-Layer Self Cooler, Power at Maximum Hotspot Temperature Reduction for 100μm die and 90% Germanium case 156
Figure 113: Bi-Layer Self Cooler, Thermal Impact Factor at Maximum Hotspot Temperature Reduction for 100μm die and 90% Germanium case 156
Figure 114: Bi-Layer, Hotspot Temperature 157
Figure 115: Bi-Layer Self Cooler, Maximum Hotspot Temperature Reduction 158
Figure 116: Bi-Layer Self Cooler, Maximum Hotspot Temperature Reduction relative to 100% Germanium cooler 159
Figure 117: Bi-Layer Self Cooler, Maximum Hotspot Temperature Reduction relative to 100% Conduction only Silicon 160
Figure 118: Bi-Layer Self Cooler, Hotspot Cooling Effectiveness 161
Figure 119: Bi-Layer Self Cooler, Power 162
Figure 120: Bi-Layer Self Cooler, Thermal Impact Factor 162
Figure 121: Bi-Layer Self Cooler, Maximum Hotspot Temperature Reduction relative to 100% Germanium cooler 164
Figure 122: Maximum Hotspot Cooling Effectiveness 165
Figure 123: Bi-Layer Self Cooler, Power at Maximum $\Delta T_{H,Ge}$ and $\Delta T_{H,Si}$ 166
Figure 124: Bi-Layer Self Cooler, Thermal Impact Factor at Maximum $\Delta T_{H,Ge}$ and $\Delta T_{H,Si}$ 167
Figure 125: Bi-Layer Self Cooler, Contact Resistance for 1400μm Cooler size, 85% Germanium, and 500μm die thickness case 168
Figure 126: Bi-Layer Self Cooler, Temperature Reduction as a function of Contact Resistance for 1400μm Cooler size, 85% Germanium, and 500μm die thickness case . 169

Figure 127: Simplified FEM Analysis Phase order 177
Figure 128: Preprocess sub steps 178
Figure 129: Simplified one dimensional residential wall 179
Figure 130: Mesh of Residential Wall example 180
Figure 131: Generic Conduction Element with assumption (54) 181
Figure 132: Solution Phase Sub Steps 185
Figure 133: Residential Wall Geometry 198
Figure 134: Unknowns for Residential Wall 199
Figure 135: Numerical Geometry of Residential Wall 201
Figure 136: Residential wall, Numerical Solution Mesh Refinement 201
Figure 137: Residential Wall, Numerical Temperature Solution 202
Figure 138: Residential Wall, Analytical and Numerical Results Comparison 203
Figure 139: Electrical Model Circuit 204
Figure 140: Electrical Circuit, Numerical Geometry 206
Figure 141: Electrical Circuit, Numerical Solution Mesh Refinement 206
Figure 142: Electrical Circuit, Numerical Voltage Solution 207
Figure 143 Electrical Circuit, Analytical and Numerical Voltage Distribution comparison 208
Figure 144: Infinite Slab with Joule Heating 209
Figure 145: Infinite Slab, Numerical Geometry 211
Figure 146: Infinite Slab, Numerical Solution Mesh Convergence for Temperature 212
Figure 147: Infinite Slab, Numerical Solution Mesh Convergence for Voltage 212
Figure 148: Infinite Slab, Numerical Solution Mesh Refinement Maximum Temperature 213
Figure 149: Infinite Slab, Numerical Solution Temperature Distribution 214
Figure 150: Infinite Slab, Numerical Solution Voltage Distribution 214
Figure 151: Infinite Slab, Temperature Distribution comparison 215
Figure 152: Infinite Slab, Voltage Distribution comparison 216
Figure 153: One Leg Thermoelectric Cooler example 216
Figure 154: One Leg Thermoelectric Cooler (TEC), Numerical Geometry 219
Figure 155: One Leg Thermoelectric Cooler (TEC), Net Cooling Mesh Convergence 220
Figure 156: One Leg Thermoelectric Cooler (TEC), Power Mesh Convergence 220
Figure 157: One Leg Thermoelectric Cooler (TEC), COP Mesh Convergence 220
Figure 158: One Leg Thermoelectric Cooler (TEC), Temperature Screenshot for $\Delta T=42$ 221
Figure 159: One Leg Thermoelectric Cooler (TEC), Electrical Potential Screenshot for $\Delta T=42$ 221
Figure 160: One Leg Thermoelectric Cooler (TEC), Percent Error for metrics 222
Figure 161: One Leg Thermoelectric Cooler (TEC), Net Cooling Comparison 223
Figure 162: One Leg Thermoelectric Cooler (TEC), Power Comparison 223
Figure 163: One Leg Thermoelectric Cooler (TEC), COP Comparison 224

Chapter 1: Introduction

1.1 *Motivation*

Roughly forty years have passed since transistor density was predicted by Moore's Law to double every 18 months or so (1). **Figure 1** projects Moore's Law logarithmic trend into the future.

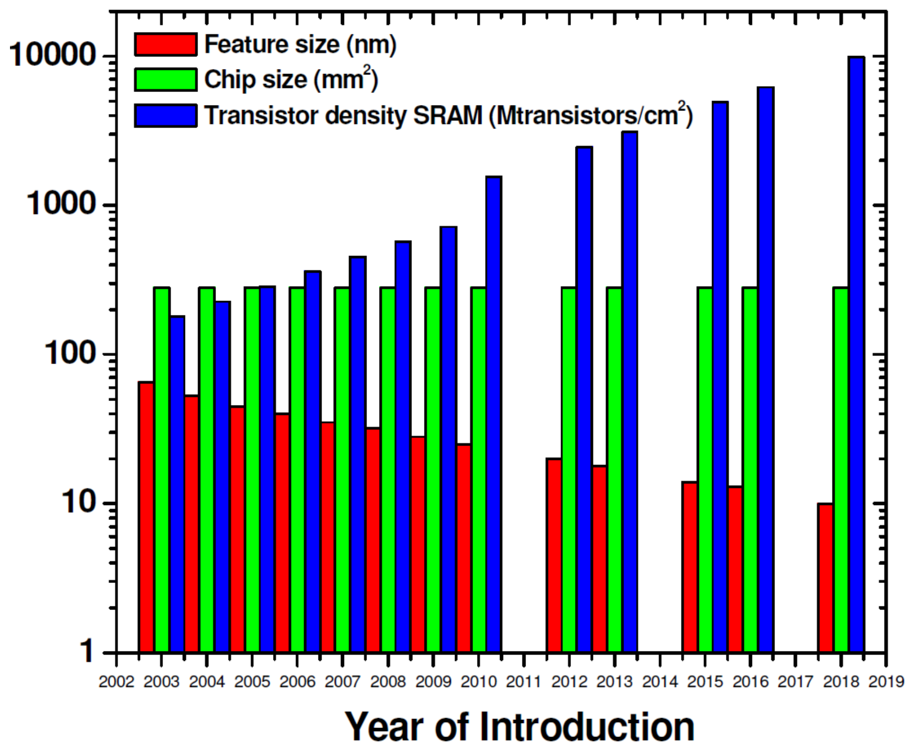

Figure 1: ITRS predictions of feature size, chip size and transistor density for high performance microprocessor chips (2)

Figure 1, published by the International Technology Roadmap for Semi conductors (ITRS), shows that even with the increase of transistor density and consequential decrease of feature size, the chip size remains relatively constant.

The relatively constant chip size and reduction of transistor size translates into a higher number of transistors per chip as well as faster chips. These consequences also increase the power dissipation as quantified by equation **1-1** (3).

1-1

$$P \approx NCV^2 f$$

$where$:
$P = power$ dissipation (W)
$N = number\ of\ transistors\ per\ chip$
$C = input\ capacity$
$V = peak - to - peak\ voltage\ of\ the\ signal$
$f = operating\ frequency$

Much effort has been made to reduce the capacitance and voltage of the devices, but the power continues to increase due to the tremendous increase of transistor density and speed.

The higher power dissipation of these devices comes at a cost of elevated temperature. Unfortunately, these elevated temperatures are one of the main causes of device failures (4). The rate of failure due to temperature is quantified by Black's equation shown in equation **1-2** (5).

1-2

$$MTF = AJ^2 e^{\frac{E_A}{k_B T}}$$

$where$:
$MTF = mean\ time\ to\ failure$
$A = constant$
$J = current\ density$
$E_A = activation\ energy$
$k_B = Boltzmann\ constant$
$T = absolute\ temperature$

Using the above equation, it is easily seen that a modest decrease of temperature, 10-15K, can double the device's reliability (6) for an activation energy of approximately 1eV.

The power dissipation of current silicon micro-processors is non-uniform because of system integration motivated by the increase of transistor density. The average heat flux is about 10-50W/cm^2, with a peak flux that can reach 6 times this value (7). **Figure 2** demonstrates an example of the heat flux variation on a silicon die.

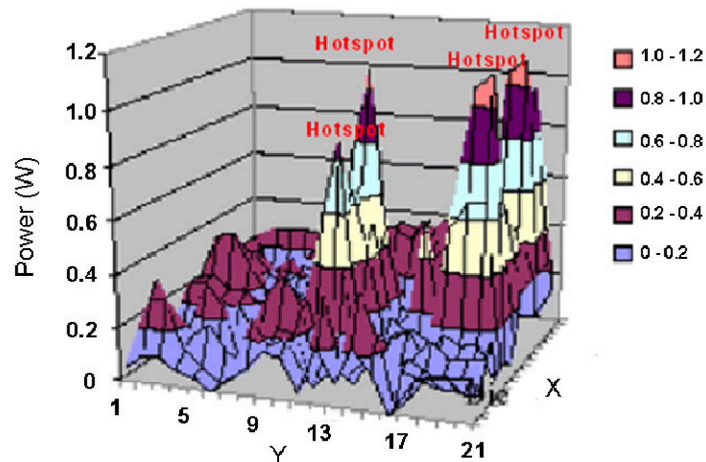

Figure 2: A typical heat flux map (8)

These highly localized high heat flux locations, or "Hotspots," produce localized high temperature zones on the silicon die shown in **Figure 3**.

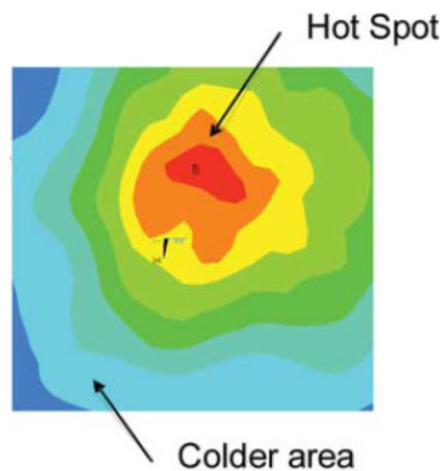

Figure 3: Temperature map corresponding to Figure 2 (8)

It is easy to see from equation **1-2** that hotspot's elevated temperatures reduce the overall reliability of semiconductor devices.

Thermal management requires that all temperatures remain below a maximum temperature, typically 90-110°C for silicon based semiconductor devices (4). As described before, hotspots have the highest temperature and cooling them adequately by conventional techniques entails reducing the temperature of the other regions far below their limit. This produces an over designed thermal management solution for the vast majority of the chip (4). Also, the cooling solution needed for devices that contain hotspots is more aggressive than solutions for uniformly heated devices. Overall, hotspots drive design and, consequently, their thermal management is an area that must be investigated to remediate their negative effects.

1.2 *Hotspot Cooling Methods*

Hotspot cooling methods have been extensively studied in the past and can be grouped into two classifications. The first discusses passive techniques and the second discusses active techniques

1.2.1 Passive Techniques

Passive cooling techniques do not have moving parts and require no external power. These typically rely on highly conductive materials, spreading layers, and natural convection. Highly conductive materials, such as aluminum (170 W/mk) and copper (about 380W/mk) are readily used to conduct heat away from temperature sensitive electronics (9). Diamond (2300W/mk) is only used for niche applications because of its high price as well difficulty of attaching to electronics (4) (9). Copper and aluminum are also used for natural convection heat sinks which use their high thermal conductivity to

transfer the heat at their base, to their fins, and ultimately to the surrounding ambient air. Their heat transfer capability is in the range of 2-25 W/m^2k (9).

There are many advantages and disadvantages associated with these techniques. Their low cost, low complexity and high reliability (no moving parts) are the main positive attributes. The limited heat removal capability when compared to hot spot heat fluxes and to active techniques is the main disadvantage. Moreover, these techniques require a large volume in which to operate.

1.2.2 Active Techniques

Active cooling technologies typically contain moving parts and require the input of external energy. The most commonly used technique involves a heat sink coupled with a fan that increases the overall heat transfer coefficient (4). This solution is widely used for moderate heat fluxes found in desktop applications but is incapable of removing localized heat fluxes associated with hotspots. Their heat transfer coefficient is in the range of 25-250 W/m^2k (9), although high performance, forced convection heat sinks can reach effective heat transfer coefficients of several kW/m^2K.

Other active techniques, such as micro-channel heat sinks and jet impingement use other fluids to remove heat from the electronics. Water has a high thermal conductivity, high density, high specific heat, and low viscosity (4). These characteristics combine to make this liquid a good fluid to remove high heat fluxes. Even though water allows the cooling solution to have a large heat transfer coefficient (100-20,000 W/m^2k), it is electrically conductive, which does not allow it to be in contact with the electronics (9). In order to sidestep this issue, copper or aluminum plates are placed onto the electronics, effectively enclosing the water, but placing several contact resistances in the

thermal stack. These contact resistances severely degrade the performance of these solutions.

In order to remove these contact resistances, di-electric fluids which are electrically non-conductive are used. However, their inherently low thermal conductivity suppresses their performance. In order to improve liquid cooling solutions (both water and dielectric fluids alike), the liquid can be pressurized and boiled. This provides an order of magnitude improvement on the heat transfer coefficient over single phase solutions and is in the range of 2500-100,000 W/m^2k (9). Even though the above solutions provide great heat transfer, they require a large system to operate. This typically includes the micro-channel heat sink, tubing, a pump, a reservoir, and a heat exchanger/condenser. Since all of these components must operate in conjunction to remove heat, the overall thermal solution volume and reliability becomes a concern.

1.2.2.1 Thermoelectric Coolers

Thermoelectrics provide an alternate active cooling solution for high flux cooling. Their high flux characteristics along with their fast time response, compact size, and reliability (no moving parts), translates into hot spot cooling capabilities (10), (11), (12), (13), (14), (15), (16). These devices can also be integrated into other cooling solutions, which further suit them for hot spot cooling (4). Conventional devices contain p-n junctions connected thermally in parallel and electrically in series by metal straps as shown by **Figure 4**.

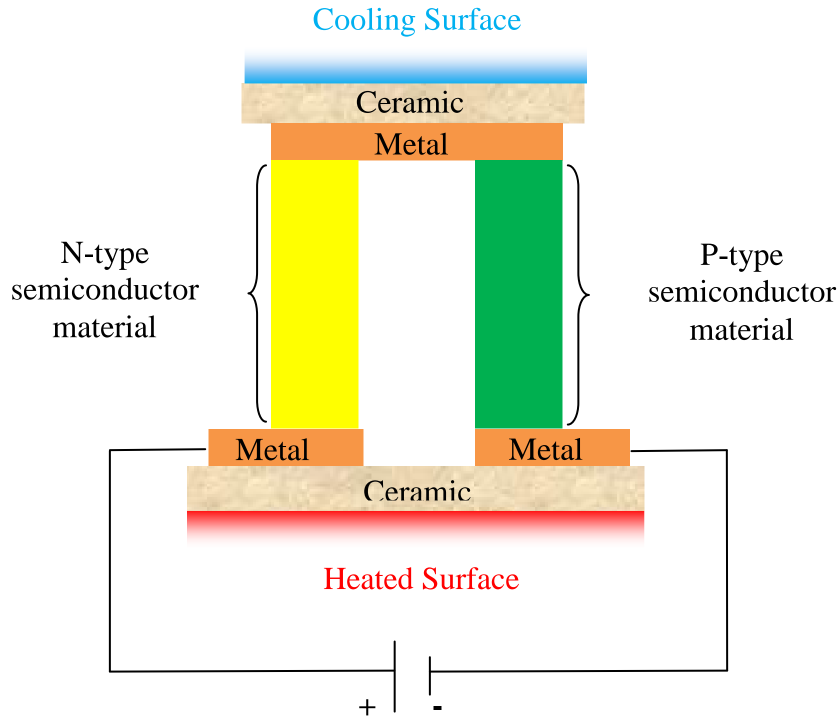

Figure 4: A 2 Leg Conventional Thermoelectric Cooler

Thermoelectric coolers use the Peltier effect to pump the heat from one surface to the other. A direct current voltage source is applied, and the transport of electrons pumps heat from one surface to another. This direction can be switched if the voltage source's terminals are switched. The amount of heat removed has been quantified in equation **1-3**.

$$Q_{Net\ Cooling} = (S_{P\ Leg} - S_{N\ Leg})T_C I - \frac{1}{2}I^2 R_e - K\Delta T \quad \textbf{1-3}$$

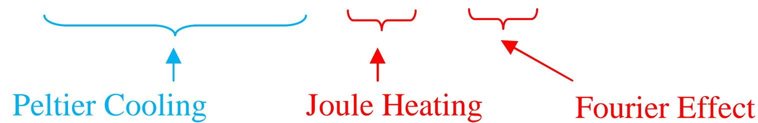

$where$:
$S = Seebeck\ Coefficient\ (V/K)$
$\Delta T = T_H - T_C\ (K)$
$R_e = Electrical\ Resistance\ (\Omega)$
$K = Thermal\ Conductance\ \left(\frac{W}{m^2K}\right)$

The cooling term is dependent on the Seebeck material property of both the p and n materials. The other terms describe the parasitic effects associated with all thermoelectric

devices. They are discussed in detail in **2.1 Main Thermoelectric Effects.** The heat removed translates into a temperature drop, and if the device is located appropriately, it can drop the temperature of the hotspot.

The main drawback of conventional thermoelectric coolers (TEC) is the inherent requirement to attach them to the electronic device being cooled. This adds several contact resistances into the thermal stack that would not have been there otherwise, and as such, severely reduces the cooling potential of these devices. Moreover, the low conductivity of these devices – when not operating - creates a thermal blockage effect. That is, at zero current the hotspot temperature could be greater than it would be if there were no thermoelectric cooler. These drawbacks motivate the research of other thermoelectric devices that are capable of hotspot cooling.

The thermoelectric device of interest for the presented work relies on the thermoelectric properties of the electronic component itself to produce the Peltier effect. Zhang and Shakouri have developed p-type boron doped ($10^{-9}cm^{-3}$) silicon micro-cooler as shown by **Figure 5** (4) (17).

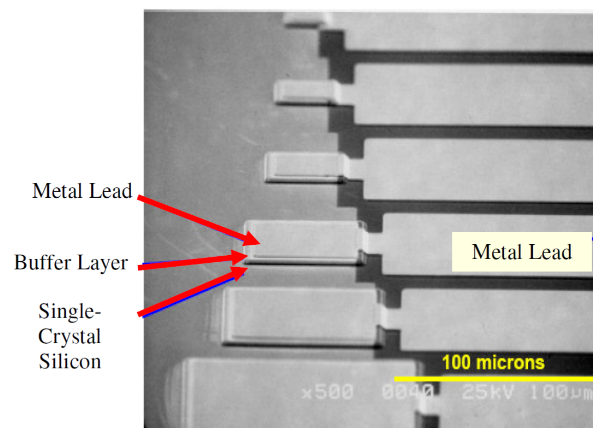

Figure 5: SEM photograph of silicon micro coolers (17)

They experimentally showed a maximum cooling of 1.2°C for a 40μm x 40μm cooler at an optimized current of 0.1A (4) (17). This produced a cooling heat flux of 580W/cm^2. Wang and Bar-Cohen were able to develop an analytical and numerical model of Zhang and Shakouri's experiment (18). These models were used in a parametric analysis that was able to demonstrate a net cooling flux to 6,000W/cm^2 for a 20μmx20μm micro cooler and a doping of 2.5×10^{19}cm^{-3} (18).

Using the above work as a foundation, Wang and Bar-Cohen moved forward to hotspot cooling using a self cooled device. It uses a silicon die as shown in **Figure 6** and **Figure 7**.

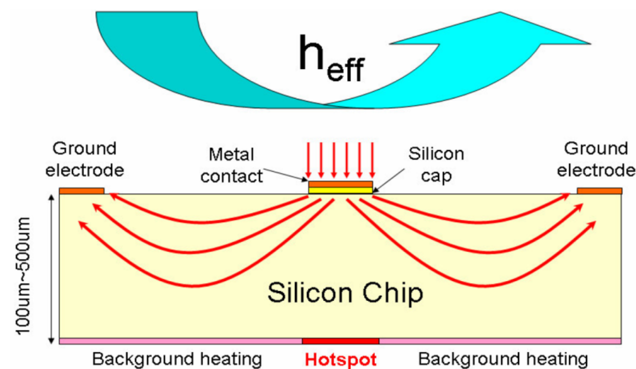

Figure 6: Side view of Silicon Self Cooler (19)

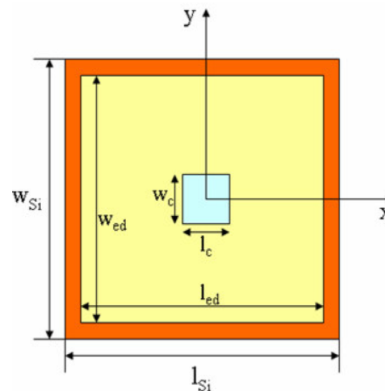

Figure 7: Top view of Silicon Self cooler (19)

A numerical and analytical model was used to understand the cooling dependence on geometrical parameters, doping concentrations, and contact resistances (19). It was

concluded that for a 70μm X 70μm hotspot on a silicon chip generating a 680 W/cm^2 heat flux and a background heating of 70 W/cm^2, hotspot cooling of 3^oC is achievable at the optimum parameters (19). More recently, Wang and Bar-Cohen were able to demonstrate 4.5^oC for a similar configuration with a germanium self cooler (20). The above results demonstrate the great potential for hotspot cooling and create the foundation for the presented work.

1.3 *Scope of Work*

Thermoelectric self coolers demonstrate great potential to provide high flux cooling required for hotspot remediation. As described above, germanium demonstrates higher self cooling capability than silicon, mainly because of its better thermoelectric properties, and as such, is the material of choice for this work. In essence, the objective of this thesis is to expand on Wang and Bar-Cohen's work on thermoelectric germanium self cooling devices. The specific contributions are: (1) validating the ANSYS 12.0 numerical models necessary for the work; (2) creating a germanium self cooling meta-model; (3) determining the difference between a constant voltage and constant current boundary condition; and (4) determining the potential for a bi-layer (Si/Ge) self cooling device.

This thesis contains both numerical and analytical simulations for germanium thermoelectric self cooler devices. It is organized into the following chapters.

Chapter 1 provides the motivation for this research which is rooted in Moore's law logarithmic trend of increasing transistor density. There is also a brief discussion on the several hotspot cooling methods, separated into passive and active techniques. Lastly,

conventional and self cooled thermoelectric devices are discussed as a promising technique for hotspot remediation.

Chapter 2 provides a brief introduction to the underlying phenomena of the thermoelectric cooler. The effects are grouped into reversible and irreversible effects and explained individually. The Peltier effect is given a solid state explanation and the equations, trends, and metrics used for thermoelectric coolers are discussed. Finally, typical configurations are discussed briefly, ending with previous research done on self cooling devices.

Chapter 3 develops a numerical simulation for Wang and Bar-Cohen's germanium thermoelectric self cooling device. Moreover, it imposes a constant voltage boundary condition. The hotspot temperatures and reductions associated with the application of current, cooler size, and die thickness are presented. The important trends are then compared to those developed from the self cooler with constant current boundary conditions. This comparison provides a bound on the performance for an actual thermoelectric self-cooler device. The detailed results of constant current are omitted because they have been previously published in reference (20) and demonstrate similar trends as the self cooler with constant voltage boundary conditions.

Chapter 4 applies Wang and Bar-Cohen's analytical silicon self cooling model to the germanium substrate. A meta-model is developed by using the numerical results from the self cooler with constant current boundary conditions and creating allocation factors which account for the non-uniform heat generation motivated by the non-uniform current path. The hotspot temperatures and reductions associated with the application of current, cooler size, and die thickness variations are compared to those from the self cooler with

constant current boundary conditions. The observed difference is found to explain the discrepancy between the meta-model and the numerical results.

Chapter 5 describes a bi-layer thermoelectric self cooling device containing one layer each of Silicon and Germanium. The percentage of germanium is varied and the hotspot temperature and hotspot reduction results are compared to those obtained with the same total die thickness of pure germanium. The bi-layer results are also compared to the same total die thickness of pure silicon . These differences demonstrate bi-layer structure benefits over single layer structures.

Chapter 6 summarizes the presented work in this thesis and provides recommendations for future work.

The Appendix is dedicated to validating the numerical models necessary for the presented work. The thermal and electrical models are validated independently and lay the foundation for the required coupling necessary to simulate thermoelectric coolers. Then, the thermal and electrical model is coupled with Joule heating, and Joule heating and the Peltier effect. These numerical coupling techniques are discussed in detail. The Joule heating coupled thermal-electrical model is validated using a classical infinite slab. The Joule heating and Peltier effect coupled thermal-electrical model is validated using a one leg thermoelectric cooler. The differences between the numerical and analytical solutions for all models are quantified and provide confidence for their use in the analysis of thermoelectric self cooling devices.

Chapter 2: The Thermoelectric Cooler

Thermoelectric cooling devices (TECs) are suitable for high flux spot thermal management applications and have high reliability due to their solid state nature (20). They are heat pumps that remove heat from one location and dissipate that energy to another location. Moreover, they convert thermal energy to electrical energy, and in the process, both reversible and irreversible phenomena occur.

2.1 Main Thermoelectric Effects discusses the effects that govern this process, and subsequently their performance. The performances of the thermoelectric devices are rooted in the interplay between the reversible effects, mainly the Peltier effect, and the irreversible effects, mainly Joule heating and the Fourier Effect (21). The Peltier effect determines the cooling potential of the device, whereas the irreversibility of Joule heating and the Fourier effect degrade the overall cooling performance.

Following the general explanation of the main effects, the Peltier effect is discussed as it pertains to a conventional thermoelectric cooler in **2.2 A Detailed analysis of the Peltier Effect**. This is done using solid state physics, for a single semi-conductor material, and then for the entire conventional package following the electron path.

Then, in **2.3 Thermoelectric Cooler Net Effects** , the reversible and irreversible effects of the conventional thermoelectric cooler are grouped to determine the net cooling power equality which demonstrates the main tradeoffs for conventional thermoelectric coolers (TEC).

Conventional Thermoelectric cooler metrics are discussed in **2.4 Thermoelectric Cooler Metrics**. These metrics reflect the performance of the coolers, and as such describe the maximum temperature difference between the cold and hot junction among

other metrics. These metrics are found by maximizing the net cooling power, balancing this equality, and then optimizing the aspect ratio of conventional thermoelectric coolers. The main metrics of concern are the power required to run the package, the coefficient of performance (COP), and the figure of merit (Z).

Section **2.5 Thermoelectric Materials and Current Devices** discusses why semiconductor materials serve as the best thermoelectric materials. It also dives into describing that high net cooling values are of interest of hotspot remediation is the design goal. Three main devices are discussed. The first two include either growing Bi_2Te_3 (or similar materials) legs or thinning the bulk material. The last device, discusses highly doping the semiconductor material containing the hotspot to deliver high P factor values. This last device presents the basic design used for the presented research.

2.1 *Main Thermoelectric Effects*

Thermoelectric coolers (TEC's) are governed by reversible and irreversible effects. The reversible effects include the Seebeck effect, the Peltier effect, and the Thomson effect (21). The parasitic or irreversible effects are an inevitable part of the solid-state package and are Joule heating and the Fourier effect (21). The Peltier effect determines the cooling potential of the device, whereas the irreversible of Joule heating and the Fourier effect degrade the overall cooling performance.

2.1.1 The Reversible Effects

The reversible effects of thermoelectric coolers describe the reversible conversion of electrical and thermal energies and consequently determine their cooling mechanisms. The reversible effects include the Seebeck effect, the Peltier effect, and the Thomson

effect (21). The effect that are of main importance to thermoelectric coolers is the Peltier effect (4).

2.1.1.1 The Seebeck effect

The Seebeck effect appears when two dissimilar materials, A and B, are joined at one end and the junction is held and a temperature (T1). **Figure 8** pictorially demonstrates the Seebeck effect.

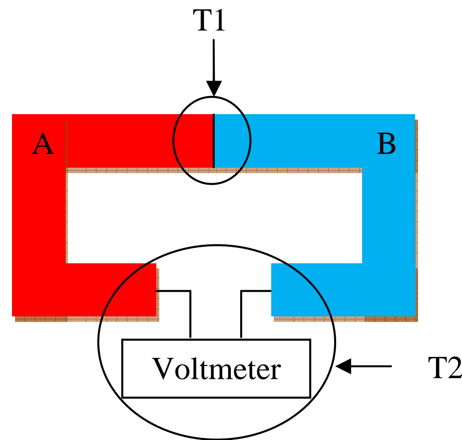

Figure 8: The Seebeck effect (2)

If the other end is held at a different temperature, T2, then the voltmeter will show a reading in micro volts (21). The voltage read is called the Seebeck Voltage (21). Consequently, the Seebeck effect discusses the phenomena of converting thermal energy to electrical energy (21).

The voltage read at the voltmeter in **Figure 8** is proportional to the temperature difference times a proportionality constant, "S", called the Seebeck coefficient. Equation **2-1** demonstrates this relationship (21).

$$dV_{Seebeck} = \pm SdT \tag{2-1}$$

$where:$
$S = Seebeck\ Coefficient\ (V/K)$
$dT = T1 - T2\ (K)$
$dV_{Seebeck} = Voltage\ (V)$

The “±” describes the switch of voltage sign when the materials “A” and “B” switch locations in **Figure 8**.

2.1.1.2 The Peltier effect

Compared to the Seebeck effect which discusses thermal to electrical energy conversion at zero current, the Peltier effect discusses the absorption or generation of heat when current is applied to the system pictorially represented in **Figure 9**.

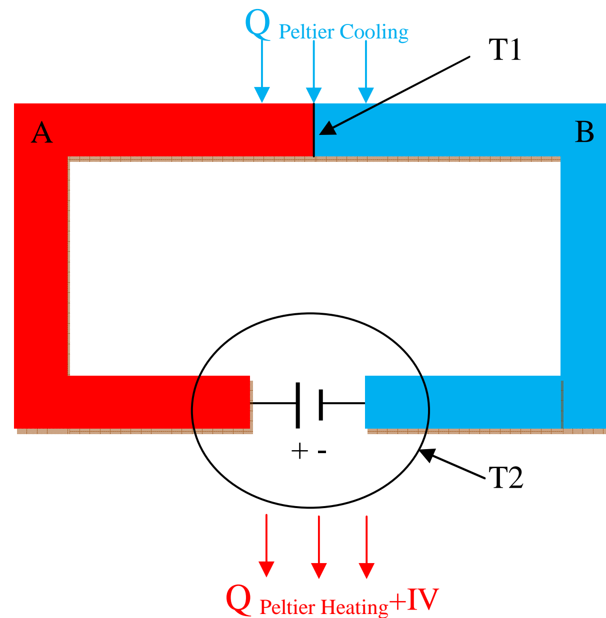

Figure 9: The Peltier Effect (2)

Two materials, A and B, have been joined in the above figure with their junctions held at T1 and T2. The amount of Peltier cooling and heating emitted from the system is proportional to the current and has been defined in equation **2-2.**

$$Q_{Peltier\ Cooling} = -\pi I \qquad \textbf{2-2}$$

$$Q_{Peltier\ Heating} = \pi I$$

$where$:
$\pi = Peltier\ Coefficient\ (V)$
$I = Applied\ current\ (A)$

The heat rejected at the "T2", or hot junction is the summation of Peltier Heating as well as the power applied to the thermoelectric device. This is because a thermoelectric device is a solid-state heat pump which transports thermal energy from one location to another, and in the process, must dissipate the energy needed for transport.

The coupling between the Seebeck and Peltier effects is described through the Kelvin relation in equation **2-4.**

2-3

$$\pi = ST$$

$where$:
$\pi = Peltier\ Coefficient\ (V)$
$S = Seebeck\ Coefficient\ (V/K)$
$T = Temperature\ (K)$
It is important to note that through the coupling of **2-2** and **2-3**, an increase in the Seebeck Coefficient directly increases the amount of Peltier and conversely thermoelectric cooling.

2.1.1.3 The Thomson effect

The Thomson effect was discovered during an experiment by William Thomson when he heated a metal bar in the middle, ran a current from one end to the other, and observed that the heat spread unequally among the two halves (21). Thus, this effect describes the absorption or generation of heat when current is passed through a homogenous material which has a maintained temperature gradient (21). This effect has been quantified by equation **2-4** (4).

2-4

$$q = \mu I \frac{\partial T}{\partial x}$$

$where$:
$\mu = Thomson\ Coeffeicent\ (\frac{\Omega}{m^2})$
$I = Current\ (A)$

$T = Temperature\ (K)$
Even though this effect is of importance, it creates a negligible effect in TECs (4).

2.1.2 The Irreversible Effects

The irreversible effects of thermoelectric coolers describe the parasitic mechanisms that degrade thermoelectric cooler performance. These parasitic effects are Joule heating and the Fourier effect.

2.1.2.1 Joule Heating

Joule heating is the volumetric heat generation that occurs when current passes though a material which has a finite electrical resistance. If the current passes through the material uniformly, then equation **2-5** can be used to quantify this effect (9).

$$Q_{Joule\ Heating} = I^2 R_{Electrical} \quad \textbf{2-5}$$

$where:$
$I = Current\ (A)$
$R_{Electrical} = Electrical\ Resistance\ (\Omega)$
This effect is readily used to quantify the amount of heat loss of a wire or resistor. **Figure 10** pictorially represents this effect.

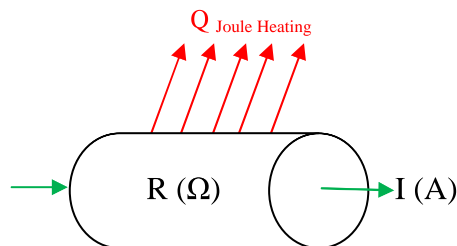

Figure 10: Joule Heating

2.1.2.2 The Fourier effect

Fourier's Law describes the one dimensional temperature distribution through the thickness of an infinite slab (infinite in the other two orthogonal directions) (9).

The Fourier heat flux is proportional to the temperature distribution times the thermal conductivity of the material. This has been quantified in equation **2-6.**

2-6

$$q''_{Fourier} = -k\frac{\partial T}{\partial x}$$

$where$:
$k = thermal\ conductivity \left(\frac{W}{mk}\right)$
$\frac{\partial T}{\partial x} = slope\ of\ the\ temperature\ distribution\ \left(\frac{K}{m}\right)$
The negative sign has been placed into the equation since heat moves in the direction of decreasing temperature (9).

Moreover, under steady state and no heat generation conditions, the temperature distribution becomes linear and equation **2-6** can be simplified to equation **2-7** (9)**.**

$$Q_{Fourier} = A_C q''_{Fourier}$$

$$Q_{Fourier} = -kA_C\frac{\partial T}{\partial x} = kA_C\frac{T_2 - T_1}{L} = kA_C\frac{\Delta T}{L}$$

$$Q_{Fourier} = kA_C\frac{T_2 - T_1}{L}$$

2-7

$$Q_{Fourier} = kA_C\frac{\Delta T}{L}$$

$L = length\ of\ infinite\ slab\ (m)$
$\Delta T = temperature\ difference\ (K)$
$A_C = cross\ sectional\ area\ (m^2)$
Figure 11 pictorially demonstrates the simplified form.

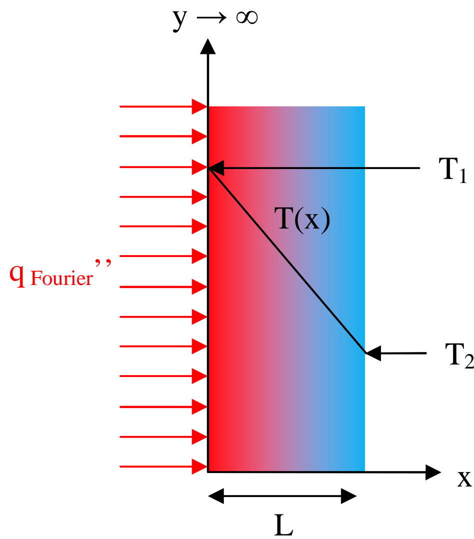

Figure 11: Fourier Law (9)

2.1.3 Summary of Thermoelectric Cooler (TEC) Effects

Thermoelectric coolers are solid-state heat pumps that remove heat from location and dissipate that energy to another location (21). This process is in general governed by reversible and irreversible thermal to electrical energy transformations. The main reversible effect is the Peltier effect. The Peltier effect determines the cooling potential of the device, whereas the irreversible of Joule heating and the Fourier effect degrade the overall cooling performance.

2.2 *A Detailed analysis of the Peltier Effect*

Thermoelectric cooler (TEC's) performance is governed by the interplay of reversible and irreversible effects. However, the main reversible cooling effect, the Peltier effect, was briefly touched upon by demonstrating the underlying formulas. A simplified conventional thermoelectric cooler (TEC) package along with solid state physics is used to describe underlying principle of the Peltier effect. Then a conventional

thermoelectric cooler (TEC) is analyzed to discuss the Peltier effect as one follows the electron path through the thermoelectric cooler (TEC).

2.2.1 Solid State Physics of the Peltier Effect

A conventional thermoelectric cooler (TEC) consists of highly doped semiconductor materials (22). Doping materials, such as silicon, reduces the resistivity, which in turn allows current to pass without excessive Joule heating. However, high levels of doping can also increase the Seebeck coefficient, which as described before, increases thermoelectric cooling (22). **Figure 12** demonstrates a simplified conventional thermoelectric cooler (TEC) package with an n-type semiconductor (in yellow) that has been highly doped to contain an excess of electrons. Moreover the conduction band electrons are the predominant charge carriers (4).

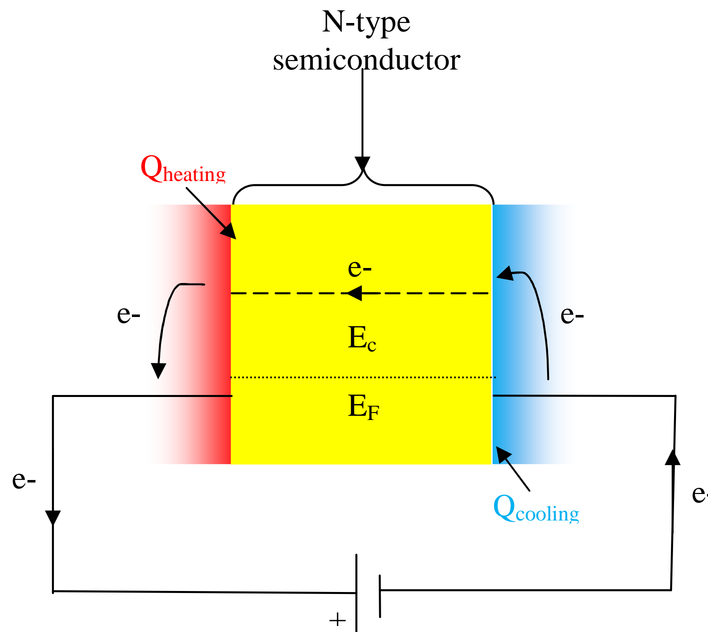

$$E_C = Conduction\ Band\ edge$$
$$E_F = Conduction\ Band\ edge$$
$$e^{-} = Electron$$
$$Q_{Cooling} = Peltier\ Cooling$$
$$Q_{Heating} = Peltier\ Heating$$

Figure 12: Simplified Conventional Thermoelectric (TEC) Cooler (4)

A constant DC voltage has been applied through metal wires to the ends of the n-type material. Viewing the orientation of the voltage source, the current runs clockwise, whereas the electrons run counter clockwise.

On the right portion of the semiconductor, electrons pass from the metal wire into the semiconductor. However, in order to accomplish this task they must jump in energy level due to difference between the conduction band edge (short dotted line) of the semiconductor and the Fermi level (long dotted line) of the metal wire (22). The difference between these energy levels, (E_F-E_C), is absorbed from the surroundings in the form of thermal energy determined by Peltier cooling.

Then, as the electrons leave the semiconductor and return back to the metal wire, they must move from the conduction band edge, back to the Fermi level, consequently releasing thermal energy in the form of Peltier heating (22). The movement of the electrons carries thermal energy from the right to the left, creating a cold flux on the right, and a hot heat flux on the left.

2.2.1.1 The Peltier Effects of a Conventional Thermoelectric

The package in **Figure 12** demonstrates a simplified thermoelectric cooling (TEC) package with one material. True conventional packages contain both n-type and p-type materials. The n-type materials, as discussed before, are doped to contain an excess of electrons, whereas the p-type materials are doped to contain an excess of protons. The excess of protons, instead of electrons, provides the same effect as discussed in **2.2.1 Solid State Physics of the Peltier Effect**, but with the Peltier cooling and Peltier heating occurring at opposite locations than the n-type material (1).

The location switch of Peltier cooling and Peltier heating is expressed explicitly through the Seebeck Coefficient sign change. N-type semiconductor materials have a negative Seebeck Coefficient, whereas p-type semiconductor materials have a positive Seebeck Coefficient. Moreover, thermoelectric coolers (TEC) use metal traces on ceramic substrates to provide structural rigidity, electrical series connection, and allow the materials, or legs, to be thermally parallel (1). This provides the thermoelectric package with a cooling surface for the electronic package and a heating surface which is usually attached to a heat sink.

Typical thermoelectric coolers (TEC) contain many p-type and n-type elements or "legs," but for the sake of simplicity, a two leg package has been displayed in **Figure 13.**

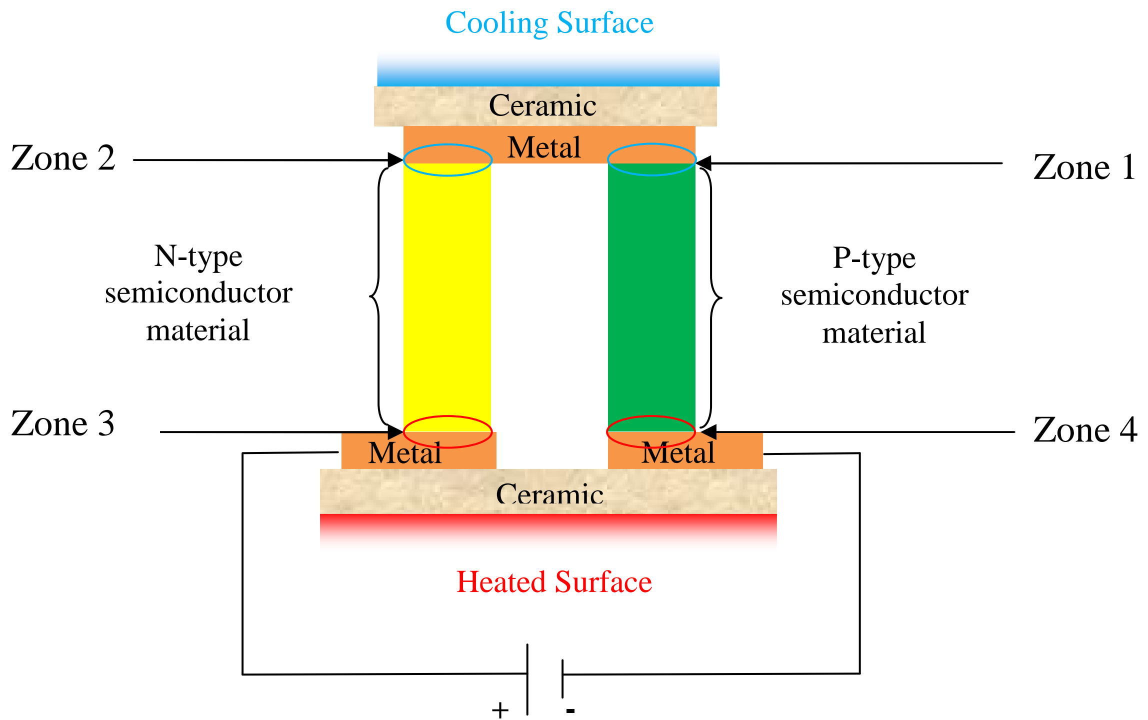

Figure 13: Conventional Two leg Thermoelectric Cooler (TEC)

The circled locations are where the semiconductor materials are joined with the metal traces, and because of the solid state physics discussed before, demonstrate either Peltier cooling or Peltier heating

2.2.2 Peltier Effect of Conventional Thermoelectric Cooler

The Peltier effect is an effect that occurs when electrons pass from one surface to another. Thus a detailed analysis that follows the electron path in **Figure 13** is presented here to show how the locations of Peltier cooling and heating. Moreover, many assumptions can be made that translate into simplified equations. They have been listed below.

1. The Thomson Effect can be neglected (23).
2. The hot and cold junctions have no effect on the electric circuits (23).
3. The p-type and n-type semiconductor materials are the same shape (23).
4. The thermal and electrical properties of the semiconductor are temperature independent (23).
5. The junction temperatures for the p-type and n-type are the same.

At Zone 1, the electrons migrate from the p-type leg to the metal, and for reasons described before, must absorb energy from their surroundings. At Zone 2 the electrons migrate through the metal/N leg interface, and consequently heat is absorbed because of their opposite doping.

Equation **2-8** formulates this heat transfer and **Figure 14** shows the electron path and the location of the cold junction temperature (20).

$$Q_{Peltier\ Cooling_{P\ Leg}} = (S_{P\ Leg} - S_{Metal})T_C I \approx S_{P\ Leg} T_C I \quad \textbf{2-8}$$

$$Q_{Peltier\ Cooling_{N\ Leg}} = (S_{Metal} - S_{N\ leg})TI \approx -S_{N\ Leg} TI$$

$$S = seebeck\ coefficient\ (\frac{V}{K})$$

$$T_C = absolute\ temperature\ of\ cold\ Juction\ (K)$$

$$I = current (A)$$

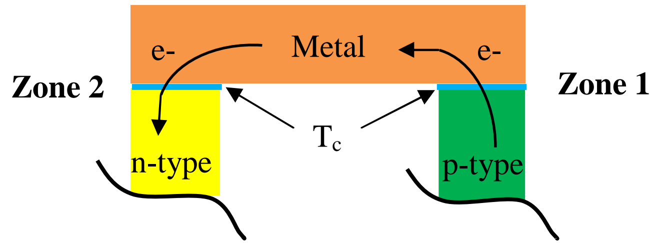

Figure 14: Zone 1 (right) and Zone 2 (right) demonstrating Peltier Cooling

The above equations assume that S_{Metal} is small when compared to that of the legs, and thus can be ignored (20).

The total Peltier Cooling can be obtained by summing the effects shown in equation **2-8** together after realizing that S_N and S_P are of opposite signs due to their opposite doping. Equation **2-9** defines the total Peltier Cooling (21).

2-9

$$Q_{Peltier\ Cooling} = (S_{P\ Leg} - S_{N\ Leg})T_{ColdSide}I$$

Peltier heating occurs at Zone 3 and 4 due to the solid state physics of thermoelectric coolers (TECs). The effects at each zone has been summed and displayed in equation **2-10** (21)**. Figure 15** displays the electron path and the location of the hot junction temperature.

2-10

$$Q_{Peltier\ Heating} = (S_{P\ Leg} - S_{N\ Leg})T_H I$$

$$T_H = absolute\ hot\ Jucntion\ temperature\ (K)$$

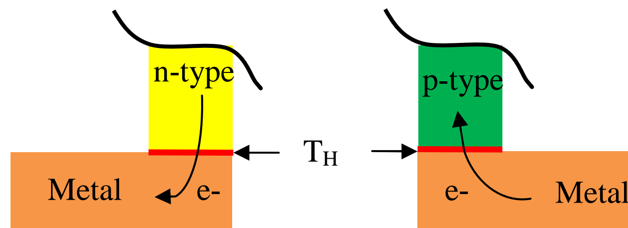

Figure 15: Zone 3 (left) and Zone 4 (right) demonstrating Peltier Heating

2.2.3 Summary of Detailed Peltier Effect Analysis

The Peltier effect occurs because electrons passing from conductors to highly doped materials (or vice versa) must either increase their energy, creating Peltier cooling, or decrease their energy, creating Peltier heating. In a conventional thermoelectric cooler, this process occurs for both p-type and n-type materials, but in opposite direction from each other due to their opposite doping. This allows the legs to be connected with metal trances in electrical series, but thermally parallel which sums the cooling and heating effects on their own respective surface.

2.3 *Thermoelectric Cooler Net Effects*

Conventional thermoelectric coolers, as shown by **Figure 13**, not only contain the Peltier effect discussed in **2.2 A Detailed analysis of the Peltier Effect**, but also contain irreversible effects. These irreversible effects limit the overall performance of the thermoelectric cooler and are Joule heating and the Fourier effect.

After some assumptions are made, the reversible and irreversible effects are clearly coupled in the net cooling power. The total Peltier cooling showed in equation **2-9** is balanced by half of the uniform volumetric heat generation through the legs (Joule heating) at the optimum current. Joule heating is typically minimized by reducing the leg height, which increases the Fourier effect, eventually balancing all three effects of the net cooling power and subsequently providing the best cooling that the thermoelectric package can provide.

2.3.1 Net Cooling Power

Determining the net cooling power is of importance because it demonstrates the coupling between the reversible effect, the Peltier effect, and the irreversible effects, Joule heating and the Fourier effect. However, before the equality is demonstrated, certain assumptions have been displayed below that simplify the analysis.

1. The Thomson Effect can be neglected (23).
2. The hot and cold junctions have no effect on the electric circuits (23).
3. Other forms of heat transfer (convection and radiation) are negligible when compared to conduction within the package and are subsequently ignored (23).
4. The p-type and n-type semiconductor materials are the same shape (23).
5. The thermal and electrical properties of the semiconductor are temperature independent (23).
6. The junction temperatures for the p-type and n-type are the same.

The Net cooling power location is at the cold junctions of the conventional thermoelectric cooler (TEC). They have been demonstrated in **Figure 17.**

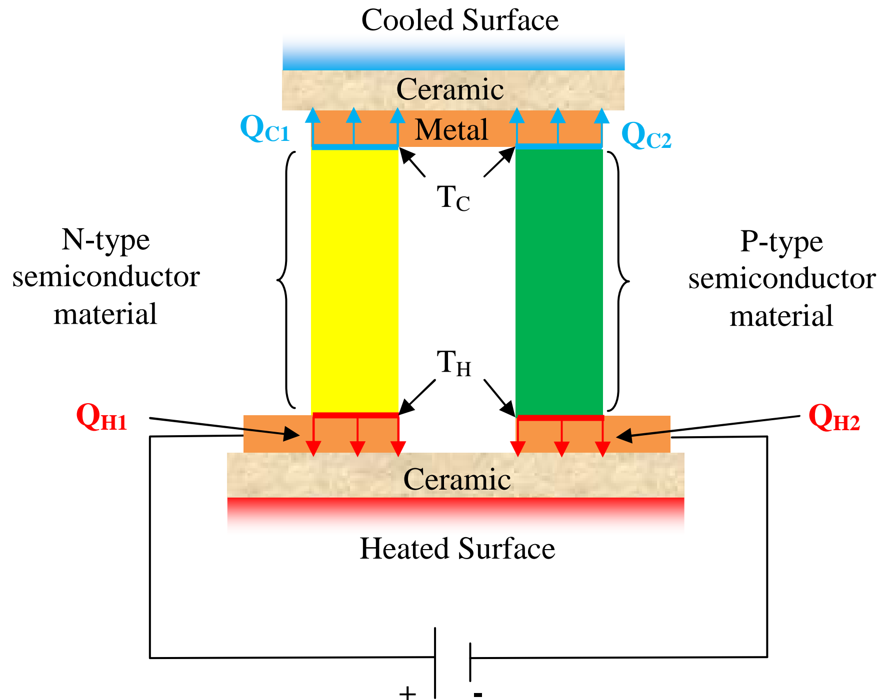

Figure 16: Conventional Thermoelectric Cooler (TEC) with Net Cooling Power Location demonstrated

Viewing the above figure, it is important to note that the net cooling power is the summation of the cooling power from the n-type and the p-type semiconductor material. Furthermore, the irreversible effects subtract from the summed Peltier cooling (equation **2-9**). This relationship has been given in equation **2-11** (4).

$$Q_{Net\ Cooling} = Q_{C1} + Q_{C2} = \left(S_{P\ Leg} - S_{N\ Leg}\right)T_C I - \frac{1}{2}I^2 R_e - K\Delta T \qquad \textbf{2-11}$$

Peltier Cooling | Joule Heating | Fourier Effect

$where:$
$\Delta T = T_H - T_C\ (K)$
$R_e = Electrical\ Resistance\ (\Omega)$
$K = Thermal\ Conductance\ \left(\frac{W}{m^2K}\right)$

The above equation contains simplified terms, specifically electrical resistance (R_e) and thermal conductance (K), which are effective terms accounting for both the p-type and n-type semiconductor materials. These base terms have been displayed in below

$$R_e = Electrical\ Resistance\ (\Omega) = \rho_p \frac{L_p}{A_p} + \rho_n \frac{L_n}{A_n}$$
$$K = Conductance\ \left(\frac{W}{m^2K}\right) = k_p \frac{L_p}{A_p} + k_n \frac{L_n}{A_n}$$

$where:$
$T_H = Absolute\ Hot\ Jucntion\ Temperature\ (K)$
$k_i = i - type\ Thermal\ Conductivity\ (\frac{W}{mK})$
$L_i = i - type\ Leg\ Height\ (m)$
$\rho_i = i - type\ Resistivity\ (\Omega m)$
$A_i = i - type\ Cross\ Section\ Area\ (m^2)$

The first term in the above equation is the linear current dependent Peltier Cooling effect. The second term is the quadratic current dependent Joule heating. This ½ coefficient arises because the uniform current passing through the legs creates uniform volumetric

heating. Thus, it is easily seen that half of the Joule Heating is felt at the top, or cold junctions, and half is felt at the bottom, or hot junctions. The last term in the equation is the Fourier Effect as described by equation **2-7**. The last two terms in the equation are appropriately subtracted from the cooling since they are parasitic. There is also a net heating power that has been displayed below in equation **2-12** (4).

$$Q_{Net\ Heating} = Q_{H1} + Q_{H2} = \underbrace{\left(S_{P\ Leg} - S_{N\ Leg}\right)T_C I}_{\text{Peltier Heating}} + \underbrace{\tfrac{1}{2} I^2 R_e}_{\text{Joule Heating}} + \underbrace{K\Delta T}_{\text{Fourier Effect}} \qquad \textbf{2-12}$$

2.3.2 Conventional Thermoelectric Cooler Cooling Tends

Understanding the typical TEC cooling trend is vital in developing viable TEC packages. Equation **2-11** will be used to explain the trend described in **Figure 17** and **Figure 18** since the net heat transfer translates into a current and leg height dependent temperature.

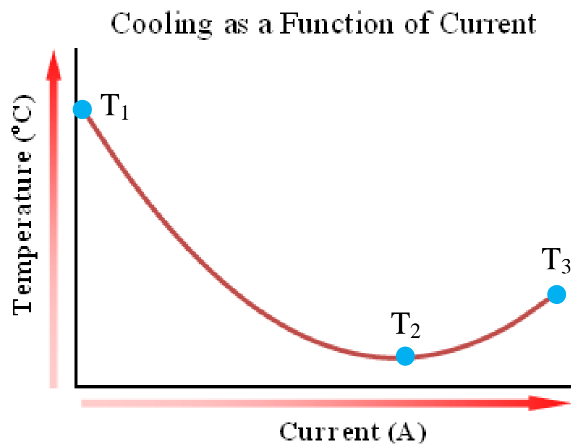

Figure 17: TEC cooling as a function of current

The cooling trend begins at temperature T_1 which occurs at zero current. As current is applied, the temperature initially drops linearly due to the Peltier cooling's linear

dependence on current. At larger currents, Joule heating becomes comparable with Peltier cooling. This balance of effects occurs at "T_2" and demonstrates the minimum temperature that can be accomplished by current. At currents larger than those that create the minimum temperature, Joule heating becomes dominate and the temperature begins to rise as demonstrated by "T_3".

Thus for each leg height, there is an optimum current that produces a minimum temperature. However, if the Joule heating was reduced, which is typically done by reducing the height of the TEC legs, the temperature would decrease further since there is less material to contribute to volumetric heating. Unfortunately, this effect is limited by the back conduction effect. This interplay between back conduction and Joule heating has been demonstrated in **Figure 18**.

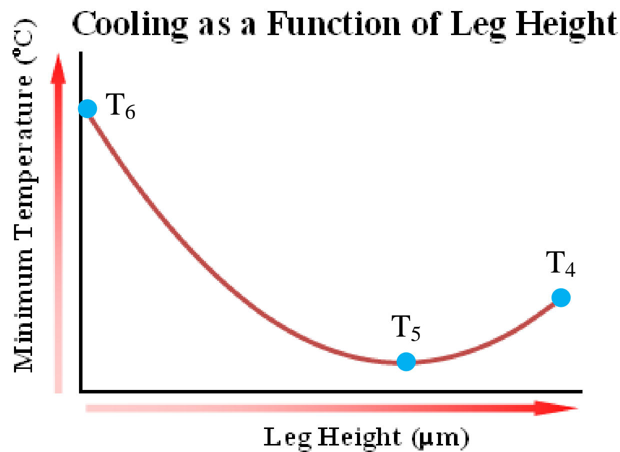

Figure 18: TEC cooling as a function of leg height

The above graph is constructed by varying the current for a specific leg height and finding the minimum temperature, as was done in **Figure 17**. Then, these minimum temperatures are recorded for various leg heights, and plotted against minimum temperature.

At T_4, the leg height is too large to produce the minimum cooling. As the leg height is reduced, volumetric heating is reduced, which reduces the temperature. At T_5, the leg height is small enough that the back conduction has become comparable to the Joule heating effect. Ss demonstrated by T_6, leg heights smaller than those that produce T_5, further degrade performance.

2.3.3 Summary of the Conventional Thermoelectric Coolers

Conventional thermoelectric coolers contain coupled reversible and irreversible effects. These effects are coupled through the net cooling power (equation **2-11**). The net cooling power demonstrates the need to several different currents, to find the balance between Peltier cooling and Joule heating. Moreover, several geometric variations are computed to balance back conduction with Joule Heating. Overall, the net cooling power demonstrates the main tradeoffs that occur in thermoelectric coolers as well as the importance of current and geometric variations.

2.4 *Thermoelectric Cooler Metrics*

The performance of conventional thermoelectric coolers is reflected in the presented metrics. Equation **2-1,** equation **2-11,** and equation **2-12** aid in the development of the power and coefficient of performance (COP) metric. The other metrics of concern are found by maximizing the net cooling power, balancing this equality, and then optimizing the aspect ratio for conventional thermoelectric coolers. This process provides the maximum temperature difference between the hot and cold junction, and the figure of merits

2.4.1 Power and Coefficient of Performance (COP)

The power applied to these devices, as well as their efficiency, or coefficient of performance (COP), is of important to thermal engineers. The power can be found by multiplying the voltage times the applied current (24). The total voltage of the thermoelectric cooler (TEC) is equal to the Seebeck voltage (see **2.1.1.1 The Seebeck effect**) plus the resistive voltage drop (21). The total voltage equality has been shown in equation **2-13** (4).

$$V_{Total} = (S_{P\,Leg} - S_{N\,Leg})\Delta T + IR_e \qquad \textbf{2-13}$$

Multiplying equation **2-13** by current provides the power required to operate the thermoelectric cooler (TEC) and is found in equation 2-14**.**

$$Power_{TEC} = (S_{P\,Leg} - S_{N\,Leg})\Delta T I + I^2 R_e \qquad \textbf{2-14}$$

The efficiency of conventional thermoelectric coolers is more easily understood when the derivation starts at equation **2-11**. They have been simplified and displayed as equation **2-15** (21).

$$Q_{\,Net\,Cooling} = (S_{P\,Leg} - S_{N\,Leg})T_C I - \frac{1}{2} I^2 R_e - K\Delta T \qquad \textbf{2-15}$$

The performance of a thermoelectric cooler (TEC) is typically viewed as the efficiency of a refrigerator or coefficient of performance (COP). It is defined by the desired output divided by the required input (25). The desired output is the net cooping power (equation **2-15**) and the required input is the power applied to the package (equation **2-14**). The COP of a thermoelectric cooler is shown in equation **2-14** (4).

$$COP_{TEC} = \frac{Q_{\,Net\,Cooling}}{Power_{TEC}} = \frac{(S_{P\,Leg} - S_{N\,Leg})T_C I - \frac{1}{2} I^2 R_e - K\Delta T}{(S_{P\,Leg} - S_{N\,Leg})\Delta T I + I^2 R_e} \qquad \textbf{2-16}$$

2.4.2 Maximum Hot and Cold Junction temperature Difference (ΔT_{Max})

In order to determine other conventional thermoelectric cooler (TEC) metrics, such as the maximum cooling between the hot and cold junction and the figure of merit, or "Z factor," the net cooling power (equation **2-15)** must be optimized.

The net cooling power is quadratic with current, and when the derivative of the function reaches zero, the maximum cooling power has been reached (21). Thus, finding this optimal current value is of importance since it provides the maximum cooling power after substituting the optimum current back into equation **2-15** (21).

The maximum cooling power occurs when the Peltier cooling, Joule Heating, and Fourier effect have balanced each other perfectly and subsequently created a thermally insulated cold junction. The solution to this outlined process has been provided in equation **2-17** (21)**.**

$$\Delta T_{Max} = \frac{\left(S_{P\ Leg} - S_{N\ Leg}\right)^2 {T_C}^2}{2KR_e} = \frac{1}{2}\ Z\ {T_C}^2 \qquad \textbf{2-17}$$

2.4.3 Figure of Merits

To determine the figure of merit for the conventional thermoelectric cooler (TEC) another optimization must be found. Viewing equation **2-17**, it is clear that the maximum temperature difference can be increased if the denominator ("KR_e") is minimized (21). This is done by assuming the lengths of n-type and p-type are the same and using the area aspect ratio as the optimization parameter (21).

After this is performed, the figure of merit, or the Z factor, is determined. It has been displayed in equation **2-18** (21).

$$Z = \frac{\left(S_{P\ Leg} - S_{N\ Leg}\right)^2}{KR_e} = \left(\frac{S_{P\ Leg} - S_{N\ Leg}}{\left(k_p\rho_p\right)^{\frac{1}{2}} + \left(k_n\rho_n\right)^{\frac{1}{2}}}\right)^2 \quad \textbf{2-18}$$

Equation **2-18** can be further simplified if the following list is held.

1. The Seebeck are assumed to be equal but opposite.
   $S_n=S_p=S$
2. both legs are Thermally equal,
   $k_n=k_p=k$
3. both legs are electrically equal,
   $\rho_n= \rho_p=\rho$
4. and both legs are geometrically equal,
   $A_n=A_p=A$
   $L_n=L=L$

This produces equation **2-19** (26)**.**

$$Z = \frac{S}{k\rho}^{2} \quad \textbf{2-19}$$

As shown by equation **2-19**, the "Z" factor is geometrically independent. Moreover, it provides a value which is proportional to the material's thermoelectric potential. In other words, higher "Z" factor materials demonstrate more thermoelectric cooling.

The above figure of merit is used when the Fourier Effect is of important. This is not always the case, especially when considering a "self cooled" geometry which uses the semiconductor device itself as the thermoelectric cooler (18). In these cases, the "Power Factor" is used, which eliminates the thermal conductivity from the "Z." This figure of merit is shown in equation **2-20.**

$$P = \frac{S^2}{\rho} \quad \textbf{2-20}$$

The above figure of merits demonstrates that the best thermoelectric materials have the highest Seebeck Coefficient, lowest electrical resistivity, and lowest thermal conductivity possible.

2.4.4 Summary of Conventional Thermoelectric Cooler Metrics

The performance of conventional thermoelectric coolers is reflected in the presented metrics. The net cooling power is vital to developing all of the presented metrics. Using the equation without modification, the power and efficiency of thermoelectric coolers (TEC) is found. The net cooling is maximized, balanced, and further optimized to find the other metrics of concern (maximum temperature difference and the figure of merits).

2.5 *Thermoelectric Materials and Current Devices*

Highly doped semiconductor materials serve as the best thermoelectric materials since they contain a high "Z" factors and "P" factors. Current thermoelectric coolers apt for hot spot remediation require a high net cooling flux that can be achieved with short Bi_2Te_3 legs. Thin Film Thermoelectric Coolers (TFTEC) are created by growing the material through co-evaporation (27), co-sputtering (28), or electrochemical deposition (29) (30) among other processes. Bulk miniaturized coolers accomplish small leg heights by thinning the bulk Bi_2Te_3 legs. The last device of interest consists of highly doping the device containing the hotspot (silicon) for high P factor values and produces the highest net cooling power of all three device types.

2.5.1 Common Materials

As shown by equation **2-20** and **2-19**, ideal thermoelectric materials demonstrate the highest "Z" factor and power factor. Such a material contains the highest Seebeck Coefficient, the lowest resistivity, and the lowest conductivity possible.

For metals the thermal conductivity is in-directionally proportional to the electrical resistivity as governed by the Wiedmann-Franz law (4). Thus it is impossible to reduce the thermal conductivity while reducing the electrical resistivity. In semiconductors, the thermal conductivity is predominantly governed by phonon movement with little dependence on electron movement (4). Thus, the electrical resistivity, which is governed by electron movement, can be decreased without great increases in thermal conductivity. This is usually accomplished through heavy doping because the "mass difference scattering in semiconductors reduces the lattice thermal conductivity with little increase of the electrical resistivity" (4), (31).

Bismuth telluride-based materials are currently the best commercial thermoelectric materials since they have the highest Z factor and P factor. The ZT (Z factor times temperature) values have recently reached values above one. Ettenberg et al. were able to create a p-type bismuth telluride material with a ZT value of 1.14 at 300K (32). This material was specifically $(Bi_{0.25}Sb_{0.75})_2(Te_{0.97}Se_{0.03})_3$ (32). Yamashita el al, have shown ZT values of 1.19 at 298K for the n-type $Bi_2(Te_{0.94}Se_{0.06})_3$ and 1.14 at 308K for the p-type $(Bi_{0.25}Sb_{0.75})_2Te_3$ alloy (4), (33), (34), (35).

Bismuth telluride legs are typically extruded or hot press sintered. This limits the dimensional to 1.8 X 3.4 X 2.4mm and 62 X 62 X 5.8mm (x,y,z dimensions) (4). Even though this provides a maximum cooling at room temperature of about 70°C, it only delivers a 5 to 10 W/mK cooling heat flux (4), (36). However, as described in **2.3.2 Conventional Thermoelectric Cooler Cooling Tends,** this heat flux potential can be substantially increased by decreasing the

leg height. Consequently, thermoelectric coolers applicable for hot spot cooling display heights in micro meters.

2.5.2 Thin Film Thermoelectric Coolers (TFTEC)

The Thin Film Thermoelectric Coolers (TFTEC) have the advantage of having low leg heights which translate into a high-flux cooling abilities and are apt for mass production (4). They use various techniques to deposit bismuth telluride-based materials. These methods include co-evaporation (27), co-sputtering (28), electrochemical deposition (29) (30), and other techniques.

Zao et al made p type and n type films using the co-evaporation technique (4) (27). He used antimony and tellurium to make p type Sb_2Te_3 films and bismuth and tellurium to make n type Bi_2Te_3 films (4) (27). These films have a Z value of $1.04E^{-3}$, which translates to a ZT (Z factor time temperature in Kelvin) of 0.32 (4) (27). The cooling performance of the experiment is shown in **Table 1** for the optimized cooling current of 55mA (4) (27).

Böttner et al developed two-wafer processes to create TFTECs (4) (28). These TFTEC were soldered together using chip-to-chip, chip-to-wafer, or wafer-to-wafer techniques (4) (28). The thermoelectric materials consisted of n-type $Bi_2(Se,Te)_3$ and p-type $(Bi,Sb)_2Te_3$ and were grown using the co-sputtering technique to the height of 20µm (4) (28). The cooling performance of the experiments is shown in **Table 1** for the optimized cooling current of 2.1A (4) (28).

Snyder et al used the MEMS process, electrochemical deposition, to make TFTECs (4) (37). The cooler contained 63 n-type legs made of Bi_2Te_3 and 63 p-type were

made of $Bi_{2-x}Sb_xTe_3$ all having heights of 20μm (4) (37). The cooling performance of the experiments is shown in **Table 1** for the optimized cooling current of 110mA (4) (37).

Su-Kyum Lim et al characterized electrodeposited bismuth-antimony-telluride (Bi-Sb-Te) and antimony-telluride films (Sb-Te) (38). Characterization was performed using a x-ray diffractometer and the Seebeck values were found at room temperature by applying a 20°C temperature difference at both ends of the films (38). The resistivity values were measured using a 4-point probe and the power factor was calculated using equation **2-20** (38). Furthermore it was hypothesized that the high power factor of the antimony-telluride films was due to their amorphous state and their stoichiometry similar to Sb_2Te_3 (38). Their experimental results are found in **Table 1**.

Chowdhury et al developed bismuth telluride based superlattice thermoelectric thin film coolers using metal-organic chemical vapor deposition (39). Bi_2Te_3/Sb_2Te_3 P type and $Bi_2Te_3/Bi_2Te_{2.83}Se_{0.17}$ superlattices were created and assembled into a 7 by 7 cooler (39). (39). The TEC was integrated into a package as shown by **Figure 19**. This figure also shows an IR image of the heaters, both hotspot and background, on the test chip.

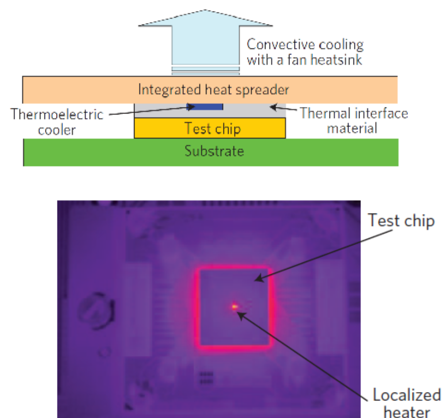

Figure 19: Chowdhury et al Thermoelectric Cooler (TEC) Package

They experimentally ran a background heating of 42.7 W/cm^2 and a hotspot (400μm x 400μm) heating of 1,2.50W/cm^2. They published a high cooling value of 15.8^{o}C on a silicon thermal chip with a hotspot. This cooling value is taken from the package without the thermoelectric device minus the cooler at optimum current (39). Moreover, 7.6^{o}C of the cooling was attributed by replacing the lower conductivity TIM over the hotspot by the higher conductivity cooler and was referred to as “Passive cooling” (39). Thus only 7.3^{o}C of cooling was observed if the point of reference only considers the package with the cooler integrated (39). Their experimental results are found in **Table 1**.

Bulman et al researched the potential of single and multistage coolers (40). They created a single level thermoelectric device using superlattice strips of epitaxial n and p-type $Bi_{2_x}Sb_xTe_{3_y}Se_y/Bi_2Te_3$ (40). They demonstrates exceptional maximum cooling in a vacuum by either powering all three stages and less cooling by powering all three states by two wires. Their experimental results are found in **Table 1**.

J. Lybeck et al studied the thermoelectric properties of other thermoelectric materials besides bismuth-telluride compounds (41). They used an atomic layer deposition technique to deposit $[Ca_2CoO_3]_{0.62}[CoO_2]$ p-type TFTECs (41). They used the temperature dependence of the annealing temperature to vary the oxygen content of the films resulting in the experimental results found in **Table 1**.

Table 1: TFTEC Cooling Performance

Author/Year	**Growth Method**	**Thermoelectric Properties p-type**	**Thermoelectric Properties n-type**	**ΔT_{max} (°C)**	**q_{max} (W/cm^2)**
Zou (**27**)	Co-	S=160μV/K	S=-200μV/K	15.5 at	N/A

/2002	evaporation	ρ=3.12E^{-5} Ω m P=0.82 mW/K^2-m	ρ=1.29E^{-5} Ω m P=3.10 mW/K^2-m	25	
Böttner **(28)** /2001	Co-sputtering	S=180μV/k ρ=1.30E^{-5} Ω m P=2.5mW/K^2-m	S=-178μV/k ρ=1.95E^{-5} Ω m P=1.57 mW/K^2-m	48 at 25	100 at 25°C
Snyder **(37)** /2001	Electrochemical Deposition	S=60-100μV/K ZT=0.01		2.0 at 80	7
Su-Kyum Lim et al **(38)** /2009	Electrodeposition	$S_{Bi-Sb-Te}$=21-71 μV/k $P_{Bi-Sb-Te}$=0.12 mW/K^2-m		-	-
		S_{Sb-Te}>250 μV/k P_{Sb-Te}=5.7 mW/K^2-m		-	-
Chowdhury **(39)** /2009	Chemical vapor deposition	ZT > 2		7.3	13,000
Bulman et al **(40)** /2009	Epitaxy	S=510μV/K ZT =0.73		102	-
J. Lybeck **(41)** /2010	Atomic layer deposition	$S_{[Ca2CoO3]0.62[CoO2]}$ 113 and 128 μV/k $S_{[Ca2CoO3]0.62[CoO2]}$ =0.11 and 0.14 mW/K^2-m		-	-

The above table demonstrates that the publications vary widely and contain “Z” factors less than one. This is due to the difficulty in maintaining the stoichiometry of bismuth telluride compounds (4).

2.5.3 Bulk Miniaturized Thermoelectric Coolers

Bulk miniaturized thermoelectric coolers benefit from the high "Z" factor of bulk bismuth telluride materials as well as a thinning process which reduces their leg heights. This thinning, as described in **2.3.2 Conventional Thermoelectric Cooler Cooling Tends**, produces significant improvements in the cooling potential of thermoelectric coolers (TEC) (4).

Semenyuk at Thermion Inc. has done significant work on bulk miniaturized thermoelectric coolers since the 1960s (4) (42). In 1967, he successfully thinned bismuth telluride legs from 1-2 mm to 130µm, and produced a net cooling of 38°C and a cooling heat flux of 95W/cm^{2} (4) (43). These results were limited by the materials of the 1960s (Z=1.8E^{-3}K^{-1}) as well as high electrical contact resistances (4) (43). In 1994 he was able to improve these results using better thermoelectric materials (Z=2.6 E^{-3} K^{-1}) (4) (42) . Then, in 2006, he improved the overall performance of the coolers by using even better thermoelectric materials (Z=3.02 E^{-3} K^{-1}) to achieve 83.5^{o}C of cooling at 85°C (4) (44). A summary of the improvements through the years accomplished by Semenyuk in bulk miniaturized thermoelectrics have been placed in **Table 2**.

Table 2: Semenyuk's Bulk Miniaturized Thermoelectric Properties trends

Year	Leg Height (µm)	ZT	ΔT_{max} (^{o}C)	q_{max} (W/cm^{2})
1967 **(43)**	130	0.54	38°C at 30°C	95
1994 **(42)**	100	0.78	50°C at 30°C	100

1997 **(45)**	200	0.78	67°C at 30°C	65
2006 **(44)**	130	0.90	64.2^{o}C at 30°C	110
			83.5^{o}C at 85°C	132

Single crystal silicon has been the semiconductor material of choice for many years, but has yet to be accepted as a conventional thermoelectric material because of its high conductivity which produces a low “Z” factor. Moreover, the high Seebeck and low resistivity provide a high Power factor, which hint at a possible advantage over conventional thermoelectrics (Bulk miniaturized and TFTEC) (18). Zhang and Shakouri have developed p-type boron doped (10^{-9}cm^{-3}) silicon coolers (4) (17) shown by **Figure 20**.

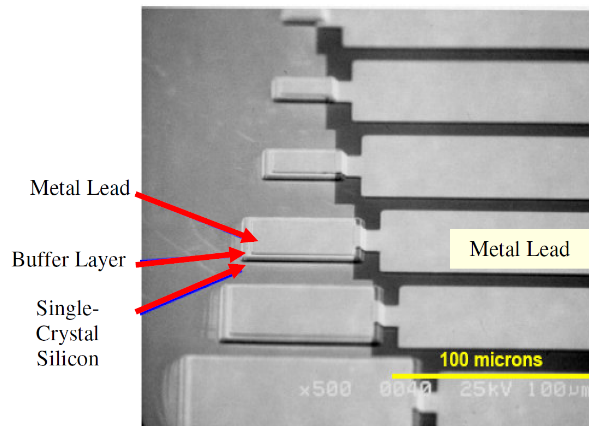

Figure 20: SEM photograph of silicon micro coolers (17)

The high level of doping, as discussed in **2.5.1 Common Materials**, increases the Seebeck coefficient without significantly increasing the resistivity. They experimentally showed a maximum cooling of 1.2^{o}C for a 40μm x 40μm cooler at an optimized current of 0.1A (4) (17). This produced a cooling heat flux of 580W/cm^{2} (4) (17).

2.5.4 Self Thermoelectric Cooler

Wang and Bar-Cohen were able to develop an analytical and numerical model of Zhang and Shakouri's experiment (18). These models allowed a parametric analysis and they were able to demonstrate a net cooling flux to 6,000W/cm^2 for a 20μmx20μm micro cooler and a doping of 2.5×10^{19}cm^{-3} (18).

Using the above work as a foundation, Wang and Bar-Cohen moved forward to hotspot cooling using a self cooled device. It uses a silicon die as shown in **Figure 21** and **Figure 22**.

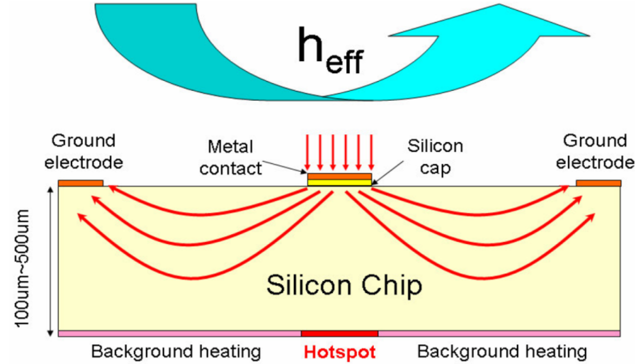

Figure 21: Side view of Silicon Self Cooler (19)

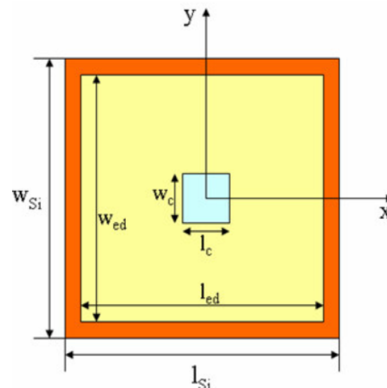

Figure 22: Top view of Silicon Self cooler (19)

A numerical and analytical model was used to understand the cooling dependence on geometrical parameters, doping concentrations, and contact resistances (19). It was

concluded that for a 70µm X 70µm hotspot area containing a 680 W/cm^2 heat flux and a background heating of 70 W/cm^2 a hotspot cooling of 3°C is available at the optimum parameters (19). More recently, Wang and Bar-Cohen were able to demonstrate 4.5^{o}C for a similar configuration with a germanium self cooler (20). The above results demonstrate great potential for hotspot cooling and create the foundation for the presented work.

2.5.5 Summary of Thermoelectric Materials and Current Devices

Highly doped semiconductor materials serve as the best thermoelectric materials since they contain a high Seebeck, low electrical resistivity, and low thermal conductivity. This produces a high "Z" factor and "P" factor. Current thermoelectric coolers apt for hot spot remediation require a high net cooling flux that can be achieved with short Bi_2Te_3 legs. Thin Film Thermoelectric Coolers (TFTEC) accomplish this by growing the material. Several grow methods are co-evaporation (27), co-sputtering (28), and electrochemical deposition (29) (30) among others. Bulk miniaturized coolers accomplish small leg heights by thinning the bulk Bi_2Te_3 legs. The last device of interest consists of highly doping the device containing the hotspot for high P factor values and produces high net cooling. This self cooled device creates the foundation for the presented research.

Chapter 3: Performance of Germanium Self Cooling Device

Wang and Bar-Cohen previously simulated a germanium self cooling device to determine its thermoelectric cooling potential to remedy hotspots (20). The model is adopted and the solution space expanded to determine the meta-model described in **Chapter 4: Germanium Self Cooling Meta Model**. This device uses the germanium die itself as the thermoelectric material to eliminate hotspots. Moreover, it assumes a constant current boundary condition at the Cooler electrode.

Practical electrodes that apply current never attain a constant current or constant voltage at their surface. In fact, they behave in a manner which is in between constant voltage and constant current performances. Thus, the performance band of the self cooling device can be predicted through the results comparison of the constant current and the constant voltage device simulations. The details of the constant current boundary conditions have been omitted since they demonstrate similar trends and tradeoffs as those in this chapter. This chapter discusses the results from the constant voltage self-cooling device and compares the two devices (constant current and constant voltage) to provide the performance band.

The geometry, material properties, and the boundary conditions of the constant voltage self cooling device are discussed in **3.1 Self Cooling Device** . The geometry and material properties for the constant current and constant voltage self cooling devices are identical for equal comparison. The device consists of a square germanium die which uses its inherent thermoelectric characteristics to provide hotspot remediation. Two

electrodes are placed on the top of die, with the peripheral electrode intended to provide the electrical ground necessary for electron transport and the other, called the Cooler, contains a constant voltage boundary condition. Because of the thermoelectric phenomena discussed in **2.3 Thermoelectric Cooler Net Effects**, the Cooler provides a localized thermoelectric cooling effect capable of hotspot remediation facilitated by the Cooler's placement in the center of the die and above the hotspot. There also exists a background heat flux surrounding the centered hotspot heat flux. The applied current, the Cooler size and the die thickness are the parametric variables used to determine the optimum germanium self cooling device.

The material properties are also discussed. It was previously found by Geballe and Hull's, that the best suited germanium die for self cooling consists of a highly doped n-type material with high Power factor ($P=S^2/\rho$) (46) (20). This translates into an arsenic doping concentration of $2.3\times10^{18}cm^{-3}$ (20) which provides a Seebeck coefficient of -467 μV/K (46) (20), an electrical resistivity of 50 μΩm (46) (20), and a thermal conductivity of 60 W/m-K (20) (47).

The boundary conditions can be split up into two parts, non-thermoelectric, and thermoelectric. The non-thermoelectric boundary conditions are identical for the constant current and constant voltage devices for equal comparison. The global cooling of the device is accomplished through an effective heat transfer coefficient over the top of the germanium layer. This value accounts for the heat transfer of a typical heat sink, heat spreader, and thermal interface materials (48) (49). The non-uniform heating at the bottom of the silicon layer is accomplished through the hot spot heat flux and a background heat flux.

The top of the Cooler electrode contains a constant voltage boundary condition which mandates a variable current translating into current and Peltier cooling/heating calculations for each element. Moreover, the non-uniform current flow through the germanium die produces non-uniform Joule heating. Thus, the thermoelectric boundary conditions are automatically calculated by the high order thermal-electrical element SOLID227 which couples the thermal and electrical field through Joule Heating and the Peltier Effect.

The cooling potential of the germanium constant voltage self cooler is discussed in **3.2 Numerical Results**. The presented results demonstrate similar trends and tradeoffs for both the constant current and voltage devices. Metrics were developed to rate the device. The temperature reduction and hotspot cooling effectiveness are also used for the constant current self cooling device. The main metric developed for the constant voltage self cooler was the efficiency or thermal impact factor. It is defined as the hotspot temperature reduction over the Power of the device.

The hotspot temperature reduction demonstrates a linear trend as the die thickness decreases with the maximum cooling of -3.9^{o}C at the 100µm die and 400µm Cooler size at 1.06A. The maximum hotspot cooling effectiveness of 0.81 occurs for the 200µm die thickness with a 700µm Cooler size at 2.29A. Moreover, the efficiency, or thermal impact factor strongly behaves like a decreasing "power trend," and as such, reaches its highest value within die thickness range tested of 13°C/W at the 100µm die thickness.

The performance band of the self cooling device is predicted through the results comparison of the constant current and the constant voltage self cooling devices as shown in **3.3 Performance Band of Germanium Self Cooling Device.** The results are different

for the self coolers because the different boundary conditions motivate different current density fields which in turn place the coolest temperature zones in different locations on the Cooler electrode. The constant current self cooler places the coolest temperature zone in the center of the Cooler electrode where the constant voltage self cooler places the coolest temperature on the Cooler electrode edge. Since the center hotspot temperature is right below the center of the Cooler, the constant current self cooler provides better performance for all cases studied.

At the 100µm die, the constant current and voltage self coolers are able to achieve maximum hotspot temperature reductions of -4.5^{o}C and -3.9^{o}C respectively. This temperature reduction decreases (absolute value) linearly due to the increase in thermal resistance between the hotspot and the Cooler electrode. At the 500µm die their temperature reductions are -4.0 ^{o}C and -2.8 ^{o}C for the constant current and voltage self coolers respectively.

The opposing effects of thermal and spreading resistance felt by varying the die thickness create an optimum die thickness and are captured in the hotspot temperature effectiveness metric. This metric determines the elimination of the temperature rise due to the introduction of the hotspot with values ranging from 1 (total elimination) to 0 (no effect). The constant current self cooler does not provide such an optimum die thickness within the range tested with values of 0.98 and 0.99 for the 300µm and 500µm dies respectively. The constant voltage self cooler is shown to provide an optimum of 0.81 at the 200µm die.

3.1 *Self Cooling Device*

The geometry for the self cooling device with constant voltage conditions (i.e. constant voltage self cooler) is adopted from the constant current self cooling device to allow for an accurate comparison and is discussed in **3.1 Self Cooling Device .** The geometry consists of a square n-type germanium die as the thermoelectric material for hotspot remediation. The hotspot is located at the bottom and center of the square die. This central location motivates the Cooler electrode to be placed directly over the hotspot and on the top of the die with the ground electrode on the top periphery of the die. This allows localized cooling above the localized high heat flux zone. The die thickness as well as cooler width are the geometric parametric variables that will lead to the best performing device discussed in **3.2 Numerical Results**.

In **3.1.2 Material Properties** Geballe and Hull's research is discussed to determine the best performing material properties. It is concluded that the n-type germanium die material whose doping concentration provides the best Power factor delivers the most hotspot cooling. The material contains a Seebeck coefficient of -467 μV/K (46) (20), an electrical resistivity of 50 μΩm (46) (20), and a thermal conductivity of 60 W/m-K (20) (47). These material properties are identical for the constant current and constant voltage devices for equal comparison.

The boundary conditions of the self cooling device, as shown in **3.1.3 Boundary Conditions** and consist of non-thermoelectric and thermoelectric boundary conditions. The non-thermoelectric boundary conditions are identical for the constant current and constant voltage devices for equal comparison. The global cooling of the device is accomplished through an effective heat transfer coefficient over the top of the germanium

layer. This value accounts for the heat transfer of a typical heat sink, heat spreader, and thermal interface materials (48) (49). The non-uniform heating at the bottom of the silicon layer is accomplished through the hot spot heat flux and a background heat flux.

The top of the Cooler electrode contains a constant voltage boundary condition which mandates a variable current and translates into calculating the current and corresponding Peltier cooling/heating for each element. Moreover, the non-uniform current flow through the germanium die produces non-uniform Joule heating. Thus, the thermoelectric boundary conditions are automatically calculated by the high order thermal-electrical element SOLID227 which couples the thermal and electrical field through Joule Heating and the Peltier Effect.

3.1.1 Self Cooling Geometry

The germanium self cooling device with constant voltage boundary conditions (i.e. constant voltage self cooler) is geometrically identical as the once used for the constant current device. The geometry has been shown in **Figure 23**.

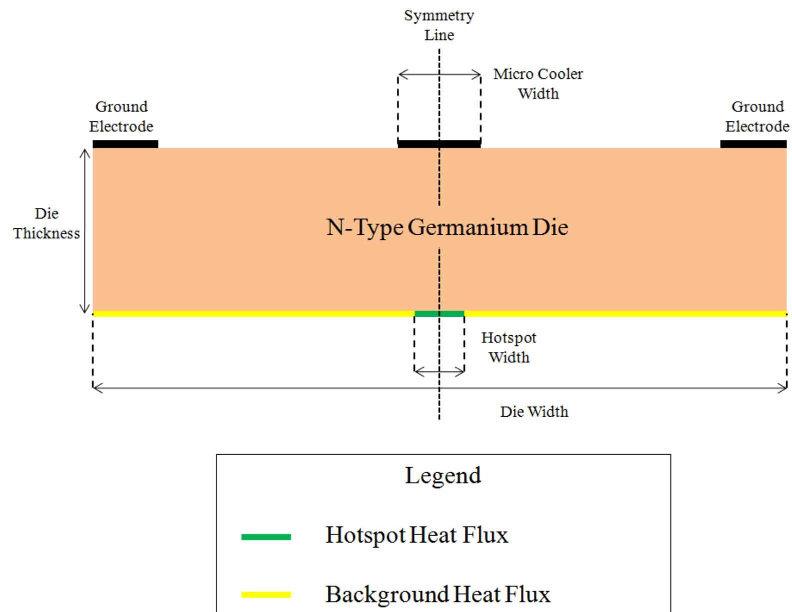

Figure 23: Germanium Self Cooling Device

As shown in **Figure 23**, there are two heat fluxes, hotspot and background, that allow the study of non-uniform heating. The Cooler is placed above the hotspot and the background heat flux surrounds the hotspot. This fact is better explained viewing **Figure 24**.

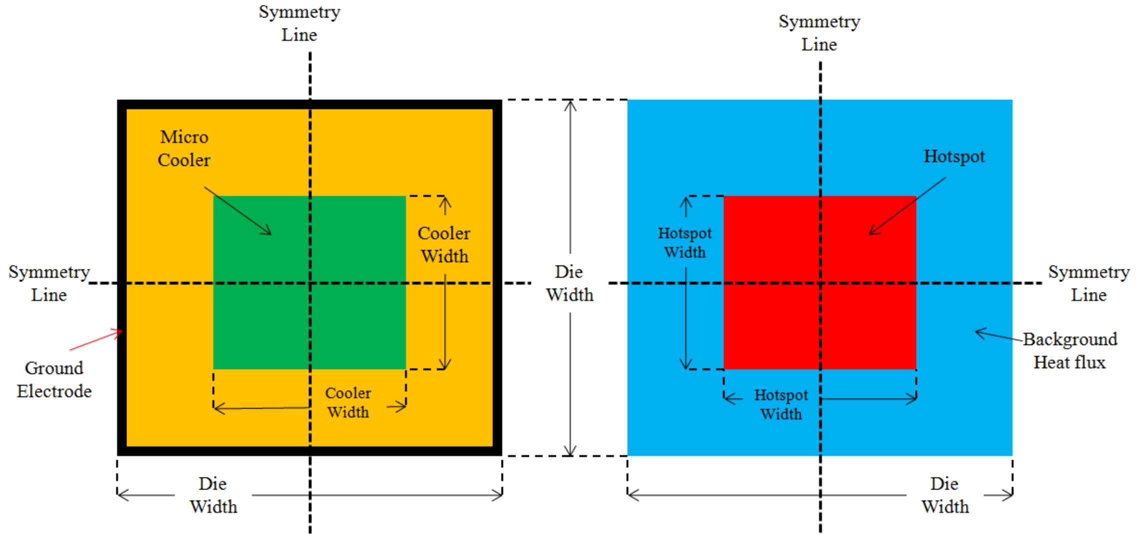

Figure 24: Germanium Self Cooling Device, Left is Top View, Right is bottom heating map (not to scale)

The die, Cooler, and hotspot are all square as shown by the above figure. Moreover, the hotspot and Cooler are in the geometric center of the die. The dimensions of the device are shown in **Table 3.**

Table 3: Constant Voltage Germanium Self Cooling Device Dimensions

Label	Dimension (µm)
Die Width	12000
Hotspot Width	70
Ground Electrode Width	500
Die Thickness	Parametric Variable
Cooler Size (square)	Parametric Variable

Various die thickness are simulated, each with a Cooler size range sufficient to determine optimum performance. Thus the parametric variables are the die thickness, Cooler size,

and current. The optimum performance is found through sequential parametric optimization of the said variables.

3.1.2 Material Properties

Wang and Bar-Cohen studied Geballe and Hull's research who determined that germanium's thermoelectric properties were dependent on doping type and that n-type germanium had superior performance over p-type (20) (46). Geballe and Hull found the Seebeck and electrical resistivity dependence on arsenic doping concentration. These curves are shown in **Figure 25** (20) (46).

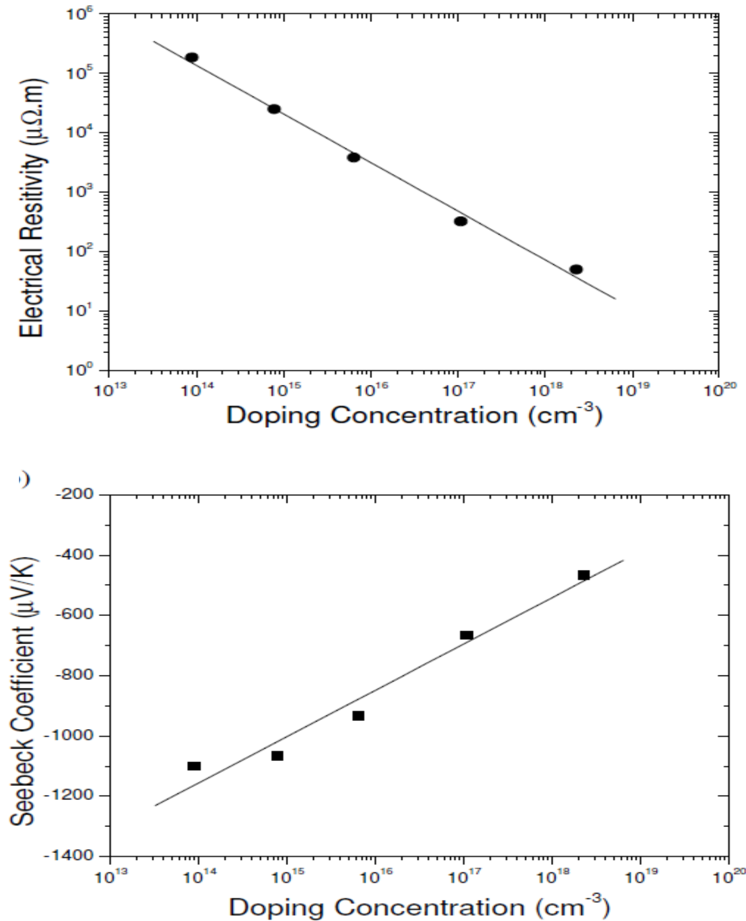

Figure 25: N-type Germanium Electrical Resistivity and Seebeck as a function of arsenic doping concentration (20) (46)

As the doping concentration increases, the electrical resistivity decreases greatly while the absolute value of the Seebeck coefficient slightly decreases. Wang and Bar-Cohen calculated the Power factor ($P=S^2/\rho$ as shown in equation **2-20**) using the above values (20). This produces the curve in **Figure 26** (20).

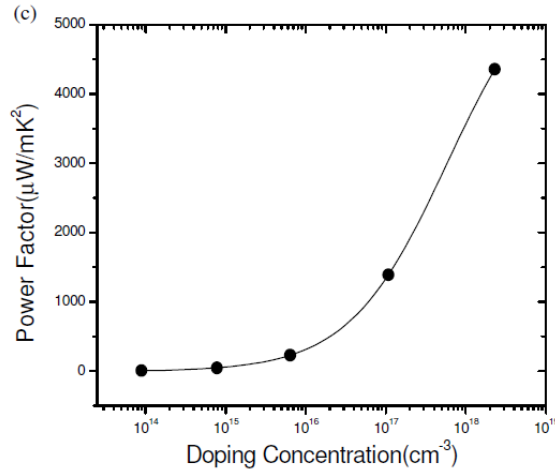

Figure 26: N-type Germanium Power factor as a function of arsenic doping concentration (20)

As the doping concentration increases, the Power factor also increases due to the great decrease in electrical resistivity overcoming the slight decrease in the Seebeck Coefficient. Wang and Bar-Cohen varied the doping concentration (and consequently the Seebeck coefficient and electrical resistivity) for the same geometry and boundary conditions explained in this chapter and were able to demonstrate a cooling dependence on doping concentration. **Figure 27** shows the curve created by Wang and Bar-Cohen for a 100μm die and 600μm micro cooler at optimized currents.

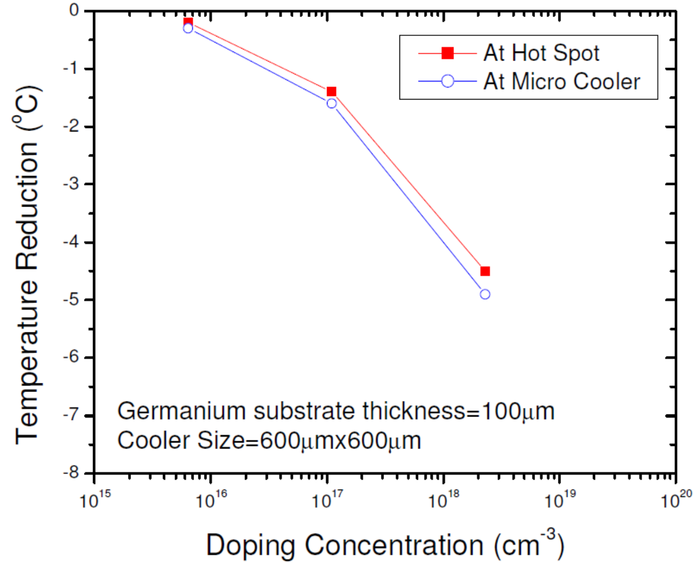

Figure 27: Wang and Bar-Cohen's Temperature reduction as a function of doping concentration (20)

Wang and Bar-Cohen demonstrated a 4.5°C of hotspot cooling at an arsenic doping of 2.3×10^{18}cm^{-3} (20). These results motivated this work to use the material properties that provide the highest hotspot cooling as shown in **Table 4**.

Table 4: Germanium Self Cooling Device Material Properties

Label	Thermal Conductivity (W/mk)	Electrical Resistivity (μΩm)	Seebeck Coefficient (μV/K)
Germanium Die (doping of **2.3×10^{18}cm^{-3}**)	60 (20) (47)	50 (20) (46)	-467 (20) (46)

3.1.3 Boundary Conditions

The germanium self cooling device with constant voltage boundary conditions (i.e. constant voltage self cooler) contains both thermoelectric and non-thermoelectric boundary conditions. The locations of these boundary conditions are shown in **Figure 28**.

The non-thermoelectric boundary conditions are identical for the constant current and constant voltage devices.

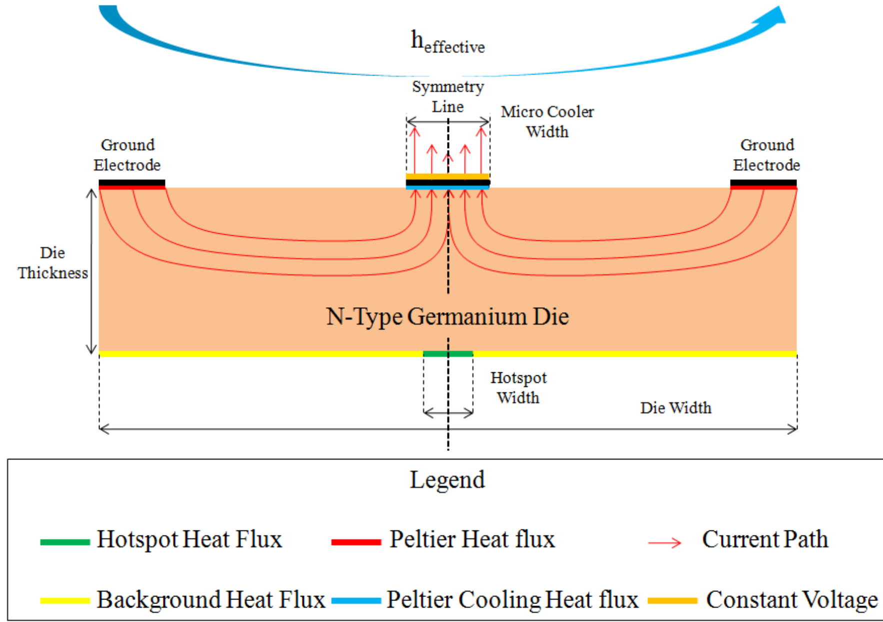

Figure 28: Constant Voltage Germanium Self Cooling Device Boundary Condition Locations

The values of the non-thermoelectric boundary conditions are displayed in **Table 5**.

Table 5: Non-Thermoelectric Boundary Conditions

	Value
$\mathbf{h_{effective}}$	8741 (W/m^2-K), $T_{ambient}$=25°C
Hotspot Heat flux	680 W/cm^2
Background Heat flux	70 W/cm^2

The heating map in **Figure 24** shows the centered hotspot surrounded by the background heat flux. The effective heat transfer coefficient ($h_{effective}$) accounts for the thermal interface, heat spreader, and air-cooled heat sink used to provide global cooling for the die (20).

3.1.3.1 Thermoelectric Boundary Conditions under Constant Current Operation

The thermoelectric phenomenon is discussed in detail in **2.1 Main Thermoelectric Effects.** This phenomenon requires the coupling between thermal and electrical effects. Peltier cooling and heating have been accounted for by equation **3-2**

and **3-3.** This is appropriate since these effects occur because of electron transport across surface interfaces and the simulation assumes a constant current between the electrode/die interface.

The parasitic effects are not accounted for by the boundary conditions. The Fourier effect is automatically accounted for by the numerical thermal model. The Joule heating effect demonstrates a non-uniform behavior following the non-uniform flow of current as shown by **Figure 28**. Thus, it is necessary to use a numerical model that couples the thermal and electrical effects with Joule heating. This model uses the ANSYS low order SOLID 69 element that is validated in **C**.3 **Thermal-Electrical Model with Joule Heating**. The validation test shows no discrepancy between the numerical and analytical solution. Thus there is much confidence in using this coupled model.

The Peltier cooling occurs at the Cooler/ germanium interface and is presented in equation **3-1** (20).

$$Q_{Peltier\ Cooling} = (S_{metal} - S_G)T_C I \approx -S_G T_C I \qquad \textbf{3-1}$$

$where$:

$S = seebeck\ coefficient\ \left(\frac{V}{K}\right)$

$T_C = absolute\ temperature\ of\ cold\ Juction\ (K) = 373.15K$

$I = current(A)$

It is assumed that the temperature of the cold junction remained constant even with the application of current. This is a suitable assumption because the center temperature reduction reported is less than 10K. As described before, the Seebeck coefficient of the metal is negligible when compared to that of the n-type germanium die. A contact resistance is imposed on the same surface with a value of 1×10^{-7} $\Omega.cm^2$ (20). This negligible value allows the study of the potential of the germanium self cooling device

(20). In order to impose a heat flux, the addition of equation **3-1** and the contact resistance is divided by the Cooler area. This produces equation **3-2** (20).

$$q_{Peltier\ Cooling\ Heat\ flux} \approx \frac{-S_G T_C I + R_C I^2}{A_{Cooler}} \qquad \textbf{3-2}$$

$where$:
$A_{Cooler} = area\ of\ the\ micro\ cooler (m^2)$
$R_C = Contact\ resistance (\Omega)$

The Peltier heat flux is found in a similar fashion with the absolute temperature of the hot junction equal to that of the cold junction. This is shown in 3-3.

$$q_{Peltier\ \ Heat\ flux} \approx \frac{S_G T_H I + R_C I^2}{A_{Electrode}} \qquad \textbf{3-3}$$

$where$:
$A_{Electrode} = ground\ electrode\ area\ (m^2)$

3.1.3.2 Thermoelectric Boundary Conditions under Constant Voltage Operation

It is common to apply a Peltier cooling and heating heat flux at the appropriate surfaces if the current across the surface is constant. Wang and Bar-Cohen used this fact to determine constant Peltier cooling and heating at the appropriate surfaces in reference (20).

These equations cannot be used to produce the results for the constant voltage self cooling device because the constant voltage boundary condition at the top of the Cooler electrode mandates a variable current. This is evident in **Figure 29** where the current around the periphery of the Cooler electrode is greater than the center.

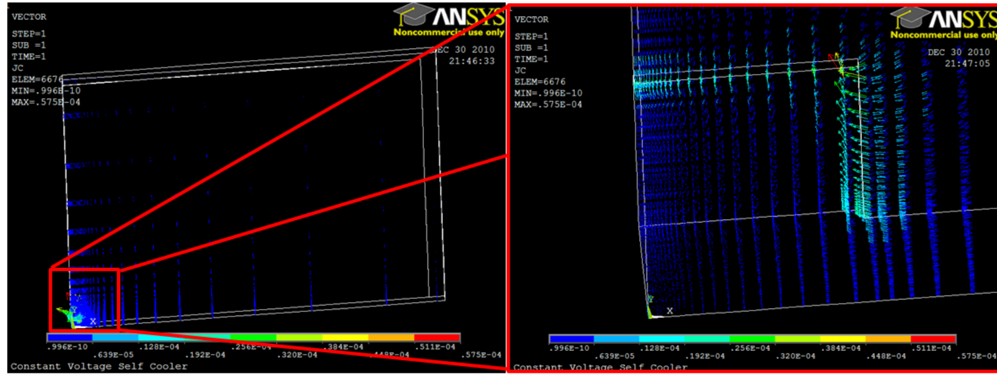

Figure 29: Typical Quarter Current plot of Constant Voltage Self Cooler, Zoomed view of Cooler on right

This variable current across the Cooler/germanium interface translates into calculating the current and corresponding Peltier cooling/heating for each element.

Moreover, the non-uniform current flow through the germanium die produces non-uniform Joule heating. Thus, the numerical simulation must solve for the thermal and electrical fields with Joule heating and the Peltier effect coupling the two. This coupling is available through the ANSYS high order SOLID 227 element validated in **C**.4 **Thermal-Electrical Model with Joule Heating and the Peltier Effect**. The validation test shows less than 1% error for Power and less than 2.5 % (absolute value) between the numerical and analytical solutions. Thus there is much confidence in using this coupled numerical simulation to provide accurate results.

3.2 *Numerical Results under Constant Voltage Operation*

The cooling potential of the germanium self cooling device with constant voltage boundary condition (i.e. constant voltage self cooler) is determined. The trends and tradeoffs discussed here are similar to the constant current device. The metrics used to rate the device are discussed in **3.2.1 Cooling Metrics**. These metrics discuss the

temperature reduction due to the constant voltage application at the Cooler electrode for the center hotspot and Cooler temperatures. The hotspot cooling effectiveness is also discussed which determines the ratio of the temperature change due to application of current to the Cooler over the temperature rise due to the hotspot. The efficiency, or thermal impact factor, is determined by the hotspot temperature reduction over the Power of the device.

The nature of numerical simulations requires that a mesh refinement be conducted to distinguish and ultimately eliminate mesh dependent solutions. As shown in **3.2.2 Mesh Convergence**, the high order thermal-electrical element SOLID227 with element counts ranging from 20k to almost 100k was used to generate the results for the constant voltage self cooler.

For all the geometries simulated, a common temperature distribution was generated and discussed in **3.2.3 Typical Temperature Distributions**. For each specific case tested, there exists a temperature profile with two inflection points around the center of the hotspot. This fact along with the symmetric temperature profile leads to two concentric rings with the inner-most consisting of slightly lower temperatures and the outer-most consisting of slightly higher temperatures.

The center hotspot temperature demonstrates a quadratic temperature reduction due to the tradeoff between the Peltier and Joule Heating effect. This allows a quadratic trend fitting to the temperature curves to determine the minimum temperature, maximum temperature reduction, the corresponding current value, and the Power of the constant voltage device.

Various Cooler sizes were run for each die thickness. In general, the temperature reduction for each die thickness demonstrates a tradeoff between the thermal resistance between the Cooler and hotspot and the thermoelectric cooling effect at the Cooler. The hotspot cooling effectiveness trend shows a similar (yet negative) trend when compared to the hotspot temperature reduction trend. Thus their optimums occur at the same Cooler size and current.

The above translates into an optimum Cooler size for each die thickness as shown in **3.2.6 Function of Die thickness.** The hotspot temperature reduction demonstrates a linear trend with the maximum cooling of -3.9^{o}C at the 100µm die and 400µm Cooler size at 1.06A. The maximum hotspot cooling effectiveness of 0.8 occurs for the 200µm die thickness with a 700µm Cooler size at 2.29A. Moreover, the efficiency, or thermal impact factor strongly behaves like a decreasing "power trend," and as such, reaches its highest value within die thickness range tested of 13°C/W at the 100µm die thickness. It is interesting to note that the Power and thermal impact factor demonstrate the same strong behavior (quadratic for Power and "power trend" for thermal impact factor) as a function of current, Cooler Width and die thickness.

3.2.1 Cooling Metrics

In order to determine the cooling potential of the germanium self cooler with constant voltage boundary conditions (i.e. constant voltage self cooler), the metrics from Peng and Bar-Cohen in reference (20) are adopted. These include the center hotspot and cooler temperature reductions and the hotspot cooling effectiveness. These metrics were outputted for the constant current and voltage devices.

The first metric determines the temperature reduction at the center hotspot and Cooler locations due to the application of current. These metrics are shown in equation **3-4** (20).

$$\Delta T_{Hotspot} = T_{@hotspot,Cooler\ on} - T_{@hotspot,Cooler\ off} \quad \textbf{3-4}$$
$$\Delta T_{Cooler} = T_{@cooler,Cooler\ on} - T_{@coolert,Cooler\ off}$$

These metrics follow the cooling trends explained in **2.3 Thermoelectric Cooler Net Effects**. At small current values, the temperature at both locations reduces linearly due to the Peltier effect. This produces a negative $\Delta T_{hotspot}$ and ΔT_{Cooler}. At larger currents, the Peltier effect is balanced by Joule heating, and $\Delta T_{hotspot}$ and ΔT_{Cooler} reach an optimum (minimum) value. Currents larger than this point produce larger (absolute value) $\Delta T_{hotspot}$ and ΔT_{Cooler} values. Thus the typical operational point for the germanium self cooling device involves applying the current that produces the maximum ΔT.

The other metric determines the hotspot cooling effectiveness due to the application of current to the Cooler. More specifically, it is the ratio of the temperature change due to application of current to the Cooler over the temperature rise due to the hotspot. This ratio is defined in equation **3-5** (20).

$$\Delta T^{*}_{Hotspot} = \frac{T_{Hotspot\ on\ ,Cooler\ off} - T_{Hotspot\ on\ ,Cooler\ on}}{T_{Hotspot\ on\ ,Cooler\ off} - T_{Hotspot\ off\ ,Cooler\ off}} \quad \textbf{3-5}$$

The metric typically ranges from zero to one. At $\Delta T^{*}_{hotspot}=1$, the temperature increase due to the hotspot is completely removed. At $\Delta T^{*}_{hotspot}=0$, the device is incapable of removing that temperature. At values between 1and 0, the device demonstrates partial removal of the hotspot temperature. Values larger than one demonstrate a device that is capable of providing temperatures lower than the no hotspot case. Negative values occur when operating in the Joule heating dominate region (large currents) where the

temperature of the hotspot with the Cooler activated is larger than when the Cooler is not activated.

The efficiency of the constant voltage self cooling device is of important to thermal engineers. **2.4.1 Power and Coefficient of Performance (COP)** formulates the coefficient of performance for conventional (leg) thermoelectric coolers (TEC). Unfortunately, the non-uniform Joule heating cannot be calculated through the bulk formulation in equation **2-13** and **2-14**. Thus, the Power and efficiency must be calculated in another manner.

This problem is solved in the simulation validated in **C**.4 **Thermal-Electrical Model with Joule Heating and the Peltier Effect**. The Power can be found by finding the voltage at the top Cooler surface (contains the constant voltage condition) and multiplying it by the applied current as shown by equation **3-6**. The Power and thermal impact factor metrics are not calculated for the constant current device since the voltage is not easily found.

$$Power = V_{Cooler} I \quad \textbf{3-6}$$

The efficiency of the device cannot be calculated through a coefficient of performance since the net cooling flux equation (equation **2-14**) uses the bulk Joule heating formulation. However, efficiency is generally defined by the desired output divided by the required input (25). For the presented case, the desired output is the center hotspot temperature reduction and the required input is the Power. This metric is called the Thermal Impact Factor (TIF) and is defined in equation **3-7** (19).

$$TIF = \frac{\Delta T_{Hotspot}}{Power} \quad \textbf{3-7}$$

3.2.2 Mesh Convergence

The germanium self cooling device with constant voltage boundary conditions (i.e. constant voltage self cooler), is numerically simulated using the high order ANSYS SOLID227 thermal-electrical element that contains Joule heating and the Peltier effect couplings. This model has been validated in **C**.4 **Thermal-Electrical Model with Joule Heating and the Peltier Effect**. The validation test shows less than 1% error for Power and less than 2.5 % (absolute value) between the numerical and analytical solutions for net cooling. This provides much confidence in the outputted results for the constant voltage self cooler.

The symmetric boundary conditions and geometry create a symmetric temperature and current distribution. Thus, a quarter model was simulated to provide the results in **3.2 Numerical Results** because quarter models can accomplish the same relative precision that a full model provides with a quarter of the elements. Moreover, this reduction in element count translates into less computational time.

The nature of numerical simulations requires that a mesh refinement be conducted to distinguish and ultimately eliminate mesh dependent solutions. This is accomplished through the increase of the element count while the pertinent temperatures are recorded. For the work in this chapter, converged meshes contain element counts from around 20k to almost 100k brick elements. This brick element shape is shown in **Figure 30** (50).

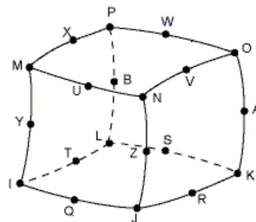

Figure 30: High Order Brick Element Shape Used for Constant Voltage Self Cooler

The meshes contain a high element density near the hotspot and Cooler regions since they contain the highest heat fluxes of the device. A sample mesh plot is shown in **Figure 31**.

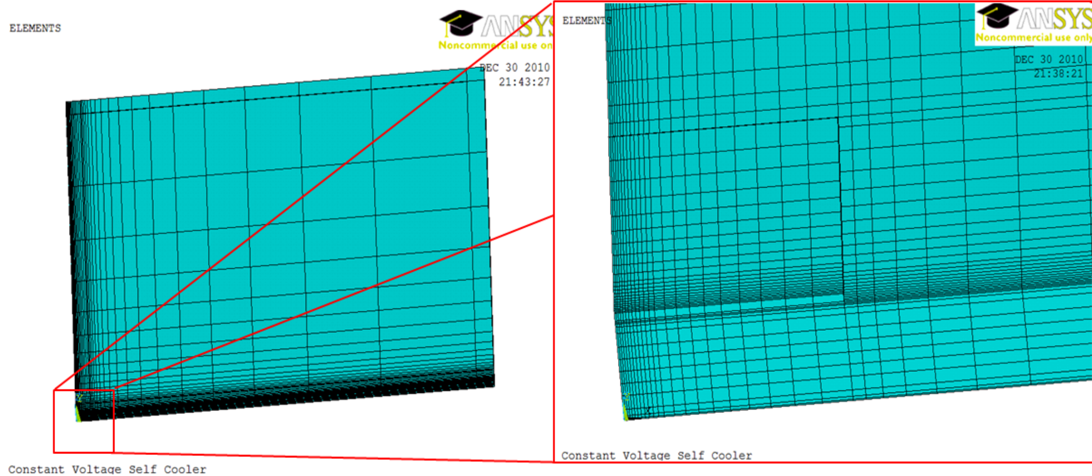

Figure 31: Typical Mesh plot of Constant Voltage Self Cooler, Zoomed view of Cooler on right

The pertinent temperatures to this study are the center hotspot and center Cooler temperature. These trends for the center hotspot and Cooler temperatures as the element count increases are shown in **Figure 32** and **Figure 33** for the 100µm die, 400µm Cooler, and 1.05 amp case.

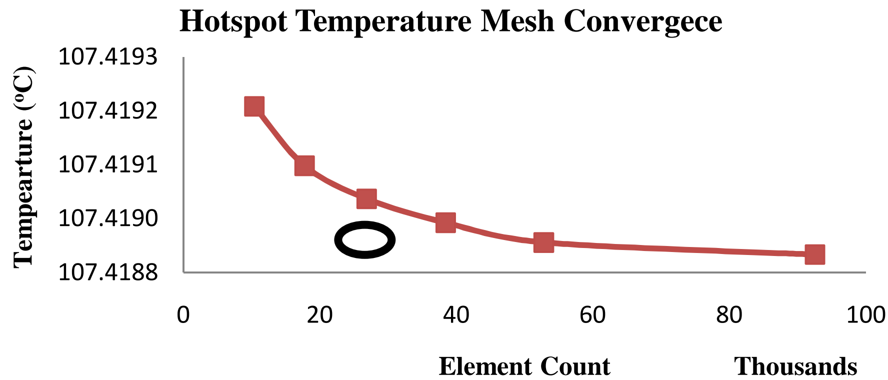

Figure 32: Hotspot Temperature Mesh convergence for 100µm Die, 400µm Cooler, and I=1.05A

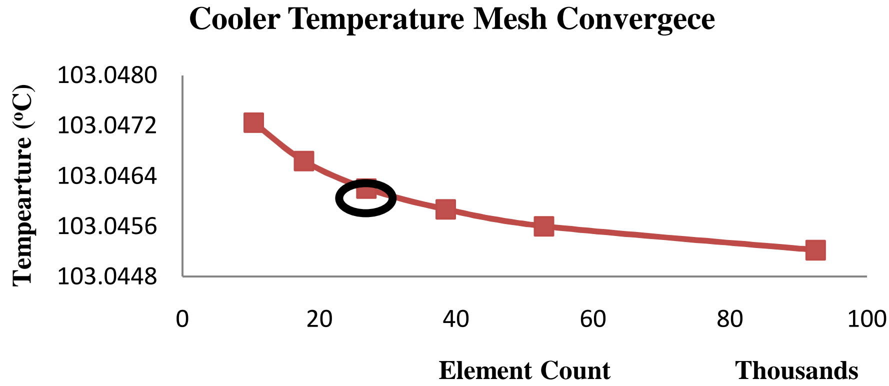

Figure 33: Cooler Temperature Mesh convergence for 100µm Die, 400µm Cooler, and I=1.05A

The temperatures vary less than 0.01°C over the element range tested which provides confidence to pick the circled high order (SOLID227) element count for the constant voltage self cooler. This point is chosen because it provides a balance between relative accuracy and computational time. The run times for the above simulations are shown in **Figure 131**.

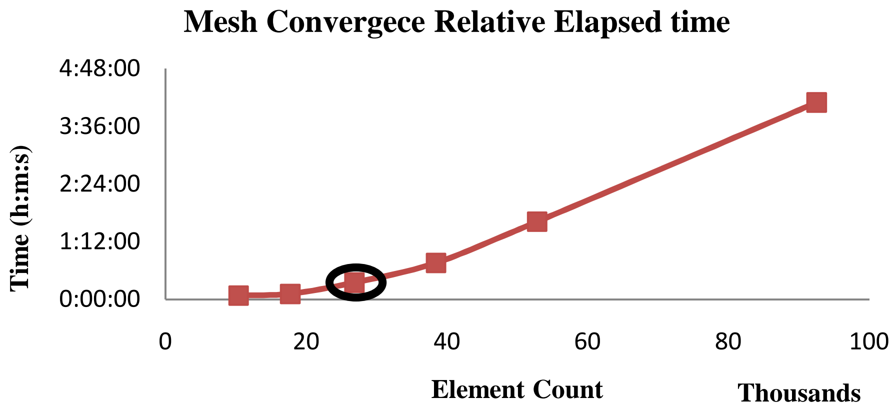

Figure 34: Mesh convergence Time for 100µm Die, 400µm Cooler, and I=1.05A

These trends for Power as the element count increases are shown in **Figure 127** for the 100µm die, 400µm Cooler, and 1.05 amp case.

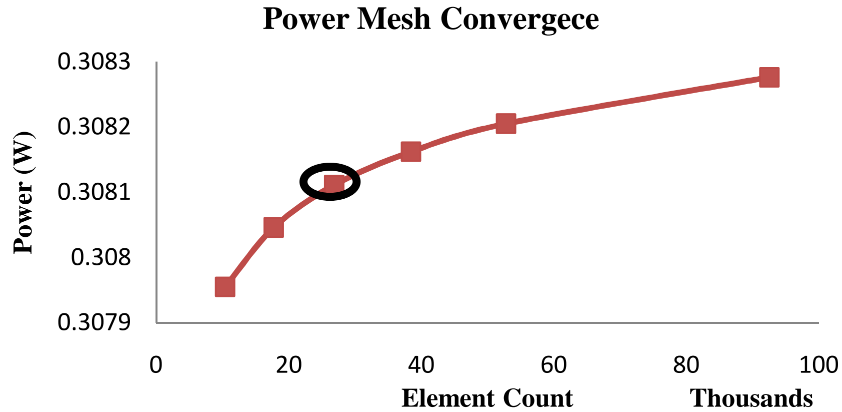

Figure 35: Power Convergence for 100µm Die, 400µm Cooler, and I=1.05A

3.2.3 Typical Temperature Distributions

The temperature distribution along the bottom of the germanium die is shown in **Figure 36** for the 100µm die and 400µm Cooler case. These temperature distributions are through the center of the die and consequently the temperatures at position zero are the center hotspot temperatures used for the metrics discussed in earlier sections. The constant voltage device is simulated using a quarter model since the geometry and boundary conditions are symmetric. Thus, the negative positioned temperatures are mirrored from their positive counterparts to provide the entire temperature distribution.

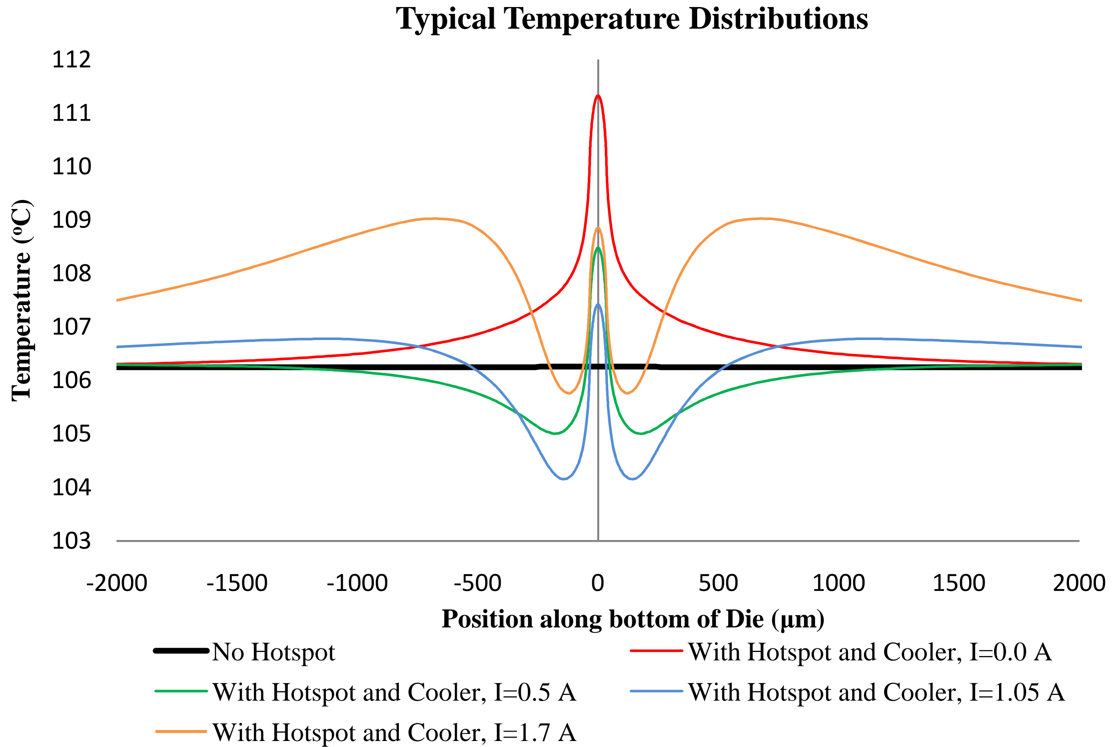

Figure 36: Constant Voltage Self Cooler, Temperature Along the bottom of the die, for the 100µm Die and 400µm Cooler (Quarter model)

As shown above, the activation of the hotspot increases the peak temperature of the device by about 5°C reaching about 111.3°C. The application of 0.5A to the Cooler reduces the middle hotspot temperature around 2.8°C. Furthermore, the application of 1.05A and 1.7A reduces the temperature 3.9°C and 2.5°C respectively hinting at the quadratic behavior of thermoelectric cooling.

It is interesting to note that the application of current to the germanium self cooling device produces a complicated temperature profile around the center hotspot temperature just as the constant current self cooling device. There are two inflection points in the temperature profile around the center of the hotspot. This fact along with the symmetric temperature profile leads to two concentric rings with the inner-most

consisting of slightly lower temperatures and the outer-most consisting of slightly higher temperatures.

3.2.4 Function of Current

Temperature reductions due to the application of current to the germanium self cooling device with constant voltage boundary conditions (i.e. constant voltage self cooler) demonstrate a quadratic behavior as discussed in **2.3 Thermoelectric Cooler Net Effects**. At "low" current values the temperature decreases linearly due to the Peltier effect. At "large" currents the temperature increases due to Joule heating. Thus, there is a current value that balances the Peltier effect and Joule heating which provides the lowest temperature. This point is exemplified using the numerical results from the 100µm die and 400µm Cooler case shown in **Figure 37**.

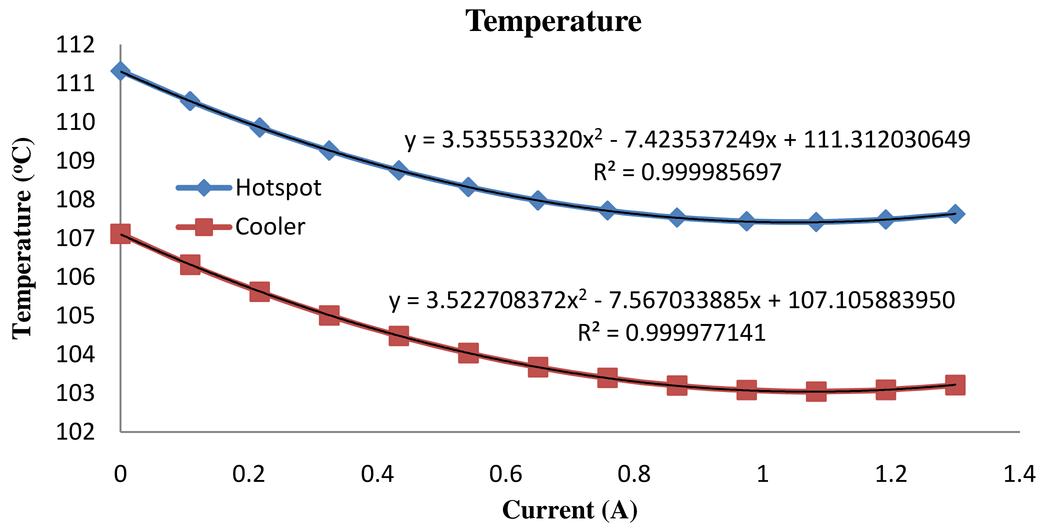

Figure 37: Constant Voltage Self Cooler, Hotspot and Cooler Temperature for 100µm Die and 400µm Cooler

The coefficient of determination (R^2) for the hotspot and Cooler temperatures signify that the curves show a strong quadratic behavior. This is true for all cases studied.

The trend equation allows the determination of the minimum temperature as well as the current that induces the effect. This is accomplished through a simple optimization procedure starting with the general equation of a quadratic curve as shown in equation **3-8**.

$$T(I) = aI^2 + bI + c \qquad \textbf{3-8}$$

$where$:

$T = temeprature\ (\,^{o}C\ or\ K)$

$I = current\ (A)$

Figure 37 shows the coefficients “a”, “b,” and “c” are determined by curve fitting the hotspot or Cooler temperature curve. Then, the above equation is differentiated and set equal to zero to find the minimum temperature current. This value is shown in **3-9**.

$$I_{Min\,Temp} = I_{MT} = \frac{-b}{2a} \qquad \textbf{3-9}$$

The above current is subsequently placed back into equation **3-8** to find the minimum temperature. This equation is shown in **3-10**.

$$T_{Minimum} = T(I_{MT})_{Min} = aI_{MT}{}^{2} + bI_{MT} + c \qquad \textbf{3-10}$$

The maximum cooling temperature is found by subtracting equation **3-10** from the temperature at zero current. This produces equation **3-11**.

$$\Delta T_{Maximum} = \Delta T(I_{MC})_{Max} = aI_{MC}{}^{2} + bI_{MC} \qquad \textbf{3-11}$$

The Power required to operate the constant voltage self cooling device is also of interest. The Power metric is found by taking the voltage at the top Cooler surface (contains the constant voltage condition) and multiplying it by the applied current as shown by equation.

$$Power = V_{Cooler}I$$

The results from the prescribed procedure are exemplified using the 100µm die and 400µm Cooler case shown in **Figure 38**.

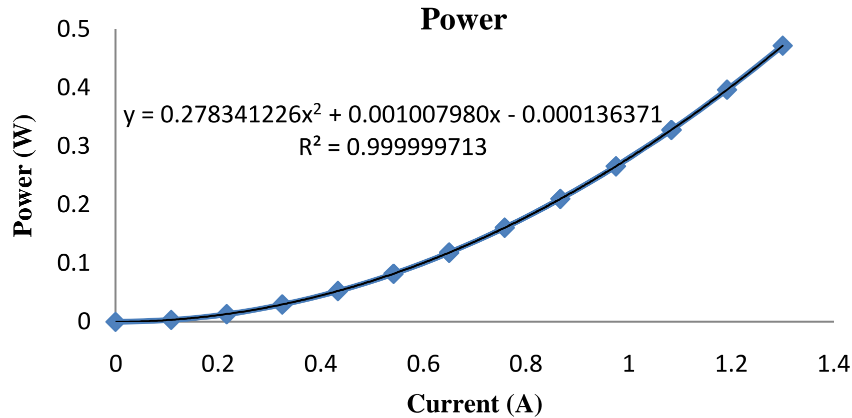

Figure 38: Constant Voltage Self Cooler, Power for 100µm Die and 400µm Cooler

Figure 38 shows the coefficients "a_P", "b_P," and "c_P" are determined by curve fitting the Power curve. Then, the minimum temperature current value (equation **3-9**) is substituted into Power trend fit. This produces equation **3-12** which calculates the Power at the minimum temperature and correspondingly the maximum hotspot temperature reduction.

$$Power_{At\,T_{min}} = P(I_{MT}) = a_P I_{MT}{}^2 + b_P I_{MT} + c_P \qquad \textbf{3-12}$$

The above procedure has many benefits over the practice of blinding applying current values in the search of the maximum cooling and corresponding current. These fully defined quadratic curves only require three current values which translates into a significant computational time savings. Moreover, using the above procedure delivers a more exact maximum cooling, maximum cooling current, and maximum cooling Power than blinding searching for them. Thus, this procedure is used to optimize the constant voltage self cooler as a function of current.

The thermal impact factor determines the efficiency or the hotspot temperature reduction divided by the required Power input to the device. The results from this division are exemplified using the 100µm die and 400µm Cooler case shown in **Figure 39**.

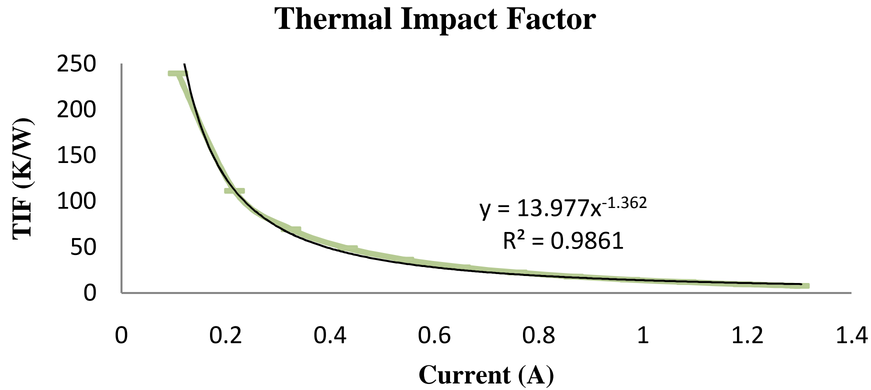

Figure 39: Constant Voltage Self Cooler, Thermal Impact Factor for 100µm Die and 400µm Cooler

As the current approaches zero, the denominator of equation **3-7** approaches zero, and consequently, the thermal impact factor approaches infinity. As the current increases, the thermal impact factor decreases rapidly closely following a “power” function with a negative exponent. Moreover, if the current reaches a value which brings the constant voltage cooling device into the Joule heating dominated region, the temperature will be higher than the temperature at zero current, making equation **3-7** negative.

3.2.5 Function of Cooler Size

The potential of the germanium self cooling device with constant voltage boundary conditions (i.e. constant voltage self cooler) is found by varying the current, Cooler size, and die thickness sequentially. For the constant voltage device the temperature reduction, cooling effectiveness, power, and thermal impact factor were recorded for all cases.

3.2.5.1 Temperature Reduction and Hotspot Cooling Effectiveness

For each die thickness, Cooler sizes are varied until the largest temperature reduction is reached. For the 100µm thick die case, the hotspot and Cooler temperature reduction is shown in **Figure 40** and **Figure 41** respectively.

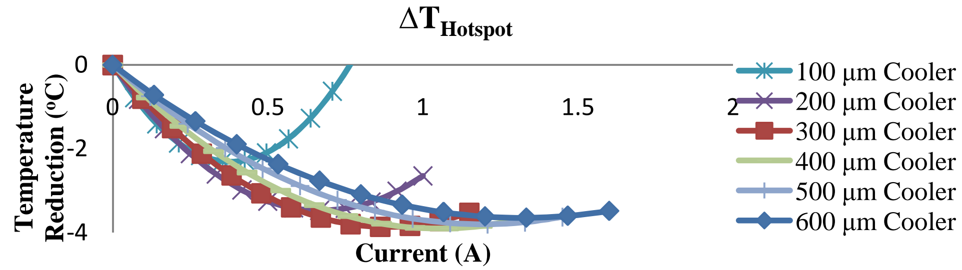

Figure 40: Constant Voltage Self Cooler, Hotspot Temperature Reduction for 100µm die

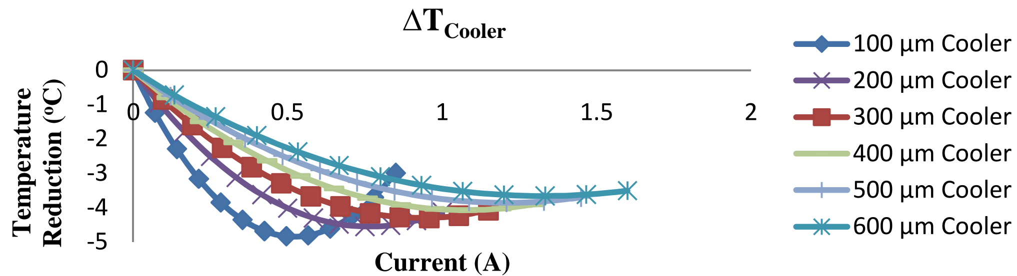

Figure 41: Constant Voltage Self Cooler, Cooler Temperature Reduction for 100µm die

As the Cooler size increases from 100µm to 600µm, the maximum hotspot temperature reduction increases (absolute value) from -3.3^{o}C to -3.9^{o}C. However larger Cooler sizes than 400µm demonstrate a decrease (absolute value) in the hotspot temperature reduction. Cooler temperature reductions increase as the Cooler size increases. This trend is due to the tradeoff between the thermoelectric cooling effect and the thermal diffusion between the hotspot and Cooler (20). At small Cooler sizes, the thermoelectric cooling effect is large, and translates into a large Cooler temperature reduction (20). However, the thermal resistance at this Cooler size is also large, and consequently, the hotspot temperature reduction is non-optimal (20). At very large cooler widths, the thermoelectric cooling effect is small and the thermal resistance is small. These two effects translate into a small hotspot and Cooler temperature reduction (20). Between these extremes, there exists a balance between the opposing effects that delivers the maximum hotspot cooling reduction. The Cooler size at which this occurs for the

100µm die is 400µm. This optimal Cooler size is easily seen in black in **Figure 42** that graphs the maximum hotspot and Cooler temperature reductions for each Cooler size.

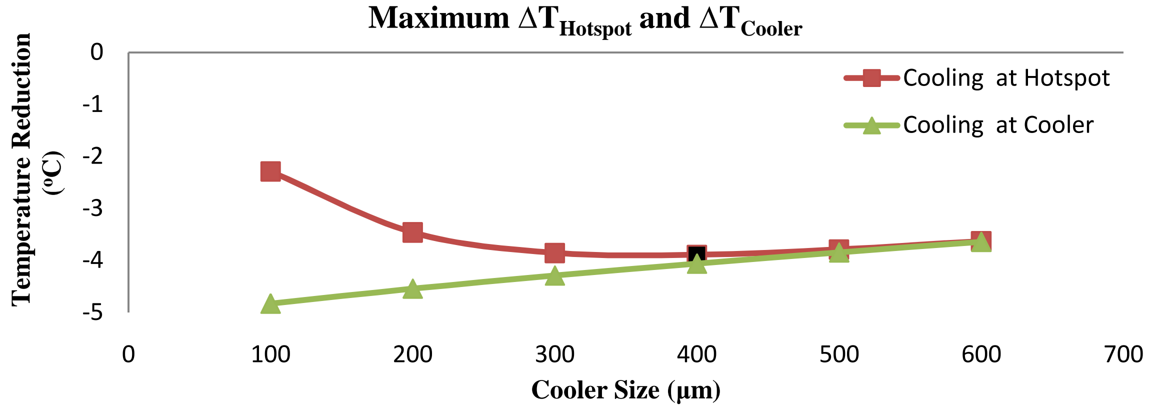

Figure 42: Constant Voltage Self Cooler, Maximum Temperature Reductions for each Cooler Width for 100µm die

Also, the maximum hotspot and Cooler temperature reductions for each die thickness approach each other at large Cooler sizes.

The hotspot temperature effectiveness is another cooling metric of interest. As shown by equation **3-5**, this metric is equal to the negative of the hotspot temperature reduction over the difference between the hotspot on and cooler off case from the hotspot off and cooler off case. The denominator changes insignificantly as a function of the Cooler size, and consequently, the hotspot temperature effectiveness demonstrates a similar, but negative, behavior to the hotspot temperature reduction curve. Demonstrating this trend, the hotspot cooling effectiveness is shown in **Figure 43** and contains a maximum value of almost 0.77 at a 400µm cooler width.

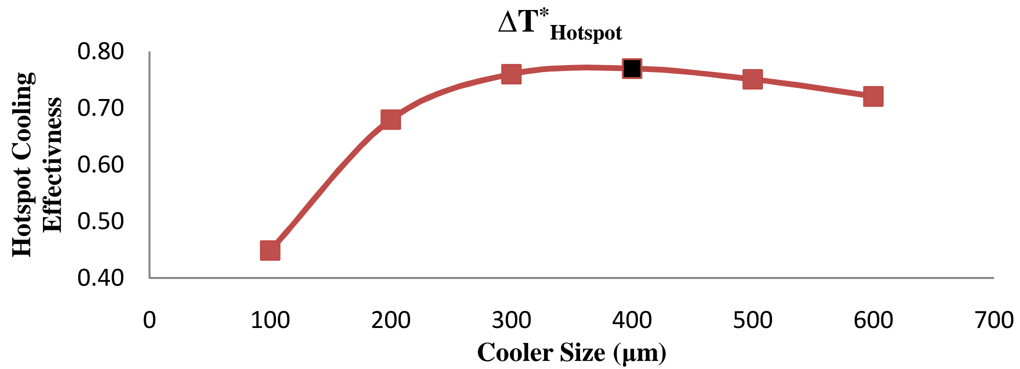

Figure 43: Constant Voltage Self Cooler, Hotspot Cooling Effectiveness for 100µm die

As a consequence of the hotspot cooling effectiveness sharing the same shape at the hotspot temperature reduction curve, their optimum occur at the same Cooler size of 400µm which is shown in black in **Figure 42** and **Figure 43.**

3.2.5.2 Power and Thermal Impact Factor

The power and thermal impact factor for the device at the maximum temperature reduction for each cooler width was recorded. For the 100µm thick die case, the Power and the thermal impact factor for each Cooler size at maximum temperature reduction is shown in **Figure 44** and **Figure 45** respectively.

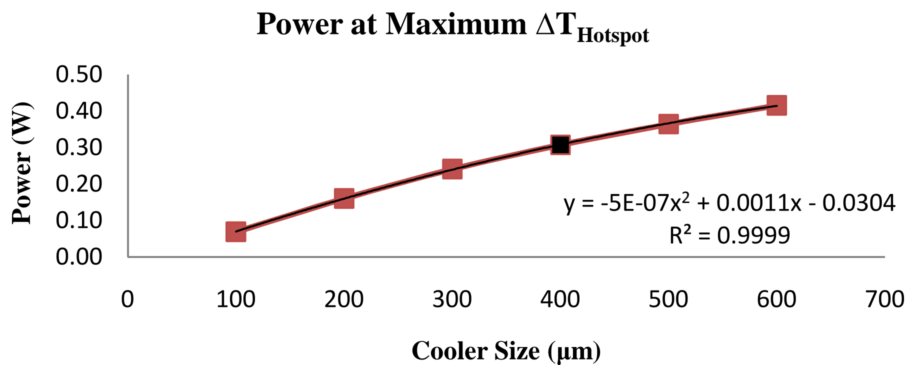

Figure 44: Constant Voltage Self Cooler, Power at Maximum Hotspot Temperature Reduction for 100µm die

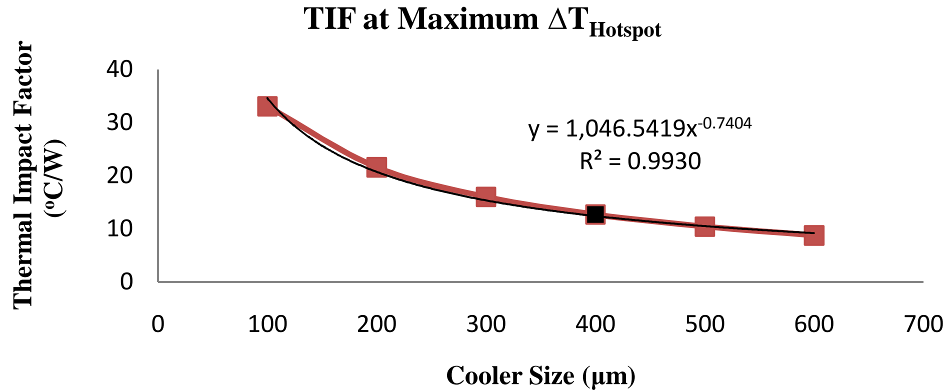

Figure 45: Constant Voltage Self Cooler, Thermal Impact Factor at Maximum Hotspot Temperature Reduction for 100µm die

It is interesting to note that Power is strongly quadratic as a function of current (as shown in **Figure 38**) as well as a function of Cooler size (as shown in **Figure 44**). The thermal impact factor also demonstrates strong a "power" trend as a function of current (**Figure 39**) and Cooler size (**Figure 45**).

3.2.6 Function of Die thickness

Using a sequential parametric optimization technique, the current and Cooler size is optimized for one die thickness at a time. Displaying the metrics as a function of die thickness for the germanium self cooling device with constant voltage boundary conditions (i.e. constant voltage self cooler) demonstrates the potential of the device. It also allows the determination of the performance band of the germanium self cooling device.

3.2.6.1 Temperature Reductions

The maximum hotspot and Cooler temperature reductions as a function of Cooler size for each die thickness are shown in **Figure 46**and **Figure 47** respectively.

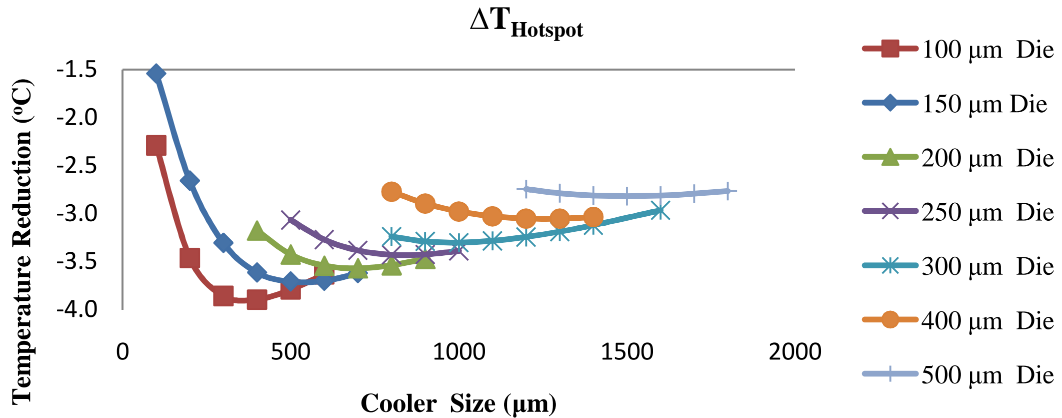

Figure 46: Constant Voltage Self Cooler, Hotspot Temperature Reduction

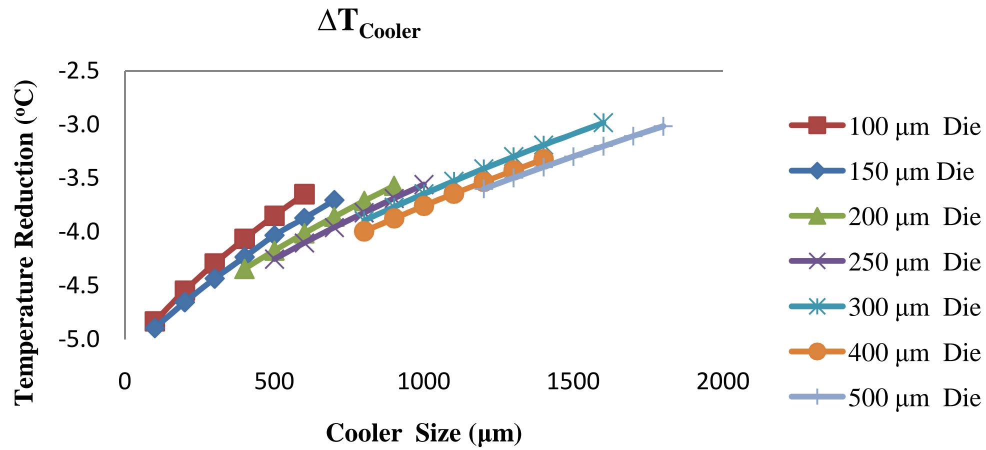

Figure 47: Constant Voltage Self Cooler, Cooler Temperature Reduction

The interplay between the thermoelectric cooling effect and the thermal resistance between the Cooler and hotspot motivate the results shown above. It is interesting to note that the optimum hotspot temperature reduction ratio of Cooler size to die thickness is shown to about 3:1 for the die thickness range of 100µm to 500µm.

Figure 48 is produced when the maximum hotspot temperature reductions for each die are plotted together.

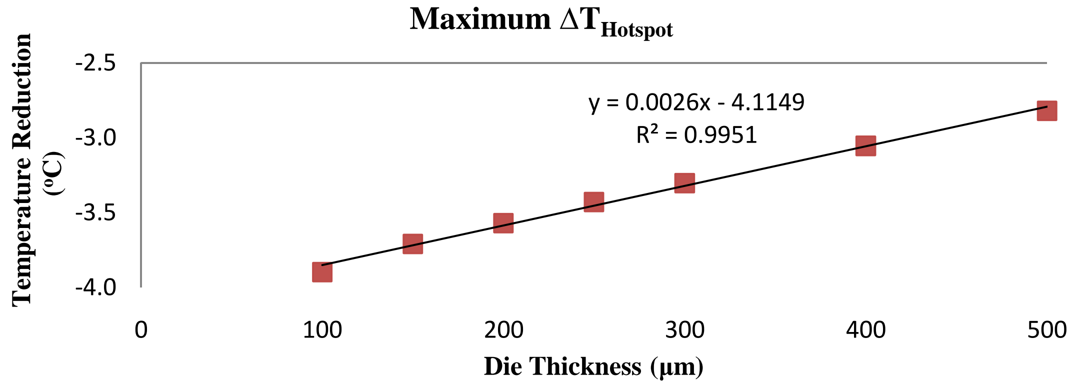

Figure 48: Constant Voltage Self Cooler, Maximum Hotspot Temperature Reduction

The maximum hotspot temperature reduction demonstrates a strong linear trend as the die thickness decreases for die thickness less than 500µm. These results arise from the decrease in thermal resistance between the Cooler and the hotspot as the die thickness decreases. The largest (absolute value) hotspot temperature reduction studied is around -3.9^{o}C at the 100µm die thickness.

The linear trend shown in **Figure 48** does not represent the trend over all die thicknesses since; its foreshadowing to larger die thicknesses demonstrates a thermoelectrically induced hotspot temperature increase when compared to the zero current case. Instead, the hotspot temperature reduction asymptotically approaches zero as the Peltier effect reaching the hotspot is dominated by the parasitic Joule heating effect. The asymptotic behavior is due to the search for the lowest thermoelectrically induced hotspot temperature. At small (from 100µm to 500µm) die thicknesses, this search provides the linear die thickness trend shown in **Figure 48**. At very large die thicknesses, the current applied to the Cooler electrode provides only hotspot temperature increases. This effectively provides zero hotspot temperature reduction which creases the “y=0” line. These two curves generate the asymptotic behavior shown in **Figure 50**

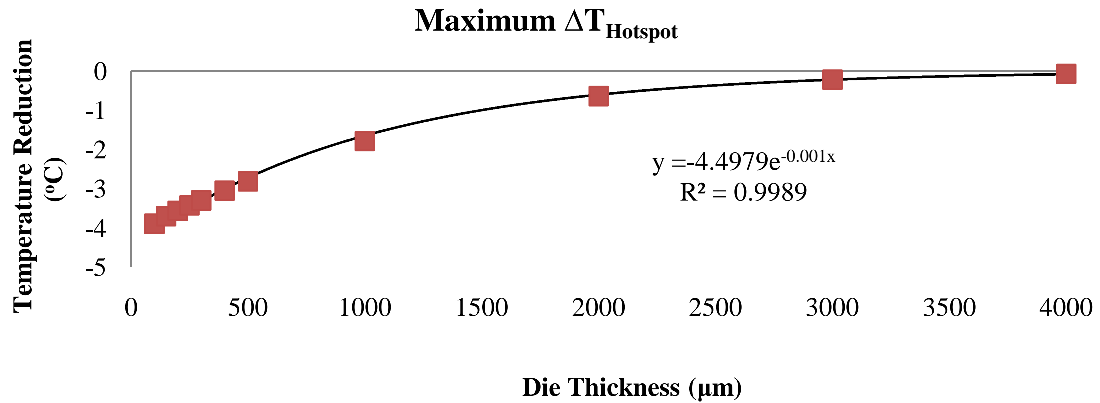

Figure 49: Constant Voltage Self Cooler, Maximum Hotspot Temperature Reduction over large die thickness range

In **Figure 50** the exponential trend agrees over the entire die thickness range tested with a coefficient of determination (R^2) greater than 0.99. However, caution should be employed when using the exponential trend for very small die thicknesses since there is a hotspot temperature reduction discrepancy of almost 0.2^0C between the exponential trend and the numerical data. Thus, for very small die thicknesses, the linear trend shown in **Figure 48** should be used.

3.2.6.2 Hotspot Cooling Effectiveness

The hotspot cooling effectiveness is also of interest to the presented work since it represents the hotspot remediation due to the application of current to the Cooler. **Figure 50** demonstrates the curves for simulated die thicknesses.

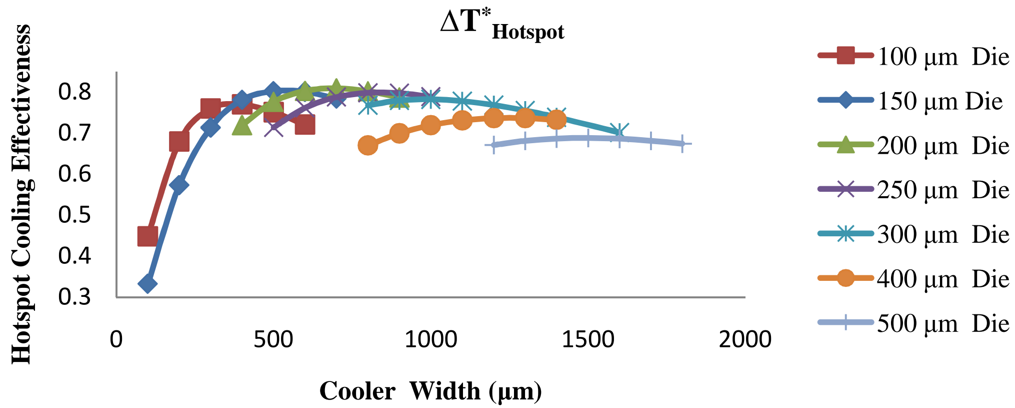

Figure 50: Constant Voltage Self Cooler, Hotspot Cooling Effectiveness

The hotspot cooling effectiveness metric is equal to the negative of the hotspot temperature reduction over the difference between the hotspot on and cooler off case from the hotspot off and cooler off case. The denominator changes insignificantly as a function of the Cooler size, and consequently, the hotspot temperature effectiveness demonstrates a similar, but negative, behavior to the hotspot temperature reduction curve. And as such, the hotspot cooling effectiveness reaches its maximum value for each die thickness at the same Cooler size as the hotspot temperature reduction metric.

Figure 51 is produced when the maximum hotspot cooling effectiveness for each die is plotted together.

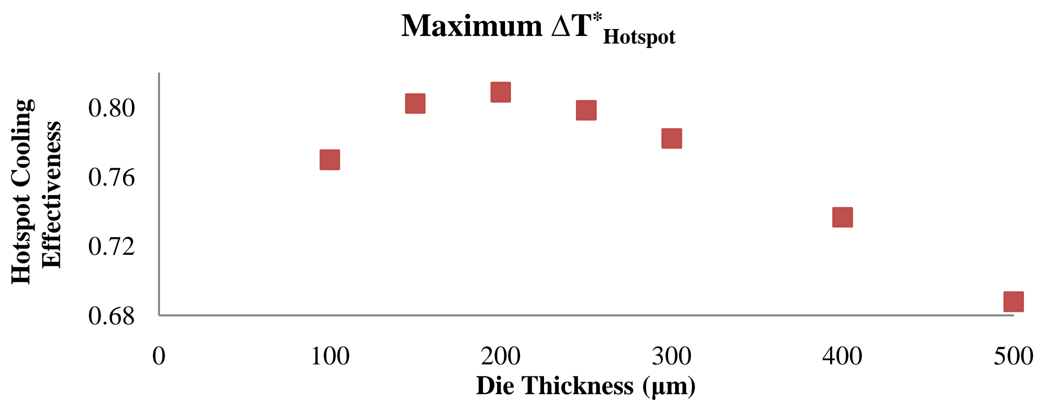

Figure 51: Constant Voltage Self Cooler, Maximum Hotspot Cooling effectiveness

Smaller die thicknesses translate into larger (absolute value) hotspot temperature reductions since the thermal resistance between the Cooler and hotspot reduces. However, smaller die thicknesses also contain an elevated hotspot temperature due to their poor spreading ability (20). Thus, there exists an optimum die thickness that balances the opposing effects of heat spreading and temperature reduction (20). This optimum was seen at the 200µm thick die with a value of 0.81.

As the die thickness increases from 200µm, the hotspot cooling effectiveness asymptotically approaches zero since the hotspot temperature reduction also approaches zero. This large die thickness trend is shown in **Figure 54**

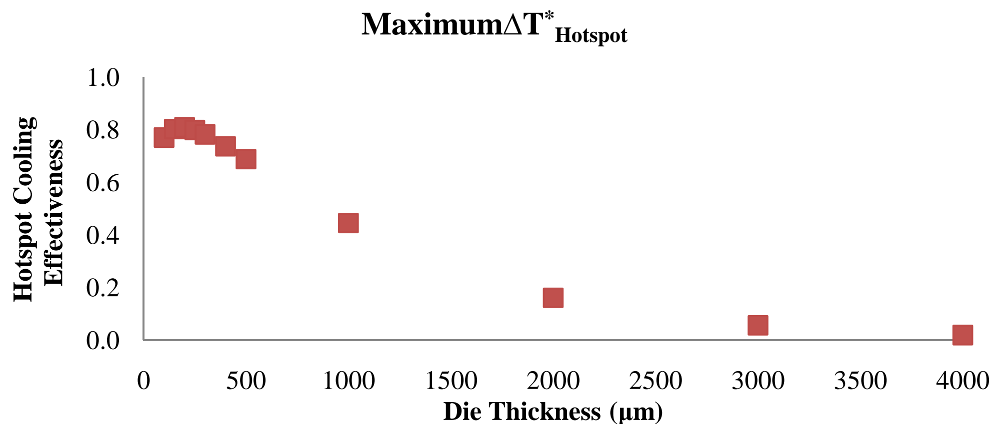

Figure 52: Constant Voltage Self Cooler, Maximum Hotspot Cooling effectiveness

3.2.6.3 Power and Thermal Impact Factor

The Power required to run the constant voltage self cooler was defined in equation **3-6** as the applied current multiplied by the voltage which is held constant at the top Cooler electrode surface. The thermal impact factor is understood as an efficiency metric as defined in equation **3-7** since it determines the hotspot temperature reduction per watt. The Power and thermal impact for each die thickness as a function of Cooler size are shown in **Figure 53** and **Figure 54** respectively.

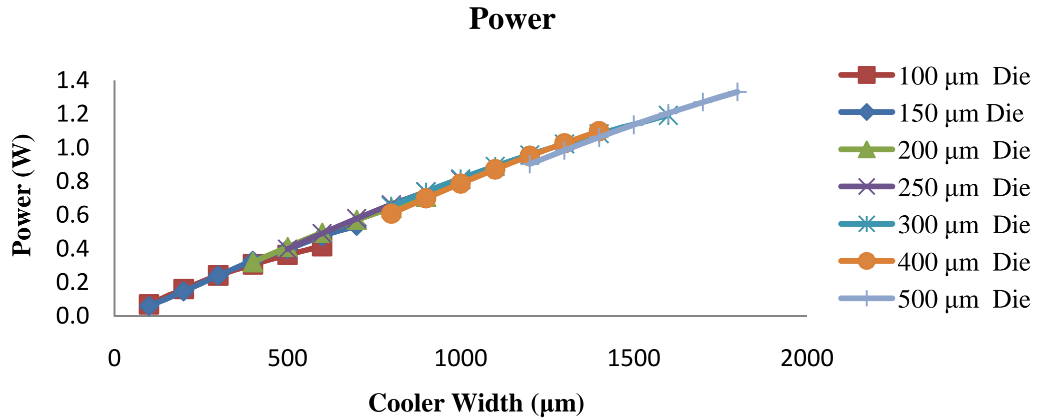

Figure 53: Constant Voltage Self Cooler, Power

Interestingly, the Power seems to linearly increase as the Cooler Width increases.

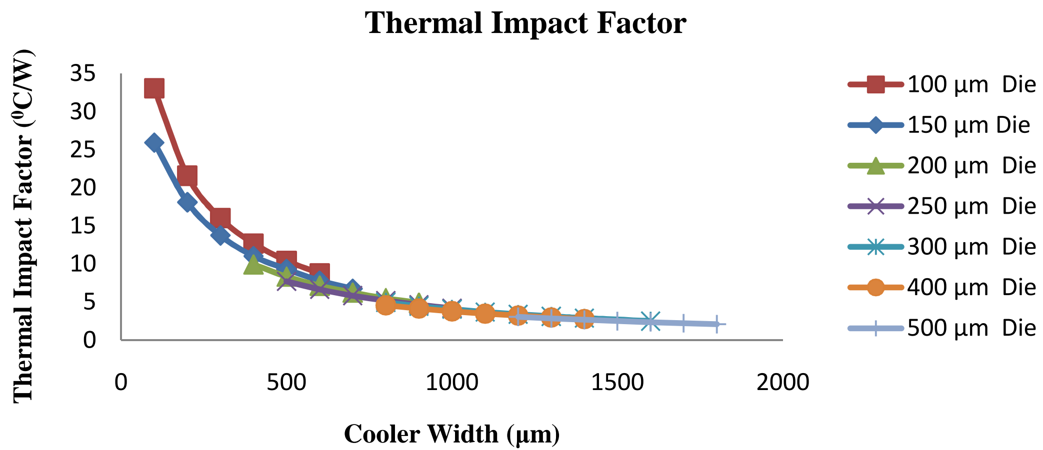

Figure 54: Constant Voltage Self Cooler, Thermal Impact Factor

The thermal impact factor demonstrates its typical "power factor" trend approaching infinity as the Cooler size approaches zero. As the Cooler size increases, there is a large decrease in the thermal impact factor, but a small decrease as the die thickness increases. Moreover, at large Cooler sizes, there is little difference between the die thicknesses. Thus, the largest thermal impact factors, and consequently the largest hotspot temperature reductions per watt are seen at small Cooler sizes and thin dies. This points is further demonstrated by viewing the thermal impact factor at maximum hotspot temperature reductions as a function of die thickness in **Figure 56**

Figure 55 and **Figure 56** respectively plot the Power and thermal impact factor at the maximum hotspot temperature reduction for each die thickness.

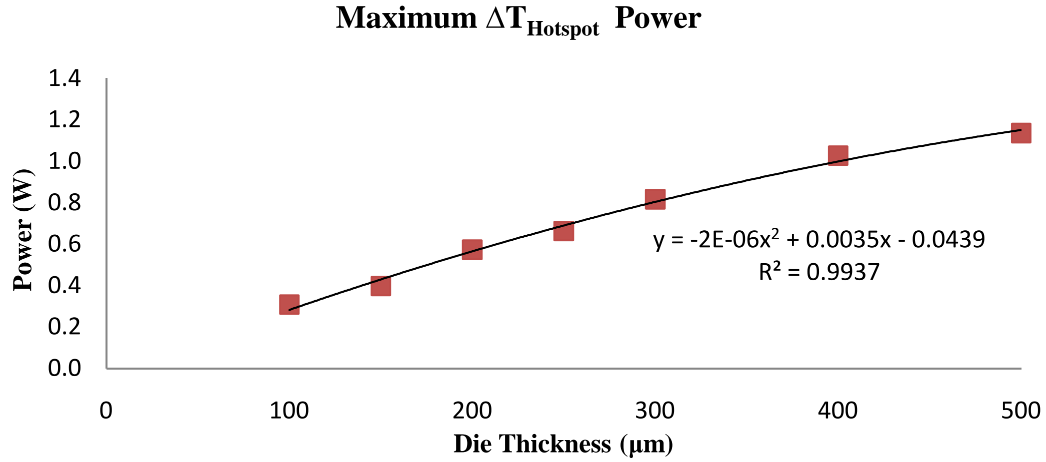

Figure 55: Constant Voltage Self Cooler, Power at Maximum $\Delta T_{Hotspot}$

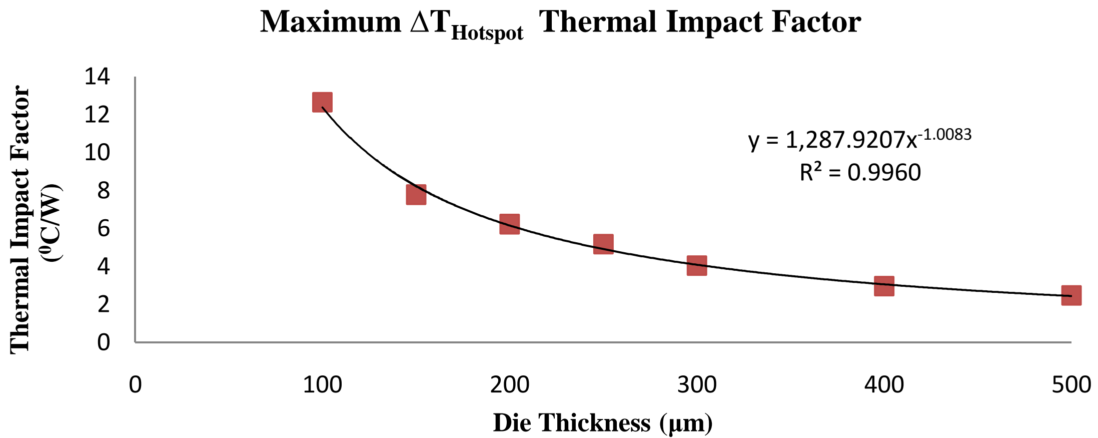

Figure 56: Constant Voltage Self Cooler, Thermal Impact Factor at Maximum $\Delta T_{Hotspot}$

The Power reaches 0.3W at the 100µm die thickness and quadraticly increases to 14W at the 500µm die thickness. The thermal impact factor demonstrates a strong decreasing "power trend" with 13°C/W at the 100µm die thickness and 2.5^{o}C/W at the500µm die thickness. This decreasing trend demonstrates that the constant voltage self cooling device provides higher temperature reductions per watt at lower die thicknesses.

It is interesting to note that Power is strongly quadratic as a function of current (as shown in **Figure 38**), as a function of Cooler size (as shown in **Figure 44**) and as a

function of die thickness as shown above. The thermal impact factor also demonstrates strong a “power factor” trend as a function of current (**Figure 39**), as a function of Cooler size (**Figure 45**), and as a function of die thickness as shown above.

3.3 *Performance Band of Germanium Self Cooling Device*

Practical electrodes that apply current never attain a constant current or constant voltage at their surface. In fact, they behave in a manner which is in between constant voltage and constant current performances. Thus, the performance band of the self cooling device can be predicted through the results comparison of the constant current and the constant voltage boundary simulations. The results of the constant current self cooling device have been omitted since their general trends and tradeoffs are similar to the constant voltage device and they are discussed in detail in reference (20). **3.2 Numerical Results** discusses the results from the constant voltage boundary condition. This section compares the two results to provide the performance band of the germanium self cooling device.

The different boundary conditions previously shown in this work motivate different electric potential (i.e. voltage) fields and different current density fields which in turn provide slightly different temperature profiles and ultimately the performance band. The electric potential fields for the self coolers are shown in **Figure 57** and **Figure 58** for the top view. It is important to note that the constant current self cooler was simulated with a full geometry and the constant voltage self cooler was simulated with a quarter geometry. They are also operating at their maximum hotspot remediation parameters with the hotspot turned off as described by their captions.

Figure 57: Hotspot off, Constant Current Self Cooler, Electric Potential Plot, 100µm die 630µm wide Cooler and 1.06A

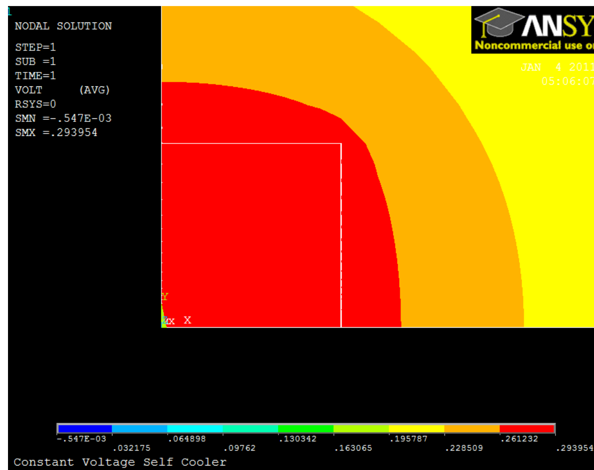

Figure 58: Hotspot off, Constant Voltage Self Cooler, Electric Potential Plot, 100µm die 400µm wide Cooler and 1.05A

Due to the boundary condition application, the constant current cooler does not maintain a constant voltage at the Cooler where the constant voltage cooler does. For the same operating conditions, the current density is displayed in **Figure 59** and **Figure 60** for the top view (left) and the side view (right).

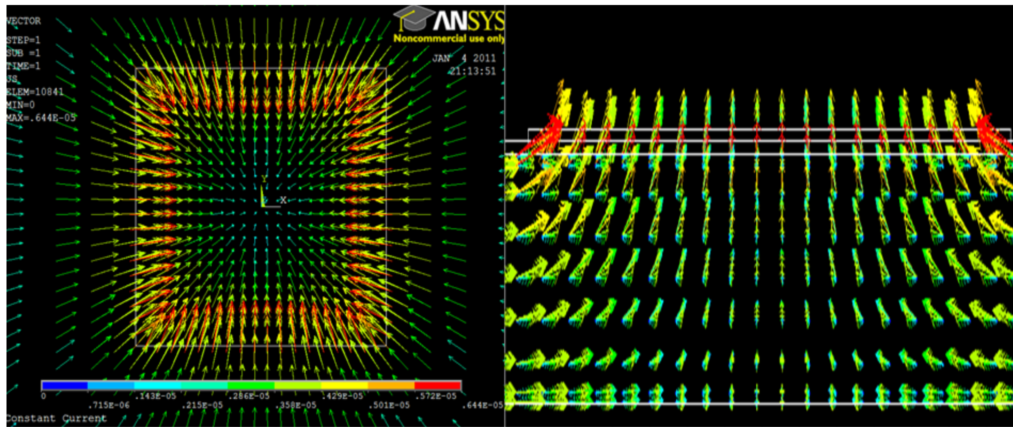

Figure 59: Hotspot off, Constant Current Self Cooler, Current Density Vector Sum Plot, 100µm die 630µm wide Cooler and 1.06A

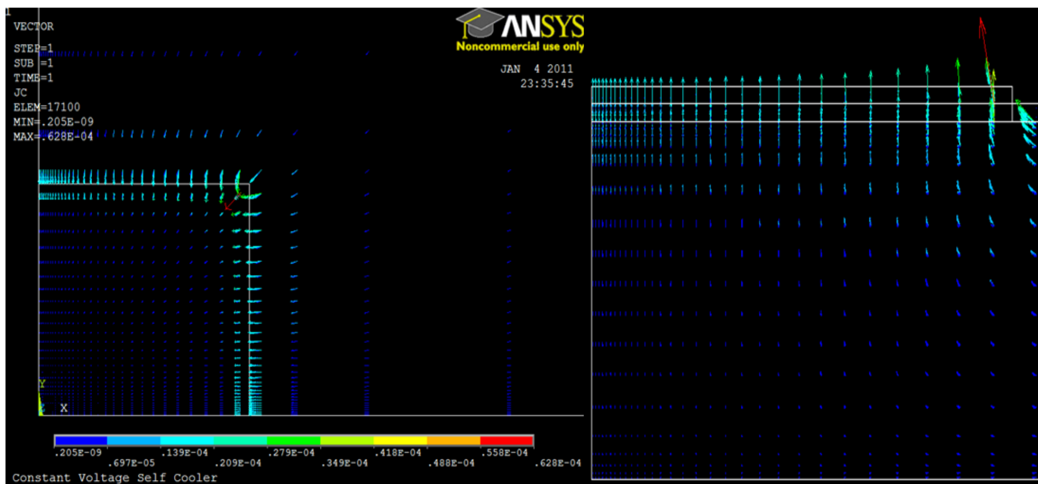

Figure 60: Hotspot off, Constant Voltage Self Cooler, Current Density Vector Sum Plot, 100µm die 400µm wide Cooler and 1.05A

The constant current self cooler shows an even current density in the Cooler electrode. The constant voltage self cooler shows its maximum at the Cooler electrode corners and quickly decreases from that value towards the center. Moreover, the current density within the Cooler electrode is much less than that of the constant current self cooler.

The Peltier effect occurs when current crosses surface interfaces as described by **2.2 A Detailed analysis of the Peltier Effect**. The different current density profiles

motivate different low temperature zones as shown by **Figure 61** and **Figure 62**. It is important to note that the hotspot is off for these plots.

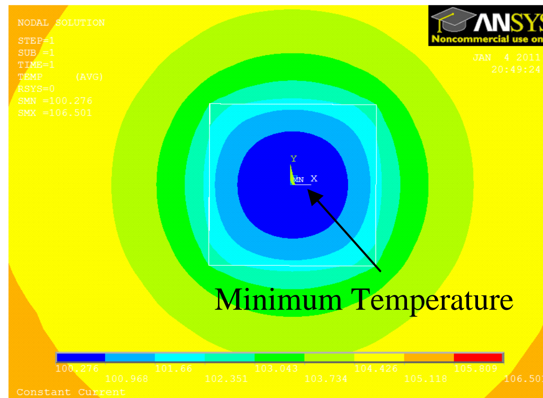

Figure 61: Hotspot off, Constant Current Self Cooler, Temperature Plot, 100μm die 630μm wide Cooler and 1.06A

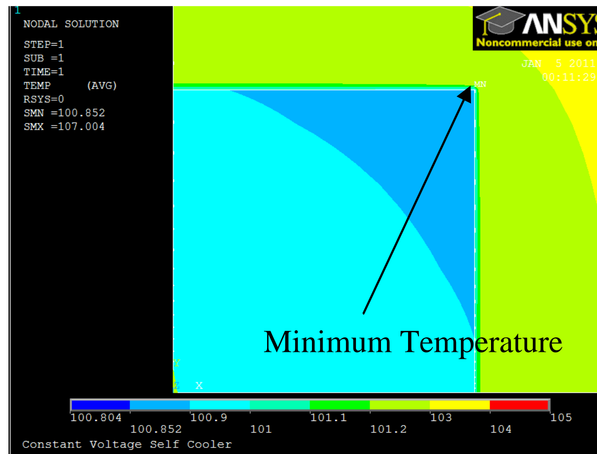

Figure 62: Hotspot off, Constant Voltage Self Cooler, Temperature Plot, 100μm die 400μm wide Cooler and 1.05A

The minimum temperature for the constant current self cooler occurs at the Cooler electrode center placing it right above the center of the hotspot. The constant voltage self cooler creates a minimum temperature at the corners of the Cooler electrode. This position places the coolest zone farther away from the hotspot, and as such demonstrates significantly less hotspot temperature reductions for all cases considered. This is evident in the minimum hotspot temperature band shown in **Figure 63**.

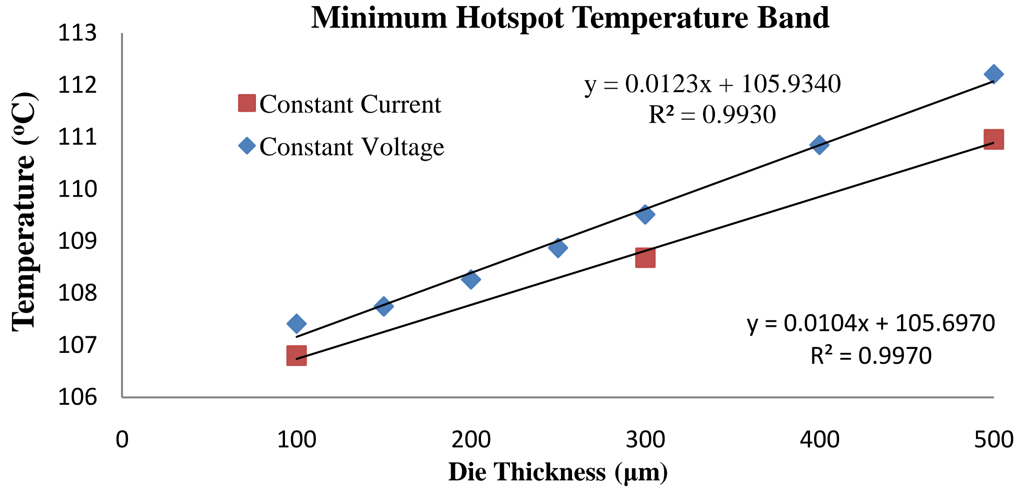

Figure 63: Minimum Hotspot Temperature Band

At the 100µm die, the constant current and voltage self coolers are able to achieve minimum hotspot temperatures of 106.9°C and 107.4°C respectively. This temperature increases linearly as the die thickness increases to 500µm due to the increase of thermal resistance between the Cooler electrode and the hotspot. At the 500µm die their temperatures are 111.0 °C and 112.2 °C for the constant current and voltage self coolers respectively. This linear trend is also evident for the maximum temperature reduction shown in **Figure 64.**

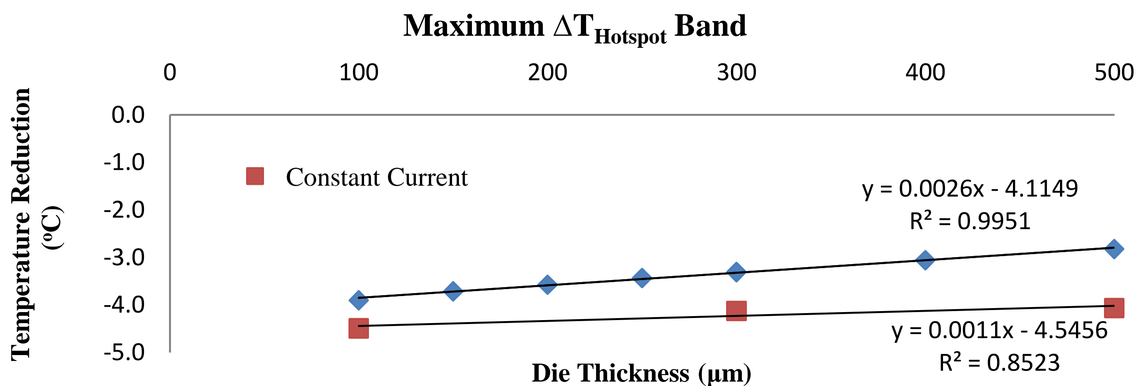

Figure 64: Maximum Hotspot Temperature Reduction Band

At the 100µm die, the constant current and voltage self coolers are able to achieve maximum hotspot temperature reductions of -4.5°C and -3.9°C respectively. This

temperature reduction decreases (absolute value) linearly as the die thickness increases to 500µm where their temperature reductions are -4.0 °C and -2.8 °C.

The hotspot cooling effectiveness determines the ability of the self coolers to remove the temperature rise induced by the introduction of the hotspot. Typical values range from "1" to "0" where "1"describes a device that is able to completely remove the temperature rise and a value of "0" describes a device that is unable to remove the temperature rise. The hotspot cooling effectiveness band is shown in **Figure 65**.

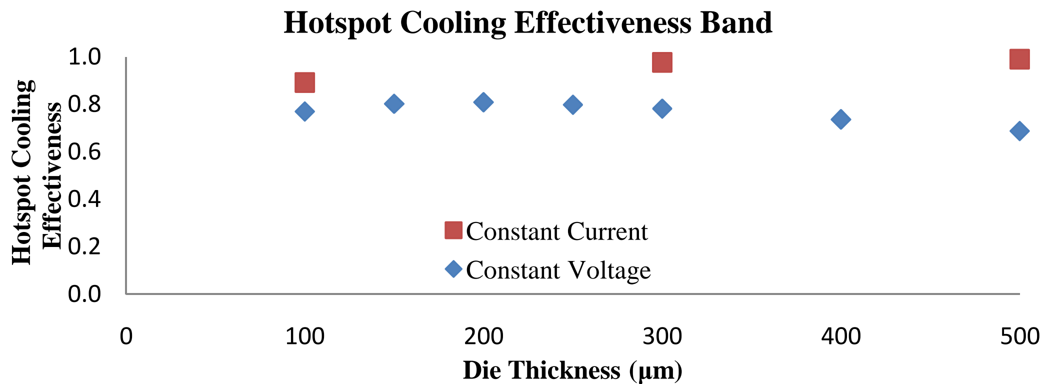

Figure 65: Maximum Hotspot Cooling Effectiveness Band

As described before, the increase in die thickness decreases the maximum hotspot temperature reduction (**Figure 64**). However, the increase in die thickness decreases the spreading resistance resulting in a smaller temperature rise due to the introduction of the hotspot (20). These two effects compete with each other, ultimately providing an optimum die thickness (20). The constant current self cooler does not provide such an optimum die thickness within the range tested with values of 0.98 and 0.99 for the 300µm and 500µm dies respectively. The constant voltage self cooler is shown to provide an optimum of 0.81 hotspot temperature effectiveness at the 200µm die. It is interesting to note that the constant current self cooler provides larger values than the constant voltage self cooler throughout the die thickness range.

The placement of the coolest zone for the constant voltage self cooler at the Cooler electrode edge produces less maximum hotspot temperature reductions than the constant current self cooler. It also produces smaller maximum hotspot temperature reduction Cooler sizes. This is evident in **Figure 66**.

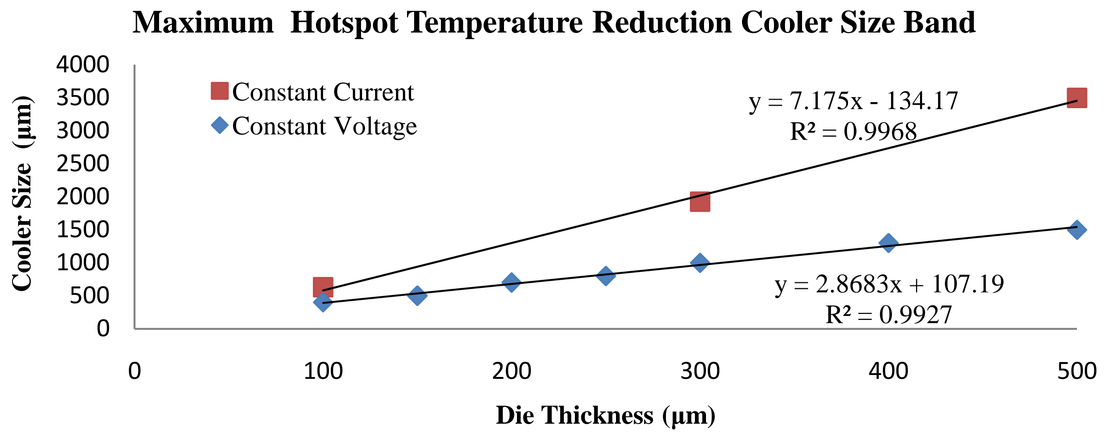

Figure 66: Cooler Width Band at Maximum Hotspot Temperature Reduction

The constant current self cooler shows larger Cooler sizes for the die thickness range studied with a 230µm difference at the 100µm die and 2000µm at the 500µm die. The difference between the optimum Cooler sizes decreases as the die thickness decreases. It is interesting to note that the Cooler size ratio for the constant current and voltage self coolers are about 7:1 and 3:1 respectively.

Chapter 4: Germanium Self Cooling Meta Model

A meta-model of the germanium constant current self cooling is developed from the numerical results. These results are omitted because their trends and tradeoffs are similar to the constant voltage device. The meta-model is a tool that determines the potential of the germanium self cooling technology. It is a faster alternative to running the several numerical simulations necessary to determine the optimum package (10 seconds versus 40 minutes per solution space iteration). It is important to read the numerical chapter before proceeding to understand this meta-model.

As shown in **4.1 Meta-Model,** the meta-model is based on the numerical simulations translating into identical geometry, material properties, and non-thermoelectric boundary conditions. The thermoelectric boundary conditions are different because of the non-uniform flow of current within the germanium die. This translates into a non-uniform Joule heating effect which is difficult and out of the present scope of this work to account for analytically. Thus, a thermal only analytical solution is used in conduction with added heat fluxes to account for the non-uniform Joule heating effects.

The first heat flux accounts for the added Joule heat felt at the center Cooler electrode and uses the alpha (α) allocation factor multiplied by the total amount of Joule heat (I^2R). The second heat flux accounts for the added Joule heat felt at the hotspot and uses the beta (β) allocation factor in the same manner as the latter. Through the procedure of separation of variables, the outputted temperatures are solved through an infinite series.

The method of solving for the allocation factor surfaces evolves three main steps as discussed in **4.2 Allocation Factor Surfaces**. The first step starts by inputting the

optimized current and corresponding center hotspot and Cooler temperature into the thermal-only analytical solution for each geometric variation. Next, the alpha and beta allocation factors are varied parametrically, and the resulting analytical center Cooler and hotspot temperatures are subtracted from their numerical counter parts. This operation produces Cooler and hotspot discrepancy planes which are intersected with the zero discrepancy plane and themselves to provide the alpha and beta pair with the lowest discrepancy.

The above operation is conducted for the whole solution space which produces alpha and beta curves as a function of Cooler size for each die thickness. The alpha allocation factor is fitted with lines and the beta allocation factor is fitted with power functions as a function of Cooler size.

The last step ties together the curve fits with one equation per allocation factor. The premise is that this surface fit equation must be equal to each curve fit equation at the corresponding die thickness. This produces six equations with six unknowns which are solved though matrix inversion. These surfaces are then placed into the meta-model, and the solution space is studied.

Overall, the meta-model displays the same behavior as a function of current, Cooler size, and die thickness as shown by the numerical simulations, and is subsequently omitted. Instead, the results of the meta-model are presented in comparison to the numerical metrics as discrepancies in **4.3 Meta-Model Discrepancy**. The total meta-model discrepancy is produced by the first two steps of the determination process since the last step, the surface fit captures the pervious step’s curve fits with negligible difference.

The maximum total temperature reduction discrepancy at optimum conditions (Cooler size and current) is around 0.1^{o}C (absolute value) for the hotspot temperature and 0.2^{o}C for the Cooler temperature for the die thicknesses studied. For the entire solution space, the maximum total temperature reduction discrepancies for the hotspot and Cooler are 0.2^{o}C and 1.2^{o}C respectively. The maximum total hotspot cooling effectiveness discrepancy at optimum conditions is less than 0.01^{o}C/W (absolute value) and 0.06^{o}C/W over the entire solution space.

The maximum hotspot temperature reduction discrepancy increased from 0.15 ^{o}C to 0.2 ^{o}C while the Cooler temperature reduction discrepancy remained constant at1.2 ^{o}C between the first and last step in determining the allocation factors. The maximum hotspot cooling effectiveness discrepancy increased from 0.01 to 0.06 between the same bounds. Thus more complicated curve fits are predicted to only decrease the total hotspot cooling effectiveness discrepancy and provide no benefit for the temperature reductions.

4.1 *Meta-Model*

A meta-model of the germanium constant current self cooling is developed from the numerical results. These results are omitted because their trends and tradeoffs are similar to the constant voltage device. As such, the geometry outlined in **4.1.1Constant Current Self Cooler** and material properties discussed in **4.1.2 Material Properties** are adopted from **3.1.1 Self Cooling Geometry** and **3.1.2 Material Properties** respectively.

The meta-model consists of coalescing the numerical solution described earlier and an analytical solution as described in **4.1.3 Analytical Solution**. However, the non-uniform flow of current within the germanium die translates into a non-uniform Joule heating effect which is difficult and out of the present scope of this work to account for

analytically. Thus, a thermal only analytical solution is used in conjunction with added heat fluxes which account for the non-uniform Joule heating effects.

The first heat flux accounts for the added Joule heat felt at the center Cooler electrode and uses the alpha (α) allocation factor multiplied by the total amount of Joule heat (I^2R). The second heat flux accounts for the added Joule heat felt at the hotspot and uses the beta (β) allocation factor in the same manner as the latter. Even though the presented work focuses on outputting the center Cooler and hotspot temperatures, a spreading resistance is placed into the meta-model. The non-thermoelectric boundary conditions are responsible for the non-uniform heating at the bottom of the die (hotspot and background heating) as well as the general cooling.

The outputted temperatures are solved through an infinite series with respective Fourier coefficients which are described in more detail in reference (19).

4.1.1 Constant Current Self Cooler

The geometry required for the analytical solution is identical to the one found in **3.1.1 Self Cooling Geometry**. It is shown in **Figure 67** for convenience.

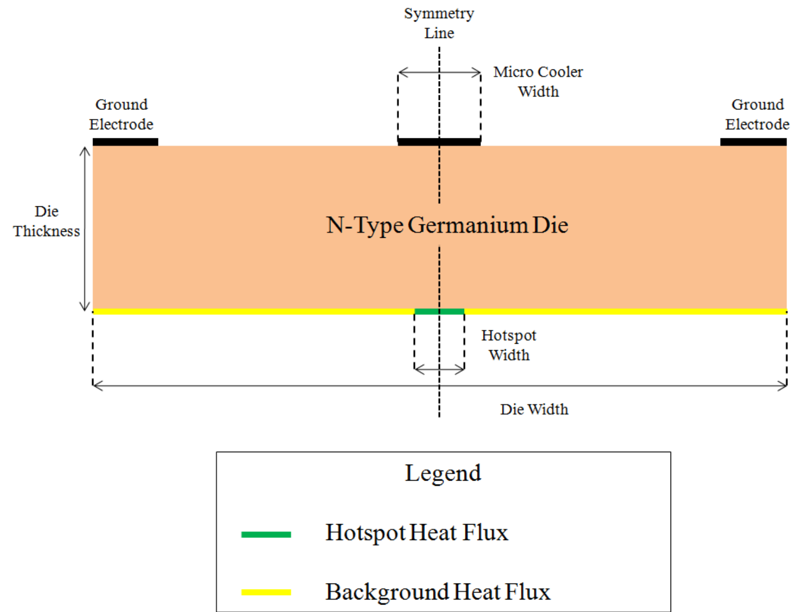

Figure 67: Germanium Self Cooling Device

As shown in **Figure 67**, there are two heat fluxes, hotspot and background, that allow the study of non-uniform heating. The Cooler is placed above the hotspot and the background heat flux surrounds the hotspot. This fact is better explained viewing **Figure 68**.

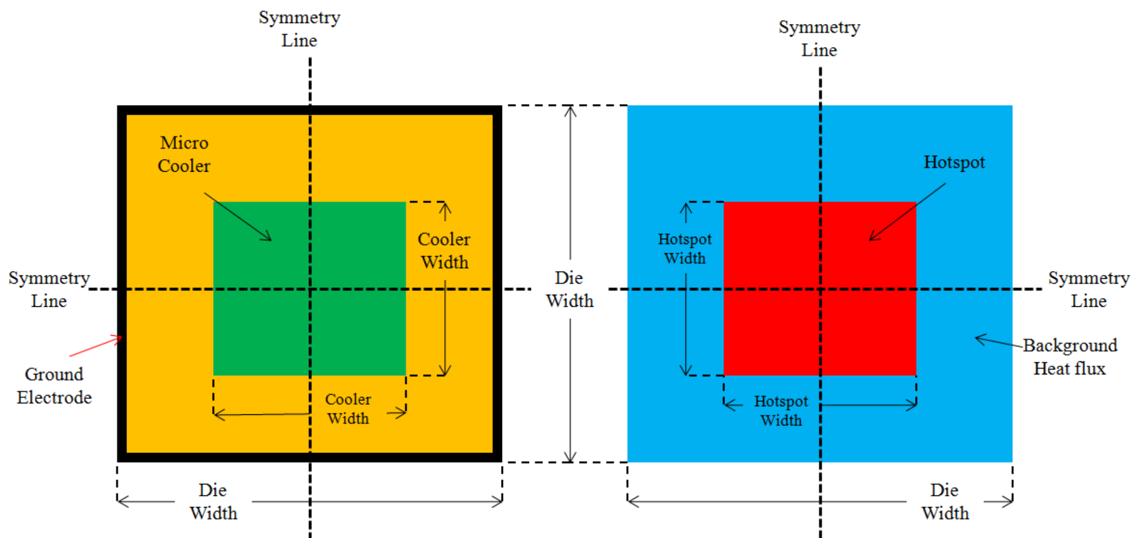

Figure 68: Germanium Self Cooling Device, Left is Top View, Right is bottom heating map (not to scale)

The die, Cooler, and hotspot are all square as shown by the above figure. Moreover, the hotspot and Cooler are in the geometric center of the die. The dimensions of the device are placed in **Table 6**.

Table 6: Germanium Self Cooling Device Dimensions

Label	Dimension (µm)
Die Width (l_{Ge})	12000
Hotspot Width (l_h)	70
Ground Electrode Width (l_{ed})	500
Die Thickness (t_{Ge})	100,300,500
Cooler size (l_C)	420-3500

The die thickness and Cooler size are the geometric variables used to explore the germanium self cooler's potential. The current runs through the ground electrode to the Cooler electrode and due to the Seebeck coefficient difference between the germanium and electrode metal, corresponding cooling or heating heat fluxes are developed at the surface interfaces. A contact resistance is also

4.1.2 Material Properties

The material properties for the germanium layer used to create the presented results in this chapter are identical to those detailed in **3.1.2 Material Properties**. The materials properties selected contained an arsenic doping of $2.3\times10^{18}cm^{-3}$ which produce the highest Power Factor in the range studied. This produces the material properties in **Table 7**.

Table 7: Meta-Model Material Properties

Label	Thermal Conductivity (W/mk)	Electrical Resistivity (µΩm)	Seebeck Coefficient (µV/K)
Germanium Die (doping of $2.3\times10^{18}cm^{-3}$)	60 (20) (47)	50 (20) (46)	-467 (20) (46)

4.1.3 Analytical Solution

The analytical solution of the steady state germanium self cooler requires the solution of the Poisson's equation (19). This is shown in equation **4-1**.

$$\frac{\partial^2 T}{\partial x^2}+\frac{\partial^2 T}{\partial y^2}+\frac{\partial^2 T}{\partial z^2}+\frac{q'''(x,y,z)}{k_{Ge}}=0 \qquad \textbf{4-1}$$

$where$:

$k_{Ge} = thermal\ conductivity \left(\frac{W}{mk}\right)$

$q''' = volumetric\ heat\ generation\ \left(\frac{W}{m^3}\right)$

As shown by

The volumetric heat generation is non-uniform due to the non-uniform current distribution (as shown by **Figure 28**). This requires equation **4-1** to be solved together with Laplace's equation of the electrical potential, which for complicated geometries is out of the scope of the presented work.

The method that is employed uses allocation factors to account for the non-uniform heat generation. These factors account from the fraction of Joule heat that reaches the Cooler electrode (α) and the hotspot (β), and as such are applied as boundary conditions. This simplifies equation **4-1** into Laplace's equation as shown by equation **4-2** (19).

$$\frac{\partial^2 T}{\partial x^2}+\frac{\partial^2 T}{\partial y^2}+\frac{\partial^2 T}{\partial z^2}=0 \qquad \textbf{4-2}$$

4.1.3.1 Boundary Conditions

The boundary condition locations for the meta-model are shown in **Figure 69**.

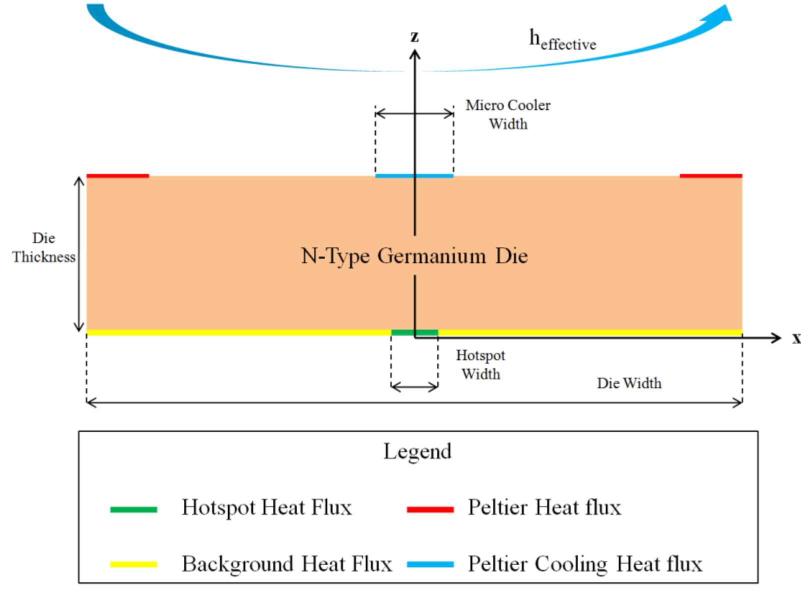

Figure 69: Meta Model, Boundary Condition Location

The non-thermoelectric boundary conditions are shown in **Table 8**.

Table 8: Meta-Model, Non-thermoelectric Boundary conditions

	Value
$\mathbf{h_{effective}}$	8741 (W/m^2-K), $T_{ambient}$=25°C
Hotspot Heat flux	680 W/cm^2
Background Heat flux	70 W/cm^2

The Peltier cooling heat flux is account for through **4-3** (19).

$$\frac{\partial T}{\partial z} = -\frac{q''_{c,eff}}{k_{Ge}}, \quad z = t_{Ge,} \;\; |x| \leq 0.5l_c \;\; |y| \leq 0.5l_c \qquad \textbf{4-3}$$

The variable "$q''_{c,eff}$" accounts for the Peltier cooling, Joule heating portion allocated to the Cooler, and Joule heating from the contact resistance. This is shown in equation **4-4** (19).

$$q''_{c,eff} = \frac{-S_{Ge}TI + I^2\left(\frac{\rho_c}{{l_c}^2}\right) + \alpha I^2 R_{Ge}}{{l_c}^2} \qquad \textbf{4-4}$$

The contact resistance (ρ_c/l_c^2) imposed contains a value of 1×10^{-7} Ω.cm^2 (20). The variable "R_{Ge}" accounts for the electrical resistance of the Cooler and is determined by the Cooler size, die thickness, and doping concentration (19). The same relationship as

shown in equation **4-5** that was previously used by (19) and adopted from (51) and (52) is used here and shown to give reasonable discrepancy between the numerical and analytical values as shown in **4.3 Meta-Model Discrepancy**. The equation approximates the electrical resistance as a circular spreading disk.

$$R_{Ge} = 0.93\left(\frac{4\rho_{Ge}}{\pi r_c^2 r_{Ge}^2}\sum_{n=0}^{\infty}\frac{1}{\tanh\left(\gamma_n t_{Ge}\right)}\frac{J_1^2(\gamma_n r_c)}{\lambda_n^3 J_1^2(\gamma_n r_c)}\right) \qquad \textbf{4-5}$$

The equivalent radii of the annular ground electrode (r_{Ge}) and the center Cooler electrode (r_c) are given by equation **4-6** (19).

$$r_c = \frac{l_c}{\sqrt{\pi}}$$

$$r_{Ge} = \frac{l_{Ge}}{\sqrt{\pi}} \qquad \textbf{4-6}$$

The eigenvalues (γ_n) are the roots of the Bessel function relation $J_o(\gamma_n)=0$ which are computed by (19) and adopted from (53) are computed using equation **4-7**.

$$\gamma_n = \frac{\chi_0}{4}\left(1 + \frac{2}{\chi_o^2} - \frac{62}{3\chi_o^4} + \frac{15116}{30\chi_o^6}\right) \qquad \textbf{4-7}$$

The temperature distribution for the entire germanium die produced by the meta-model has yet to be determined and further research is needed to determine if the above equations are sufficient for the presented material properties.

The Peltier heating heat flux is account for through **4-8** (19).

$$\frac{\partial T}{\partial z} = -\frac{S_{Ge}TI}{k_{Ge}(l_{Ge}^2 - l_{ed}^2)},\ \ z = t_{Ge,}\ \ 0.5l_{ed} \leq |x| \leq 0.5l_{ed},$$

$$0.5l_{ed} \ \leq\ |y| \leq 0.5l_{ed}\ \ , 0.5l_{Ge}\ \leq\ |y| \leq 0.5l_{Ge} \qquad \textbf{4-8}$$

The effective heat transfer coefficient that provides general cooling to the self cooler through conduction through thermal interface, heat sink, and conduction to room temperature (25°C) air is accounted for by equation **4-9** (19).

$$\frac{\partial T}{\partial z} = -\frac{h_{eff}}{k_{Ge}}(T - T_{ambient}), \;\; z = t_{Ge}, \;\; |x| \leq 0.5l_{Ge} \;\; |y| \leq 0.5l_{Ge} \qquad \textbf{4-9}$$

The non-uniform heat dissipated by the electronics at the bottom of the germanium die is simulated through two different heat fluxes, effective hotspot heat flux ($q''_{hs,eff}$), and the background heat flux (q''_{bg}) (19). These heat fluxes are quantified in equation **4-12** (19).

$$\frac{\partial T}{\partial z} = -\frac{q''_{hs,eff}}{k_{Ge}}, z = 0, \;\; |x| \leq 0.5l_h \;\; |y| \leq 0.5l_h$$

$$\frac{\partial T}{\partial z} = -\frac{q''_{bg}}{k_{Ge}}, z = 0, \;\; |x| \geq 0.5l_h \;\; |y| \geq 0.5l_h \qquad \textbf{4-10}$$

The effective hotspot heat flux ($q''_{hs,eff}$) accounts for the hotspot heat flux and the allocated heat due to the non-uniform heat generation as shown by equation **4-11** (19).

$$q''_{hs,eff} = q''_{hs} + \frac{\beta I^2 R_{Ge}}{{l_h}^2} \qquad \textbf{4-11}$$

The edges of the germanium die are modeled as insulated as shown by **4-12** (19).

$$\frac{\partial T}{\partial x} = 0 \;\; x = \pm 0.5l_{Ge}, \;\; |y| \leq 0.5l_{Ge} \; 0 \leq z \leq t_{Ge},$$

$$\frac{\partial T}{\partial y} = 0 \;\; y = \pm 0.5l_{Ge}, \;\; |x| \leq 0.5l_{Ge} \; 0 \leq z \leq t_{Ge}, \qquad \textbf{4-12}$$

4.1.3.2 Hotspot and Cooler Temperature Solutions

The analytical solution to the temperature distribution of the meta-model is found through the separation of variables technique. This technique assumes the temperature has the form of function of “x,” times a function of “y,” times and function of “z.” This is shown in equation **4-13** (19).

$$T(x) = X(x)Y(y)Z(z) \quad \textbf{4-13}$$

Solving Laplace's equation (equation **4-2**) with the boundary conditions described in equation **4-12** produces the general temperature solution which is of the form of infinite series (19). However, the purpose of the current study is to determine the center Cooler and center hotspot temperature, which require the application of the other boundary conditions (equation **4-3** to **4-11**) to determine the Fourier coefficients (19).

The above operations produce the center Cooler temperature and center hotspot temperature shown in equation **4-14** (19) and **4-15** (19).

$$T_h(0,0,0) = T_{ambient} + F_{00} + \sum_{m=1}^{\infty} F_{m0} + \sum_{n=1}^{\infty} F_{0n} + \sum_{m=1}^{\infty}\sum_{n=1}^{\infty} F_{mn} \quad \textbf{4-14}$$

$$\begin{aligned} T_C(0,0,t_{Ge}) = T_{ambient} + F_{00} + E_{00}t_{Ge} \\ + \sum_{m=1}^{\infty} [E_{m0}\sinh(\alpha_m t_{Ge}) + F_{m0}\cosh(\alpha_m t_{Ge})] \\ + \sum_{n=1}^{\infty} [E_{0n}\sinh(\beta_n t_{Ge}) + F_{0n}\cosh(\beta_n t_{Ge})] \\ + \sum_{m=1}^{\infty}\sum_{n=1}^{\infty} E_{mn}\sinh(\gamma_{mn} t_{Ge}) + F_{mn}\cosh(\gamma_{mn} t_{Ge}) \end{aligned} \quad \textbf{4-15}$$

$where$:

$$\gamma_{mn} = \pi\sqrt{\frac{2m^2}{l_{Ge}} + \frac{2n^2}{l_{Ge}}}$$

The Fourier coefficients have been omitted here and are discussed in reference (19).

The above temperature solutions are in the form of infinite series which mandates understanding at which integer value the solutions converge. For the 300µm die, 500µm Cooler size and zero current case, the summation integer was varied while recording the

center Cooler and hotspot temperatures. These operations produced **Figure 70** and **Figure 71**.

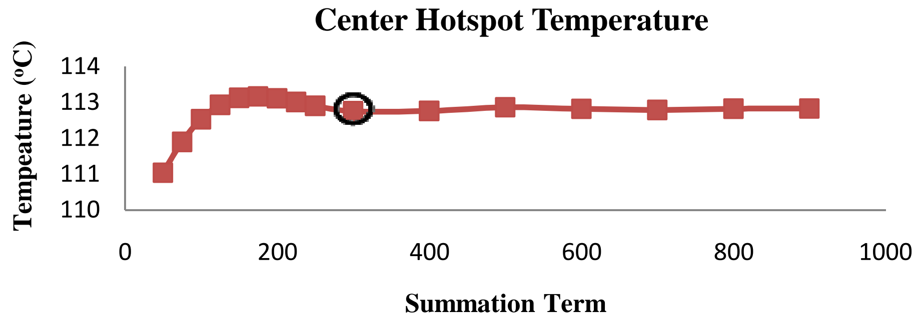

Figure 70: Hotspot Temperature summation integer study; 300µm die, 500µm Cooler size, I=0

The center hotspot temperature converges to a value of about 113°C, but 300 summation terms are used for results since it produces less than 0.07^{0}C difference between the temperature produced by 900 summation terms. This trend was independent of Cooler size and die thickness. Consequently, all results presented in this chapter used 300 summation terms for the center hotspot temperature.

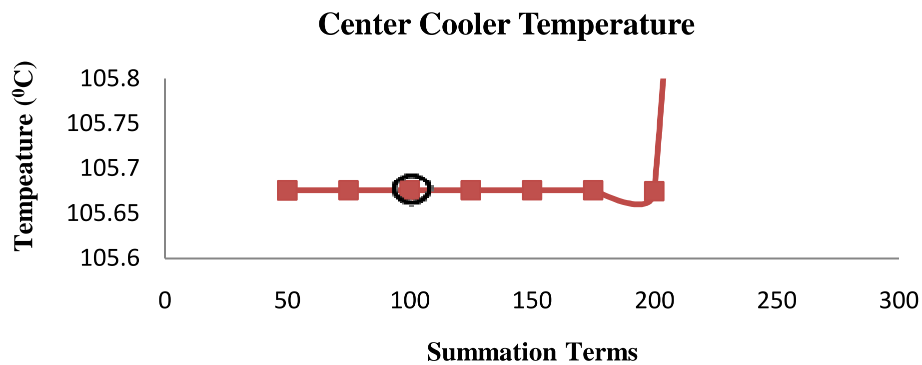

Figure 71: Cooler Temperature summation integer study; 300µm die, 500µm Cooler size, I=0

The center Cooler temperature remains almost at 105.7^{o}C and eventually diverges at 175 summation terms. The divergent term count is independent of Cooler size but is dependent of die thickness. Consequently for the results presented in this chapter, the

summation term used for the center Cooler temperature are 300, 100, and 40 for the 100µm, 300µm, and 500µm die thicknesses respectively.

4.2 *Allocation Factor Surfaces*

The method of solving for the allocation factor surfaces evolves three main steps. The first step, discussed in **4.2.1 Surface Intersection Method**, starts with the numerical temperature results. For each geometry (Cooler size and die thickness), the optimum temperature and current are recorded. Next, the alpha and beta allocation factors are varied parametrically, and the resulting analytical center Cooler and hotspot temperatures are subtracted from their numerical counter parts. This operation produces Cooler and hotspot discrepancy planes. Finally, both discrepancy equation planes are intersected with the zero discrepancy plane and themselves to provide the alpha and beta pair with the lowest discrepancy.

The above operation is conducted for the solution space and as shown in **4.2.2 Curve Fit**, produces alpha and beta curves for each die thickness. These curves are then fitted as a function of die thickness. The alpha allocation factor is fitted with lines and the beta allocation factor is fitted with power functions.

In **4.2.3 Surface Fit**, these curve fits are tied together with one equation per allocation factor. The premise of this step is that the surface fit equation must be equal to each curve fit equation at the corresponding die thickness. This produces six equations with six unknowns which are solved though matrix inversion. This surface fit is shown to provide negligible difference between it and the curve fits at the die thicknesses studied.

It is important to note that each of the operations to determine the allocation factors have associated discrepancies between the outputted meta-model and numerical metrics. These discrepancies are detailed in **4.3 Meta-Model Discrepancy**.

4.2.1 Surface Intersection Method

The first step in solving for the allocation factors evolves reviewing the numerical data from the constant current self cooler. For each specific geometry (Cooler with and die thickness), there exists an optimum current that provides maximum hotspot temperature reduction. Using the optimized current as a starting point for the meta-model is intuitive since it is the operation point of the device.

The analytical solution is set up to match the geometry (Cooler size and die thickness) and optimized current. Next, the alpha and beta allocation factors are varied parametrically, and the resulting analytical center Cooler and hotspot temperatures are subtracted from their numerical counter parts. This operation produces Cooler and hotspot discrepancy planes exemplified by **Figure 72** and **Figure 73**.

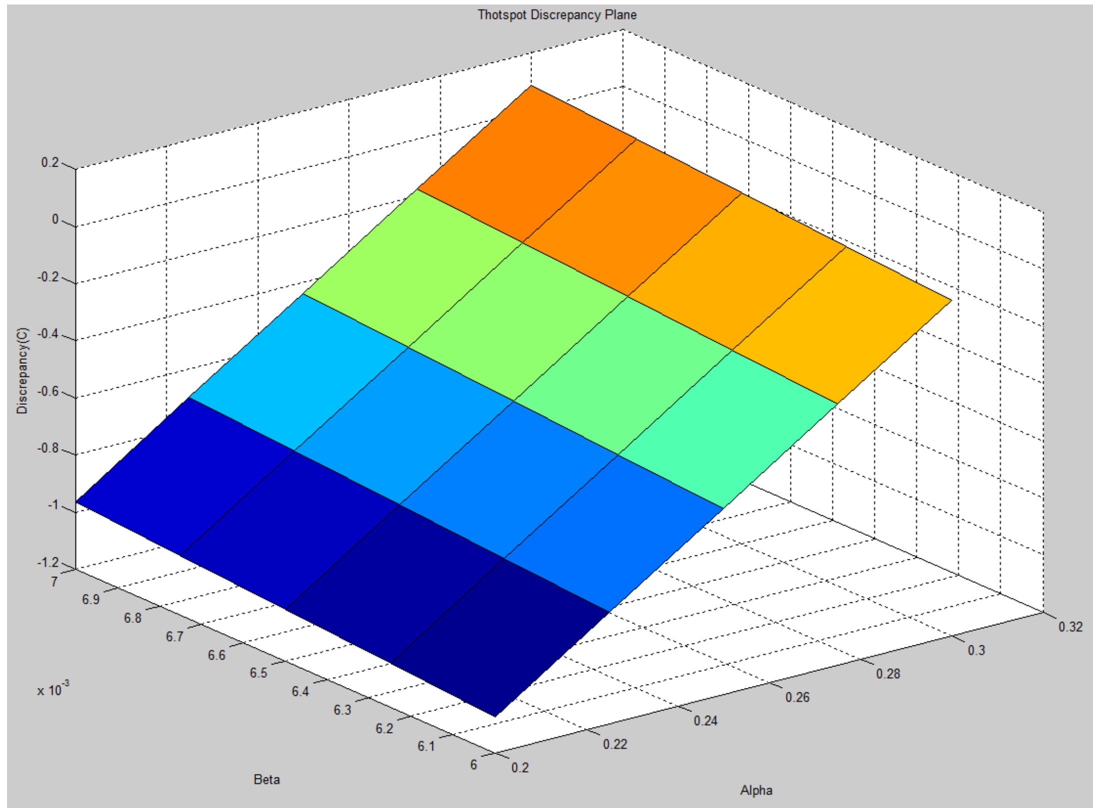

Figure 72: Cooler Discrepancy Plane for 300μm die, 1015μm Cooler Width, I=3.35A

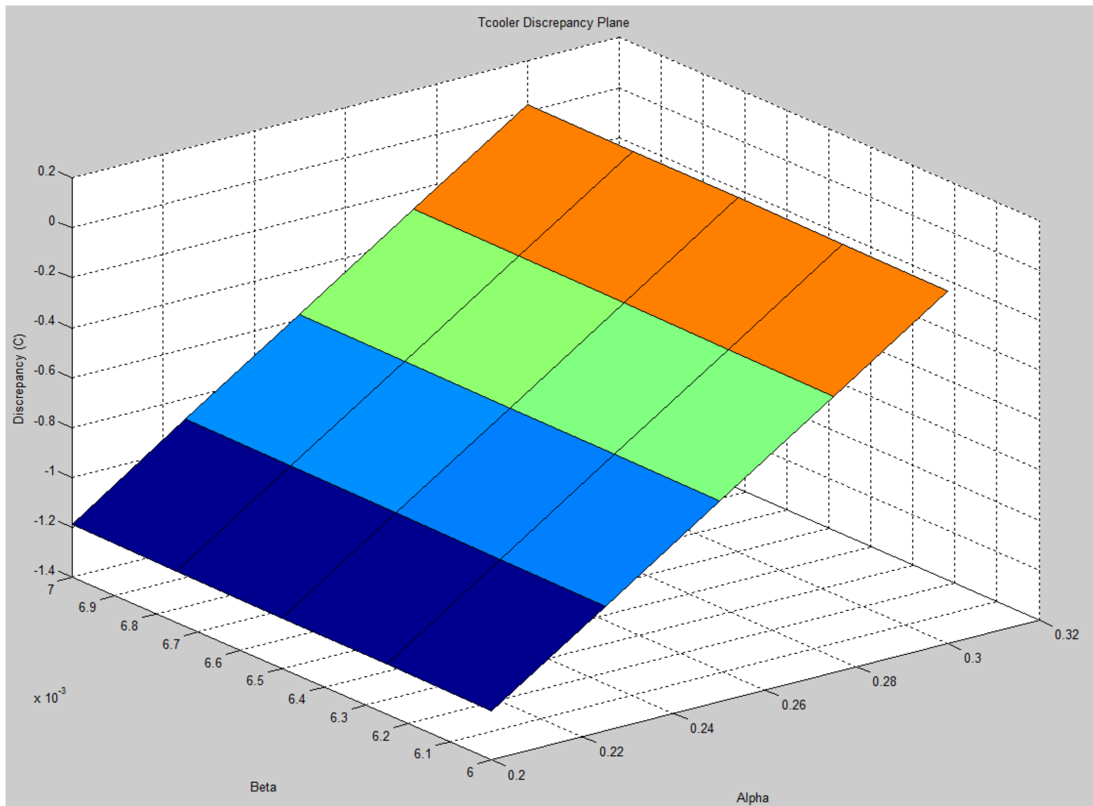

Figure 73: Hotspot Discrepancy Plane for 300μm die, 1015μm Cooler Width, I=3.35A

Next, the plane equations for the above planes are found through simple single variable Calculus. This process requires three points to make two vectors which are crossed to create a normal vector. Then the normal vector is "doted" with one of the original vectors to create the equation of the plane. Generic equations for these planes are shown in equation **4-16**.

$$a_{Cooler}x + b_{Cooler}y + c_{Cooler}z = d_{Cooler}$$
$$a_{Hotspot}x + b_{Hotspot}y + c_{Hotspot}z = d_{Hotspot} \quad \textbf{4-16}$$

The resulting plane equations are checked for accuracy against the original discrepancy through a simple subtraction of values. This produces **Figure 74** and **Figure 75** for the center Cooler and hotspot error planes.

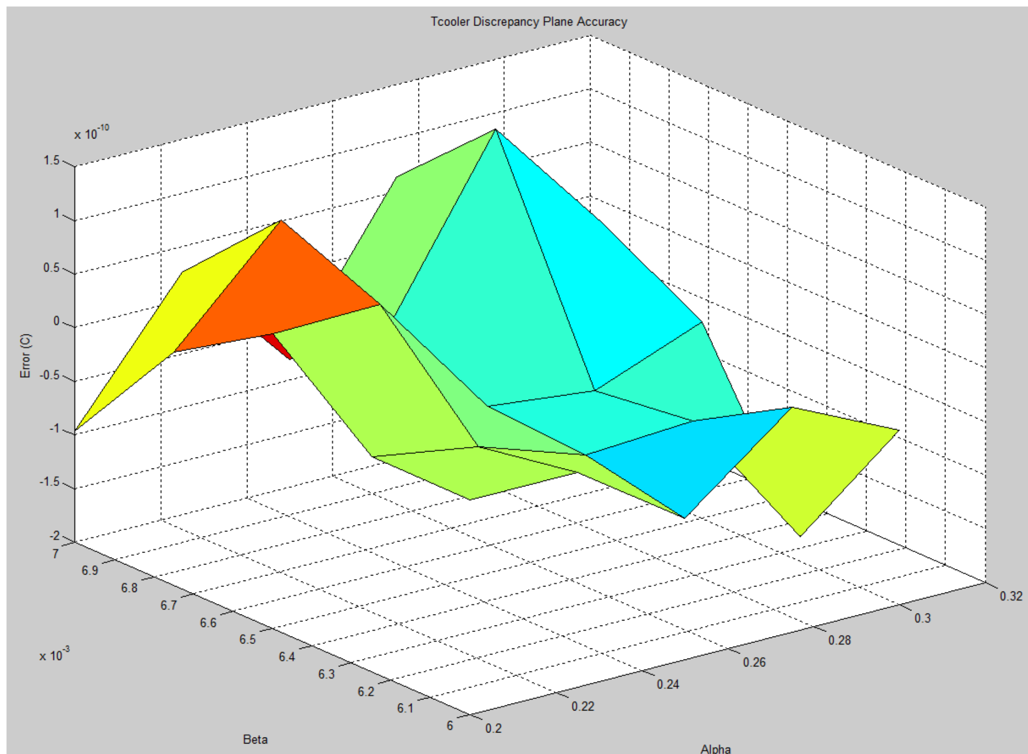

Figure 74: Cooler Discrepancy Equation Accuracy for 300μm die, 1015μm Cooler Width, I=3.35A

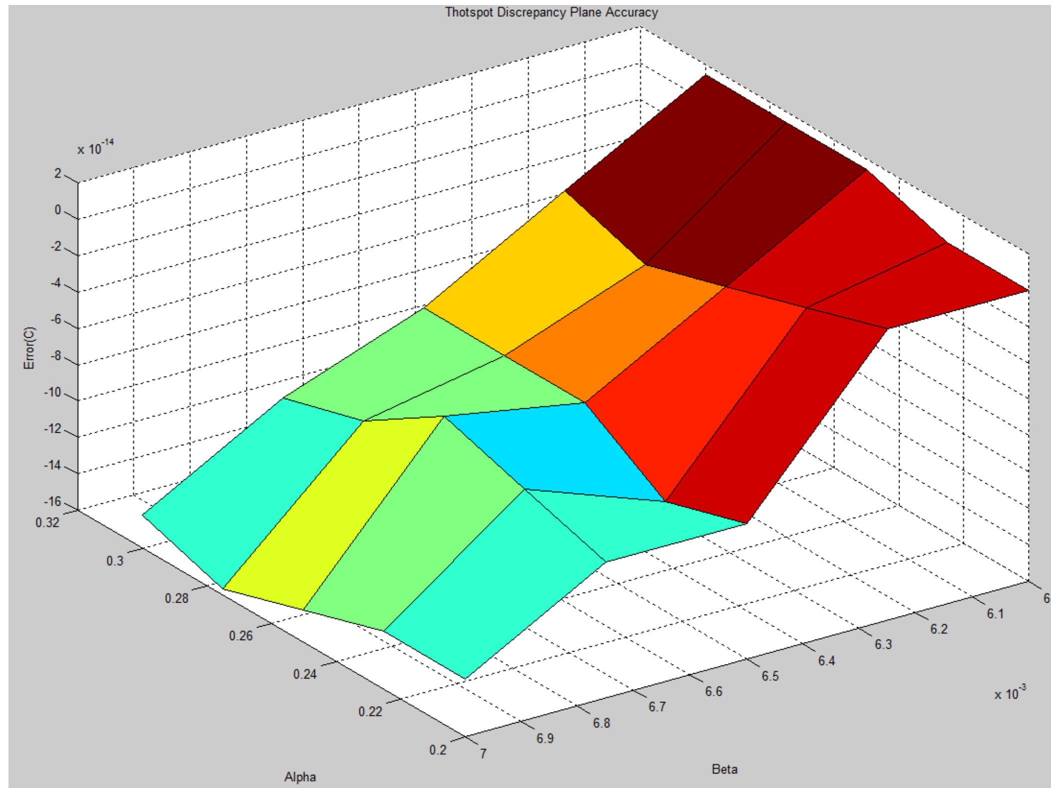

Figure 75: Hotspot Discrepancy Equation Accuracy for 300µm die, 1015µm Cooler Width, I=3.35A

As is shown above, the mathematic operations provide a maximum of 2e-10 error for the Cooler temperature and 2e-14 error for the hotspot temperature. This low error between the equation planes and the data discrepancy planes are typical of all cases studied.

Finally, both discrepancy equation planes are intersected with the zero discrepancy plane and themselves to provide the zero discrepancy alpha and beta pair (providing the name of this step). This is accomplished through the following steps.

Both planes cross the zero discrepancy plane (z=0) creating two independent lines as shown below.

$$a_{Cooler}x + b_{Cooler}y = d_{Cooler}$$

$$a_{Hotspot}x + b_{Hotspot}y = d_{Hotspot}$$

The above line equations are placed into standard form in equation **4-17**.

$$f_{Cooler}(x) = -\frac{a_{Cooler}}{b_{Cooler}}x + \frac{d_{Cooler}}{a_{Cooler}}$$

4-17

$$f_{Hotspot}(x) = -\frac{a_{Hotspot}}{b_{Hotspot}}x + \frac{d_{Hotspot}}{a_{Hotspot}}$$

These lines are subsequently intersected to provide the one alpha and beta order pair that provides zero discrepancy for the center Cooler and hotspot temperature. This process is outlined below.

The first line from equation **4-17** is rearranged so that x is solved for as shown below.

$$\left(\frac{d_{Cooler}}{a_{Cooler}} - y\right)\frac{b_{Cooler}}{a_{Cooler}} = x$$

This value is then substituted into the second line of equation **4-17** as shown below.

$$y = -\frac{c}{b_{Hotspot}}\left(\left(\frac{d_{Cooler}}{a_{Cooler}} - y\right)\frac{b_{Cooler}}{a_{Cooler}}\right) + \frac{d_{Hotspot}}{a_{Hotspot}}$$

The variable "y" is solved for and is equal to the alpha allocation beta. This value is then substituted back into "x," subsequently solving for the alpha allocation factor as shown in equation **4-18**.

$$\beta = y = \frac{\frac{a_H d_C b_C}{b_H {a_C}^2} - \frac{d_H}{a_H}}{\frac{a_H b_C}{b_H a_C} - 1}$$

4-18

$$\alpha = x = \left(\frac{d_{Cooler}}{a_{Cooler}} - \left(\frac{\frac{a_H d_C b_C}{b_H {a_C}^2} - \frac{d_H}{a_H}}{\frac{a_H b_C}{b_H a_C} - 1}\right)\right)\frac{b_{Cooler}}{a_{Cooler}}$$

$where$:
$i_H = i_{Hotspot}$
$i_C = i_{Cooler}$

The above operations are accomplished for all geometries in the solution space. This produces allocation factors as a function of Cooler size for each die thickness as shown in

Figure 76 and **Figure 77.** Before understanding the below figures, it is important to understand that the allocation factors account for the portion of Joule heat reaching the Cooler electrode (α) and hotspot (β). Moreover, as shown by **Figure 28**, the current flows from the top peripheral ground electrode to the center Cooler electrode.

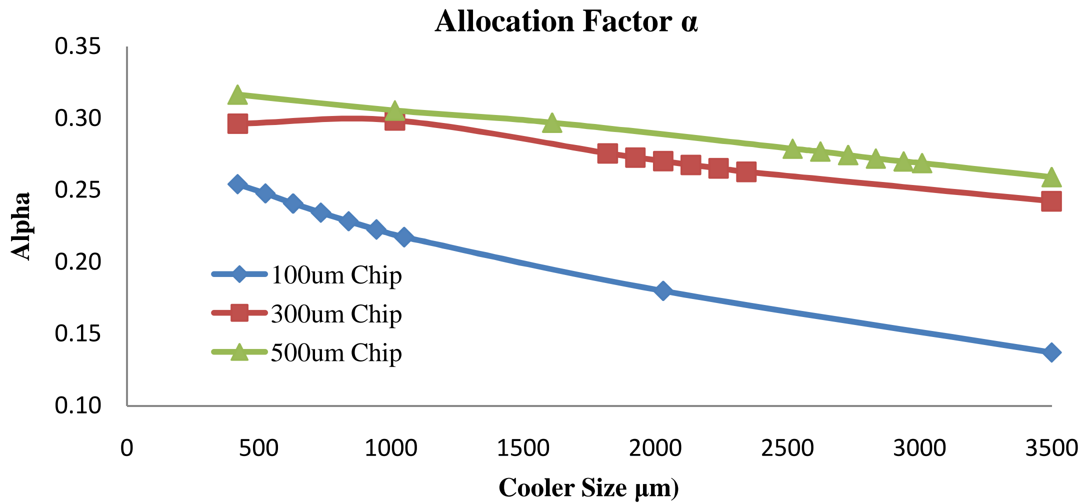

Figure 76: Alpha as a function of Cooler size for each die thickness

As the Cooler size increases, the current density underneath the Cooler electrode decreases somewhat linearly. This translates into decreased Joule heating and subsequently decreased alpha values. As the die thickness is decreased, the current is de-constricted, resulting in significantly less Joule heating for the same current value. However, the optimum current values which balance the Peltier cooling and Joule heat increase dramatically as the die thickness increases, creating an overall increase in Joule heat, and subsequently alpha values.

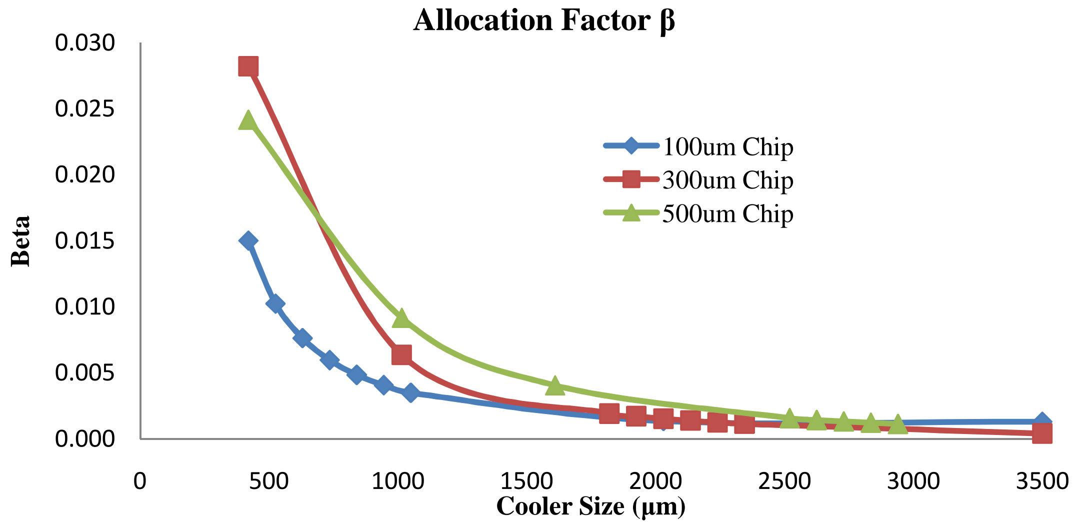

Figure 77: Beta as a function of Cooler size for each die thickness

The overall values for the beta allocation factor are smaller (at least one order of magnitude) than the alpha allocation factor since the majority of the current remains near the top surface. This translates into less current density near the hotspot, less Joule heat, and subsequently less beta values. As the Cooler size increases, the current density decreases, eventually translating into exponentially decreasing beta values. These values asymptotically approach zero for all die thicknesses at large Cooler sizes. Only at "small" Cooler sizes do the die thickness demonstrate different beta values.

4.2.2 Curve Fit

The data from **Figure 76** and **Figure 77** provides the alpha and beta values for each cooler width and die thickness. A curve fit is used to express the allocation factors as a function of Cooler size. A linear curve fit is used for alpha and a power fit is used for beta. The allocation factors and their curve fits are shown in **Figure 78** and **Figure 79.**

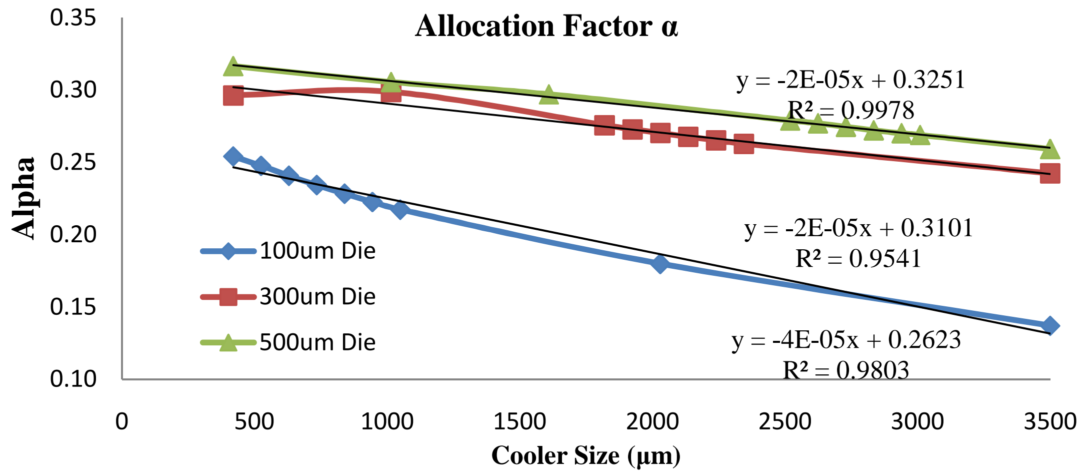

Figure 78: Linear Curve Fit Alpha

Higher order curve fits would have provided better accuracy ($R^2 \approx 1$) at the cost of more complicated polynomials. Thus, a linear curve fit is chosen because it provides moderate accuracy ($R^2 > 0.95$). These curve fits have the form detailed by equation **4-19**.

$$\alpha(c) = A_i c + B_i \quad \textbf{4-19}$$

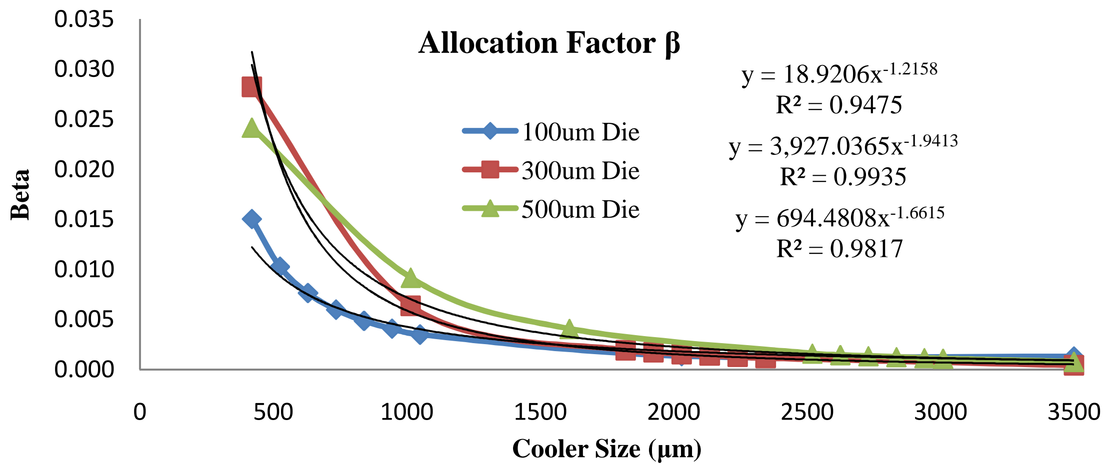

Figure 79: Power Fit Beta

A power curve fit is chosen because it provides moderate accuracy ($R^2 > 0.94$). These curve fits have the form detailed by equation **4-20**.

$$\beta(c) = A_i \mathrm{c}^{(B_i)} \quad \textbf{4-20}$$

Since there is moderate difference between the surface intersection allocation values and the curve fit allocation factor values, there is moderate temperature discrepancy added by the curve fitting operation as shown by **4.3.2 Total Discrepancy**.

4.2.3 Surface Fit

A two dimensional curve fit, or surface fit, is determined to provide allocation factor functions over the entire solution space.

4.2.3.1 Alpha Surface Fit

The alpha surface fit entails creating a formula that ties in the polynomials that are a function of Cooler size into one function that is a function of Cooler size and die thickness. Assuming that the curve fits are generic polynomials, the generic formula for the surface fit is shown in equation **4-21**.

$$\alpha_{Polynomical}(c,t) = \sum_{n=0}^{m} p_{1+(k+1)n} c^{m-n} t^{0} + p_{1+(k+1)n} c^{m-n} t^{1} + p_{1+(k+1)n} c^{m-n} t^{2} + \cdots + p_{1+(k+1)n} c^{m-n} t^{k} \qquad \textbf{4-21}$$

$where:$
$c = Cooler\ width\ (\mu m)$
$t = die\ thickness\ \mu m$
$m = curve\ fit\ order$
$k = number\ of\ die\ thicknesses$

The above equation is simplified by acknowledging that linear curve fits (first order polynomial) are used and that only three die thicknesses are studied. Since three die thicknesses are studied, a quadratic curve fit though die thickness is used for the surface fit as shown by the coefficients of "t" in equation **4-22**.

$$\alpha_{Linear}(c,t) = \sum_{n=0}^{1} p_{1+3n}c^{m-n}t^0 + p_{1+3n}c^{m-n}t^1 + p_{1+3n}c^{m-n}t^2 \quad \textbf{4-22}$$

Equation **4-22** can be expanded into equation **4-23**.

$$\alpha_{Linear}(c,t) = p_1c + p_2ct + p_3ct^2 + p_4 + p_5t + p_6t^2 \quad \textbf{4-23}$$

Even though the equation for the alpha surface fit is known, its coefficients are still to be determined. They can be determined if the surface fit equation is set equal to each curve fit equation at the corresponding die thickness. This process is detailed below.

$$\alpha_{Linear}(c,t_i) = p_1c + p_2ct_i + p_3c{t_i}^2 + p_4 + p_5t_i + p_6{t_i}^2 = A_ic + B_i$$

The above is accomplished for all three die thickness curve fits, which produces six equations and six unknowns as shown through matrix notation in equation **4-24**.

$$\begin{bmatrix} 1 & t_1 & {t^2}_1 \\ 1 & t_2 & {t^2}_2 \\ 1 & t_3 & {t^2}_3 \end{bmatrix} \begin{bmatrix} p_1 \\ p_2 \\ p_3 \end{bmatrix} = \begin{bmatrix} A_1 \\ A_2 \\ A_3 \end{bmatrix}; \begin{bmatrix} 1 & t_1 & {t^2}_1 \\ 1 & t_2 & {t^2}_2 \\ 1 & t_3 & {t^2}_3 \end{bmatrix} \begin{bmatrix} p_4 \\ p_5 \\ p_6 \end{bmatrix} = \begin{bmatrix} B_1 \\ B_2 \\ B_3 \end{bmatrix} \quad \textbf{4-24}$$

The surface fit coefficients are easily solved through matrix inversion shown in equation **4-25**.

$$\underline{K} \begin{bmatrix} p_1 \\ p_2 \\ p_3 \end{bmatrix} = \underline{A}; \underline{K} \begin{bmatrix} p_4 \\ p_5 \\ p_6 \end{bmatrix} = \underline{B}$$

$$\begin{bmatrix} p_1 \\ p_2 \\ p_3 \end{bmatrix} = \underline{K}^{-1}\underline{A}; \begin{bmatrix} p_4 \\ p_5 \\ p_6 \end{bmatrix} = \underline{K}^{-1}\underline{B} \quad \textbf{4-25}$$

$where$:

$$\underline{K} = \begin{bmatrix} 1 & t_1 & {t^2}_1 \\ 1 & t_2 & {t^2}_2 \\ 1 & t_3 & {t^2}_3 \end{bmatrix}; \underline{A} = \begin{bmatrix} A_1 \\ A_2 \\ A_3 \end{bmatrix}; \underline{B} = \begin{bmatrix} B_1 \\ B_2 \\ B_3 \end{bmatrix}$$

The above process onto the data shown in **Figure 78** produces the alpha coefficients in equation **4-26** which correspond to equation **4-23**.

$$\begin{bmatrix} p_1 \\ p_2 \\ p_3 \\ p_4 \\ p_5 \\ p_6 \end{bmatrix}_{Linear\ Alpha} = \begin{bmatrix} -5.271e-5 \\ 1.748e-7 \\ 2.131e-10 \\ 0.2262 \\ 4.020e-4 \\ -4.086e-7 \end{bmatrix} \quad \textbf{4-26}$$

The alpha coefficients from equation **4-26** which correspond to equation **4-23** produce the alpha surface shown in **Figure 80**. The surface demonstrates its quadratic behavior through the die thickness as well as linear behavior through the Cooler size.

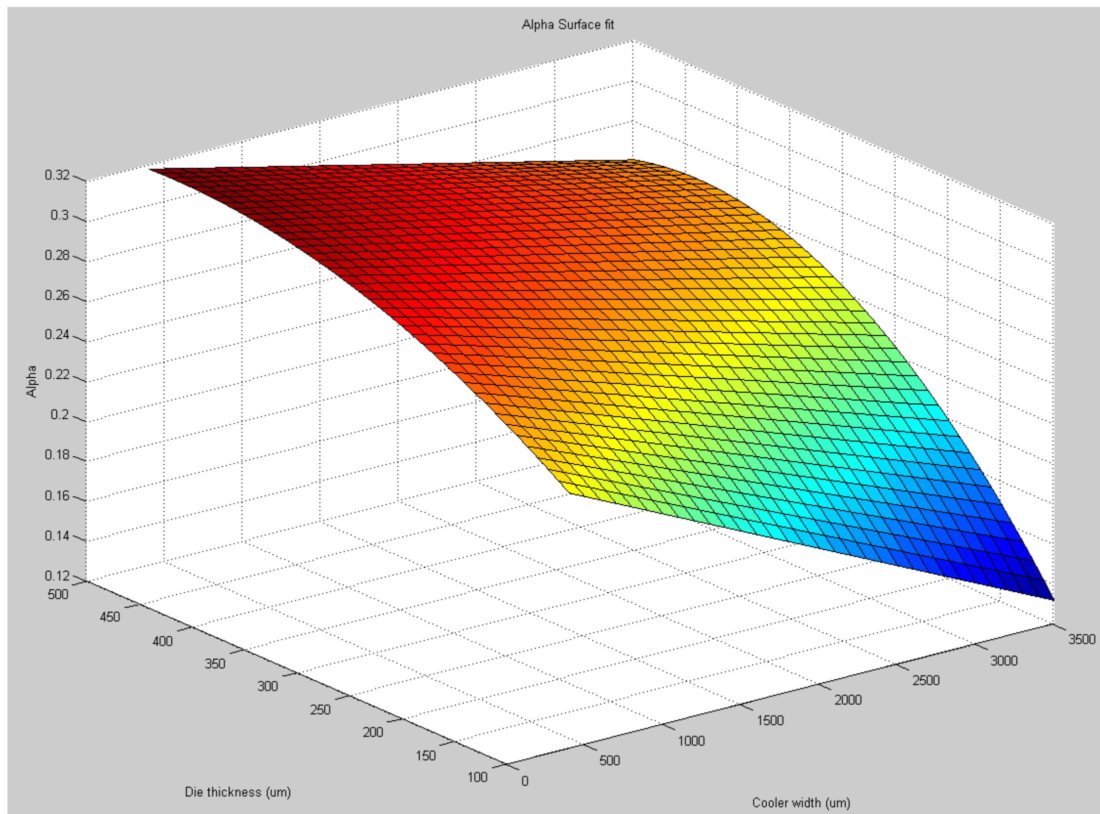

Figure 80: Alpha Allocation Factor Surface

There is negligible (<2e-18) alpha value difference between the curve fits and the surface fit equations as shown by **Figure 81**. Thus, the surface fit operation produces no added discrepancy between the numerical and meta-models.

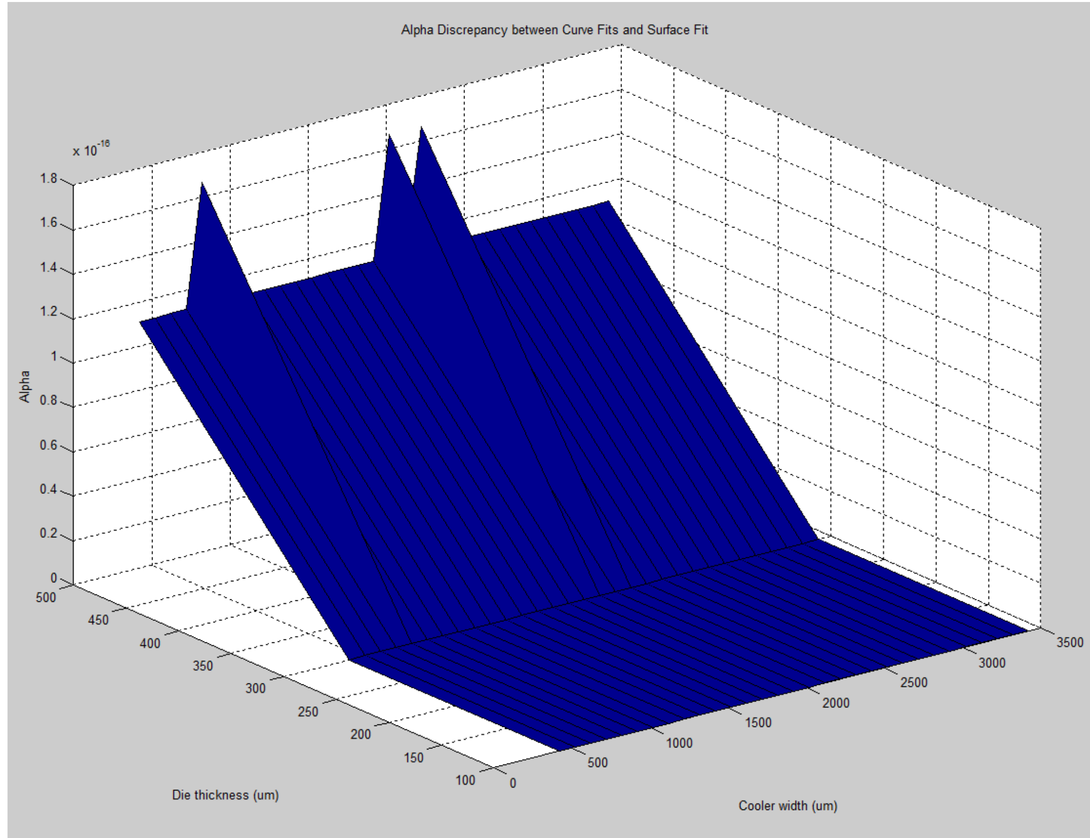

Figure 81: Alpha value Surface Fit Discrepancy from Curve Fit

4.2.3.2 Beta Surface Fit

The beta surface fit entails creating a formula that ties the power curve fits that are a function of Cooler size into one function that is a function of Cooler size and die thickness. Assuming that the curve fits are generic power functions, the generic formula for the surface fit is shown in equation **4-27**.

$$\beta_{Power}(c,t) = \left(\sum_{n=0}^{k} q_{n+1} t^n\right) c^{\sum_{n=0}^{k} q_{n+k+2} t^n} \quad \textbf{4-27}$$

The above equation is simplified by acknowledging that only three die thicknesses are studied. Thus, a quadratic curve fit though die thickness is used for the surface fit as shown by the coefficients of "t" in equation **4-28**.

$$\beta_{Power}(c,t) = \left(\sum_{n=0}^{2} q_{n+1} t^{n}\right) c^{\sum_{n=0}^{2} q_{n+4} t^{n}} \quad \textbf{4-28}$$

Equation **4-28** can be expanded into equation **4-29**.

$$\beta_{Power}(c,t) = (q_1 + q_2 t + q_3 t^2) c^{q_4 + q_5 t + q_6 t^2} \quad \textbf{4-29}$$

Even though the equation for the beta surface fit is known, its coefficients are still to be determined. They can be determined if the surface fit equation is set equal to each curve fit equation at the corresponding die thickness. This process is detailed below.

$$\beta_{Power}(c,t_i) = (q_1 + q_2 t_i + q_3 {t_i}^2) c^{q_4 + q_5 t_i + q_6 {t_i}^2} = A_i \mathrm{c}^{(B_i)}$$

The above is accomplished for all three die thickness curve fits, which produces six equations and six unknowns as shown through matrix notation in equation **4-30**.

$$\begin{bmatrix} 1 & t_1 & {t^2}_1 \\ 1 & t_2 & {t^2}_2 \\ 1 & t_3 & {t^2}_3 \end{bmatrix} \begin{bmatrix} q_1 \\ q_2 \\ q_3 \end{bmatrix} = \begin{bmatrix} A_1 \\ A_2 \\ A_3 \end{bmatrix}; \begin{bmatrix} 1 & t_1 & {t^2}_1 \\ 1 & t_2 & {t^2}_2 \\ 1 & t_3 & {t^2}_3 \end{bmatrix} \begin{bmatrix} q_4 \\ q_5 \\ q_6 \end{bmatrix} = \begin{bmatrix} B_1 \\ B_2 \\ B_3 \end{bmatrix} \quad \textbf{4-30}$$

The surface fit coefficients are easily solved through matrix inversion shown in equation **4-31**.

$$\underline{K} \begin{bmatrix} q_1 \\ q_2 \\ q_3 \end{bmatrix} = \underline{A}; \underline{K} \begin{bmatrix} q_4 \\ q_5 \\ q_6 \end{bmatrix} = \underline{B}$$

$$\begin{bmatrix} q_1 \\ q_2 \\ q_3 \end{bmatrix} = \underline{K}^{-1} \underline{A}; \begin{bmatrix} q_4 \\ q_5 \\ q_6 \end{bmatrix} = \underline{K}^{-1} \underline{B} \quad \textbf{4-31}$$

$where$:

$$\underline{K} = \begin{bmatrix} 1 & t_1 & {t^2}_1 \\ 1 & t_2 & {t^2}_2 \\ 1 & t_3 & {t^2}_3 \end{bmatrix}; \underline{A} = \begin{bmatrix} A_1 \\ A_2 \\ A_3 \end{bmatrix}; \underline{B} = \begin{bmatrix} B_1 \\ B_2 \\ B_3 \end{bmatrix}$$

The above process onto the data shown in **Figure 79** produces the alpha coefficients in equation **4-32** which correspond to equation **4-29**.

$$\begin{bmatrix} q_1 \\ q_2 \\ q_3 \\ q_4 \\ q_5 \\ q_6 \end{bmatrix}_{Power\ Beta} = \begin{bmatrix} -4.613e+3 \\ 5.524e+1 \\ -8.926e-2 \\ -0.4760 \\ -8.655e-3 \\ 1.257e-5 \end{bmatrix} \quad \textbf{4-32}$$

The alpha coefficients from equation **4-32** which correspond to equation **4-29** produce the beta surface shown in **Figure 82**.

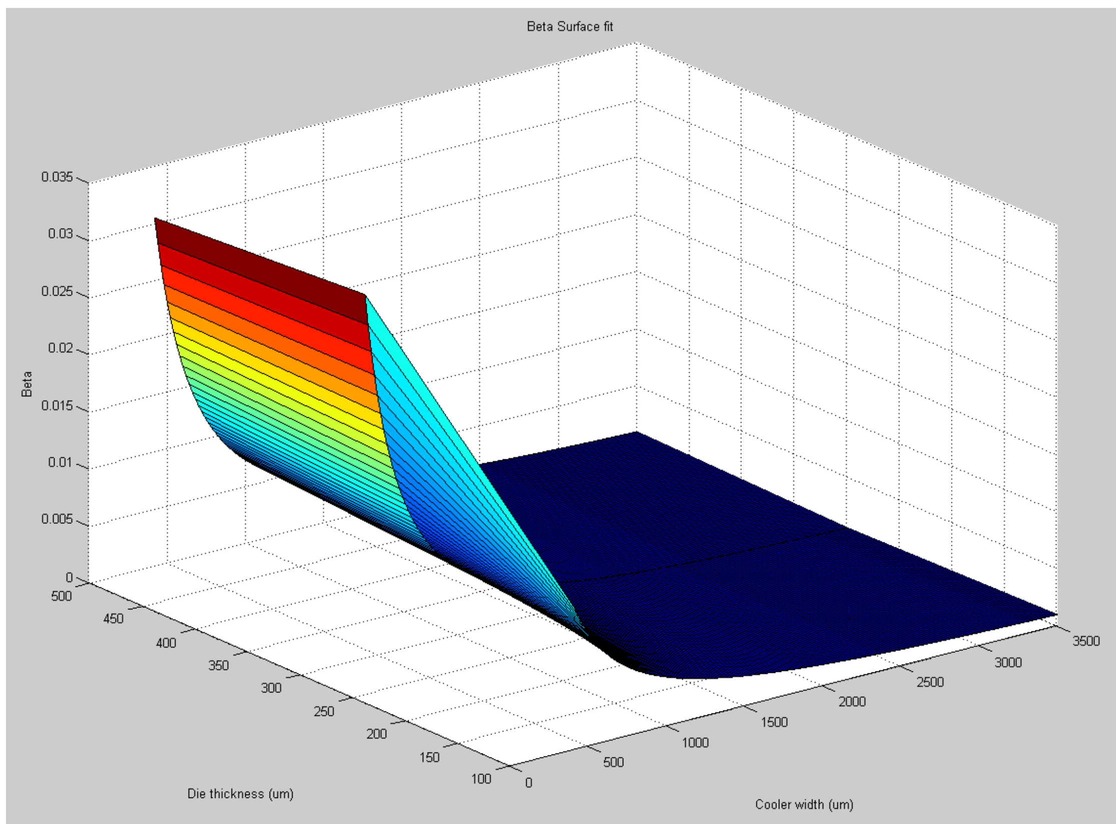

Figure 82: Beta Allocation Factor Surface

There is negligible (<3e-16) beta value difference between the curve fits and the surface fit equations as shown by **Figure 97**.

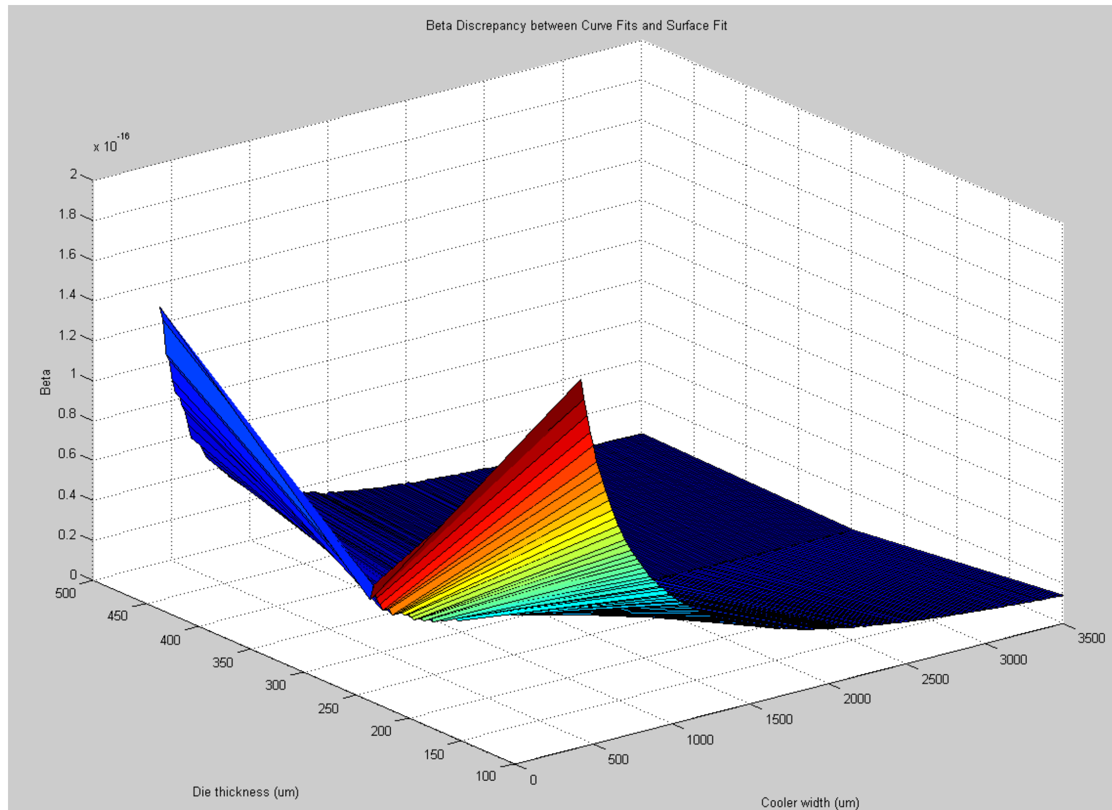

Figure 83: Beta value Surface Fit Discrepancy from Curve Fit

Due to the nature of the beta surface fit, some caution must be employed if the meta-model is used to output results for die thicknesses in between those used to create the surface (100 to 300 and 300 to 500). As shown in **Figure 84**, there is a maximum beta value around 0.24 around the 130µm die thickness.

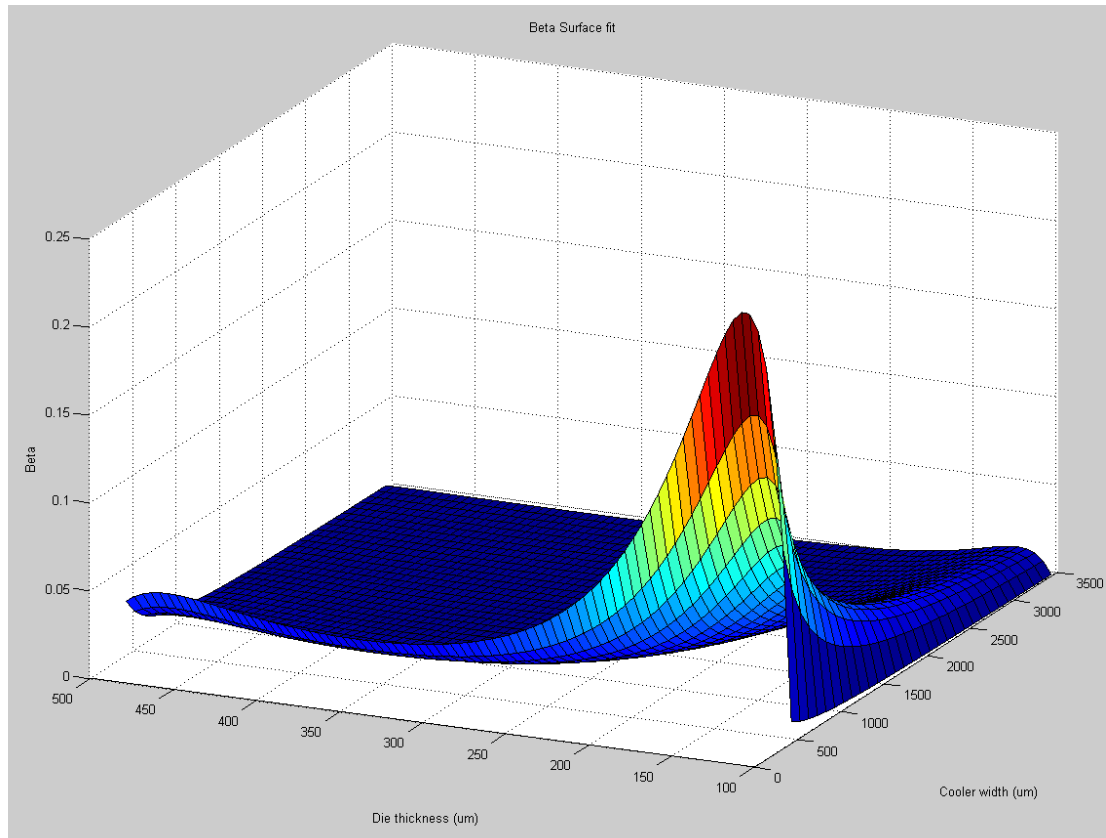

Figure 84: Beta Surface Problems

The maximum is an order of magnitude larger than the values found through the presented process. However, since the130µm die thickness was not numerically simulated, it is impossible to determine if the surface is correctly foreshadowing the performance of other die thicknesses. This is an item where further research is needed to determine the surface's accuracy and foreshadowing power.

4.3 *Meta-Model Discrepancy*

Overall the meta-model displays the same behavior as a function of current, Cooler size, and die thickness as shown by the numerical results. The numerical results demonstrate similar values, trends, and tradeoffs as the constant voltage self-cooler, and

thus were omitted. Moreover, the results of the meta-model are presented in comparison to the numerical results since this is of more interest.

The constant current specific metrics discussed in **3.2.1 Cooling Metrics** are recorded for the meta-model and the differences between it and the numerical results are shown as discrepancies.**4.3.1 Plane Intersection Discrepancy** discusses the discrepancies associated with the first step in determining the allocation factors.

The maximum temperature reduction discrepancy at optimum Cooler sizes is less than 0.02^{o}C for the hotspot temperature and 0.17^{o}C for the Cooler temperature for all die thicknesses studied. For the entire solution space, the maximum hotspot and Cooler temperature reduction discrepancies are 0.15^{o}C (absolute value) and 1.2^{o}C respectively. The hotspot cooling effectiveness discrepancy at optimum Cooler sizes demonstrates less than 0.007^{o}C/W for all die thicknesses studied. The maximum hotspot cooling effectiveness discrepancy is around 0.01^{o}C/W.

4.3.2 Total Discrepancy discusses the total meta-model discrepancies produced by the first two steps of the determination process. The last step, the surface fit, does not contribute to the total discrepancy within the die thicknesses studied. This is because the allocation factor surfaces capture the pervious step's curve fits with negligible difference. Thus, any added discrepancy is attributed to the curve fit step. Thus the total discrepancy is the combination of the plane intersection step and the curve fit step.

The maximum total temperature reduction discrepancy at optimum Cooler sizes is around 0.1^{o}C (absolute value) for the hotspot temperature and 0.2^{o}C for the Cooler temperature. For the entire solution space, the maximum total temperature reduction discrepancies for the hotspot and Cooler are 0.2^{o}C and 1.2^{o}C respectively. The maximum

total hotspot cooling effectiveness discrepancy at optimum Cooler sizes is less than 0.01^{o}C/W (absolute value) for all die thicknesses studied. For the entire solution space, the maximum total hotspot cooling effectiveness discrepancy is around 0.06^{o}C/W.

The maximum hotspot temperature reduction discrepancy increased from 0.15 to 0.2 between the first (plane intersection) and last (surface fit) step in determining the allocation factors. The maximum Cooler temperature reduction discrepancy remained constant at1.2 through all the steps. The maximum hotspot cooling effectiveness discrepancy increased from 0.01 to 0.06 between the first (plane intersection step) and last (surface fit) step in determining the allocation factors. Thus more complicated curve fits are predicted to only decrease the total hotspot cooling effectiveness discrepancy and provide no benefit for the temperature reductions.

4.3.1 Plane Intersection Discrepancy

The plane intersection step is the first step in determining the allocation factors. As such, it contains the first amount of discrepancy between the meta-model and the numerical results. The discrepancy is shown for the temperature, temperature reduction, and hotspot cooling effectiveness.

4.3.1.1 Temperature

The temperature discrepancy for the 100µm die is shown in **Figure 85**.

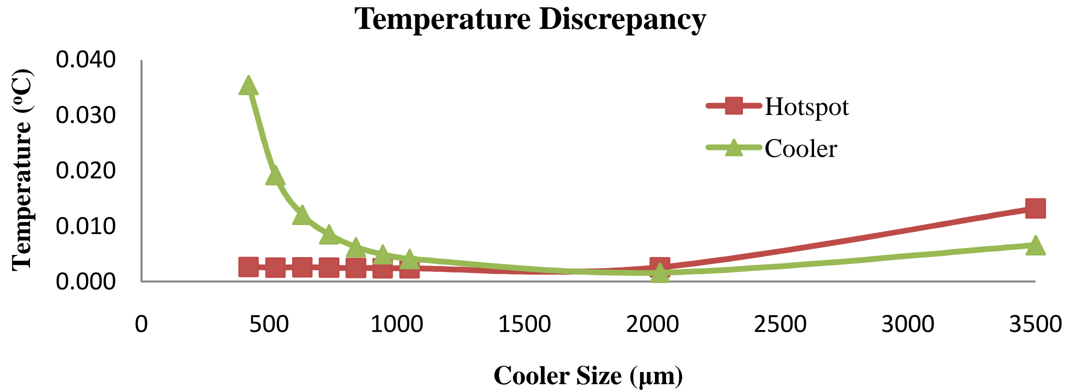

Figure 85: Temperature Plane Intersection discrepancy for 100µm die

The hotspot temperature discrepancy is significantly lower than the corresponding Cooler values. This is true for all die thicknesses tested. It is of interest to group the temperature discrepancy for the optimum Cooler sizes (and corresponding currents) of each die. They are 630µm, 2030µm, and 3500µm for the 100µm, 300µm, and 500µm respective die thickness. The temperature discrepancies for these Cooler sizes are shown in **Figure 86**.

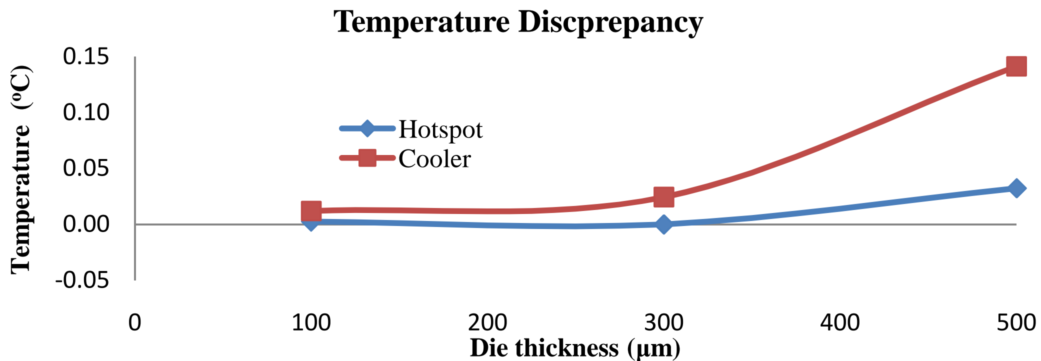

Figure 86: Temperature Plane Intersection discrepancy at optimum Cooler sizes

The maximum temperature discrepancy at optimum Cooler sizes is around 0.03°C for the hotspot temperature and 0.15°C for the Cooler temperature. This provides confidence that the meta-model is accurately capturing the non-uniform Joule heating effect, especially at the hotspot.

Reviewing the entire solution space, the maximum hotspot and Cooler temperature discrepancies are 0.03°C and 1.2°C respectively.

4.3.1.2 Temperature Reduction

The temperature reduction discrepancy for the 100µm die is shown in **Figure 87**.

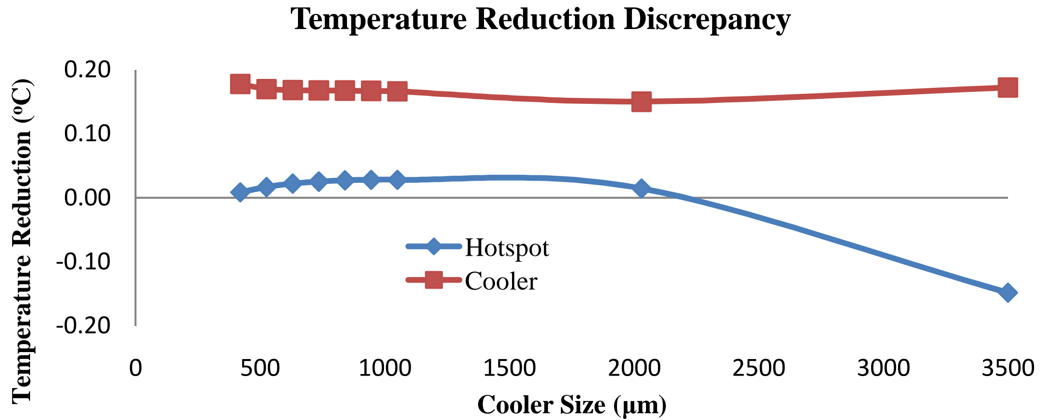

Figure 87: Temperature Reduction Plane Intersection discrepancy for 100µm die

The hotspot temperature reduction discrepancy is significantly lower than the corresponding Cooler values. This is true for all die thicknesses tested. It is of interest to group the temperature discrepancy for the optimum Cooler sizes (and corresponding currents) of each die. They are 630µm, 2030µm, and 3500µm for the 100µm, 300µm, and 500µm respective die thickness. The temperature reduction discrepancies for these Cooler sizes are shown in **Figure 88**.

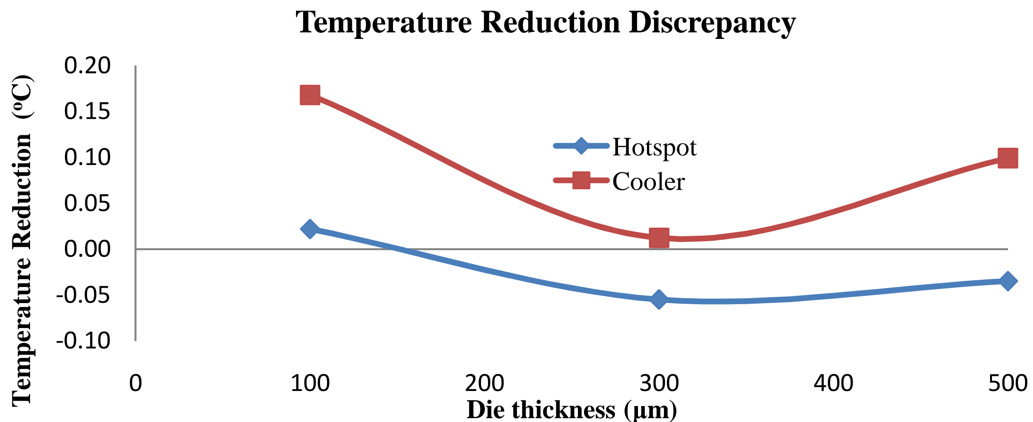

Figure 88: Temperature Reduction Plane Intersection discrepancy at optimum Cooler sizes

The maximum temperature reduction discrepancy at optimum Cooler sizes is around 0.05^{o}C for the hotspot temperature and 0.17^{o}C for the Cooler temperature. This provides confidence that the meta-model is accurately capturing the Peltier and non-uniform Joule heating effect, especially at the hotspot.

Reviewing the entire solution space, the maximum hotspot and Cooler temperature reduction discrepancies are 0.15^{o}C (absolute value) and 1.2^{o}C respectively.

4.3.1.3 Hotspot Cooling Effectiveness

The hotspot cooling effectiveness discrepancy for the 100µm die is shown in **Figure 89**.

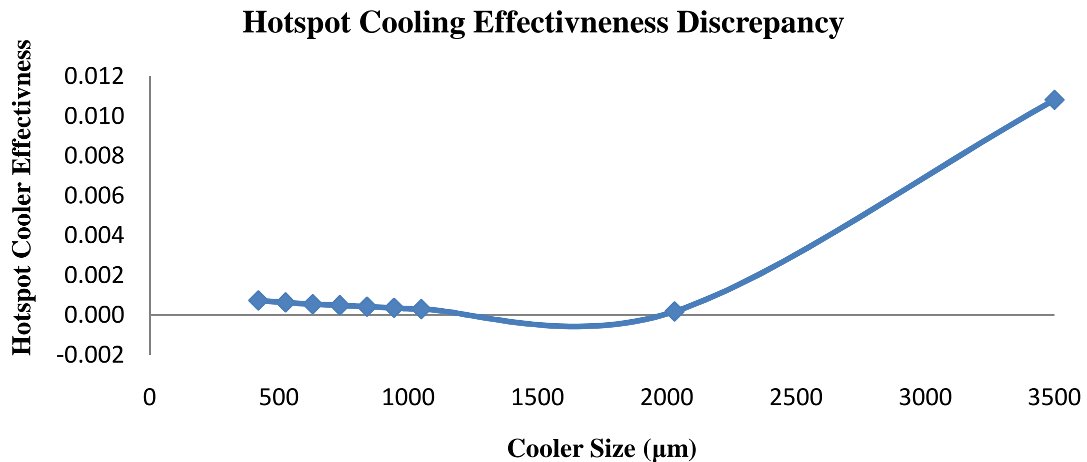

Figure 89: Hotspot Cooling effectiveness Plane Intersection discrepancy for 100µm die

The largest discrepancy is felt at the largest Cooler size and is probably due to light mesh convergence issues. It is of interest to group the temperature discrepancy for the optimum Cooler sizes (and corresponding currents) of each die. They are 630µm, 2030µm, and 3500µm for the 100µm, 300µm, and 500µm respective die thickness. The hotspot cooling effectiveness discrepancy for these Cooler sizes are shown in **Figure 90**.

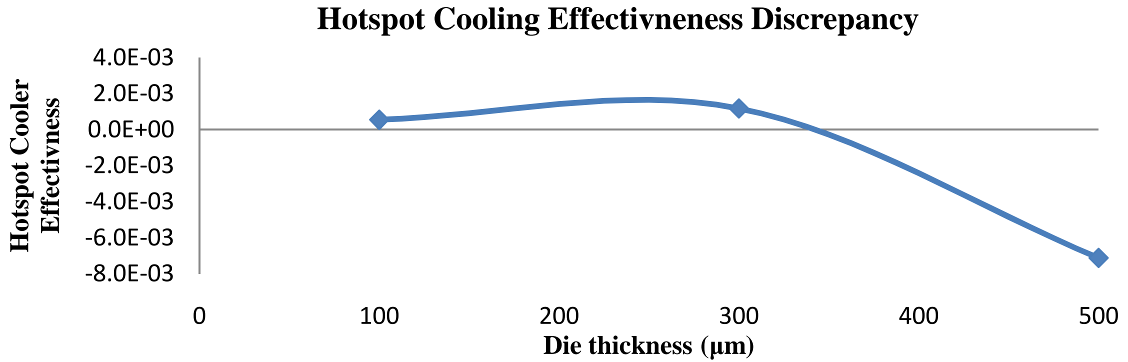

Figure 90: Hotspot Cooling effectiveness Plane Intersection discrepancy at optimum Cooler sizes

The maximum hotspot cooling effectiveness discrepancy at optimum Cooler sizes is less than 0.007°C/W. This provides confidence that the meta-model is accurately capturing the Peltier and non-uniform Joule heating effect, especially at the hotspot.

Reviewing the entire solution space, the maximum hotspot cooling effectiveness discrepancy is around 0.01°C/W.

4.3.2 Total Discrepancy

As shown by **Figure 78** and **Figure 79 t**he second step in determining the allocation factors is to place a curve fit as a function of Cooler size for each die thickness. A linear curve was chosen for alpha and a power function was chosen for beta. Even though the next step, the surface fit, provides the total discrepancy for the meta-model, the surface fit step does not add any more discrepancy. As shown by **Figure 81** and **Figure 83,** the allocation factor surfaces capture the pervious step's curve fits with negligible difference. Thus, any added discrepancy is attributed to the curve fit step. Thus the total discrepancy is the combination of the plane intersection step and the curve fit step and is shown for the temperature, temperature reduction, and hotspot cooling effectiveness.

4.3.2.1 Temperature

The total temperature discrepancy for the 100μm die thickness is shown in **Figure 91**.

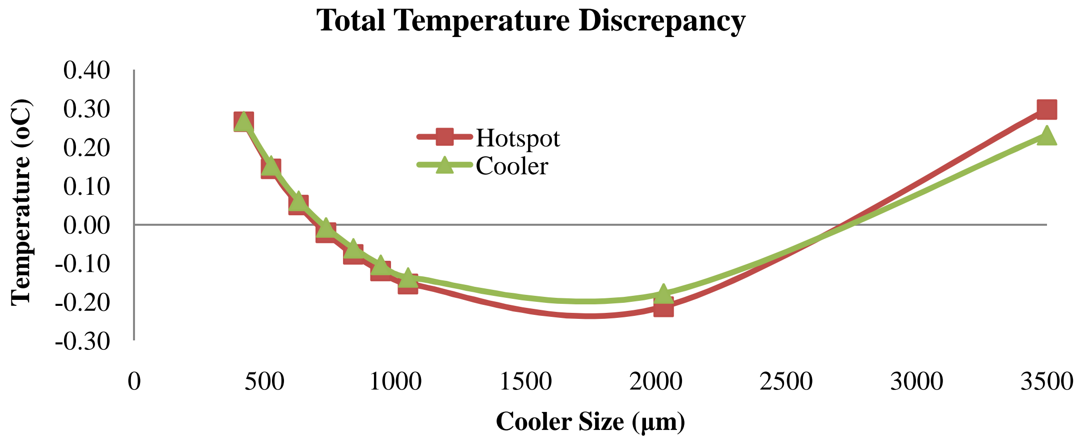

Figure 91: Total Temperature Discrepancy for 100μm die thickness

The total temperature discrepancy demonstrates more discrepancy than the plane intersection discrepancy. It is of interest to group the total temperature discrepancy for the optimum Cooler sizes (and corresponding currents) of each die. They are 630μm, 2030μm, and 3500μm for the 100μm, 300μm, and 500μm respective die thickness. The total temperature discrepancies for these Cooler sizes are shown in **Figure 92**.

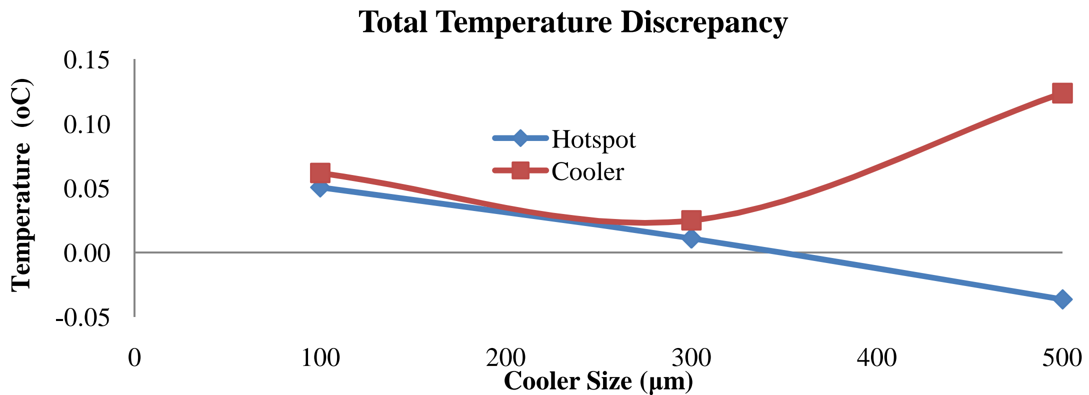

Figure 92: Total Temperature Discrepancy at Optimum Cooler sizes

The maximum total temperature discrepancy at optimum Cooler sizes is less than 0.05°C (absolute value) for the hotspot temperature and around 0.12°C for the Cooler temperature. This provides confidence that the meta-model is accurately capturing the non-uniform Joule heating effect, especially at the hotspot.

Reviewing the entire solution space, the maximum hotspot and Cooler temperature discrepancies are 0.3°C and 1.6°C respectively.

4.3.2.2 Temperature Reduction

The total temperature reduction discrepancy for the 100μm die is shown in **Figure 93**. Figure 94

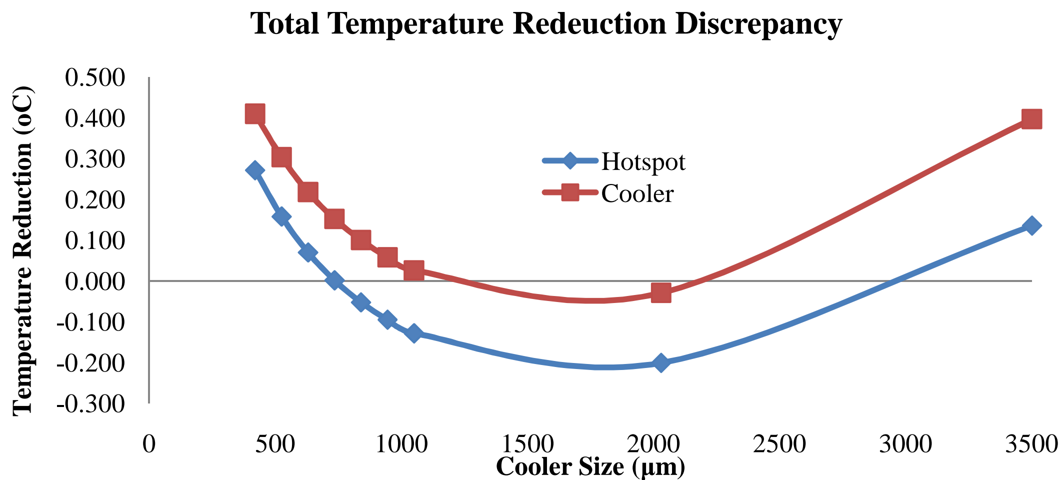

Figure 93: Total Temperature Reduction Discrepancy for the 100μm die thickness

For all die thicknesses the total temperature reduction discrepancy demonstrates the same shape as its total temperature discrepancy. It is of interest to group the total temperature discrepancy for the optimum Cooler sizes (and corresponding currents) of each die. They are 630μm, 2030μm, and 3500μm for the 100μm, 300μm, and 500μm respective die thickness. The total temperature discrepancies for these Cooler sizes are shown in **Figure 94**.

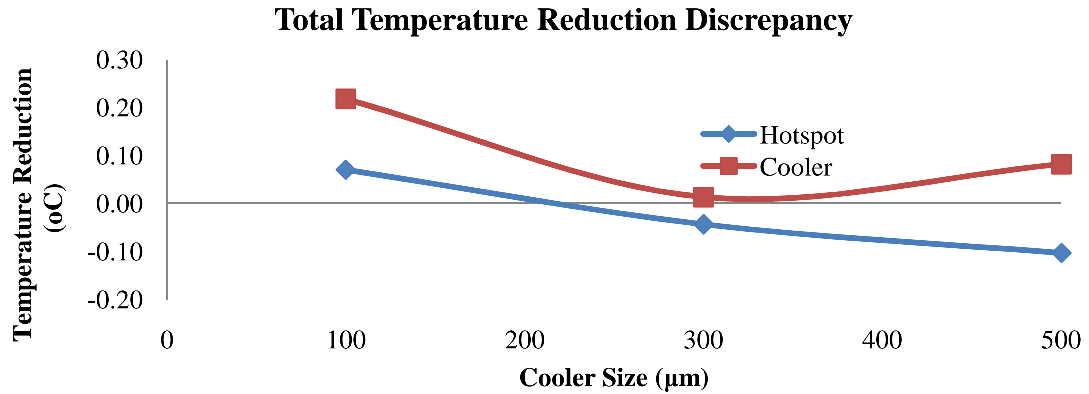

Figure 94: Total Temperature Reduction Discrepancy at Optimum Cooler sizes

The maximum total temperature reduction discrepancy at optimum Cooler sizes is around 0.1°C (absolute value) for the hotspot temperature and 0.2°C for the Cooler temperature. This provides confidence that the meta-model is accurately capturing the Peltier and non-uniform Joule heating effect, especially at the hotspot.

Reviewing the entire solution space, the maximum hotspot and Cooler temperature reduction discrepancies are 0.2°C and 1.2°C respectively.

4.3.2.3 Hotspot Cooling Effectiveness

The total hotspot cooling effectiveness discrepancy for the 100µm die is shown in **Figure 95**.

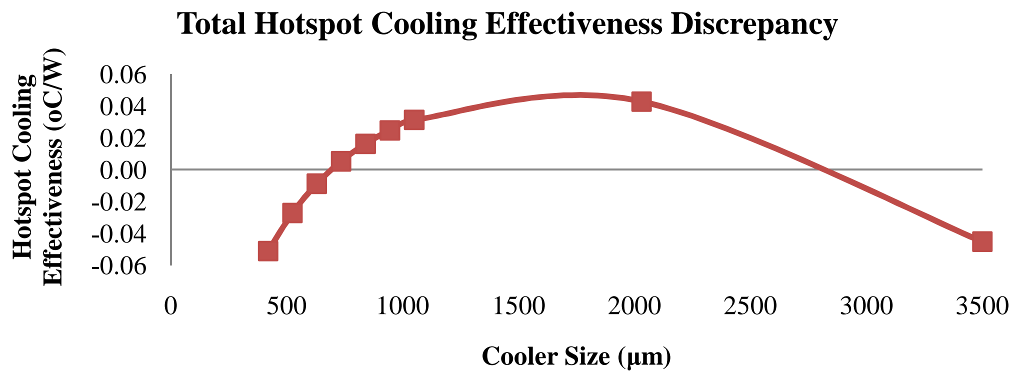

Figure 95: Total Hotspot Cooling Effectiveness Discrepancy for the 100μm die thickness

It is of interest to group the temperature discrepancy for the optimum Cooler sizes (and corresponding currents) of each die. They are 630μm, 2030μm, and 3500μm for the 100μm, 300μm, and 500μm respective die thickness. The total hotspot cooling effectiveness discrepancy for these Cooler sizes are shown in **Figure 96**.

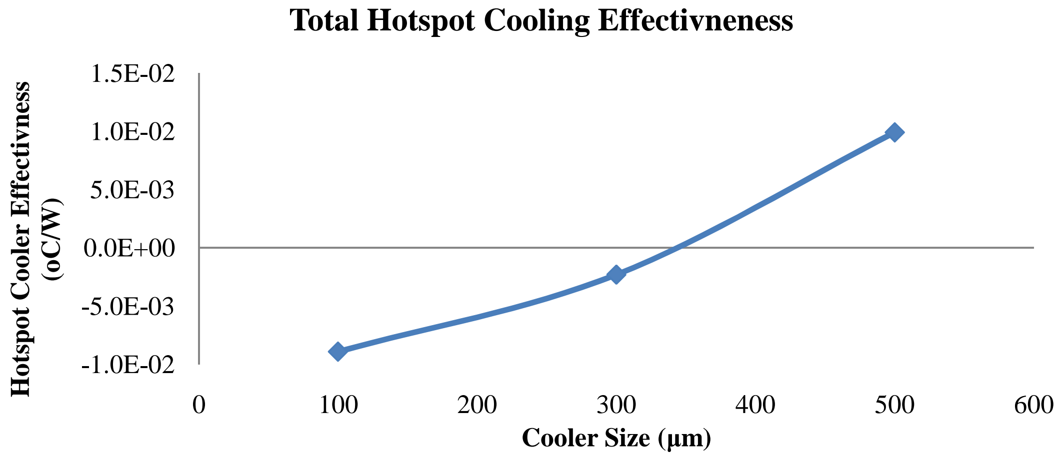

Figure 96: Total Hotspot Cooling Effectiveness Discrepancy at Optimum Cooler sizes

The maximum total hotspot cooling effectiveness discrepancy at optimum Cooler sizes is less than 0.01^{o}C/W (absolute value). This provides confidence that the meta-model is accurately capturing the Peltier and non-uniform Joule heating effect, especially at the hotspot.

Reviewing the entire solution space, the maximum total hotspot cooling effectiveness discrepancy is around 0.06^{o}C/W.

Chapter 5: Germanium and Silicon Bi-Layer Self Cooling

Wang and Bar-Cohen previously simulated a germanium self cooling device that uses the germanium die as the thermoelectric material to remedy the temperature rise due to high flux hotspots (20). Their constant current self cooler is adopted in and the solution space increased to create the meta-model discussed in **Chapter 4: Germanium Self Cooling Meta Model.** A constant voltage self cooler is developed and discussed in **Chapter 3: Performance of Germanium Self Cooling Device**. The comparison between the constant current and voltage cooler solutions provides the performance band of that device.

This chapter discusses a self cooler that contains a germanium layer on top of an electrically insulated silicon layer with high thermal conductivity. This device contains a manufacturing advantage over that of the 100% germanium self cooler since the bottom layer consists of silicon which is the industry standard. The top germanium layer can then be grown through chemical or vapor techniques or attached. Moreover, the silicon provides a high thermal conductivity at the location of the hotspot providing superior thermal spreading.

This bi-layer self cooler contains similar geometry, material properties, and boundary conditions as the constant voltage self cooler with the exception of the electrically insulated bottom silicon layer with high thermal conductivity as shown in **5.1 Bi-layer Self Cooling Device**.

The non-thermoelectric boundary conditions consist of a centered high heat flux hotspot surrounded by low heat flux background heating. The top of the Cooler electrode contains a constant voltage boundary condition which mandates a variable current and

translates into calculating the current and corresponding Peltier cooling/heating for each element. Moreover, the non-uniform current flow through the germanium top layer produces non-uniform Joule heating. Thus, the thermoelectric boundary conditions are automatically calculated by the high order thermal-electrical element SOLID227 which couples the thermal and electrical field through Joule Heating and the Peltier Effect.

5.2 Bi-Layer Numerical Results outlines the advantages of the bi-layer self cooling device. Several metrics used to rate the device. These metrics discuss the temperature reductions at the center hotspot and Cooler temperatures. Other temperature reductions introduced are the hotspot temperature reduction relative to the 100% conduction only silicon device ($\Delta T_{H,Si}$) and the 100% germanium constant voltage self cooler ($\Delta T_{H,Ge}$).. The hotspot cooling effectiveness is also discussed and determines the devices ability to remove the temperature rise induced by the introduction of the hotspot. The efficiency, or thermal impact factor, is determined by the hotspot temperature reduction over the Power of the device.

As the germanium percentage increases, the hotspot temperature reduction increases (absolute value) to that of the 100% germanium constant voltage self cooler due to the de-constriction of the current within the top germanium layer. It is important to note that the bottom silicon layer is electrically insulated and contains a high thermal conductivity.

This high thermal conductivity plays a major role in $\Delta T_{H,Si}$ and $\Delta T_{H,Si}$ metrics. These metrics demonstrate a tradeoff between two opposing effects. As described before, the hotspot temperature reduction increases as the germanium percentage increases. However, the thermal spreading ability of the bottom silicon layer decreases as the

germanium percentage increases. Thus, these two competing effects provide an optimum percentage which allows for a hotspot temperature below that of the 100% conduction only silicon device and the 100% germanium self cooler.

$\Delta T_{H,Ge}$ increases (absolute value) quasi-linearly as the die thickness increases; starting at -0.3^{o}C for the 100μm die, and reaches -1.2^{o}C for the 500μm die. $\Delta T_{H,Si}$ decreases (absolute value) quasi-linearly as the die thickness increases; starting at -1.9^{o}C for the 100μm die, and falls to less than -0.1^{o}C for the 500μm die. The comparison between these devices demonstrates the bi-layer self cooler's ability to outperform both the conduction only silicon device and the 100% germanium self cooler.

As the die thickness increases the hotspot temperature reduction increases. However, the temperature rise due to the introduction of the hotspot decreases, ultimately providing an optimum die thickness for the hotspot cooling effectiveness metric. This die thickness was shown to be 300μm for the bi-layer self cooler with a value of 0.94. Moreover, the bi-layer self cooler is more capable of removing the hotspot temperature rise than the 100% germanium self cooler for all die thicknesses studied due to the high conductivity of the bottom silicon layer.

The efficiency, or thermal impact factor, at optimum $\Delta T_{H,Ge}$ germanium percentage decreases as the die thickness increases with its largest value of 13.56 at the 100μm die thickness. Moreover, there is little difference between the thermal impact factor of the bi-layer and 100% germanium self cooler.

Contact resistances were placed between the bottom silicon and top germanium layer to determine their impact on thermal performance. As the thermal contact resistance is increased from zero to 1e^{-5} Km^{2}/W, the hotspot temperature reduction relative to the

100% germanium self cooler migrates from -1.2^{o}C to almost 7.0^{o}C. The hotspot temperature reduction relative to the 100% silicon self cooler migrates from less than -0.1^{o}C to almost 8.0^{o}C. It is thus important to ensure good contact between the die layers if the optimum performance of the bi-layer device is sought.

5.1 *Bi-layer Self Cooling Device*

The geometry for the bi-layer self cooling device with constant voltage conditions (i.e. bi-layer self cooler) is adopted from the constant voltage self cooling device as discussed in **5.1.1 Geometry.** The geometry consists of a square n-type germanium layer placed over an electrically insulated silicon layer. The hotspot is located at the bottom center of the square silicon layer. This central location motivates the Cooler electrode to be placed on the top center of the germanium layer. This allows localized cooling above the localized high heat flux zone. The germanium percentage, die thickness, and cooler width are the geometric parametric variables for this study.

The material properties for the constant voltage self cooling device (**3.1.2 Material Properties**) are adopted as discussed in **5.1.2 Material Properties**. The top germanium layer contains the thermoelectric properties required for thermoelectric cooling. The bottom electrically insulated silicon layer contains a 100W/mk thermal conductivity that provides better heat spreading than the germanium (60 W/mk).

These boundary conditions of the bi-layer self cooler are identical to those shown in **3.1.2 Material Properties** with the exception of bottom insulated silicon layer forcing the current to only flow through the top germanium layer. They consist of non-thermoelectric and thermoelectric boundary conditions. The non-thermoelectric boundary conditions consist of a centered high heat flux hotspot surrounded by low heat flux

background heating. The top of the Cooler electrode contains a constant voltage boundary condition which mandates a variable current and translates into calculating the current and corresponding Peltier cooling/heating for each element. Moreover, the non-uniform current flow through the germanium top layer produces non-uniform Joule heating. Thus, the thermoelectric boundary conditions are automatically calculated by the high order thermal-electrical element SOLID227 which couples the thermal and electrical field through Joule Heating and the Peltier Effect.

5.1.1 Geometry

The germanium and silicon self cooling device with constant voltage boundary conditions (i.e. bi-layer self cooler) contains a germanium layer on top of an electrically insulated silicon layer. The temperatures of interest for this study are the center Cooler and center hotspot temperature as shown by **Figure 97**.

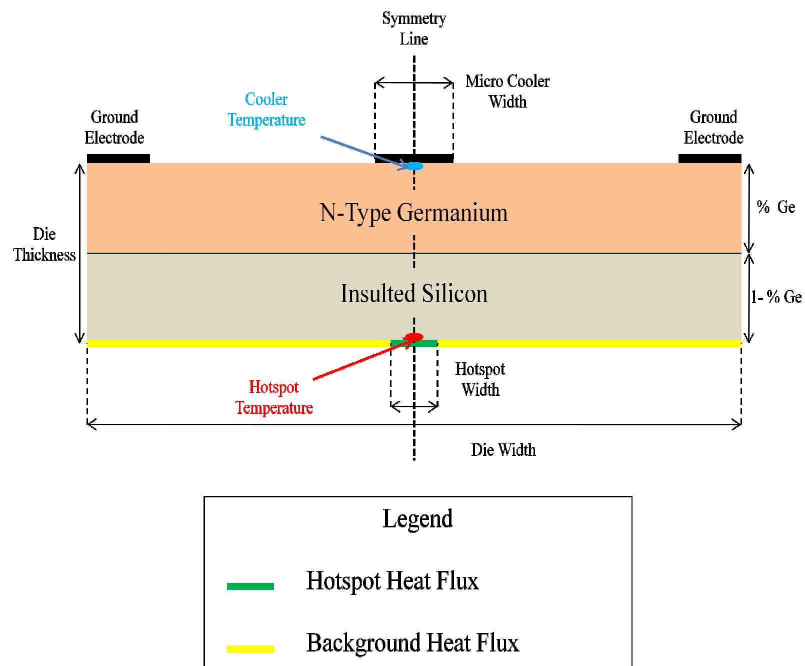

Figure 97: Bi-Layer Self Cooling Device

As shown in **Figure 97**, there are two heat fluxes, hotspot and background, that allow the study of non-uniform heating. The Cooler is placed vertically above the hotspot and the background heat flux surrounds the hotspot. This fact is better explained viewing **Figure 98**.

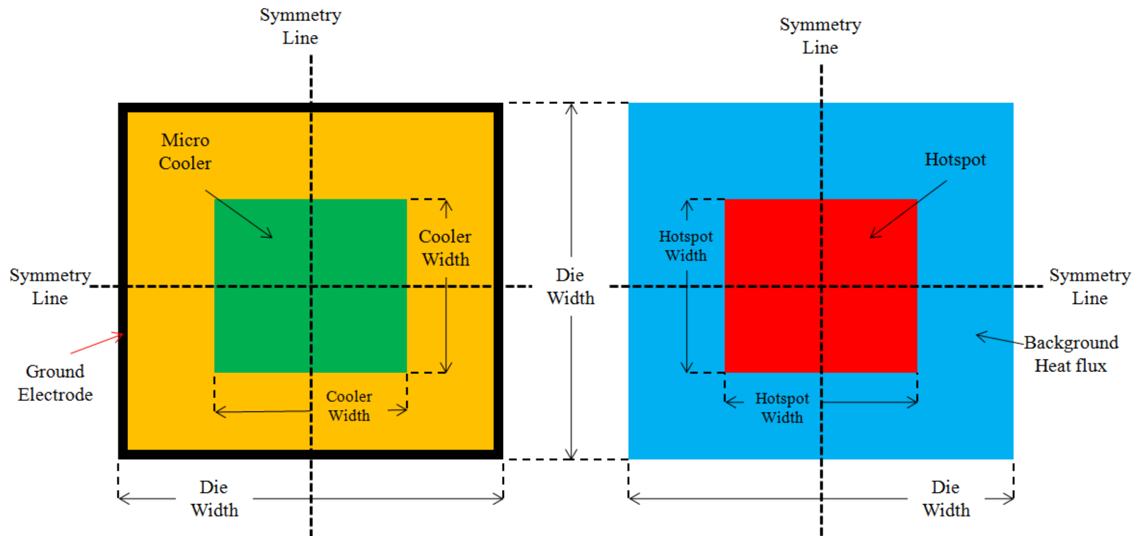

Figure 98: Bi-Layer Self Cooling Device, Left is Top View, Right is bottom heating map (not to scale)

The die, Cooler, and hotspot are all square as shown by the above figure. Moreover, the hotspot and Cooler are in the geometric center of the die. The dimensions of the device are shown in **Table 9.**

Table 9: Bi-Layer Self Cooling Device Dimensions

Label	Dimension (µm)
Die Width	12000
Hotspot Width	70
Ground Electrode Width	500
Die Thickness	100,300,500
Cooler size	Variable
Germanium Percentage	Variable

Various die thickness are simulated, each with a germanium percentage and Cooler size range sufficient to determine optimum performance. Thus the parametric variables are the

germanium percentage, die thickness, Cooler size, and current. The optimum performance is found through sequential parametric optimization of the said variables.

5.1.2 Material Properties

The material properties for the germanium layer used to create the presented results in this chapter are identical to those detailed in **3.1.2 Material Properties**. The materials properties selected contained an arsenic doping of 2.3×10^{18}cm^{-3} which produce the highest Power Factor in the range studied. This produces the material properties in **Table 10**.

Table 10: Bi-Layer Self Cooling Device Material Properties

Label	Thermal Conductivity (W/mk)	Electrical Resistivity (µΩm)	Seebeck Coefficient (µV/K)
Germanium Die (doping of 2.3×10^{18}cm^{-3})	60 (20) (47)	50 (20) (46)	-467 (20) (46)
Silicon	100	1e18	0e-6

5.1.3 Boundary Conditions

The bi-layer self cooling device with constant voltage boundary conditions (i.e. bi-layer self cooler) contains both thermoelectric and non-thermoelectric boundary conditions. The locations of these boundary conditions are shown in **Figure 99**. These boundary conditions are identical to those shown in **3.1.3 Boundary Conditions** with the exception of bottom insulated silicon layer forcing the current to only flow through the top germanium layer.

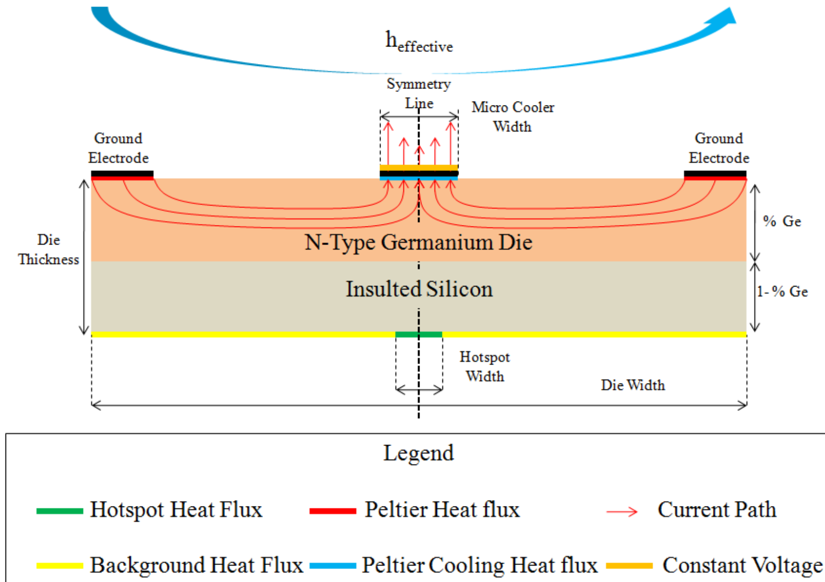

Figure 99: Bi-Layer Self Cooling Device Boundary Condition Locations

It is important to note that the top of the Cooler electrode has a constant voltage constraint and, due to Ohm's law, the current at the Cooler electrode is not constant.

The values of the non-thermoelectric boundary conditions are displayed in **Table 11**.

Table 11: Bi-Layer Non-Thermoelectric Boundary Conditions

	Value
$\mathbf{h_{effective}}$	8741 (W/m^2-K), $T_{ambient}$=25°C
Hotspot Heat flux	680 W/cm^2
Background Heat flux	70 W/cm^2

The heating map in **Figure 24** shows the centered hotspot surrounded by the background heat flux. The effective heat transfer coefficient ($h_{effective}$) accounts for the thermal interface, heat spreader, and air-cooled heat sink used to provide global cooling for the die (20).

5.1.3.1 Bi-Layer Thermoelectric Boundary Conditions

It is common to apply a Peltier cooling and heating heat flux at the appropriate surfaces if the current across the surface is constant. Wang and Bar-Cohen used this fact

to determine constant Peltier cooling and heating at the appropriate surfaces in reference (20).

These equations cannot be used to produce the results for the bi-layer self cooler because the constant voltage boundary condition at the top of the Cooler electrode mandates a variable current. Consequently, the calculation of current corresponding Peltier cooling/heating for each element is required to determine the boundary conditions.

Moreover, the non-uniform current flow through the germanium die produces non-uniform Joule heating. Thus, the numerical simulation must solve for the thermal and electrical fields with Joule heating and the Peltier effect coupling the two. This coupling is available through the ANSYS high order SOLID 227 element validated in **C**.4 **Thermal-Electrical Model with Joule Heating and the Peltier Effect**. The validation test shows less than 1% error for Power and less than 2.5 % (absolute value) between the numerical and analytical solutions. Thus there is much confidence in using this coupled numerical simulation to provide accurate results.

5.2 *Bi-Layer Numerical Results*

The potential and advantages of the bi-layer self cooling device are investigated. The metrics used to rate the device are discussed in **5.2.1 Bi-Layer Cooling Metrics**. These metrics discuss the temperature reductions at the center Hotspot and Cooler temperatures. Another temperature reduction is introduced which is the hotspot temperature reduction relative to the corresponding 100% constant voltage germanium self cooler. The hotspot cooling effectiveness is also discussed and determines the devices ability to remove the temperature rise induced by the introduction of the hotspot.

The efficiency, or thermal impact factor, is determined by the hotspot temperature reduction over the Power of the device.

The nature of numerical simulations requires that a mesh refinement be conducted to distinguish and ultimately eliminate mesh dependent solutions. As shown in **5.2.2 Mesh Convergence**, the high order thermal-electrical element SOLID227 with element counts ranging from 25k to almost 105k was used to generate the results for the bi-layer self cooler.

For all the geometries simulated, a common temperature distribution was generated and discussed in **5.2.3 Typical Bi-layer Temperature Distributions**. For each specific case tested, there exists a temperature profile with two inflection points around the center of the hotspot. This fact along with the symmetric temperature profile leads to two concentric rings with the inner-most consisting of slightly lower temperatures and the outer-most consisting of slightly higher temperatures. This temperature distribution is similar to the 100% germanium constant voltage self cooler discussed in **3.2.3 Typical Temperature Distributions**.

The center hotspot temperature demonstrates a quadratic temperature reduction as a function of current due to the tradeoff between the Peltier and Joule Heating effects. This allows a quadratic trend fitting to the temperature curves to determine the minimum temperature, maximum hotspot temperature reduction, and the Power of the bi-layer self cooler. This process is detailed in **5.2.4 Function of Current** and is identical to that in **3.2.4 Function of Current**.

Their trends demonstrate tradeoffs as shown in **5.2.5 Function of Cooler** . In general, the temperature reduction for each germanium percentage demonstrates a

tradeoff between the thermal resistance between the Cooler and hotspot and the thermoelectric cooling effect at the Cooler. The hotspot cooling effectiveness trend shows a similar (yet negative) trend when compared to the hotspot temperature reduction trend. Thus their optimums occur at the same Cooler size and current.

The above translates into an optimum Cooler size for each germanium percentage as shown in **5.2.6 Function of Germanium Percentage.** As the germanium percentage increases, the hotspot temperature of the bi-layer device migrates from the 100% conduction only silicon device to that of the 100% germanium constant voltage self cooling device. The hotspot temperature reduction increases (absolute value) to that of the 100% germanium self cooler due to the de-constriction of the current within the top germanium layer. It is important to note that the bottom silicon layer is electrically insulated and contains a high thermal conductivity.

The hotspot temperature reduction relative to the 100% germanium self cooler demonstrates a tradeoff between two opposing effects. As described before, the hotspot temperature reduction increases as the germanium percentage increases. However, the thermal spreading ability of the bottom silicon layer decreases as the germanium percentage increases. Thus, these two competing effects provide an optimum percentage which allows for a hotspot temperature below that of the 100% germanium cooler. These tradeoffs are also true for the hotspot temperature reduction relative to the 100% conduction only silicon device.

The hotspot cooling effectiveness follows this same trend since its equation mandates the same tradeoff effects. The power increases linearly as the germanium

percentage increases and remains below that of the 100% germanium self cooler for all percentages studied.

The above translates into optimum germanium percentages for each die thickness as shown in **5.2.7 Function of Die Thickness**. The bi-layer self cooler is capable of achieving a lower hotspot temperature than the 100% germanium self cooler at optimum conditions ($\Delta T_{H,Ge}$). This advantage increases (absolute value) quasi-linearly as the die thickness increases; starting at -0.3^{o}C for the 100µm die, and reaches -1.2^{o}C for the 500µm die. The bi-layer self cooler can also demonstrate hotspot temperatures lower than the 100% conduction only silicon device. This advantage decreases (absolute value) quasi-linearly as the die thickness increases; starting at -1.9^{o}C for the 100µm die, and falls to less than -0.1^{o}C for the 500µm die. The comparison between these devices demonstrates the bi-layer self cooler's ability to outperform both the conduction only silicon device and the 100% germanium self cooler.

As the die thickness increases the hotspot temperature reduction increases. However, the temperature rise due to the introduction of the hotspot decreases, ultimately providing an optimum die thickness for the hotspot cooling effectiveness metric. This die thickness was shown to be 300µm for the bi-layer self cooler with a value of 0.94. Moreover, the bi-layer self cooler is more capable of removing the hotspot temperature rise than the 100% germanium self cooler for all die thicknesses studied due to the high conductivity of the bottom silicon layer. Since the conduction only silicon device cannot sustain current flow, it does not sustain a hotspot temperature reduction, and produces zero hotspot cooling effectiveness values for all die thicknesses.

The efficiency, or thermal impact factor, at optimum $\Delta T_{H,Ge}$ germanium percentage decreases as the die thickness increases with its largest value of 13.56 at the 100µm die thickness. Moreover, there is little difference between the thermal impact factor of the bi-layer and 100% germanium self cooler. Since the 100% conduction only silicon device requires no power to operate and creates no hotspot temperature reduction, the thermal impact factor approaches infinity divided by zero, which is undefined, and consequently its thermal impact factor is undefined.

Contact resistances were placed between the bottom silicon and top germanium layer to determine their impact on thermal performance in **5.2.8 Thermal Contact Resistance**. As the thermal contact resistance is increased from zero to $1e^{-5}$ Km^2/W, the hotspot temperature reduction relative to the 100% germanium self cooler migrates from -1.2°C to almost 7.0°C. The hotspot temperature reduction relative to the 100% silicon self cooler migrates from less than -0.1°C to almost 8.0°C. It is thus important to ensure good contact between the die layers if the optimum performance of the bi-layer device is sought.

5.2.1 Bi-Layer Cooling Metrics

In order to determine the cooling potential of the bi-layer self cooler, the metrics from the constant current self cooling device found in **3.2.1 Cooling Metrics** are adopted. These include the temperature reductions and the hotspot cooling effectiveness. The first metric determines the temperature reduction at the center hotspot and Cooler locations due to the application of current. These metrics are shown in equation **5-1** (20).

$$\Delta T_{Hotspot} = T_{@hotspot,Cooler\ on} - T_{@hotspot,Cooler\ off} \qquad \textbf{5-1}$$
$$\Delta T_{Cooler} = T_{@cooler,Cooler\ on} - T_{@coolert,Cooler\ off}$$

These metrics follow the cooling trends explained in **2.3 Thermoelectric Cooler Net Effects**. At small current values, the temperature at both locations reduces linearly due to the Peltier effect. This produces a negative $\Delta T_{hotspot}$ and ΔT_{Cooler}. At larger currents, the Peltier effect is balanced by Joule heating, and $\Delta T_{hotspot}$ and ΔT_{Cooler} reach an optimum (minimum) value. Currents larger than this point produce larger (absolute value) $\Delta T_{hotspot}$ and ΔT_{Cooler} values. Thus the typical operational point for the bi-layer self cooler involves applying the current that produces the maximum $\Delta T_{hotspot}$.

The above metrics are studied for several cooler widths, germanium percentages, and die thicknesses. Then at the optimum Cooler size and current for each germanium percentage and die thickness, the minimum hotspot temperature are compared to the 100% Germanium constant voltage self cooler (**Chapter 5**) with comparable die thickness as shown by equation **5-2**.

$$\Delta T_{H,Ge} = T_{@hotspot,Bi-layer} - T_{@hotspot,100\%\ Germanium\ Constant\ Voltage} \quad \textbf{5-2}$$

At the optimum Cooler size and current for each germanium percentage and die thickness, the minimum hotspot temperature are also compared to the 0% germanium bi-layer self cooler. This geometry corresponds to 100% electrically insulated silicon die which remediates the hotspot temperature only through conduction as shown by **5-4**.

$$\Delta T_{H,Si} = T_{@hotspot,Bi-layer} - T_{@hotspot,100\%\ Silicon} \quad \textbf{5-3}$$

Another metric determines the hotspot cooling effectiveness of the bi-layer self cooler. More specifically, it is the ratio of the temperature change due to application of current to the Cooler over the temperature rise due to the hotspot. This ratio is defined in equation **5-4** (20).

$$\Delta T^{*}_{Hotspot} = \frac{T_{Hotspot\ on,Cooler\ off} - T_{Hotspot\ on\ ,Cooler\ on}}{T_{Hotspot\ on\ ,Cooler\ off} - T_{Hotspot\ off\ ,Cooler\ off}} \quad \textbf{5-4}$$

The metric typically ranges from zero to one. At $\Delta T^{*}_{hotspot}=1$, the temperature increase due to the hotspot is completely removed. At $\Delta T^{*}_{hotspot}=0$, the device is incapable of removing that temperature. At values between 1and 0, the device demonstrates partial removal of the hotspot temperature. Values larger than one demonstrate a device that is capable of providing temperatures lower than the no hotspot case. Negative values occur when operating in the Joule heating dominate region (large currents) where the temperature of the hotspot with the Cooler activated is larger than when the Cooler is not activated.

The efficiency of the bi-layer self cooling device is of important to thermal engineers. **2.4.1 Power and Coefficient of Performance (COP)** formulates the coefficient of performance for conventional (leg) thermoelectric coolers (TEC). Unfortunately, the non-uniform Joule heating cannot be calculated through the bulk formulation in equation **2-13** and **2-14**. Thus, the Power and efficiency must be calculated in another manner.

This problem is solved in the simulation validated in **C**.4 **Thermal-Electrical Model with Joule Heating and the Peltier Effect**. The Power can be found by finding the voltage at the top Cooler surface (contains the constant voltage condition) and multiplying it by the applied current as shown by equation **5-5**.

$$Power = V_{Cooler} I \quad \textbf{5-5}$$

The efficiency of the device cannot be calculated through a coefficient of performance since the net cooling flux equation (equation **2-14**) uses the bulk Joule heating formulation. However, efficiency is generally defined by the desired output divided by the required input (25). For the presented case, the desired output is the center hotspot

temperature reduction and the required input is the Power. This metric is called the Thermal Impact Factor (TIF) and is defined in equation **5-6** (19).

$$TIF = \frac{\Delta T_{Hotspot}}{Power} \quad \textbf{5-6}$$

5.2.2 Mesh Convergence

The bi-layer self cooler is numerically simulated using the high order ANSYS SOLID227 thermal-electrical element that contains Joule heating and the Peltier effect couplings. This model has been validated in **C**.4 **Thermal-Electrical Model with Joule Heating and the Peltier Effect**. The validation test shows less than 1% error for Power and less than 2.5 % (absolute value) between the numerical and analytical solutions for net cooling. This provides much confidence in the outputted results for the constant voltage self cooler.

The symmetric boundary conditions and geometry create a symmetric temperature and current distribution. Thus, a quarter model was simulated to provide the results in **5.2 Bi-Layer Numerical Results** because quarter models can accomplish the same relative precision that a full model provides with a quarter of the elements. Moreover, this reduction in element count translates into less computational time.

The nature of numerical simulations requires that a mesh refinement be conducted to distinguish and ultimately eliminate mesh dependent solutions. This is accomplished through the increase of the element count while the pertinent temperatures are recorded. For the work in this chapter, converged meshes contain element counts from around 20k to almost 100k brick elements. This brick element shape is shown in **Figure 100** (50).

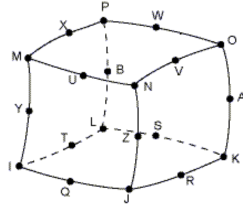

Figure 100: High Order Brick Element Shape Used for Bi-Layer Self Cooler

The meshes contain a high element density near the hotspot and Cooler regions since they contain the highest heat fluxes of the device. A sample mesh plot is shown in **Figure 101**.

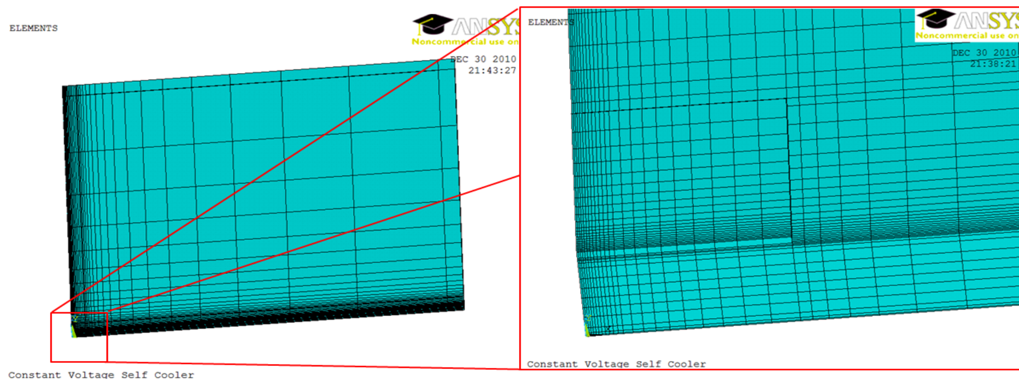

Figure 101: Typical Mesh plot of for Bi-Layer Self Cooler, Zoomed view of Cooler on right

The pertinent temperatures to this study are the center hotspot and center Cooler temperature. These trends for the center hotspot and Cooler temperatures as the element count increases are shown in **Figure 102** and **Figure 103** for the 500µm die, 85% Germanium, 1400µm Cooler, and 4.6 amp case.

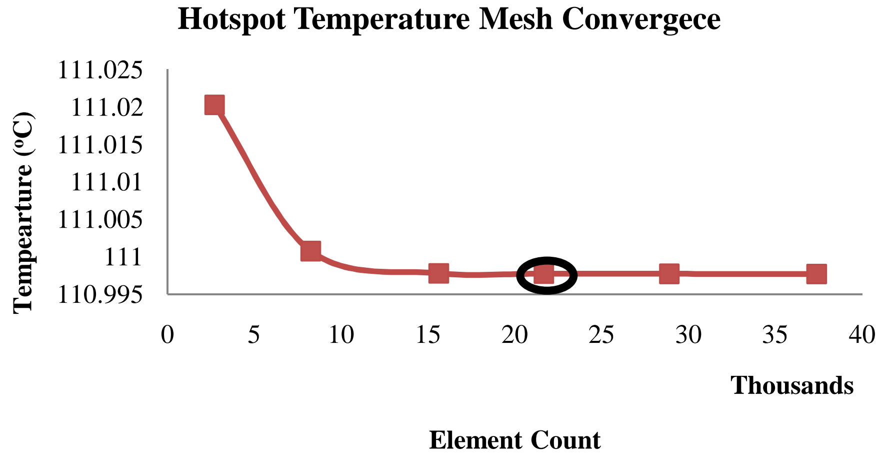

Figure 102: Hotspot Temperature Mesh convergence for 500µm Die, 85% Germanium, 1400µm Cooler, and I=4.6A

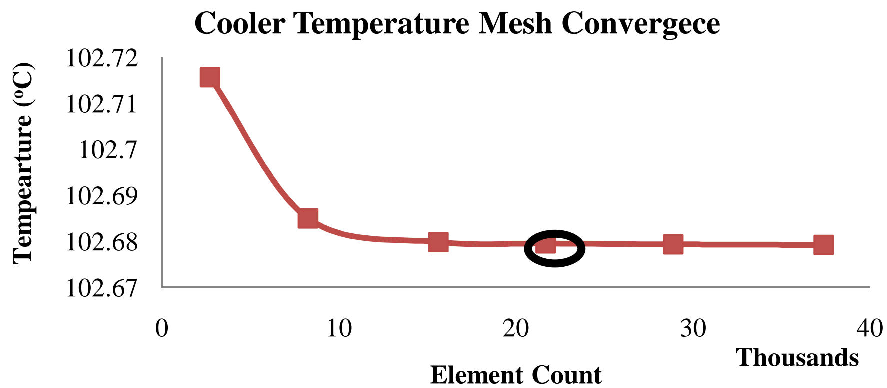

Figure 103: Cooler Temperature Mesh convergence for 500µm Die, 85% Germanium, 1400µm Cooler, and I=4.6A

The temperatures vary about 0.1°C over the element range tested which provides confidence to pick the circled high order (SOLID227) element count for the constant voltage self cooler. This point is chosen because it provides a balance between relative accuracy and computational time. The run times for the above simulations are shown in **Figure 104**.

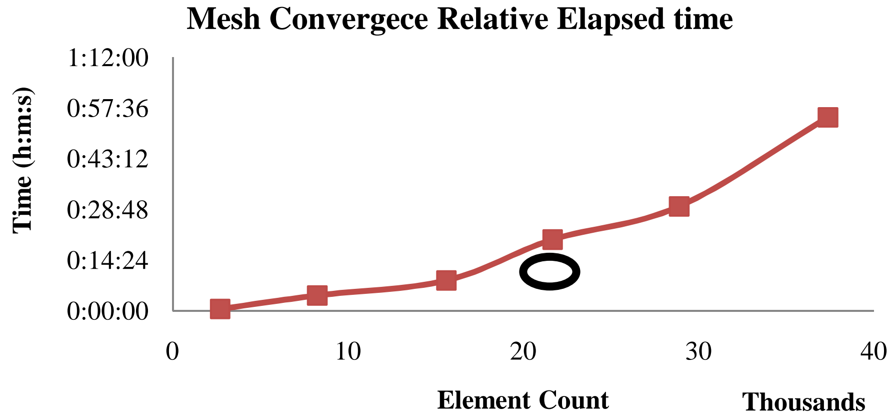

Figure 104: Mesh convergence Time for 500µm Die, 85% Germanium, 1400µm Cooler, and I=4.6A

These trends for Power as the element count increases are shown in **Figure 105** for the 500µm die, 85% Germanium, 1400µm Cooler, and 4.6 amp case.

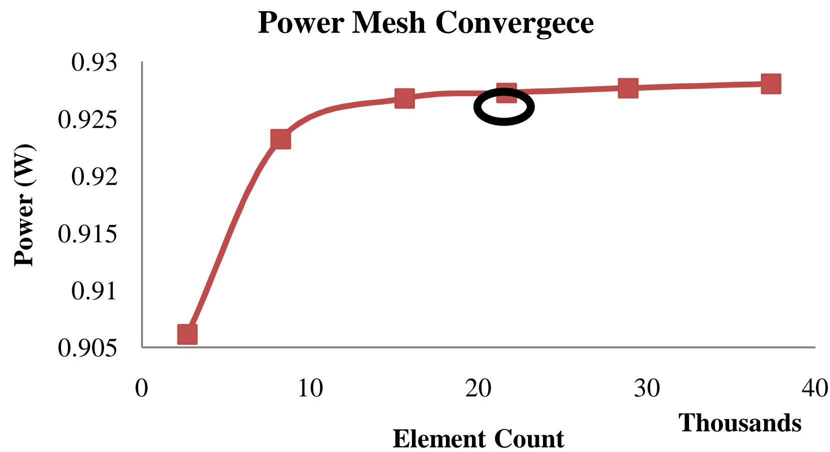

Figure 105: Mesh convergence Time for 500µm Die, 85% Germanium, 1400µm Cooler, and I=4.6A

5.2.3 Typical Bi-layer Temperature Distributions

The temperature distribution along the bottom of the germanium die is shown in **Figure 106** for the 100µm die, 90% Germanium, and 350µm Cooler case. These temperature distributions are through the center of the die and consequently the temperatures at position zero are the center hotspot temperatures used for the metrics discussed in earlier sections. The bi-layer self cooler is simulated using a quarter model

since the geometry and boundary conditions are symmetric. Thus, the negative positioned temperatures are mirrored from their positive counterparts to provide the entire temperature distribution.

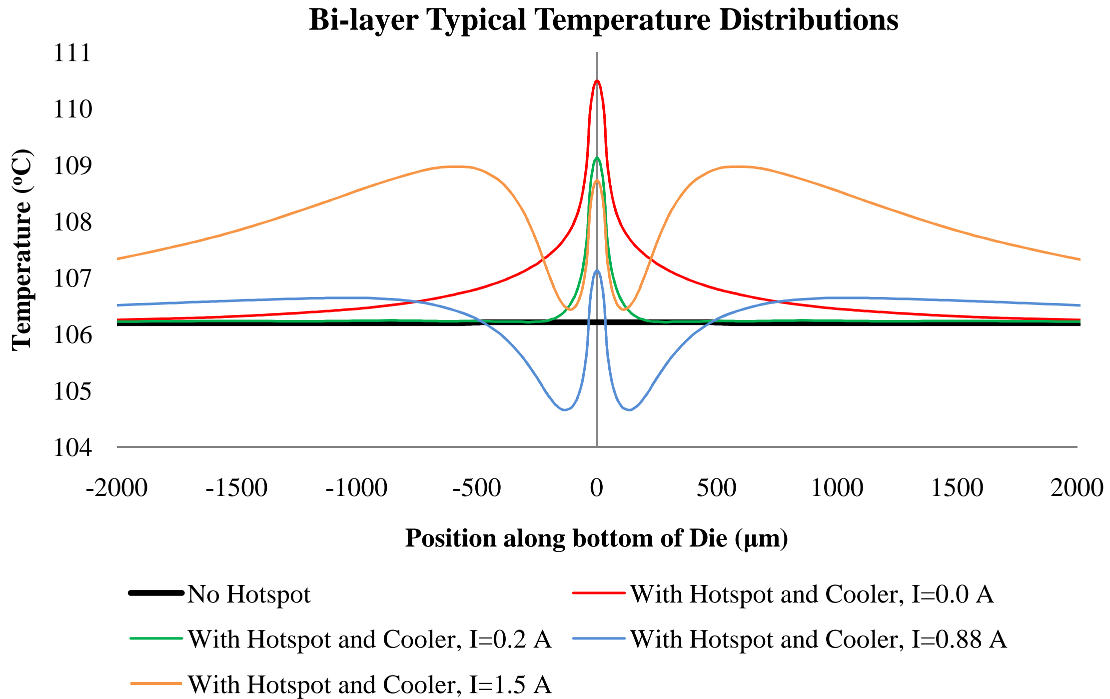

Figure 106: Bi-layer Self Cooler, Temperature Along the bottom of the die, 100µm Die, 90% Germanium, 350µm Cooler (Quarter model)

As shown above, the activation of the hotspot increases the peak temperature of the device by about 4.3°C reaching about 110.5°C. The application of 0.2A to the Cooler reduces the middle hotspot temperature around 1.4°C. Furthermore, the application of 0.88A and 1.5A reduces the temperature 3.4°C and 1.8°C respectively hinting at the quadratic behavior of thermoelectric cooling.

The application of current to the germanium self cooling device produces a complicated temperature profile around the center hotspot temperature. There are two inflection points in the temperature profile around the center of the hotspot. This fact along with the symmetric temperature profile leads to two concentric rings with the

inner-most consisting of slightly lower temperatures and the outer-most consisting of slightly higher temperatures.

This temperature profile exists for all self coolers studied, including the constant current , the constant voltage self cooler, and the bi-layer self cooler.

5.2.4 Function of Current

The optimum performance is found through sequential parametric optimization of the current, Cooler size, germanium percentage, and die thickness. Temperature reductions due to the application of current to the bi-layer self cooling device demonstrate a quadratic behavior as discussed in **2.3 Thermoelectric Cooler Net Effects**. At “low” current values the temperature decreases linearly due to the Peltier effect. At “large” currents the temperature increases due to Joule heating. Thus, there is a current value that balances the Peltier effect and Joule heating which provides the lowest temperature. This point is exemplified using the numerical results from the 100µm die, 90% Germanium, and 350µm Cooler case shown in **Figure 107**.

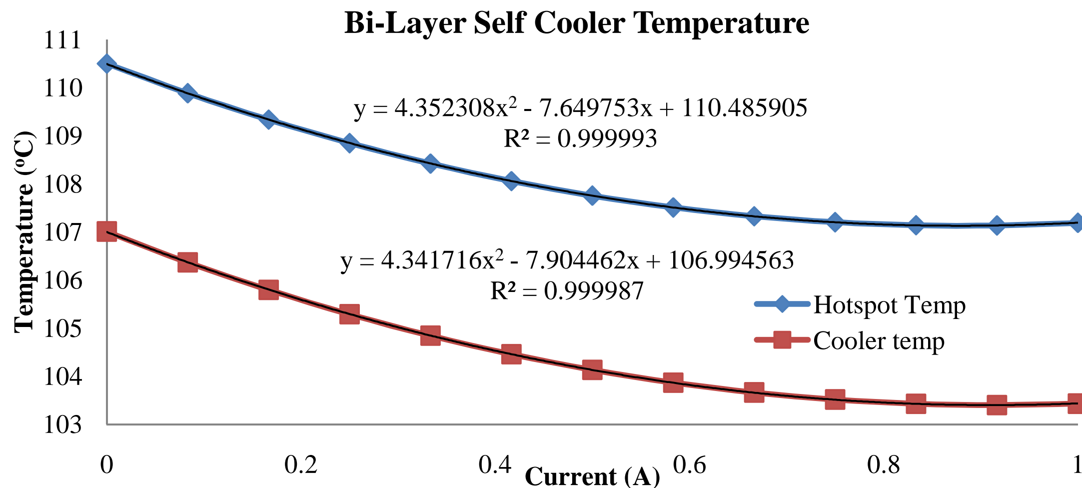

Figure 107: Bi-Layer Self Cooler, Hotspot and Cooler Temperature for 100µm Die, 90% Germanium, 350µm Cooler

The coefficient of determination (R^2) for the hotspot and Cooler temperatures signify that the curves show a strong quadratic behavior. This is true for all cases studied and the below process is the same as demonstrate for the constant voltage self cooling device discussed in **3.2.4 Function of Current**.

The trend equation allows the determination of the minimum temperature as well as the current that induces the effect. This is accomplished through a simple optimization procedure starting with the general equation of a quadratic curve as shown in equation **5-7**.

$$T(I) = aI^2 + bI + c \qquad \textbf{5-7}$$

$where:$
$T = temeprature\ (\,^{o}C\ or\ K)$
$I = current\ (A)$

Figure 107 shows the coefficients "a," "b," and "c" are determined by curve fitting the hotspot or Cooler temperature curve. Then, the above equation is differentiated and set equal to zero to find the minimum temperature current. This value is shown in **5-8**.

$$I_{Min\,Temp} = I_{MT} = \frac{-b}{2a} \qquad \textbf{5-8}$$

The above current is subsequently placed back into equation **5-7** to find the minimum temperature. This equation is shown in **5-9**.

$$T_{Minimum} = T(I_{MT})_{Min} = aI_{MT}{}^{2} + bI_{MT} + c \qquad \textbf{5-9}$$

The maximum temperature reduction is found by subtracting equation **5-9** from the temperature at zero current. This produces equation **5-10**.

$$\Delta T_{Maximum} = \Delta T(I_{MC})_{Max} = aI_{MC}{}^{2} + bI_{MC} \qquad \textbf{5-10}$$

The Power required to operate the constant voltage self cooling device is also of interest. The Power metric is found by taking the voltage at the top Cooler surface (contains the constant voltage condition) and multiplying it by the applied current as shown by equation.

$Power = V_{Cooler}I$

The results from the prescribed procedure are exemplified using 100µm die, 90% Germanium, and 350µm Cooler case shown in **Figure 108**.

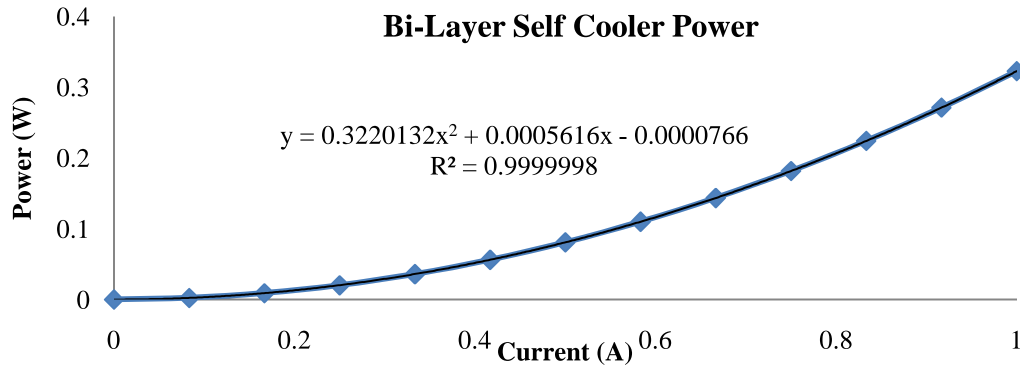

Figure 108: Bi-Layer Self Cooler, Power for 100µm Die, 90% Germanium, and 350µm Cooler

Figure 108 shows the coefficients "a_P", "b_P," and "c_P" are determined by curve fitting the Power curve. Then, the minimum temperature current value (equation **5-8**) is substituted into Power trend fit. This produces equation **5-11** which calculates the Power at the minimum temperature and correspondingly the maximum hotspot temperature reduction.

$$Power_{At\,T_{min}} = P(I_{MT}) = a_P {I_{MT}}^2 + b_P I_{MT} + c_P \qquad \textbf{5-11}$$

The above procedure has many benefits over the practice of blinding applying current values in the search of the maximum cooling and corresponding current for each case (Cooler size, germanium percentage, and die thickness). These quasi-defined quadratic curves only require three current values which translates into a significant computational time savings. Moreover, using the above procedure delivers a more exact maximum cooling and maximum cooling Power than blinding searching for them. Thus, this procedure is used to optimize the bi-layer self cooler as a function of current.

The thermal impact factor determines the efficiency or the hotspot temperature reduction divided by the required Power input to the device. The results from this division are exemplified using the 100µm die, 90% Germanium, and 350µm Cooler case shown in **Figure 109**.

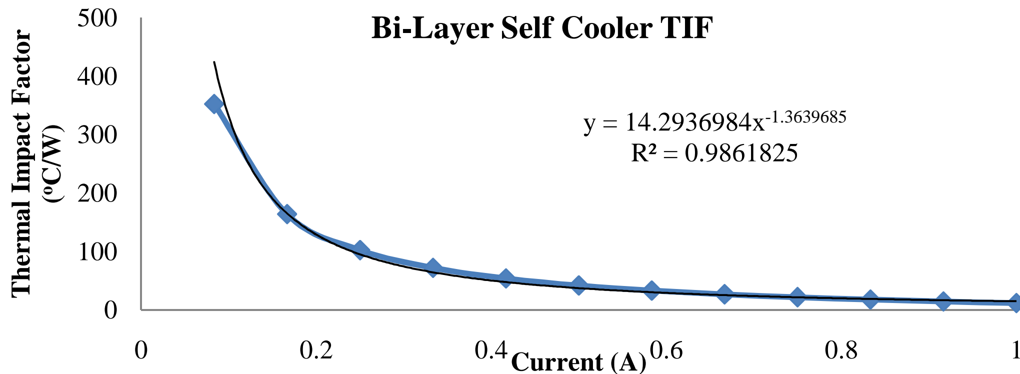

Figure 109: Bi-Layer Self Cooler, Thermal Impact Factor for 100µm Die, 90% Germanium, 350µm Cooler

As the current approaches zero, the denominator of equation **5-6** approaches zero, and consequently, the thermal impact factor approaches infinity. As the current increases, the thermal impact factor decreases rapidly closely following a “power” function with a negative exponent. Moreover, if the current reaches a value which brings the constant voltage cooling device into the Joule heating dominated region, the temperature will be higher than the temperature at zero current, making equation **5-6** negative.

5.2.5 Function of Cooler Size

Using a sequential parametric optimization technique, the current is optimized for various Cooler sizes for one germanium percentage and die thickness at a time. The important trends outputted as a function of Cooler size are the temperature reduction, hotspot cooling effectiveness, power, and thermal impact factor.

5.2.5.1 Temperature Reductions

Temperature reduction and hotspot cooling effectiveness trends as a function of Cooler size are outputted for each die thickness and germanium percentage. They are similar to those found in **3.2.5.1 Temperature Reduction and Hotspot Cooling Effectiveness**. The temperature reduction as a function of Cooler size is due to the tradeoff between the thermoelectric cooling effect and the thermal diffusion between the hotspot and Cooler (20). At small Cooler sizes, the thermoelectric cooling effect is large, and translates into a large Cooler temperature reduction (20). However, the thermal resistance at this Cooler size is also large, and consequently, the hotspot temperature reduction is non-optimal (20). At very large cooler widths, the thermoelectric cooling effect is small and the thermal resistance is small. These two effects translate into a small hotspot and Cooler temperature reduction (20). Between these extremes, there exists a balance between the opposing effects that delivers the maximum hotspot cooling reduction. The Cooler size at which this occurs for the 100µm die and 90% germanium is 350µm. This optimal Cooler size is easily seen in black in **Figure 110** that graphs the maximum hotspot and Cooler temperature reductions as a function of Cooler size for the 100µm die and 90% Germanium case.

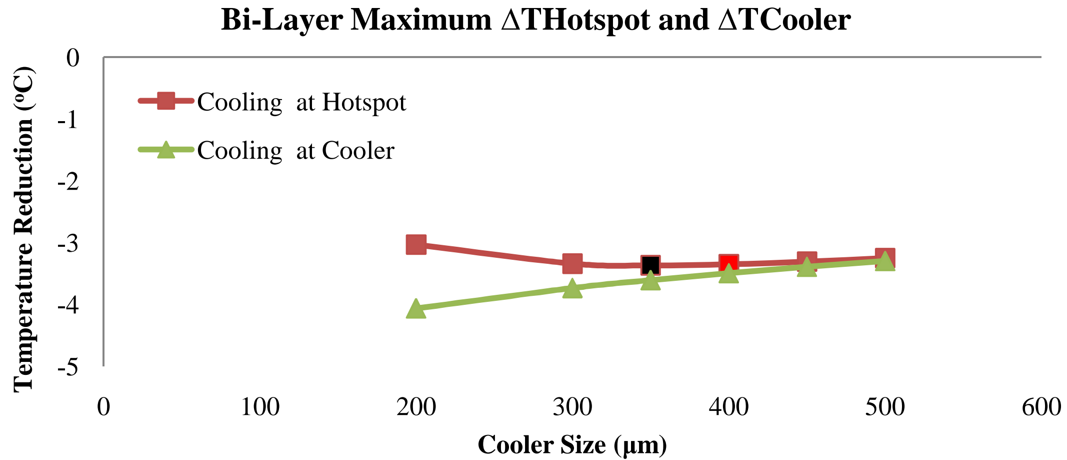

Figure 110: Bi-Layer Self Cooler, Maximum Temperature Reductions for each Cooler Width for 100µm die, and 90% Germanium

Also, the maximum hotspot and Cooler temperature reductions for each die thickness approach eachother at large Cooler sizes.

5.2.5.2 Hotspot Cooling Effectiveness

The hotspot temperature effectiveness is another cooling metric of interest. As shown by equation **5-4**, this metric is equal to the negative of the hotspot temperature reduction over the difference between the hotspot on and cooler off case from the hotspot off and cooler off case. The denominator changes insignificantly as a function of the Cooler size, and consequently, the hotspot temperature effectiveness demonstrates a similar, but negative, behavior to the hotspot temperature reduction curve. Demonstrating this trend, the hotspot cooling effectiveness for the 100µm die and 90% Germanium case is shown in **Figure 111** and contains a maximum value of almost 0.78 at a 350µm cooler width.

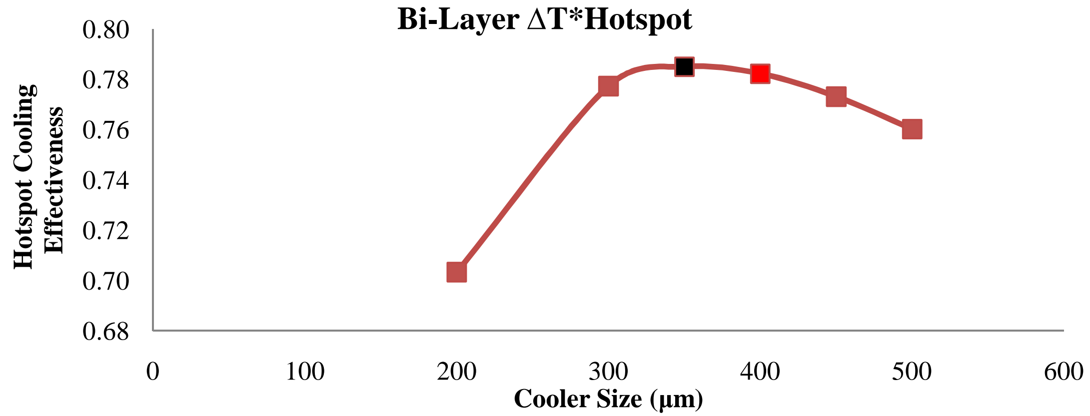

Figure 111: Bi-Layer Self Cooler, Hotspot Cooling Effectiveness for 100µm die and 90% Germanium case

As a consequence of the hotspot cooling effectiveness sharing the same shape at the hotspot temperature reduction curve, their optimum occur at the same Cooler size of 350µm which is shown in black in **Figure 110** and **Figure 111**.

5.2.5.3 Power and Thermal Impact Factor

The power and thermal impact factor for the device at the maximum temperature reduction for each cooler width was recorded. For the for the 100µm die and 90% Germanium case, the Power and the thermal impact factor for each Cooler size at maximum temperature reduction is shown in **Figure 112** and **Figure 113** respectively.

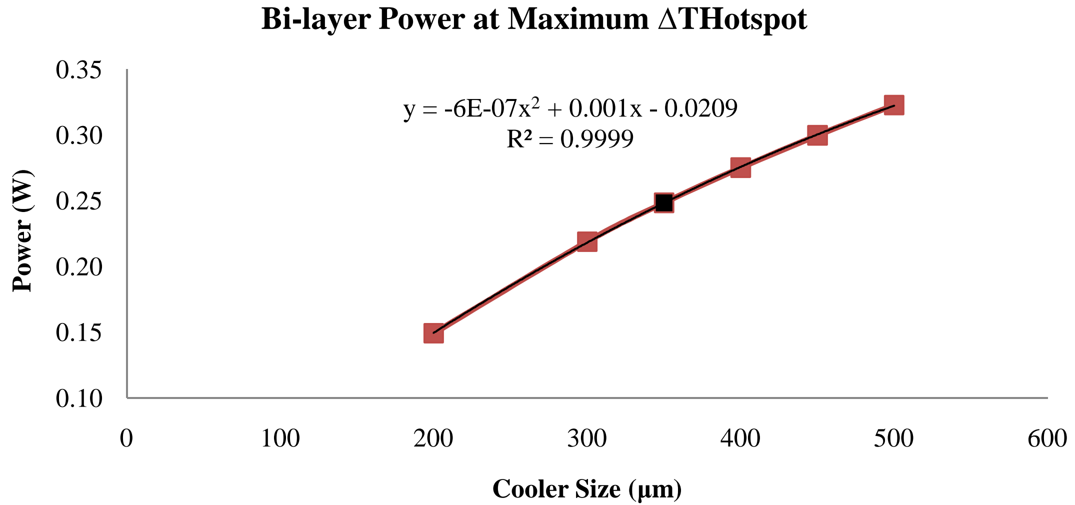

Figure 112: Bi-Layer Self Cooler, Power at Maximum Hotspot Temperature Reduction for 100µm die and 90% Germanium case

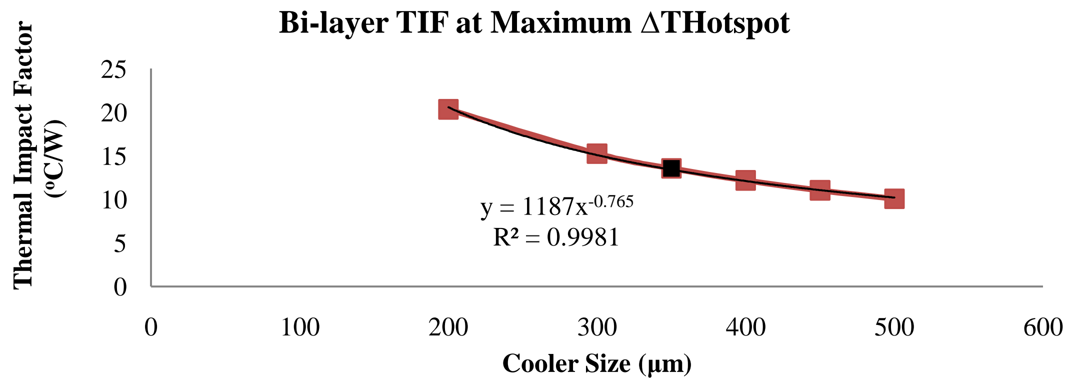

Figure 113: Bi-Layer Self Cooler, Thermal Impact Factor at Maximum Hotspot Temperature Reduction for 100µm die and 90% Germanium case

It is interesting to note that Power is strongly quadratic as a function of current (as shown in **Figure 108**) as well as a function of Cooler size (as shown in **Figure 112**). The thermal impact factor also demonstrates strong a "power" trend as a function of current (**Figure 109**) and Cooler size (**Figure 113**).

5.2.6 Function of Germanium Percentage

Using a sequential parametric optimization technique, the germanium percentage is parametrically optimized for one die thickness at a time. The important trends as a function of germanium percentage are the temperature, temperature reductions, hotspot cooling effectiveness, power, and thermal impact factor.

The hotspot temperature as a function of germanium percentage is shown in **Figure 114**.

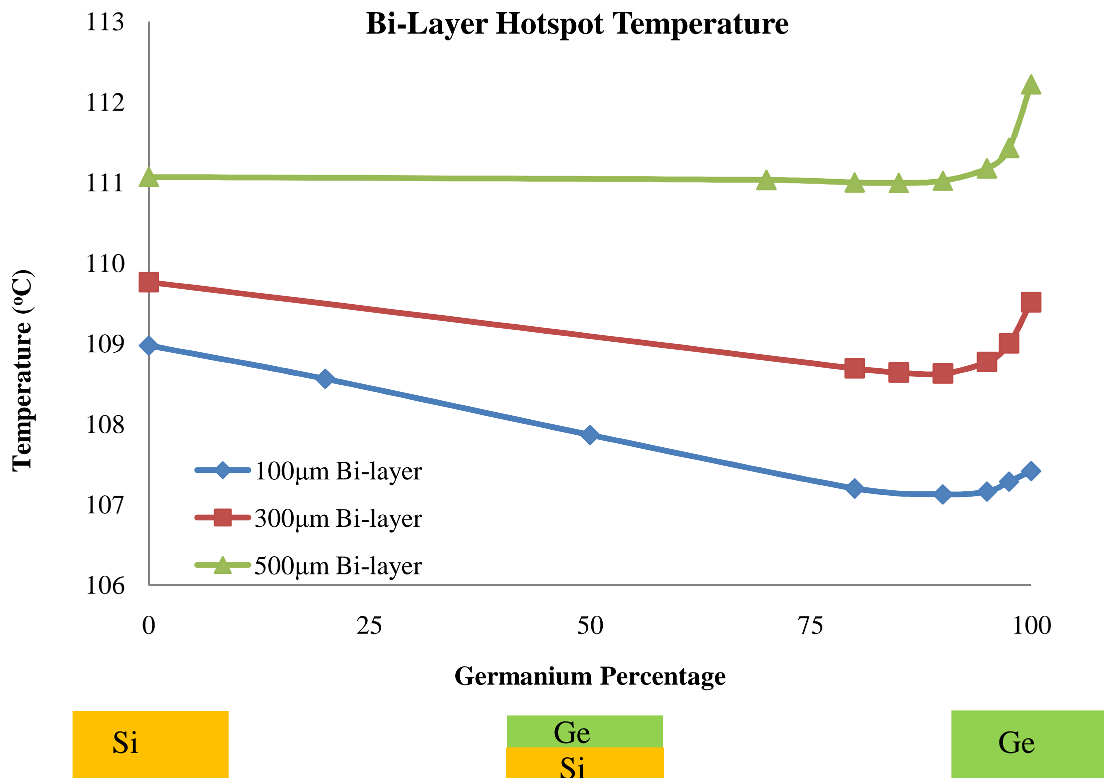

Figure 114: Bi-Layer, Hotspot Temperature

The values at zero germanium percentage describe a device which consists of zero percent germanium or 100% silicon. Moreover, the silicon used for this study contains a high thermal conductivity (100W/mk) and is electrically insulated. Thus, the device at this low extreme does not “self cool,” but rather uses pure conduction to spread the heat.

The values at 100% germanium describe a device which consists of zero percent silicon, or 100% germanium constant voltage self cooler. This device is discussed in detail in **3.2 Numerical Results**.

Viewing the entire solution space at once, it is evident that the 100% germanium constant voltage self cooler is not always capable of providing a lower hotspot temperature than the 100% conduction only silicon device. However, the bi-layer self cooler is capable of providing hotspot temperatures below that of the 100% silicon conduction only device as well as the 100% germanium self cooler for all die thicknesses studied. The following metrics quantify these benefits.

5.2.6.1 Temperature Reductions

As the germanium percentage is varied for each die thickness, a linear hotspot temperature reduction trend is demonstrated as shown by **Figure 115**.

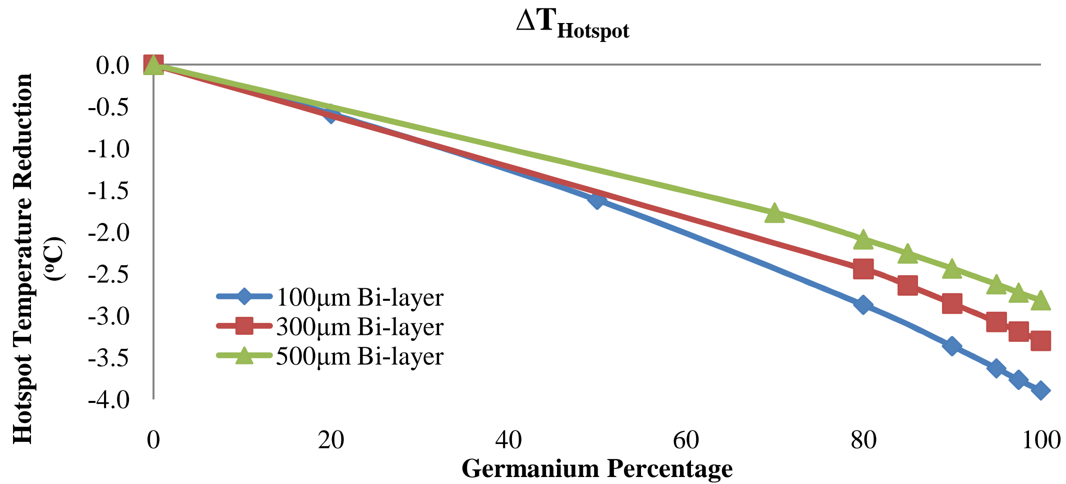

Figure 115: Bi-Layer Self Cooler, Maximum Hotspot Temperature Reduction

At germanium percentage equal to zero, the entire die consists of only silicon, mandating zero hotspot temperature reduction due to its electrically insulated nature. At low germanium percentages, the current within the germanium percentage is constricted, but

because of the Peltier effect, the bi-layer is capable of producing a temperature reduction. As the germanium percentage increases, the current restriction decreases, increasing the maximum hotspot temperature reduction which eventually approaches that of the constant voltage self cooler presented in **3.2 Numerical Results**.

The temperature reduction relative to the 100% germanium constant voltage self cooler demonstrates an advantage of the bi-layer configuration. This metric is defined in equation **5-2**. As the germanium percentage is varied for all die thickness studied, **Figure 116** is outputted.

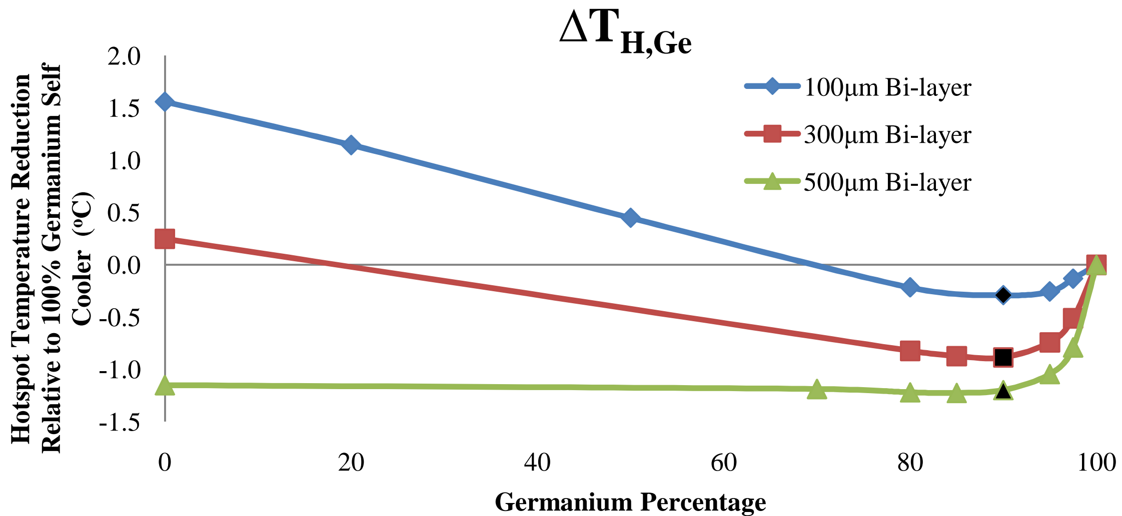

Figure 116: Bi-Layer Self Cooler, Maximum Hotspot Temperature Reduction relative to 100% Germanium cooler

The maximum temperature reduction as shown by **Figure 115** increases as the germanium percentage increases (absolute value). However, the thermal spreading ability of the high “k” bottom silicon layer decreases as the germanium percentage increases. Thus, these two competing effects provide an optimum percentage which allows for a hotspot temperature below that of the 100% germanium cooler as shown in black in the above figure.

The temperature reduction relative to the 100% conduction only silicon device ($\Delta T_{H,Si}$) demonstrates another main advantage of the bi-layer configuration as shown by **Figure 117.**

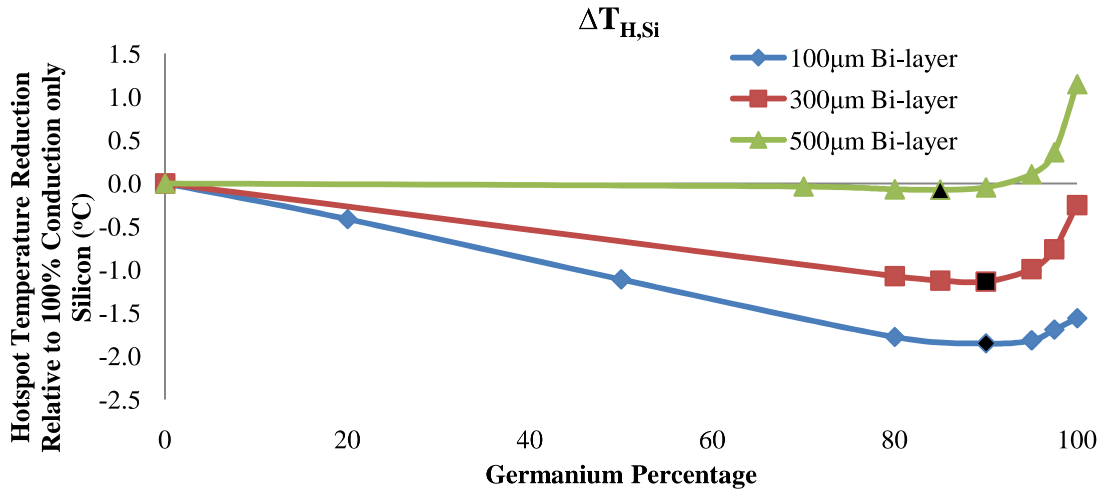

Figure 117: Bi-Layer Self Cooler, Maximum Hotspot Temperature Reduction relative to 100% Conduction only Silicon

Following the same tend causes as $\Delta T_{H,Ge}$, there exist optimum germanium percentages which provide temperatures below that of the 100% conduction only silicon device. The optimum germanium percentages for $\Delta T_{H,Si}$ and $\Delta T_{H,Ge}$ are shown to be identical. These are 90%, 90%, and 85% for the 100µm, 300µm, and 500µm respective die thicknesses.

Thus, the bi-layer self cooler can produce temperature below that of the 100% constant voltage self cooler as well as the 100% silicon conduction only device. These facts provide a main advantage of the bi-layer self cooler.

5.2.6.2 Hotspot Cooling Effectiveness

The hotspot temperature effectiveness is another cooling metric of interest. As shown by equation **5-4**, this metric is equal to the negative of the hotspot temperature

reduction over the difference between the hotspot on and Cooler off case from the hotspot off and Cooler off case.

The denominator decreases as the germanium percentage increases due to the thermal spreading of the high “k” bottom silicon layer. The numerator increases from zero as the germanium percentage increases as shown by **Figure 115**. These two effects describe the general increasing trend. There is however an optimum percentage which allows for an optimum hotspot cooling effectiveness as shown by **Figure 118**. The optimum hotspot cooling effectiveness values are shown by the black data points.

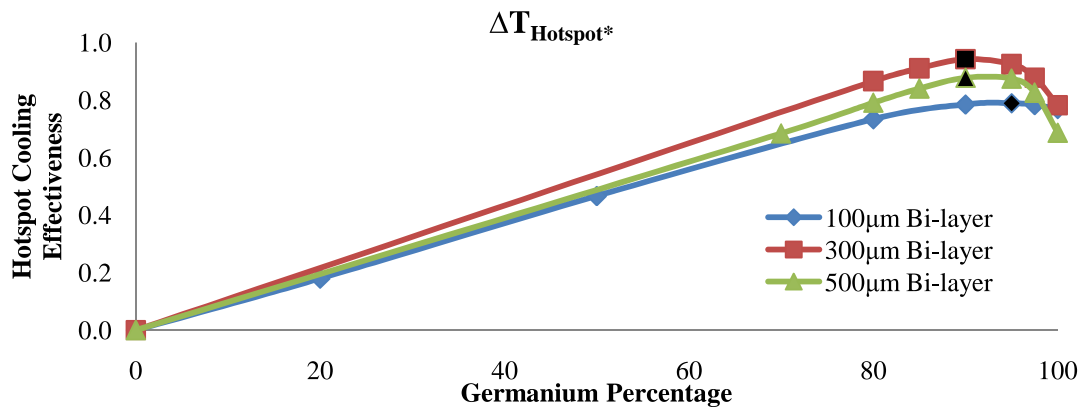

Figure 118: Bi-Layer Self Cooler, Hotspot Cooling Effectiveness

The optimum germanium percentage for this metric are 95%, 90% and 90% for the 100µm, 300µm, and 500µm dies respectively.

5.2.6.3 Power and Thermal Impact Factor

The power was recorded at the maximum hotspot temperature reduction and demonstrates the trend shown in **Figure 119** for each die thickness.

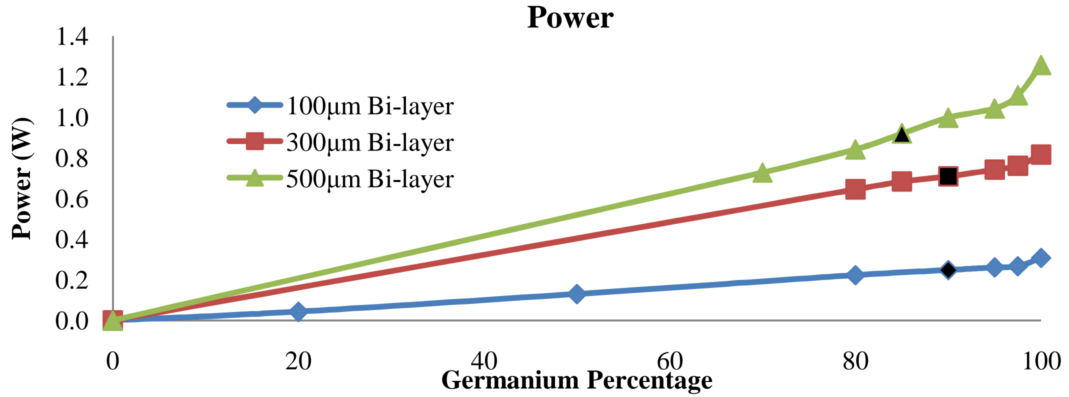

Figure 119: Bi-Layer Self Cooler, Power

As shown above, the electrical insulation of the 100% conduction only silicon device requires no power to run. The Power does seem to increase linearly as the germanium percentage increases. It however, remains below that of the 100% germanium self cooler for all germanium percentages studied. This is true for all die thickness studied. The black data points are those at optimum for $\Delta T_{H, Ge}$ and $\Delta T_{H,Si}$ (are evident at the same germanium percentage).

The thermal impact factor determines the hotspot temperature reduction efficiency of the bi-layer self cooler. It is defined in equation **5-6** as the negative of the hotspot temperature reduction divided by the power and its trend for each die thickness is shown in **Figure 120**.

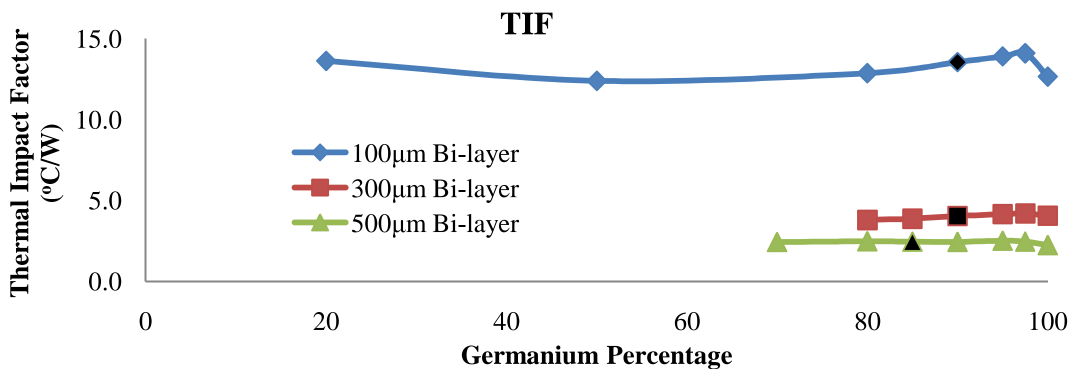

Figure 120: Bi-Layer Self Cooler, Thermal Impact Factor

Since the 100% conduction only silicon device requires no power to operate and creates no hotspot temperature reduction, the thermal impact factor approaches infinity divided by zero, which is undefined, and consequently is not graphed above.

Viewing all the die thicknesses together, it is apparent that the increasing hotspot temperature reduction and Power translate into quasi-quadratic trends. $\Delta T_{H,Ge}$ and $\Delta T_{H,Si}$ reach an optimum at high germanium percentages, and the corresponding thermal impact factor's are shown in black in the above figure. Moreover, these data points are larger than the 100% germanium self cooler which demonstrates a more efficient hotspot temperature reduction. This is due to the bottom high "k" silicon layer which easily spreads the heat due to the hotspot.

5.2.7 Function of Die Thickness

The die thickness is the last variable in the sequential parametric optimization. This variable demonstrates the full benefit of the bi-layer self cooler when the results are compared to the 100% conduction only silicon device and 100% germanium constant voltage cooler. The important trends as a function of die thickness are the temperature reductions, the hotspot cooling effectiveness, power, and thermal impact factor.

5.2.7.1 Temperature Reductions

The hotspot temperature reduction relative to the 100% constant voltage germanium self cooler ($\Delta T_{H,Ge}$) and 100% conduction only silicon device ($\Delta T_{H,Si}$) demonstrates a main advantage of the bi-layer self cooler. **Figure 121** demonstrates these trends as a function of die thickness when the optimum values from **Figure 116** and **Figure 117** are plotted together.

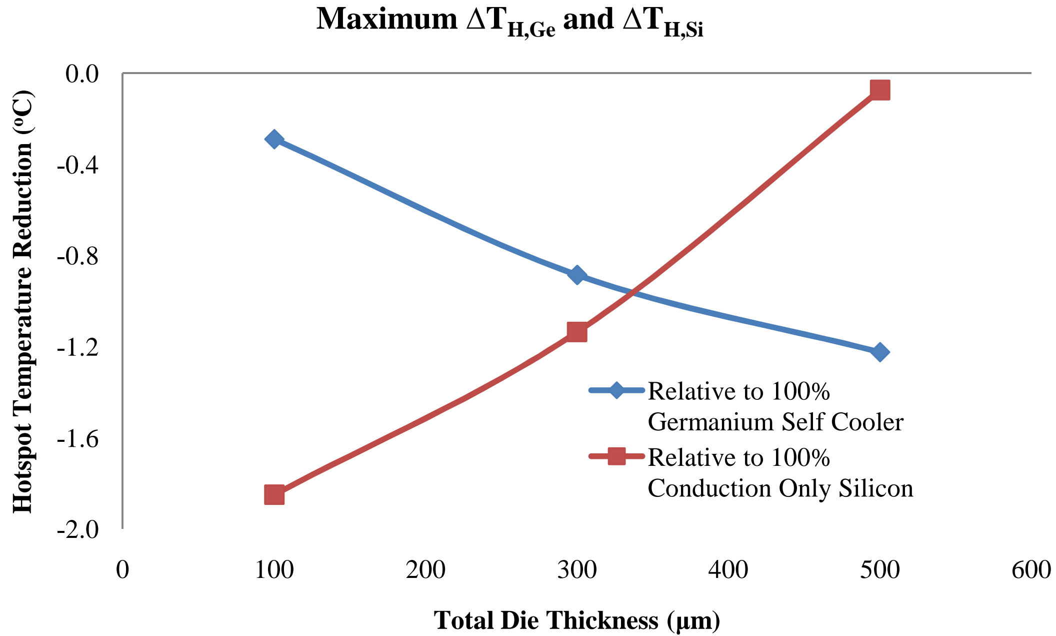

Figure 121: Bi-Layer Self Cooler, Maximum Hotspot Temperature Reduction relative to 100% Germanium cooler

The maximum $\Delta T_{H,Ge}$ values for the 100µm, 300µm, and 500µm are -0.3°C, -0.9°C, and -1.22°C respectively demonstrating a quasi-linear trend. The maximum $\Delta T_{H,Si}$ values for the 100µm, 300µm, and 500µm are -1.9°C, -1.°C, and -0.1°C respectively demonstrating a quasi-linear trend.

The above trends demonstrate that the bi-layer self cooler is capable of providing lower temperatures than the 100% conduction only silicon device as well as the 100% germanium self cooler.

5.2.7.2 Hotspot Cooling Effectiveness

Another main advantage of the bi-layer self cooler is the increase in hotspot cooling effectiveness over the 100% conduction only silicon device and 100% germanium constant voltage cooler. As shown by equation **5-4**, this metric is equal to the

negative of the hotspot temperature reduction over the difference between the hotspot on and Cooler off case from the hotspot off and Cooler off case.

Figure 122 plots the maximum hotspot cooling effectiveness values for the bi-layer self cooler (**Figure 118**), 100% germanium self cooler (**Figure 50**), and the 100% conduction only silicon device.

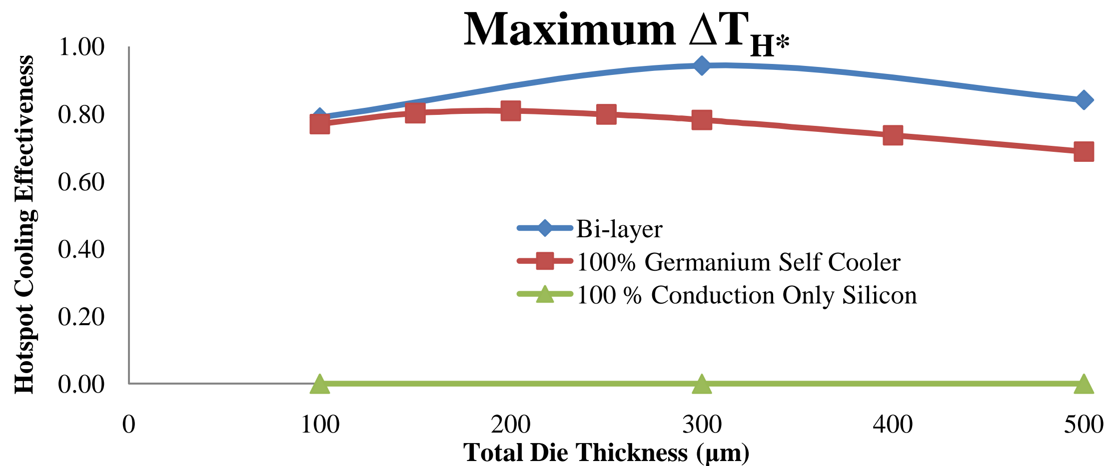

Figure 122: Maximum Hotspot Cooling Effectiveness

Smaller die thicknesses translate into larger (absolute value) hotspot temperature reductions since the thermal resistance between the Cooler and hotspot reduces. However, smaller die thicknesses also contain an elevated hotspot temperature due to their poorer spreading ability (20). Thus, there exists an optimum die thickness that balances the opposing effects of heat spreading and temperature reduction (20). For the bi-layer self cooler, this optimum was seen at the 300µm thick die with a value of 0.94. It is believed that if more die thickness were studied, the true optimum would be seen in between 100µm and 300µm.

Moreover, the bi-layer self cooler provides larger hotspot cooling effectiveness values than the 100% germanium cooler for all die thickness tested. This increase is more

dramatic at the larger (100μm and 300μm) die thickness. This difference is due to the increased spreading that the high “k” silicon layer provides to the device that overpowers the reduced hotspot temperature reductions of the bi-layer device.

Since the 100% silicon device cannot provide a hotspot temperature reduction, the hotspot cooling effectiveness is equal to zero for all die thicknesses tested. Thus, the bi-layer self cooler is capable of removing the temperature rise due to the hotspot more effectively than the 100% germanium self cooler and the 100% conduction only silicon device.

5.2.7.3 Power and Thermal Impact Factor

Figure 123 is produced when the Power values at the corresponding germanium percentages which produced the maximum $\Delta T_{H,Ge}$ and $\Delta T_{H,Si}$ (are evident at the same germanium percentage) are plotted together.

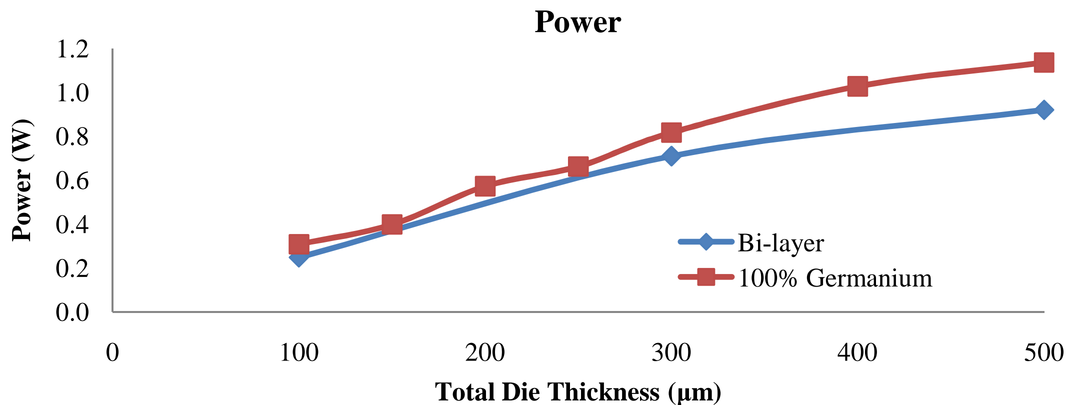

Figure 123: Bi-Layer Self Cooler, Power at Maximum $\Delta T_{H,Ge}$ and $\Delta T_{H,Si}$

The Power required to run the bi-layer self cooler increases as the die thickness increases, but generally remains below or at that of the 100% germanium self cooler.

The thermal impact factor determines the hotspot temperature reduction efficiency of the bi-layer self cooler. It is defined in equation **5-6** as the negative of the

hotspot temperature reduction divided by the Power. **Figure 124** is produced when the thermal impact values at the corresponding germanium percentages which produced the maximum $\Delta T_{H,Ge}$ and $\Delta T_{H,Si}$ (are evident at the same germanium percentage) are plotted together.

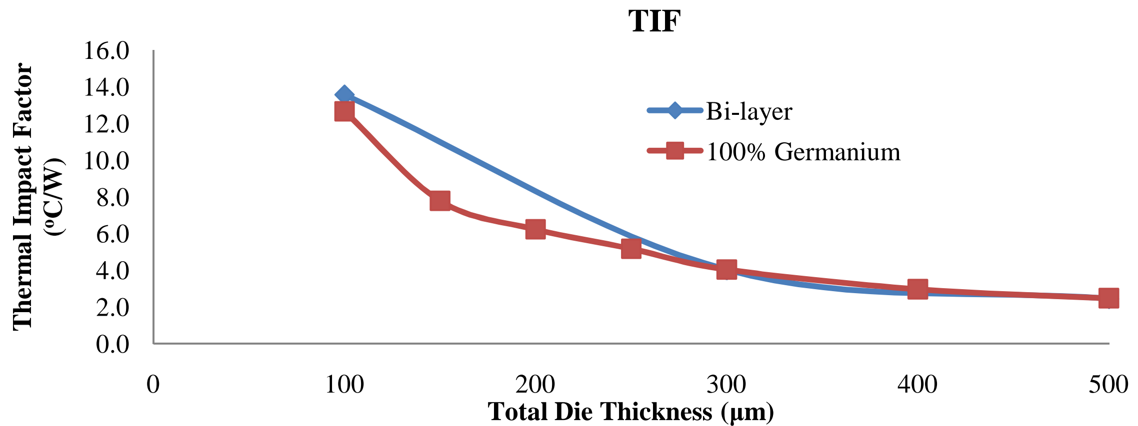

Figure 124: Bi-Layer Self Cooler, Thermal Impact Factor at Maximum $\Delta T_{H,Ge}$ and $\Delta T_{H,Si}$

Both the bi-layer and 100% germanium self cooler thermal impact factor's decrease as the die thickness decreases. The bi-layer thermal impact factor values start at 13.4 for the 100µm die and end at 2.5 for the 500µm die. There is negligible difference in thermal impact factor between the bi-layer and 100% germanium self cooler.

5.2.8 Thermal Contact Resistances

The previous sections describe the thermal advantage the bi-layer self cooler over the 100% conduction only silicon device and the 100% germanium self cooler. The bi-layer self cooler also has a manufacturing advantage since the bottom silicon layer is the industry standard. However the attachment of the top germanium layer introduces a thermal constant resistance which is explored below.

As an example of the performance loss caused by poor contact resistances the geometry which provided the largest hotspot temperature reduction relative to the 100%

germanium self cooler was simulated. This geometry was the 1400µm Cooler size, 85% germanium, and 500µm die thickness. The bi-layer self cooler contained contact resistances of $1e^{-7}$ Km^2/W, $1e^{-6}$ Km^2/W, and $1e^{-5}$ Km^2/W.

The introduction of contact resistances was accomplished by creating a 5µm volume between the required layers, and transforming the constant resistances to thermal conductivities in the "z" or upwards direction. The thermal conductivity in the planar direction ("x-y") was set to zero to eliminate any spreading within the constant resistance volume. This transformation is outlined in equation **5-12** for the $1e^{-7}$ Km^2/W contact resistance.

$$k_{Constant\ Resistance\ Volume} = \frac{Volume\ Thickness}{R_{Contact}} = \frac{5e^{-6}m}{\frac{1e^{-7}Km^2}{W}} = 50\frac{W}{mK} \qquad \textbf{5-12}$$

The corresponding "z" direction thermal conductivities are 50W/m-K, 5 W/m-K, and 0.5 W/m-K for the contact resistances of $1e^{-7}$ Km^2/W, $1e^{-6}$ Km^2/W, and $1e^{-5}$ Km^2/W respectively.

The hotspot temperature as a function of contact resistance is shown in

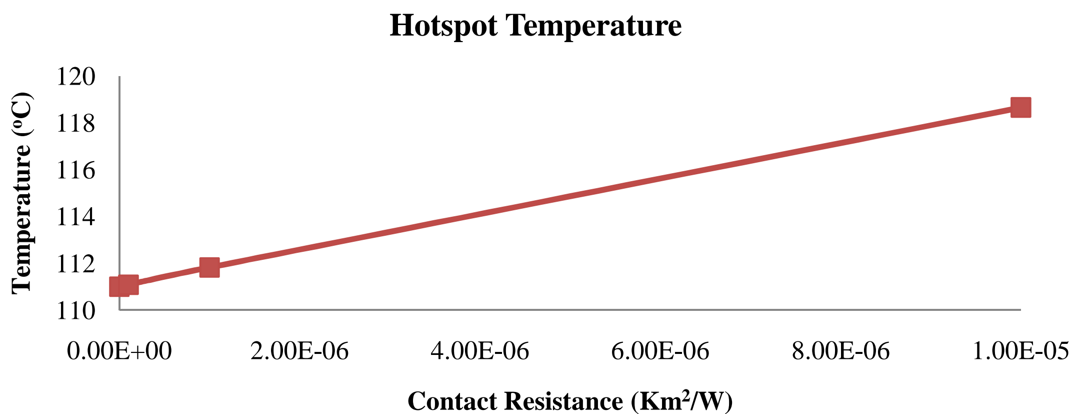

Figure 125: Bi-Layer Self Cooler, Contact Resistance for 1400µm Cooler size, 85% Germanium, and 500µm die thickness case

As the contact resistance increases, the hotspot temperature does also. The hotspot temperature reduction relative to the 100% conduction only silicon device and 100% germanium self cooler is also of importance. This metric is shown in **Figure 125**.

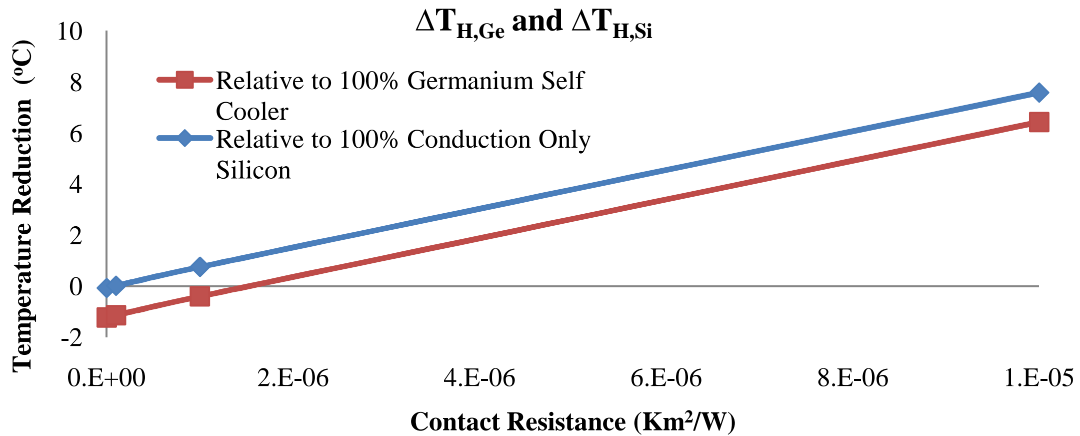

Figure 126: Bi-Layer Self Cooler, Temperature Reduction as a function of Contact Resistance for 1400µm Cooler size, 85% Germanium, and 500µm die thickness case

As the contact resistance increases, the hotspot temperature benefit felt by the bi-layer self cooler quickly is eliminated. As the thermal contact resistance is increased from zero to $1*10^{-5}$ Km^2/W, the hotspot temperature reduction relative to the 100% germanium self cooler migrates from -1.2°C to almost 7.0°C. The hotspot temperature reduction relative to the 100% silicon self cooler migrates from less than -0.1°C to almost 8.0°C. It is consequently important to ensure good thermal contact between the silicon and germanium if the full advantage (lower hotspot temperature and better hotspot cooling effectiveness) is sought.

Chapter 6: Conclusions and Future Work

This work builds on the thermoelectric self cooling foundation laid by Dr. Avram Bar-Cohen and Dr. Peng Wang. It begins with the germanium self cooler which uses the inherent thermoelectric properties of the n-type germanium substrate to remediate a localized high heat flux zone. Peng and Bar-Cohen previously showed that 4.5^{o}C of thermoelectric cooling at a 680 W/cm^2 hotspot can be achieved through the sequential parametric optimization of the self cooler. The presented work moved the technology forward by numerically determining the performance band of the self-cooler through the comparison of the current application boundary condition, namely a constant voltage and a constant current. This comparison is appropriate because practical electrodes that apply current never attain a constant current or constant voltage at their surface. In fact, they behave in a manner which is between these two ideal boundary conditions

Following the performance band discussion, a meta-model is developed for the germanium self cooler which combines a thermal analytical solution determined through the separation of variables technique with the constant current numerical results. The numerical simulation is integrated into the analytical solution through the application of heat fluxes which are proportional to the total Joule heat multiplied by appropriate allocation factors. These allocation factors are found through a three step process which provides low discrepancies for all cases studied. Moreover, the outputted meta-model is capable of demonstrating the potential of the germanium self cooling technology within a time span several orders of magnitude lower than running numerical simulations.

Finally a bi-layer structure is introduced that contains a germanium layer on top of an electrically insulated silicon layer with high thermal conductivity. This device

contains a manufacturing advantage over that of the pure germanium self cooler since the bottom layer consists of the industry standard. The top germanium layer can then be grown through chemical or vapor techniques or attached. Moreover, the silicon provides a high thermal conductivity at the location of the hotspot providing superior thermal spreading, translating into lower hotspot temperatures than comparable devices. The conclusions reached in this work are summarized below:

6.1.1 Germanium Self Cooler Performance:

The Peltier effect occurs at current crossing surfaces. Moreover, the constant current and constant voltage boundary conditions generate different current densities at the cooler electrode/germanium interface. The constant current boundary condition provides a uniform flow of current at the interface whereas the constant voltage boundary condition provides a high current flow in the corner of the electrode which quickly decreases towards the center. This provides a thermoelectrically induced cold spot at the center of the electrode for the constant current boundary condition and a cold spot at the corner for the constant voltage.

Since the hotspot is vertically centered below the cooler electrode, the constant current boundary condition provides higher temperature reductions as well as higher hotspot temperature reductions than the constant voltage.

6.1.2 Germanium Self Cooler Meta-Model:

Despite generally very good agreement, small discrepancies were determined between the meta-model and the numerical results. It was found that the meta-model can accurately predict the hotspot temperature reduction at optimum conditions within 0.2^{o}C.

It was also found that the hotspot temperature reduction due to the introduction of the hotspot at optimum conditions was within 0.01K of the numerical results. These small discrepancies provide confidence in using the meta-model to quickly determine the potential of the self cooling device.

6.1.3 Bi-Layer Self Cooler:

One of the main parametric variables, the germanium percentage, provides a clear comparison to the 100% germanium constant voltage self cooler as well as the 100% conduction only silicon device. As the germanium percentage increases, the hotspot temperature reduction increases (absolute value) to that of the 100% germanium constant voltage self cooler due to the de-constriction of the current within the top germanium layer. At the same time, the thermal spreading of the bottom high thermal conductivity silicon layer decreases. The tradeoff between these opposing effects creates minimum temperatures lower than the 100% germanium constant voltage self cooler and the 100% conduction only silicon device. The bi-layer device can provide a 1.2^{o}C lower hotspot temperature when compared to the 100% germanium constant voltage self cooler and a 1.9^{o}C lower hotspot temperature when compared to the 100% conduction only silicon device.

The hotspot temperature rise in the bi-layer device due to the introduction of the hotspot is dependent on the die thickness. As the die thickness increases, the hotspot temperature reduction increases. However, at zero current, the hotspot temperature rise due to the introduction of the hotspot decreases. These opposing effects provide a die thickness which demonstrates 94% elimination of the hotspot temperature rise.

The quality of the thermal attachment of the germanium layer to the silicon layer is investigated through the parameterization of contact resistances. As the thermal contact resistance is increased from zero to $1*10^{-5}$ Km^2/W, the hotspot temperature migrates from 1.2^oC lower, to 7.0^oC higher when compared to the 100% germanium only constant voltage self cooler. A similar trend is shown for the hotspot temperature when compared to the 100% conduction only silicon device. It is thus important to ensure good thermal contact between the die layers if the optimum performance of the bi-layer device is sought.

6.2 *Future Work*

The presented work pushes the self cooling technology forwards through the description of the performance band, the meta-model, and the bi-layer device. There is however, more work that needs to be done to develop this novel hotspot remediation technique from a research project into a standard industry thermal solution.

6.2.1 Experimental Validation:

This work relies heavily on numerical simulations of the thermoelectric effect within a germanium chip. Even though this numerical technique has been proven to provide a reliable prediction of real life phenomena, a physical self cooling experiment is worth undertaking. This experiment will provide insight into the true physics of the device that might not be clear in the numerical simulations. Such experiments will likely begin with the self cooling of a highly doped silicon chip since the techniques and skills required to accomplish the task have been studied and validated vigorously. A detailed

study of the germanium self cooler will subsequently follow because it is not often used for electronic packages.

6.2.2 Bi-layer Comparisons

The bi-layer self cooler is compared to a 100% germanium self cooler as well as a 100% silicon device that only employs conduction within the die to remediate hotspots. In the latter comparison, the germanium percentage for constant die thicknesses is varied and compared to the equivalent non-self cooled silicon device die thickness. It is proposed that a new comparison should be developed to more accurately describe the advantage of attaching a germanium layer onto a silicon die. In this new comparison, the silicon layer thickness will be constant and the germanium layer thickness will be varied. The results from this bi-layer device will then be compared to the non-self cooled silicon device with die thickness equal to the bi-layer's silicon layer thickness.

Appendices Introduction

A large percentage of the presented work relies on the Finite Element Modeling (FEM) commercial software, ANSYS. Consequently the appendix is dedicated to providing a brief introduction to the theory as it applies to heat transfer problems as well as providing a detailed description of the thermal-electric model.

Appendix A **FEM Phases** describes the main phases and sub steps of any FEM analysis. The vehicle for this explanation was a thermal example of a layered wall with convective boundary conditions from Moaveni's book titled "Finite Element Analysis; Theory and Application with ANSYS". The three main phases are the "Preprocessing phase," the "Solution phase," and the "Post-Processing Phase" and all contain several sub steps (54).

Appendix B **The Thermal-Electrical Model** provides a model for thermoelectric devices by coupling thermal and electrical effects. The thermal effect is determined by the heat diffusion equation and the electric effect is determined by the continuity of electric charge (9) (55). These two effects, thermal and electrical, are run simultaneously and coupled with Joule heating and the Peltier effect.

The previous sections discuss the pertinent models that are necessary to analyze thermoelectric devices. **Appendix** C **ANSYS 12.0 Thermal and Electrical Validation** is dedicated to validating the models so thermoelectric devices can be analyzed in ANSYS 12.0 with confidence. Analytical and numerical solutions are created for all models and compared. The validation begins with the thermal model using the residential wall example discussed in **Appendix** A **FEM Phases**. Then the electrical model is validated using several resistors in series. Both of these models contain no difference between the

analytical and numerical solutions. This provides confidence in moving forward to validating their coupling mechanisms. The first coupling mechanism discussed was Joule heating using an infinite slab problem with constant temperature sides and uniform current running through it. The second coupling mechanism is the Peltier effect and is studied along with Joule heating, since they occur simultaneously in thermoelectric devices. A conventional one leg thermoelectric cooler is studied and little difference (less than 3% for all metrics) is found between the analytical and numerical solutions.

FEM analysis, and more specifically ANSYS 12.0, is a valid method in analyzing thermoelectric devices since it is rooted in the same theory as the analytical equations, and provides little difference between the analytical and numerical solutions for all models and coupling mechanisms concerned.

Appendix A FEM Phases

A FEM analysis can be broken up into three phases which are the “Preprocessing phase,” the “Solution phase,” and the “Post-Processing Phase (54).” These phases do not necessary occur in a linear fashion as presented here. The analysis may require several iterations of certain phases, and thus creates a looped pattern. This loop has been omitted in the presented discussion for simplicity. **Figure 127** displays the simplified linear order of the phases.

Figure 127: Simplified FEM Analysis Phase order

Each of the above phases contain sub several steps. These steps have been grouped under their respective phases, but it important to note that this organizational scheme is intended to convey the main steps in an FEM analysis. The steps do not necessary occur in the order that they have been presented.

The vehicle for this explanation of the analysis was a thermal example of a layered wall with convective boundary conditions from Moaveni’s book titled “Finite Element Analysis; Theory and Application with ANSYS.” Even though the solution to this problem is well known, its simplicity provides the perfect case to demonstrate the main FEM steps and a good foundation to understand the thermal-electrical model.

A .1.1 **Preprocessing Phase**

The preprocessing phase of a FEM analysis is the first main phase and contains several sub steps. They are listed below

1. Build the geometry
2. Mesh the geometry
3. Assume a solution
4. Develop element conductance matrix
5. Assemble global conductance matrix

The above list has been pictorially represented in **Figure 128**.

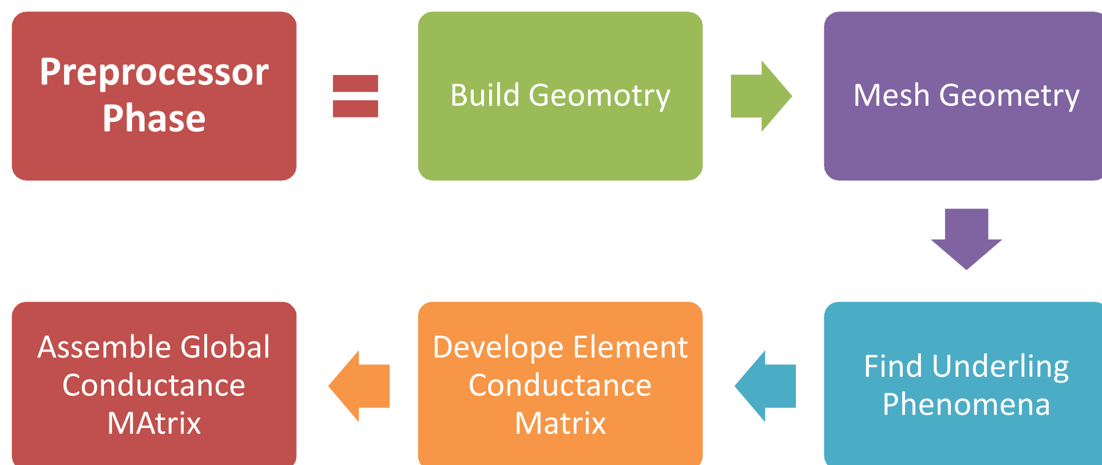

Figure 128: Preprocess sub steps

A.1.1.1Build Geometry

The first sub-step in the preprocessor requires the construction of the geometry in question. This can be accomplished through CAD/CAM software, and then imported into FEM software such as ANSYS, or done directly in the FEM software.

The example that will be used to explain the analysis is a residential wall with several layers. These layers account for the siding, sheathing, insulation batt, and the

gypsum board of the wall and accordingly have different thicknesses and thermal conductivities (54). The following analysis will provide the through thickness temperature distribution far away from the corners or sides of the walls. Thus, the height and through the page length of the wall can be assumed to be infinite. This provides significant simplification to the example by creating a dimensional problem. The simplified model has been presented in Figure 129.

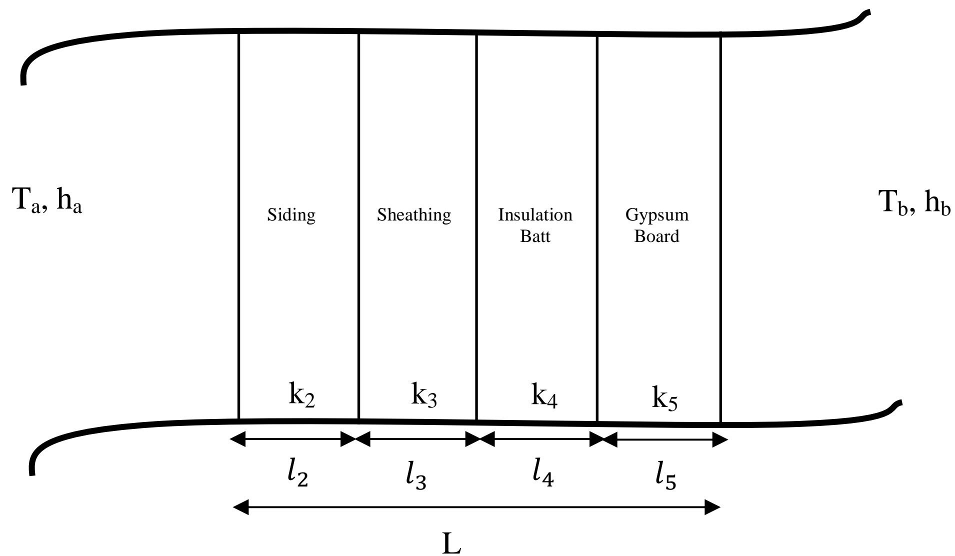

Figure 129: Simplified one dimensional residential wall

A.1.1.2Mesh Geometry

The next step in the Preprocessor phase is to mesh the geometry. This requires the geometries to be discretized into elements of dimension equal (in general) to that of the geometry. The residential wall is one dimensional, and as such, the elements are also one dimensional.

The edges of each element contain at least two nodes. Each node contains one to several degrees of freedom, which are unique to the problem at hand. The degree of freedom for the wall is temperature and the elements only contain two nodes.

Meshing the wall produces Figure 130 where the black dots are the nodes and the numbers represent the number of each element.

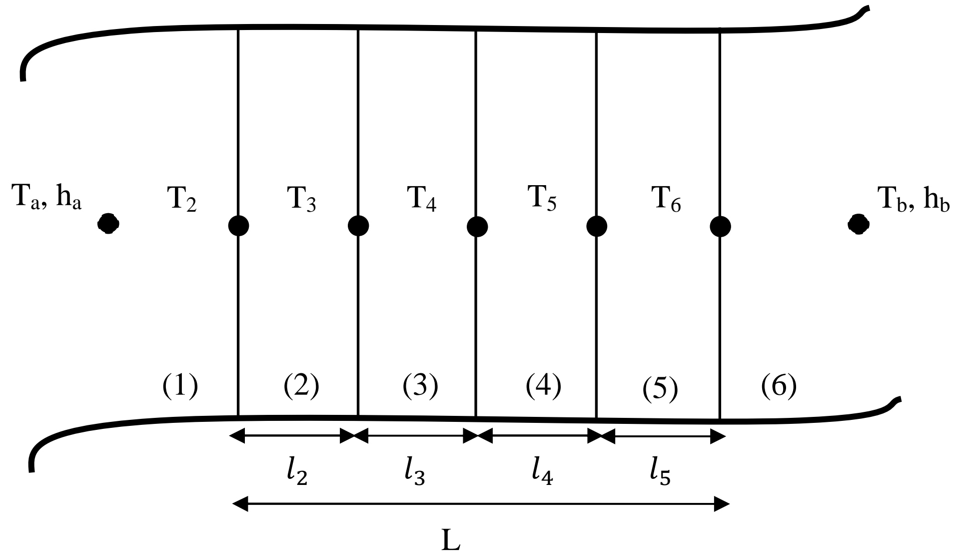

Figure 130: Mesh of Residential Wall example

There is only one element per wall layer because it is known that the temperature distribution is linear (equation **2-7**). Moreover, the two nodes in each element create a linear temperature distribution which approximates the true temperature distribution. Thus, more elements per residential wall layer would only increase computing time.

A.1.1.3Find Underling Phenomena

Assuming the correct solution requires understanding the underlying phenomena associated with the problem at hand. For inside the wall (elements 2 through 4), it has been well known that the temperature distribution is described by conduction. The Fourier Law (equation **2-7**) describes conduction and the equation has been displayed below for convenience as equation **A- 1**.

$$Q_{Fourier} = A_C q''_{Fourier} = -kA_C \frac{\partial T}{\partial x} = kA_C \frac{T_2 - T_1}{l} = kA_C \frac{\Delta T}{l} \qquad \textbf{A- 1}$$

The sides of wall (element 1 and 6) contain convective boundary conditions. Convection is governed by Newton's law of cooling and this equation has been displayed in equation **A- 2** (9).

$$Q_{Convection} = A_C q''_{Convection} = hA_C(T_{Surface} - T_{Ambient}) \quad \textbf{A- 2}$$

$where$:

$$h = Heat\ Transfer\ Coefficient\ \left(\frac{W}{mk}\right)$$

$$T_{Surface} = Temperature\ of\ Surface\ with\ convective\ boundary (K)$$

$$T_{Ambient} = Temperature\ of\ Ambient\ Fluids\ of\ \ (K)$$

A.1.1.4Element Conductance Matrix

The FEM analysis requires applying the physics to a generic element of the same type as chosen by the previous sub-step (Meshing the geometry). For inside the wall (elements 2 through 4), the elements contain two nodes, each with one degree of freedom (temperature). Applying equation **A- 1** to the generic element on the inside of the wall (elements 2 through 4) creates **Figure 131**.

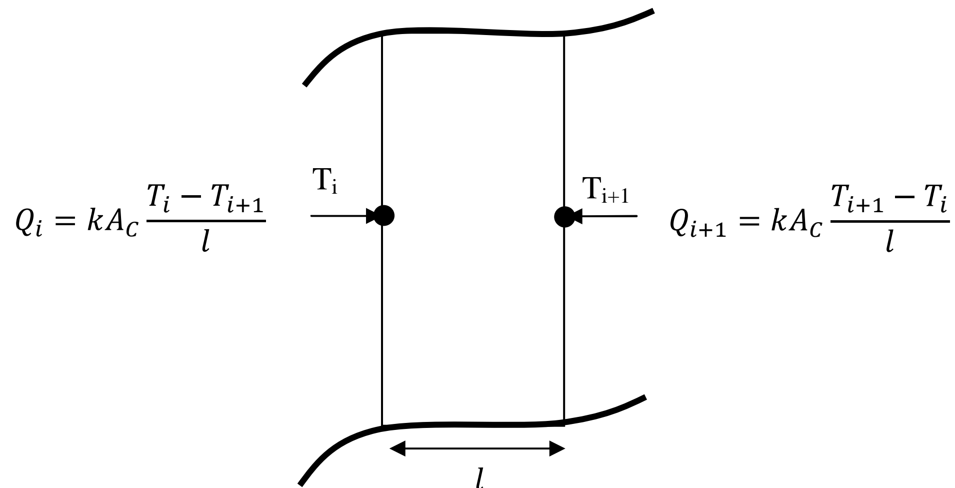

Figure 131: Generic Conduction Element with assumption (54)

It is important to note that for the **Figure 131**, energy is conserved, that is the sum of the heat flow ($Q_i + Q_{i+1}$) equals zero (54). The heat flow equations can be grouped into matrix form as shown below. (54)

$$\begin{Bmatrix} Q_i \\ Q_{i+1} \end{Bmatrix} = \frac{kA_c}{l} \begin{bmatrix} 1 & -1 \\ -1 & 1 \end{bmatrix} \begin{Bmatrix} T_i \\ T_{i+1} \end{Bmatrix} \; for\ nodes\ i = 2,3,4$$

The above equation demonstrates the application of the physics onto the generic conductive conductance element and demonstrates the only assumption in the entire FEM analysis. Thus understanding the phenomena as well as choosing the correct element for the given problem is of utmost importance.

The generic element is often in terms of the thermal transmittance coefficient "U." The equation for the U-factor has been displayed below.

$$U = \frac{k}{l}$$

This reduces the generic conductive conductance element to equation **A- 3** (54).

$$\begin{Bmatrix} Q_i \\ Q_{i+1} \end{Bmatrix} = UA_c \begin{bmatrix} 1 & -1 \\ -1 & 1 \end{bmatrix} \begin{Bmatrix} T_i \\ T_{i+1} \end{Bmatrix} \; for\ nodes\ i = 2,3,4 \qquad \textbf{A- 3}$$

For the convective elements, a generic element must also be created. In the same spirit that was done to create equation **A- 3, e**quation **A- 2** (Newton's law of cooling) must be used to generate the generic convection conductance element displayed below in equation **A- 4** (54).

$$\begin{Bmatrix} Q_i \\ Q_{i+1} \end{Bmatrix} = hA_c \begin{bmatrix} 1 & -1 \\ -1 & 1 \end{bmatrix} \begin{Bmatrix} T_i \\ T_{i+1} \end{Bmatrix} \quad for\ nodes\ i = 1\ \&\ 5 \qquad \textbf{A- 4}$$

The above equality assumes that both sides of the element contain convective boundaries, which according to the example, is untrue. However, the application of the boundary condition (T_a and T_b) will eliminate the unneeded boundary condition and represent the

example problem statement (54). The U-factor can also be used to simplify the generic convective conductance element (54).

$U = h$

This reduces the generic convective conductance element to equation **A- 5** (54**).**

$$\begin{Bmatrix} Q_i \\ Q_{i+1} \end{Bmatrix} = UA_c \begin{bmatrix} 1 & -1 \\ -1 & 1 \end{bmatrix} \begin{Bmatrix} T_i \\ T_{i+1} \end{Bmatrix} \; for\ nodes\ i = 1\ \&\ 5 \qquad \textbf{A- 5}$$

Equation **Error! Reference source not found.Error! Reference source not found.** and equation **Error! Reference source not found.Error! Reference source not found.** both contain the same center matrix that is called the "Element Conductance Matrix" and has been placed below in equation **A- 6** (54).

$$[\mathbf{K}]^e = UA_c \begin{bmatrix} 1 & -1 \\ -1 & 1 \end{bmatrix} \text{t} \qquad \textbf{A- 6}$$

A .1.2 **General Conductance Matrix**

Equation **A- 6** must be applied to each element and assembled into a global conductance matrix. This process starts by initiating the global conductance matrix which is an N X N matrix where N equals the number of nodes. This general matrix has been presented below multiplied by the temperature matrix.

$$[\mathbf{K}]^{0G}[\mathbf{T}] = UA_c \begin{bmatrix} 0 & 0 & 0 & 0 & 0 & 0 & 0 \\ 0 & 0 & 0 & 0 & 0 & 0 & 0 \\ 0 & 0 & 0 & 0 & 0 & 0 & 0 \\ 0 & 0 & 0 & 0 & 0 & 0 & 0 \\ 0 & 0 & 0 & 0 & 0 & 0 & 0 \\ 0 & 0 & 0 & 0 & 0 & 0 & 0 \\ 0 & 0 & 0 & 0 & 0 & 0 & 0 \end{bmatrix} \begin{bmatrix} T_1 \\ T_2 \\ T_3 \\ T_4 \\ T_5 \\ T_6 \\ T_7 \end{bmatrix}$$

The below conductance matrix is for element 1.

$$[\mathbf{K}]^{1G} = U_1 A_c \begin{bmatrix} 1 & -1 & 0 & 0 & 0 & 0 & 0 \\ -1 & 1 & 0 & 0 & 0 & 0 & 0 \\ 0 & 0 & 0 & 0 & 0 & 0 & 0 \\ 0 & 0 & 0 & 0 & 0 & 0 & 0 \\ 0 & 0 & 0 & 0 & 0 & 0 & 0 \\ 0 & 0 & 0 & 0 & 0 & 0 & 0 \\ 0 & 0 & 0 & 0 & 0 & 0 & 0 \end{bmatrix}$$

The below conductance matrix is for element 2.

$$[\mathbf{K}]^{2G} = U_2 A_c \begin{bmatrix} 0 & 0 & 0 & 0 & 0 & 0 & 0 \\ 0 & 1 & -1 & 0 & 0 & 0 & 0 \\ 0 & -1 & 1 & 0 & 0 & 0 & 0 \\ 0 & 0 & 0 & 0 & 0 & 0 & 0 \\ 0 & 0 & 0 & 0 & 0 & 0 & 0 \\ 0 & 0 & 0 & 0 & 0 & 0 & 0 \\ 0 & 0 & 0 & 0 & 0 & 0 & 0 \end{bmatrix}$$

The above pattern follows for each element. The elements are then assembled into the global matrix by summing the above matrices (54). This process has been placed in equation **A- 7** (54).

$$[\mathbf{K}]^{G} = [\mathbf{K}]^{1G} + [\mathbf{K}]^{2G} + [\mathbf{K}]^{3G} + [\mathbf{K}]^{4G} + [\mathbf{K}]^{5G} \qquad \textbf{A- 7}$$

The above addition was completed on the global conductance matrix and shown below as equation **A- 8** (54).

$$[\mathbf{K}]^{G} = A_C \begin{bmatrix} U_1 & -U_1 & 0 & 0 & 0 & 0 & 0 \\ -U_1 & U_1 + U_2 & -U_2 & 0 & 0 & 0 & 0 \\ 0 & -U_2 & U_2 + U_3 & -U_3 & 0 & 0 & 0 \\ 0 & 0 & -U_3 & U_3 + U_4 & -U_4 & 0 & 0 \\ 0 & 0 & 0 & -U_4 & U_4 + U_5 & -U_5 & 0 \\ 0 & 0 & 0 & 0 & -U_5 & U_5 + U_6 & -U_6 \\ 0 & 0 & 0 & 0 & 0 & -U_6 & U_6 \end{bmatrix} \qquad \textbf{A- 8}$$

A .1.3 **Solution Phase**

The solution phase of a FEM analysis is the second main phase and contains two sub steps. They are listed below

1. Apply boundary Conditions
2. Solve

The above list has been pictorially represented in **Figure 132**.

Figure 132: Solution Phase Sub Steps

A.1.3.1Apply Boundary Conditions

The application of the boundary conditions requires recalling the general conductance matrix (equation **A- 8**). It has been displayed below.

$$[\mathbf{K}]^G = A_C \begin{bmatrix} U_1 & -U_1 & 0 & 0 & 0 & 0 & 0 \\ -U_1 & U_1+U_2 & -U_2 & 0 & 0 & 0 & 0 \\ 0 & -U_2 & U_2+U_3 & -U_3 & 0 & 0 & 0 \\ 0 & 0 & -U_3 & U_3+U_4 & -U_4 & 0 & 0 \\ 0 & 0 & 0 & -U_4 & U_4+U_5 & -U_5 & 0 \\ 0 & 0 & 0 & 0 & -U_5 & U_5+U_6 & -U_6 \\ 0 & 0 & 0 & 0 & 0 & -U_6 & U_6 \end{bmatrix}$$

The above matrix assumes that the convective element contains two convective boundaries. However, the example problem statement, demonstrates that there are constant temperatures at the exterior nodes of the mesh. Thus, the convective boundaries that do not match the problem statement must be eliminated. This process was done below, and it can be seen that T_1 equals T_a and T_7 equals T_b which matches the problem statement (54).

$$A_C\begin{bmatrix} 1/A_C & 0 & 0 & 0 & 0 & 0 & 0 \\ -U_1 & U_1+U_2 & -U_2 & 0 & 0 & 0 & 0 \\ 0 & -U_2 & U_2+U_3 & -U_3 & 0 & 0 & 0 \\ 0 & 0 & -U_3 & U_3+U_4 & -U_4 & 0 & 0 \\ 0 & 0 & 0 & -U_4 & U_4+U_5 & -U_5 & 0 \\ 0 & 0 & 0 & 0 & -U_5 & U_5+U_6 & -U_6 \\ 0 & 0 & 0 & 0 & 0 & 0 & 1/A_C \end{bmatrix}\begin{Bmatrix} T_1 \\ T_2 \\ T_3 \\ T_4 \\ T_5 \\ T_6 \\ T_7 \end{Bmatrix} = \begin{Bmatrix} T_a \\ 0 \\ 0 \\ 0 \\ 0 \\ 0 \\ T_b \end{Bmatrix}$$

After the top row is deleted and the highlighted portions of the above equality have been moved to the right side, the bottom equality is produced (54).

$$A_C\begin{bmatrix} U_1+U_2 & -U_2 & 0 & 0 & 0 \\ -U_2 & U_2+U_3 & -U_3 & 0 & 0 \\ 0 & -U_3 & U_3+U_4 & -U_4 & 0 \\ 0 & 0 & -U_4 & U_4+U_5 & -U_5 \\ 0 & 0 & 0 & -U_5 & U_5+U_6 \end{bmatrix}\begin{Bmatrix} T_2 \\ T_3 \\ T_4 \\ T_5 \\ T_6 \end{Bmatrix} = \begin{Bmatrix} U_1 A_C T_1 \\ 0 \\ 0 \\ 0 \\ U_6 A_C T_7 \end{Bmatrix}$$

This produces the general equality in which all steady state heat transfer problems are solved. The general equation says that the general conductance matrix times the temperature matrix equals the heat flow matrix. The general equality or finite element formulation has been displayed in equation **A- 9**.

$$[\mathbf{K}]^G[\mathbf{T}] = [\mathbf{Q}] \qquad \textbf{A- 9}$$

A.1.3.2Solve

All FEM steady state heat transfer problems are reduced to equation **A- 9** and then solved for their DOF (temperature) (54). For the residential wall example, this can be done easily by inverting the general conductance matrix as shown equation **A- 10**.

$$[\mathbf{T}] = [\mathbf{K}]^{G^{-1}}[\mathbf{Q}] \qquad \textbf{A- 10}$$

A.1.3.3Post Processor phase

The last phase entails obtaining any other relevant information. Of course this depends on the problem at hand, but for the residential wall example, finding the heat transfer through an element (equation **A- 11**) or through the entire structure (equation **A- 12**) is also of importance (54).

$Q = UA(T_{i+1} - T_i) for\ nodes\ i = 1\ through\ 6$ **A- 11**

$Q = U_{Total}A(T_1 - T_7)$ **A- 12**

It is important to note that since the example is steady state with no heat generation, the above two equalities should equal each other due to conservation of energy (54).

A.1.3.4FEM Phases Summary

The vehicle for the explanation is an example of a layered wall with convective boundary conditions from Moaveni's book titled "Finite Element Analysis; Theory and Application with ANSYS". The three phases, Preprocessor, Solution and Post Processing phase are discussed. This includs building the geometry, meshing the geometry, assuming a solution, solving, and obtaining any other relevant information.

Appendix B The Thermal-Electrical Model

The thermal-electrical model allows the thermoelectric cooler (TEC) to be studied using FEM analysis. This is accomplished by coupling thermal and electrical effects determined by heat diffusion and the continuity of electric charge respectively.

The underlying phenomenon that governs both heat diffusion and the continuity of electric charge are presented and discussed. These two equations are then coupled together using Joule heating and the Peltier effect to have the capacity to correctly analyze a thermoelectric device. The Galerkin FEM procedure is then used to develop the thermal-electric finite element equation. This procedure includes applying a temperature and electrical potential assumption throughout the elements, which creates the only assumption used in the FEM analysis.

B.1 Underlying Phenomenon

The underlying phenomenon of thermoelectric coolers (TEC) relies on the coupling of two main effects. This model consists of the thermal and electric effect. The thermal effect is determined by the heat diffusion equation (9). The electric effect is determined by the continuity of electric charge (55).

B .1.1 **Heat Diffusion**

The heat diffusion derivation is out of the scope of this work, but can be derived from a differential control volume in which the energies entering, leaving, being generated, and stored are placed in the conservation of energy equality (9). The resulting equation has been displayed below in equation **B- 1** (9).

$$\frac{\partial}{\partial x}\left(k_x \frac{\partial T}{\partial x}\right) + \frac{\partial}{\partial y}\left(k_y \frac{\partial T}{\partial y}\right) + \frac{\partial}{\partial z}\left(k_z \frac{\partial T}{\partial z}\right) + q''' = \rho C_p \frac{\partial T}{\partial t} \qquad \textbf{B- 1}$$

$where$:

$k_i = thermal\ conductivity\ in\ i\ dirrection\ \left(\frac{W}{mk}\right)$

$q''' = volumetric\ heat\ generation\ \left(\frac{W}{m^3}\right)$

$\rho = density\ \left(\frac{kg}{m^3}\right)$

$C_p = specific\ heat\ capacity\ at\ constant\ pressure\ \left(\frac{J}{kgK}\right)$

The terms on the left of equation B- 1 account for heat diffusion through the medium. The last term on the left accounts for heat generation and the term on the right accounts for the amount of energy stored in the system over a period of time. It is customary to shorthand equation **B- 2** by using the del operator shown in equation **B- 3** (56).

$$\nabla[\mathbf{a}] = \frac{\partial}{\partial x} a_x + \frac{\partial}{\partial y} a_y + \frac{\partial}{\partial z} a_z \qquad \textbf{B- 2}$$

Using the dell operator (equation **B- 2**) on the heat diffusion equation (equation **B- 1)** results in equation **B- 3.**

$$\nabla \cdot ([\mathbf{K}]\nabla[\mathbf{T}]) + q''' = \rho C_p \frac{\partial T}{\partial t} \qquad \textbf{B- 3}$$

$where$:

$[\mathbf{K}] = thermal\ conductivity\ \left(\frac{W}{mk}\right) = \begin{bmatrix} k_x & 0 & 0 \\ 0 & k_y & 0 \\ 0 & 0 & k_z \end{bmatrix}$

$[\mathbf{T}] = Tempearture\ (K)$

B .1.2 **Continuity of Electric Charge**

The electrical effect is dependent of the continuity of electric charge. The continuity of electric charge has been displayed in equation **B- 4** (55)**,** (50).

$$\nabla \cdot \left([\mathbf{J}] \cdot \frac{\partial \mathbf{D}}{\partial t}\right) = 0 \qquad \textbf{B- 4}$$

$where$:

$[\mathbf{J}] = electric\ current\ density\ vector\ \left(\frac{A}{m^2}\right)$

$\mathbf{D} = electric\ flux\ density\ vector \left(\frac{C}{m^2}\right)$

The constitutive equations for the electric current density ([**J**]) and electric flux density vector (**D**) are useful to the presented work and have been displayed in equation **B- 5** (55) (50).

$$[\mathbf{J}] = [\sigma][\mathbf{E}]$$
$$[\mathbf{D}] = [\boldsymbol{\epsilon}][\mathbf{E}] \qquad \textbf{B- 5}$$

$where$:

$[\sigma] = electric\ conductivity\ matrix\ \left(\frac{A}{m^2}\right) = \begin{bmatrix} \sigma_x & 0 & 0 \\ 0 & \sigma_y & 0 \\ 0 & 0 & \sigma_z \end{bmatrix}$

$[\boldsymbol{v}] = velocity\ vector\ \left(\frac{m}{s^2}\right) = \begin{bmatrix} v_x \\ v_y \\ v_z \end{bmatrix}$

$[\boldsymbol{\epsilon}] = electrical\ permittivity\ matrix\ \left(\frac{F}{m}\right) = \begin{bmatrix} \epsilon_x & 0 & 0 \\ 0 & \epsilon_y & 0 \\ 0 & 0 & \epsilon_z \end{bmatrix}$

$[\boldsymbol{E}] = electric\ field\ intencity\ vector\ \left(\frac{V}{m}\right)$

In the absence of a time varying magnetic field, the electric field intensity vector ([**E**]) becomes equation **B- 6** (55).

$$[\boldsymbol{E}] = -\nabla\varphi \qquad \textbf{B- 6}$$

$where$:

$\varphi = electric\ scalar\ potential\ (V)$

B.2 Coupling of Thermal and Electric Effects

The two effects discussed above are the thermal (equation **B- 3**) and the electric effect (equation **B- 4**). These two equations have been displayed below for convenience.

$$\rho C_p \frac{\partial T}{\partial t} - \nabla \cdot ([\mathbf{K}]\nabla[\mathbf{T}]) = q'''$$

$$\nabla \cdot \left([\mathbf{J}] \cdot \frac{\partial \mathbf{D}}{\partial t}\right) = 0$$

The first equation describes heat diffusion and the second equation describes the continuity of electric charge. The displacement current term in the second equation ($\frac{\partial \mathbf{D}}{\partial t}$) accounts for fast transient responses and has been included for completeness (55).

The above equations account for each effect independently, and their coupling mandates that the diffusion equation be in a simpler form. The heat diffusion equation can be simplified using the below equality.

$$\mathbf{q} = -([\mathbf{K}]\nabla \cdot [\mathbf{T}])$$

This produces the simplified diffusion equation demonstrated in equation **B- 7**

$$\rho C_p \frac{\partial T}{\partial t} + \nabla \cdot \mathbf{q} = q''' \qquad \textbf{B- 7}$$

As described above for the un-simplified heat diffusion equation, equation **B- 5** does not directly take into account the joule heating associated with running current through a conductor or the Peltier heating and cooling effects. These coupling effects can be accounted for by providing a new heat flow equality demonstrated in equation **B- 8** (55), (50).

$$\mathbf{q} = \underbrace{\mathrm{T}[\alpha][\mathbf{J}]}_{\text{Joule Heating, Peltier Heating and Cooling}} - \underbrace{([\mathbf{K}]\nabla[\mathbf{T}])}_{\text{Heat Diffusion}} \qquad \textbf{B- 8}$$

where:

$\mathrm{T}[\alpha] = \textit{peltier coefficient matrix}\ (V)$

$$[\alpha] = seebeck\ coefficient\ matrix\ \left(\frac{V}{K}\right) = \begin{bmatrix} \alpha_x & 0 & 0 \\ 0 & \alpha_y & 0 \\ 0 & 0 & \alpha_z \end{bmatrix} = \begin{bmatrix} S_x & 0 & 0 \\ 0 & S_y & 0 \\ 0 & 0 & S_z \end{bmatrix}$$

In equation **Error! Reference source not found.Error! Reference source not found.**, there are two terms on the right hand side that are of important to discuss. The first term accounts for heat generation (Joule heating) as well as Peltier heating and cooling (Peltier effects). The second term accounts for heat diffusion.

The continuity of electric charge (equation **B- 4**) needs to be coupled to the heat diffusion equation through Joule heating and the Peltier Effects. This is done by updating the electric current density vector (equation **B- 5**) to contain the electric power to work against the Seebeck field (55) as shown in equation **B- 9**.

$$[\mathbf{J}] = [\boldsymbol{\sigma}]([\mathbf{E}\,] - [\alpha]\nabla \cdot [\mathbf{T}]) \qquad \textbf{B- 9}$$

The electric power to work against the Seebeck field is the second term in the above equation.

Equations **B- 6**, **B- 7**, **B- 8**, and **B- 9** are now placed into equations **B- 4** and **B- 6** to produce the coupled equations of thermoelectricity (55). These equations have been displayed in equation **B- 10** and **B- 11** (55)**,** (50).

$$\rho C_p \frac{\partial T}{\partial t} + \nabla \cdot (\mathrm{T}[\alpha][\mathbf{J}]) - \nabla \cdot ([\mathbf{K}] \cdot \nabla[\mathbf{T}]) = q''' \qquad \textbf{B- 10}$$

$$\nabla \cdot \left([\boldsymbol{\epsilon}] \cdot \nabla \frac{\partial \varphi}{\partial t}\right) + \nabla \cdot ([\sigma] \cdot [\alpha]\nabla \cdot [\mathbf{T}]) + \nabla \cdot ([\sigma] \cdot \nabla\varphi) = 0 \qquad \textbf{B- 11}$$

Similar to the thermal example given in **Appendix** A **FEM Phases** were the Fourier law and Newton’s cooling law were the phenomena for that analysis, the above equations constitute the thermal-electrical phenomenon that FEM places on the analysis to correctly analyze thermoelectric devices.

B .2.1 **Finite Element Formulation**

Finding the finite element formulation was accomplished using the Galerkin FEM procedure which includes the following steps (55), (57):

1. Approximating the temperature and scalar potential over a finite element
2. Writing the system of equations (equation **B- 11** and **B- 12**) in a weak projective form. This means that the two effects must be iteratively run at least two times to reach convergence (55).
3. Integrating the projective equations by parts
4. Taking into account the Neumann boundary conditions

The first step creates the following element equations for temperature and scalar electrical potentials (55).

$\mathrm{T} = \boldsymbol{N} \cdot \boldsymbol{T_e}$

$\varphi = \boldsymbol{N} \cdot \boldsymbol{\varphi_e}$

$where$:

$\mathrm{T} = Temperature\ distribution\ of\ thermoelectric\ (K)$

$\varphi = vector\ of\ nodal\ electrical\ potentials$

$\boldsymbol{N} = vector\ of\ element\ shape\ function$

$\boldsymbol{T_e} = vector\ of\ nodal\ temperatures$s

As discussed in the simple thermal example in **A**.1.1.4 **Element Conductance Matrix,** the above equations constitute for the only assumption for the entire FEM analysis.

A .1 The other steps in the Galerkin FEM procedure are out of the scope of this work and produce the following finite element equation, equation **B- 12** (55)**,** (50). This equation is then extended to include the entire geometry (analogous to **A** .1.2 **General Conductance Matrix**) and then solved similarly to the discussion in **A** .1.3 **Solution Phase**.

$$\begin{bmatrix} C^{TT} & 0 \\ 0 & C^{\varphi\varphi} \end{bmatrix} \begin{bmatrix} \dot{T}_e \\ \dot{\varphi}_e \end{bmatrix} + \begin{bmatrix} K^{TT} & 0 \\ K^{\varphi T} & K^{\varphi\varphi} \end{bmatrix} \begin{bmatrix} T_e \\ \varphi_e \end{bmatrix} = \begin{bmatrix} Q + Q^p + Q^e \\ I \end{bmatrix} \quad \textbf{B- 12}$$

$where$:

$$K^{TT} = thermal\ stiffness\ matrix = \int_V \boldsymbol{N}^T[\mathbf{K}]\boldsymbol{N}dV$$

$$K^{\varphi\varphi} = electric\ stiffness\ matrix = \int_V \boldsymbol{N}^T[\sigma]\boldsymbol{N}dV$$

$$K^{\varphi T} = seebeck\ stiffness\ matrix = \int_V \boldsymbol{N}^T[\alpha][\sigma]\boldsymbol{N}dV$$

$$C^{TT} = thermal\ dampining\ matrix = \rho\int_V C\boldsymbol{N}^T\boldsymbol{N}dV$$

$$C^{\varphi\varphi} = dielectric\ dampining\ matrix = \int_V \boldsymbol{N}^T[\boldsymbol{\epsilon}]\boldsymbol{N}dV$$

$$Q = vector\ of\ combined\ heat\ generation\ loads$$

$$Q^{\mathrm{p}} = Peltier\ heat\ load\ vector = \int_V \boldsymbol{N}^T\mathrm{T}[\alpha][\mathbf{J}]dV$$

$$Q^{\mathrm{e}} = electric\ power\ load\ vector = \int_V \boldsymbol{NE}\cdot[\mathbf{J}]dV$$

$$[\mathbf{K}] = thermal\ conductivity\ matrix\ \left(\frac{W}{mk}\right) = \begin{bmatrix} k_x & 0 & 0 \\ 0 & k_y & 0 \\ 0 & 0 & k_z \end{bmatrix}$$

$$[\sigma] = electric\ conductivity\ matrix\ \left(\frac{A}{m^2}\right) = \begin{bmatrix} \sigma_x & 0 & 0 \\ 0 & \sigma_y & 0 \\ 0 & 0 & \sigma_z \end{bmatrix}$$

$$[\alpha] = seebeck\ coefficient\ matrix\ \left(\frac{V}{K}\right) = \begin{bmatrix} \alpha_x & 0 & 0 \\ 0 & \alpha_y & 0 \\ 0 & 0 & \alpha_z \end{bmatrix} = \begin{bmatrix} \mathrm{S}_x & 0 & 0 \\ 0 & \mathrm{S}_y & 0 \\ 0 & 0 & \mathrm{S}_z \end{bmatrix}$$

$$\mathrm{T}[\alpha] = peltier\ coefficient\ matrix\ (V)$$

$$[\boldsymbol{\epsilon}] = electrical\ permittivity\ matrix\ \left(\frac{F}{m}\right) = \begin{bmatrix} \epsilon_x & 0 & 0 \\ 0 & \epsilon_y & 0 \\ 0 & 0 & \epsilon_z \end{bmatrix}$$

It is important to note that equation **B- 12** allows for thermoelectric devices in general to be analyzed.

B.3 Summary of Thermal-Electrical Model

The thermal-electrical model accounts for both thermal and electrical effects by coupling them together with Joule heating and the Peltier effect. Thus, it can be readily used for thermoelectric devices. The thermal and electrical effects are determined by heat

diffusion and the continuity of electric charge respectively. Furthermore, the thermoelectric finite element equation is then simplified and compared to the steady state thermal finite element equation to discuss its similarities and differences.

Appendix C ANSYS 12.0 Thermal and Electrical Validation

Trusting ANSYS to deliver accurate and repeatable results underpins the presented work, and as such requires validation of all presented numerical models. The numerical models validated are the thermal, electrical, and thermal-electrical coupled models.

The numerical solutions are found by using three dimensional elements, negating edge effects, and applying the appropriate properties and boundary conditions. The numerical solutions use three dimensional elements because the presented work relies on three dimensional structures and thus three dimensional elements. The edge effects are negating in order to accurately compare the numerical solutions to the analytical solutions. This is accomplished by simulating the lengths and heights (these are equal to create a square slab) almost two orders of magnitude larger than the width through which the information is recorded. The heights and lengths these are equal to create square slabs. Moreover, the information is recorded through the middle of the slabs to further negate any edge effects.

The nature of numerical simulations requires that a mesh refinement be conducted to distinguish and ultimately eliminate mesh dependent solutions. This is done by running the simulation several times with increasing element counts (increasing mesh density). However, for each model, the numerical solutions for each mesh follow the same discretized curves. This places the distributions on top of the each other. Thus curves containing information as a function of element count and distance through the slabs is contained in Error! Reference source not found.Error! Reference source not found. Error!

Reference source not found.Error! Reference source not found. This section also contains contour plots of the slabs for each model.

The thermal model is validated by using the residential wall example discussed in **Appendix** A **FEM Phases**. The analytical solution is developed from the conservation of energy. The electrical model is validated in a similar fashion using resistors connected in series. Both of these experiments show no difference between analytical and numerical solutions. Thus the numerical (and more specifically ANSYS 12.0) thermal and electrical models are valid. This provides confidence and allows the study of the coupling between the two models.

The coupling between the thermal and electrical model is then verified. The Joule Heating coupling effect is validated through an infinite slab with constant side temperatures and uniform current running through it. As before, this experiment shows no difference between the analytical and numerical solutions. Thus the numerical (and more specifically ANSYS 12.0) thermal-electrical model with Joule Heating coupling is valid.

The Peltier coupling effect in the thermal-electric model is validated using a conventional one leg thermoelectric cooler. Analytical and numerical solutions require the Joule heating coupling effect since both coupling effects occur simultaneously in thermoelectric devices. The analytical solution uses the equations discussed in **Chapter 2:The Thermoelectric Cooler**. The comparison between the analytical and numerical solutions shows little difference. Thus the numerical (and more specifically ANSYS 12.0) thermal-electrical model with Joule Heating and the Peltier effect coupling is valid.

This validation process provides confidence in using the ANSYS 12.0 thermal-electric model to analyze thermoelectric devices.

C.1 Thermal Model Validation

The ANSYS 12.0 thermal model is validated using the residential wall example discussed in **Appendix** A **FEM Phases**. A figure of the one dimensional simplification of the wall has been presented in **Figure 133**.

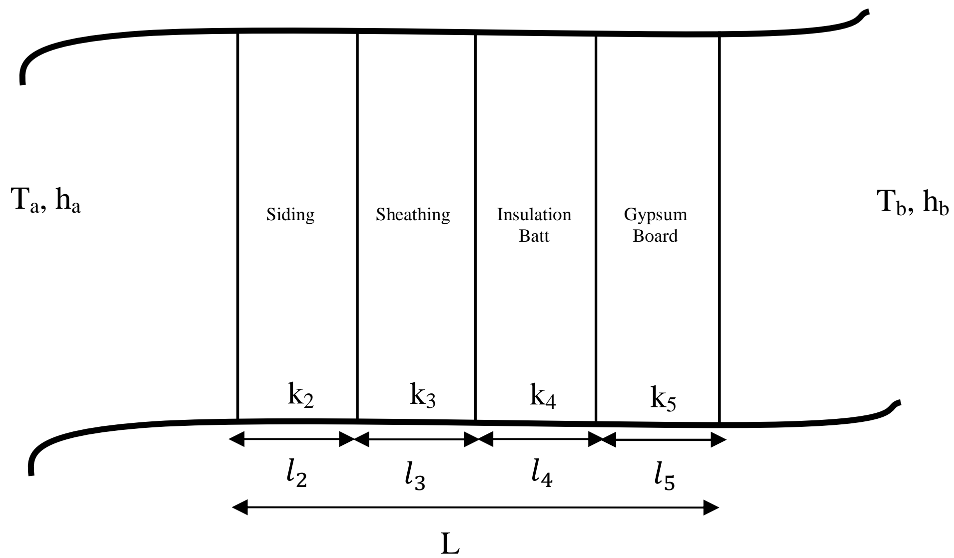

Figure 133: Residential Wall Geometry

The material properties (9), geometry, and boundary conditions of the residential wall are presented in **Table 12**. The cross sectional area of the geometry is 100m^2.

Table 12: Residential Wall Material Properties, Geometry, and Boundaries Conditions

	Thermal Conductivity (W/mK)	**Length (m)**	**Temperature (°C)**	**Heat Transfer Coefficient (W/m^{2}K)**
Siding	0.1	0.025	-	-
Sheathing	0.04	0.0575	-	-
Insulation	0.02	0.15	-	-

Batt				
Gypsum Board	0.17	0.0175	-	-
Ta	-	-	-5	-
Tb	-	-	25	-
h_a	-	-	-	20
h_b	-	-	-	5

The unknowns for this problem are the temperatures at the interfaces of the wall layers as well as the wall temperature distribution. These temperatures are pictorially represented in **Figure 134** with the interface numbers inside of parenthesis.

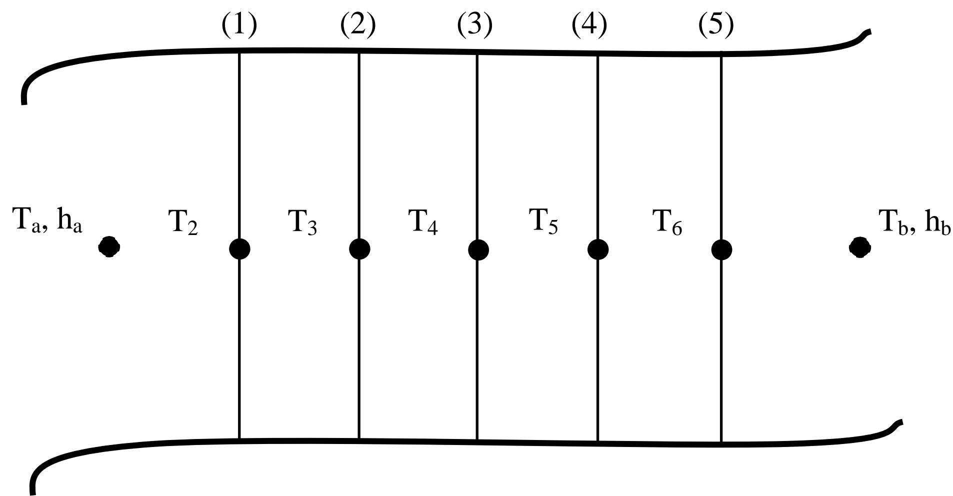

Figure 134: Unknowns for Residential Wall

Analytical and numerical solutions are developed for the residential wall temperature distribution.

C .1.1 Analytical solution

The analytical solution requires using the conservation of energy at each interface. The general conservation of energy equation of a differential control volume has been presented below (9).

$$E_{in} - E_{out} + E_{gen} = E_{stored}$$

$where$:

$E_{in} = energy\ entering\ the\ control\ volume = (W)$

$E_{out} = \ energy\ leaving\ the\ control\ volume = (W)$

$E_{gen} = \ energy\ generated\ in\ the\ control\ volume = (W)$

$$E_{stored} = \ energy\ stored\ in\ the\ control\ volume = (W)$$

The above equality accounts for energies entering, leaving, being generated, and stored in a control volume (9). For the current analysis on the interfaces of the wall, there are no generating energies and the problem is steady state. This allows the last two quantities in the above equation to be dropped creating equation **C- 1**.

$$E_{in} = E_{out} \qquad \textbf{C- 1}$$

The below equality is developed using equation **C- 1** for the first interface with convective boundary heat transfer coefficient h_a and ambient temperature Ta.

$$h_a A_C (T_2 - T_a) = k_1 A_C \frac{T_3 - T_2}{l_1}$$

This is done for each interface and provides five equations with five unknowns which can be easily solved. The solution to this analytical problem has been presented in **C** .1.3 **Analytical and Numerical comparison**.

The analytical solution as currently stated only provides the temperatures at the interfaces, not the entire distribution through the individual layers. However, since no energy is being generated or stored, the temperature distribution within each layer is linear (9). Thus the distribution can be constructed after the interface temperatures are found by connecting the temperatures with straight lines.

C .1.2 **Numerical solution**

A numerical solution of the temperature distribution of the residential is developed in ANSYS 12.0 using the thermal element Solid70 (50). The numerical solution geometry shown in **Figure 135** has a 100m^2 cross sectional area and a 0.25m width.

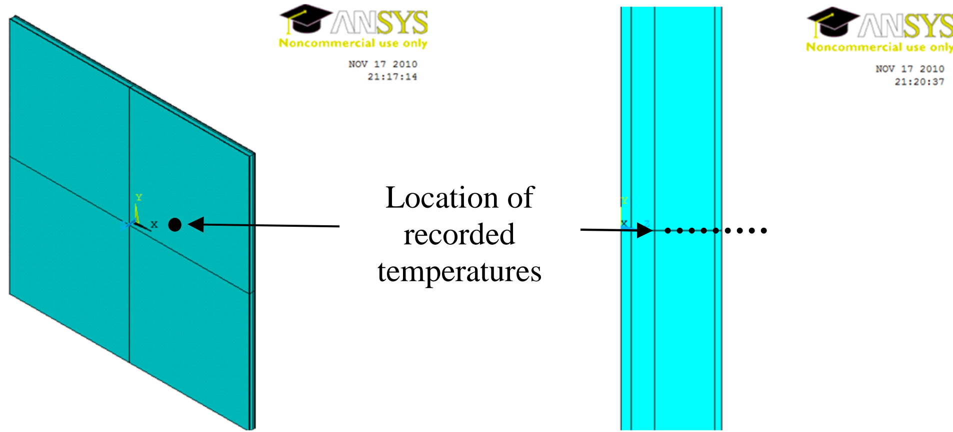

Figure 135: Numerical Geometry of Residential Wall

The nature of numerical simulations requires that a mesh refinement be conducted to distinguish and ultimately eliminate mesh dependent solutions. Thus a graph of the temperatures at the layer interfaces as a function of element count is shown in **Figure 136**.

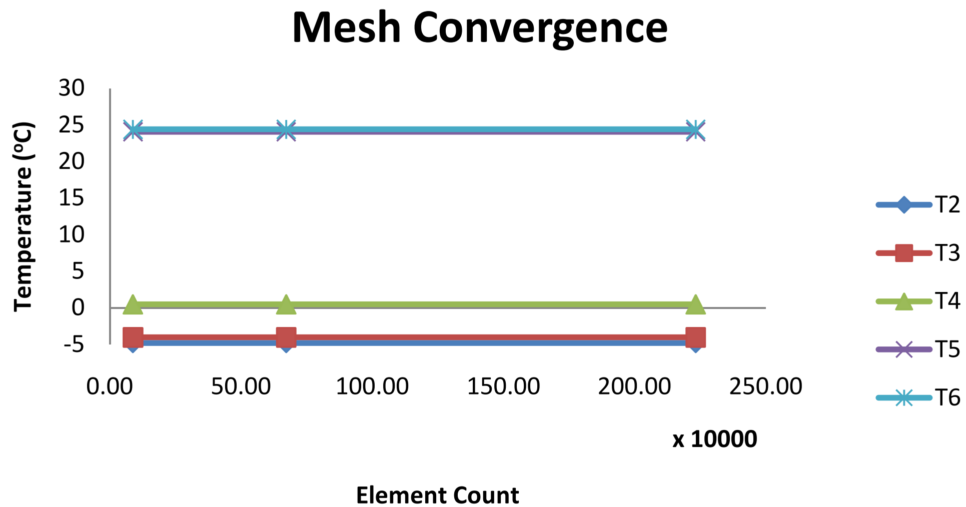

Figure 136: Residential wall, Numerical Solution Mesh Refinement

The curves show no dependence on element count. Screen shots of the entire temperature distribution are shown in **Figure 137**.

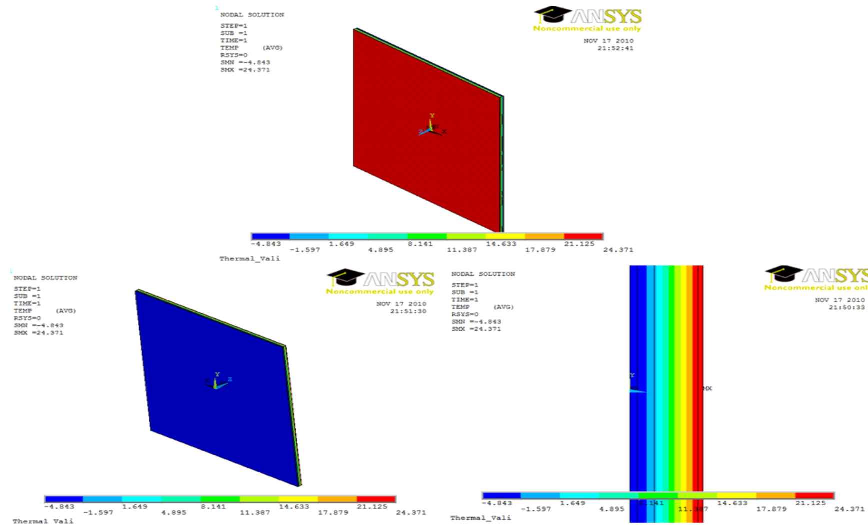

Figure 137: Residential Wall, Numerical Temperature Solution

C .1.3 Analytical and Numerical comparison

Following the prescribed procedures for both the analytical and numerical solution, results were calculated and compared in **Table 16**.

Table 13: Residential Wall, Analytical and Numerical Results Comparison

	Analytical Value	Numerical Value	Difference
T_1 (^{o}C)	-4.843	-4.843	0.00
T_2 (^{o}C)	-4.057	-4.057	0.00
T_3 (^{o}C)	0.464	0.464	0.00
T_4 (^{o}C)	24.05	24.05	0.00
T_5 (^{o}C)	24.37	24.37	0.00

The above table shows no difference between the analytical and numerical temperatures at the interfaces of the layers. The analytical and numerical temperature distributions through the layers are compared in **Figure 138**.

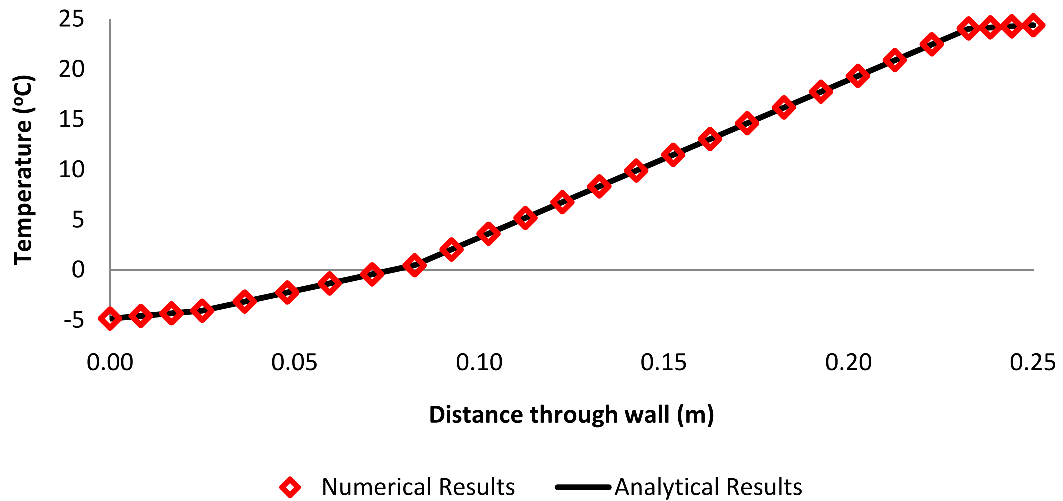

.

Figure 138: Residential Wall, Analytical and Numerical Results Comparison

Table 13 and **Figure 138** demonstrate that the numerical temperatures predict the analytical temperatures exactly and consequently that the FEM (and more specifically ANSYS12.0) numerical thermal model is valid.

C.2 Electrical Model Validation

The ANSYS 12.0 electrical model is validated using a simple circuit containing a voltage source and four resistors connected in series. A figure of this electrical circuit has been displayed in **Figure 139**.

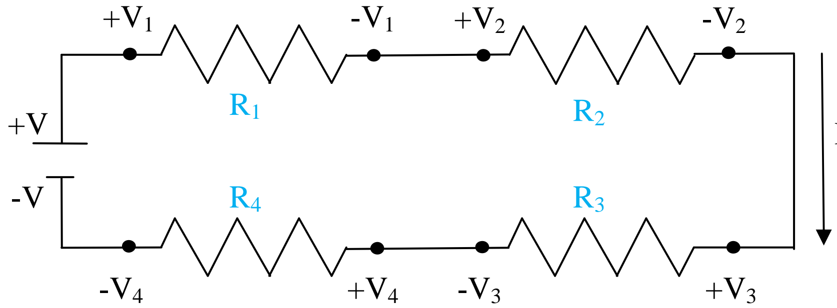

Figure 139: Electrical Model Circuit

The circuit properties have been displayed in **Table 14**.

Table 14: Electrical Circuit Properties

Label	Resistance (Ω)	Voltage (V)
R_1	1	-
R_2	6	-
R_3	1	-
R_4	6	-
V	-	2.5

The unknowns found in the analytical and numerical solutions are displayed in **Table 15**.

Table 15: Electrical Model Circuit, Unknowns

Label
V_1
V_2
V_3
V_4
I

C .2.1 Analytical solution

The analytical solution to the electrical circuit is rooted in Ohm's law. This simple equality relates the voltage, current and resistance and has been displayed in equation **C-2** (58).

$$V = IR_{Electrical} \tag{C- 2}$$

$where$:
$V = voltage\ (V)$
$R_{Electrical} = electrical\ resistance\ (\Omega)$
$I = current\ (A)$

The above equality allows the calculation of current for the whole circuit since the current is shared by all the resistors. However, the total resistance must be found following equation **C- 3** (24).

$$R_{Total} = R_1 + R_2 + R_3 + R_4 \tag{C- 3}$$

Then, the voltage drop across each resistor can be calculated using equation **Error! Reference source not found.Error! Reference source not found.** using the resistor's voltage. This operation however, only produces the voltages at the interfaces. The voltage distribution through each resistor is found using the linear in length relationship demonstrated in equation **C- 4** (58).

$$R = \frac{\rho L}{A_C} \tag{C- 4}$$

$where$:
$\rho = resistivity\ (\Omega m)$
$L = length\ of\ resistor (m)$
$A_C = cross\ sectional\ area\ of\ the\ resistor\ (m^2)$

The voltage distribution through each resistor can be constructed after the interface voltages are found by connecting the voltages with straight lines.

C .2.2 **Numerical solution**

The numerical solution of the voltage distribution of the electrical circuit is developed in ANSYS 12.0 using the thermal-electrical element Solid226 with the thermal

capability and coupling disabled (50). The numerical solution geometry demonstrated in **Figure 140** has a 0.01m^2 square cross sectional area and a 0.004m width.

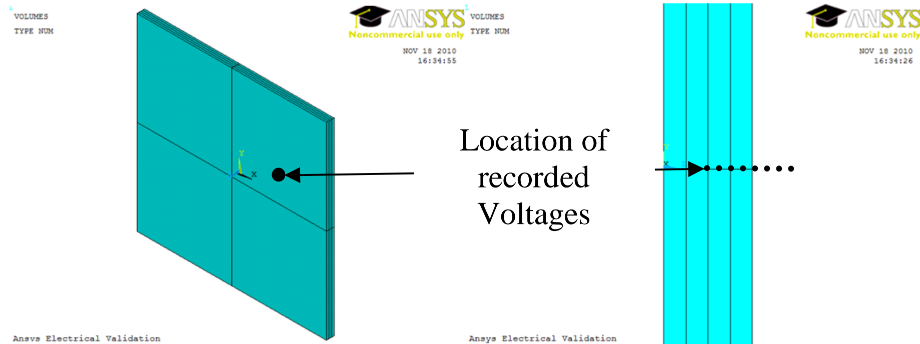

Figure 140: Electrical Circuit, Numerical Geometry

The nature of numerical simulations requires that a mesh refinement be conducted to distinguish and ultimately eliminate mesh dependent solutions. Thus a graph of the voltages at the layer interfaces as a function of element count is shown in as **Figure 141**

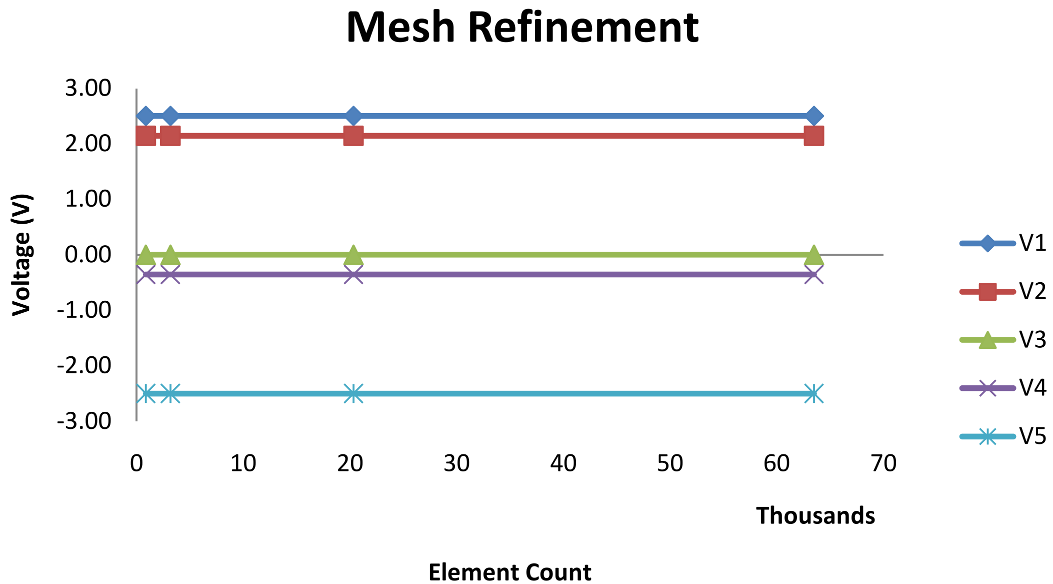

Figure 141: Electrical Circuit, Numerical Solution Mesh Refinement

The curves show no dependence on element count. Screen shots of the entire voltage distribution are shown in **Figure 142**.

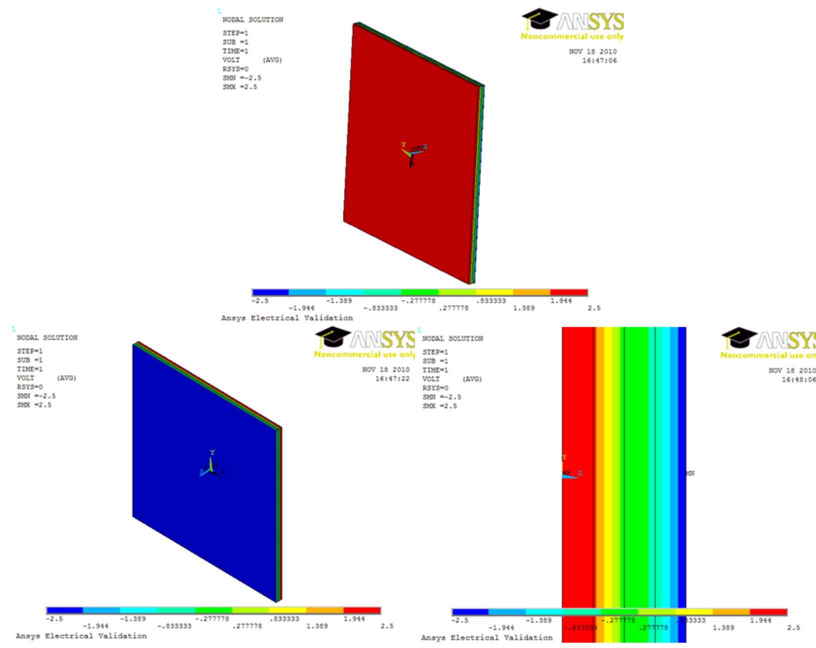

Figure 142: Electrical Circuit, Numerical Voltage Solution

C .2.3 Analytical and Numerical comparison

Following the prescribed procedures for both the analytical and numerical solution, results were calculated and compared in **Table 16**.

Table 16: Electrical Model Circuit, Analytical and Numerical Comparison

	Analytical Value	Numerical Value	Difference
V_1 (V)	0.3571	0.3571	0.00
V_2 (V)	2.1429	2.1429	0.00
V_3 (V)	0.3571	0.3571	0.00
V_4 (V)	2.1429	2.8571	0.00
I (A)	0.3571	0.3571	0.00

As shown above by the “Difference” quantities, the numerical and analytical methods show the same current and voltage drops across each resistor.

The analytical and numerical voltage distributions are compared in **Figure 153**.

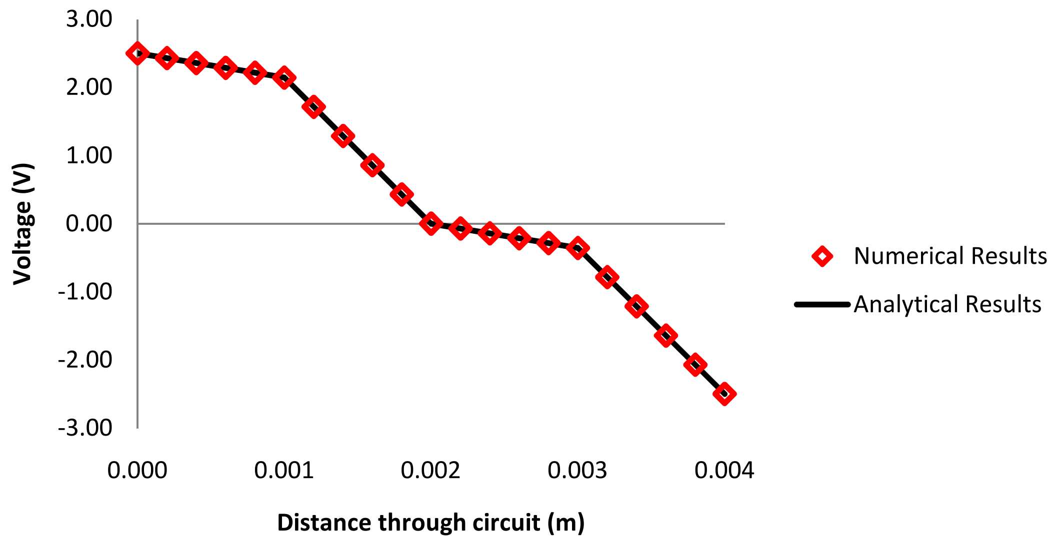

Figure 143 Electrical Circuit, Analytical and Numerical Voltage Distribution comparison

The above figure demonstrates that the through thickness numerical voltages are exactly what the analytical trend predicted. This information, along with **Table 16**, shows the FEM (and more specifically ANSYS12.0) numerical electrical model to be valid.

C.3 Thermal-Electrical Model with Joule Heating

The thermal and electrical models are coupled with the Joule heating effect. The example used to validate the ANSYS 12.0 Joule heating coupling effect is an infinite slab with constant temperature boundary conditions, ground on one side, and current entering the other side. Joule heating arises because of the current. Moreover, the current runs through the slab uniformly, creating a uniform Joule heating effect which translates into a uniform heat generation. The infinite slab example has been shown in **Figure 144**.

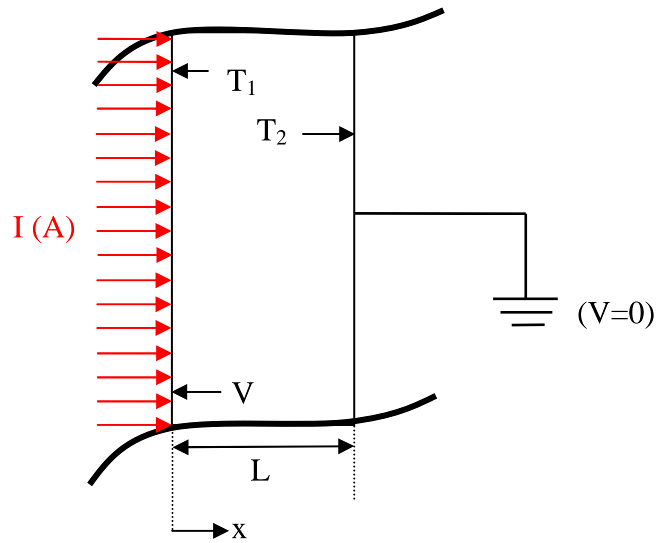

Figure 144: Infinite Slab with Joule Heating

The properties for the above slab example have been shown in **Table 17.**

Table 17: Infinite Slab Example Properties

	Thermal Conductivity (W/mK)	Electrical Resistivity (Ω m)	Length (m)	Temperature (^{o}C)	Current (A)
Slab	60	5e6	0.01	-	-
T_1	-	-	-	30	-
T_2	-	-	-	20	-
I	-	-	-	-	3

The unknowns for this example are the temperature and voltage distribution through the slab as well as the uniform heat generation (Joule heating) of the slab.

C .3.1 **Analytical solution**

The electrical analytical solution is found using the equality that relates resistivity to resistance (equation **C- 4**) and then Ohm's law (equation **C- 2**). This provides the voltage on the left side of **Figure 144**, as well as the voltage distribution throughout the entire slab.

The coupling of interest is the heat generation caused by Joule heating and must be placed into the thermal analytical equation. This is accomplished by dividing equation **2-5** by the volume of the infinite slab as shown by equation **C- 5.**

$$q''' = \frac{I^2 R_{Electrical}}{V_{Slab}} \qquad \textbf{C- 5}$$

The thermal analytical solution is found by simplifying the three dimensional diffusion equation (equation **B- 1**) to a steady state, one dimensional version accounting for uniform heat generation (from equation **C- 5**). This equality has been shown below in equation **C- 6** (9).

$$\frac{d^2T}{dx^2} + \frac{q'''}{k} = 0 \qquad \textbf{C- 6}$$

$where$:

$q''' = uniform\ heat\ generation\ \left(\frac{W}{m^3}\right)$

$k = thermal\ conductivity\ \left(\frac{W}{m^2K}\right)$

The above equation is integrated twice creating two constants of integration. These constants are solved by applying the constant temperature surface boundary conditions according to the displacement convention provided in **Figure 144**. This provides the general equality shown in equation C- 7.

$$T(x) = \frac{q''' Lx}{2k}\left(1 - \frac{x}{L}\right) + T_1\left(1 - \frac{x}{L}\right) + T_2\frac{x}{L} \qquad \textbf{C- 7}$$

$where$:

$L = total\ length\ of\ slab\ (m)$

$x = position\ along\ slab\ (m)$

Equation C- 7 provides a quadratic temperature distribution through the thickness of the slab, but does not find its maximum temperature or maximum temperature position. The maximum temperature position is found by differentiating equation C- 7 and setting that equality to zero (no heat crosses that portion of the slab) as in the below operations. The position of maximum temperature has been shown in equation **C- 8**.

$$0 = \frac{d}{dx}(T(x)) = \frac{d}{dx}\left(\frac{q'''L}{2k}\left(x - \frac{x^2}{L}\right) + T_1\left(1 - \frac{x}{L}\right) + T_2\frac{x}{L}\right)$$

$$0 = \frac{q'''L}{2k}(1 - 2x) + \frac{T_2 - T_1}{L}$$

$$x = \frac{T_2 - T_1}{2L} \cdot \frac{k}{q'''} \qquad \textbf{C- 8}$$

The solution of equation **C- 8** can then be placed into equation C- 7 to find the maximum temperature in the infinite slab.

C .3.2 **Numerical solution**

The numerical solution of the temperature and voltage distribution of the infinite slab is developed in ANSYS 12.0 using the thermal-electrical element Solid226 (50). The numerical solution geometry demonstrated in **Figure 145** has a 1m^2 cross sectional area and a 0.01m width.

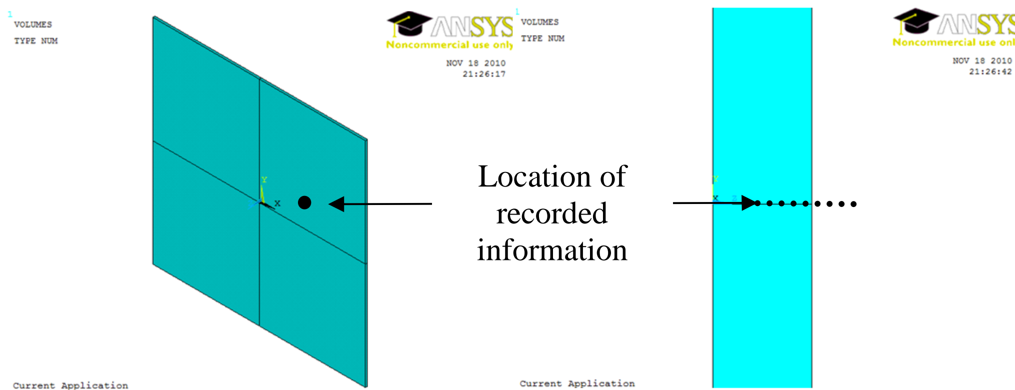

Figure 145: Infinite Slab, Numerical Geometry

The nature of numerical simulations requires that a mesh refinement be conducted to distinguish and ultimately eliminate mesh dependent solutions. Thus graphs of the temperatures and voltages every 0.001 meters through the slab as a function of element count are shown in **Figure 146** and **Figure 147**. The curves show no dependence on element count.

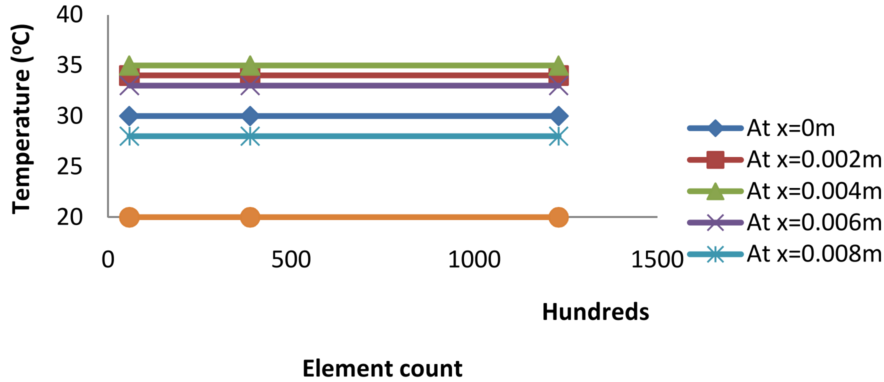

Figure 146: Infinite Slab, Numerical Solution Mesh Convergence for Temperature

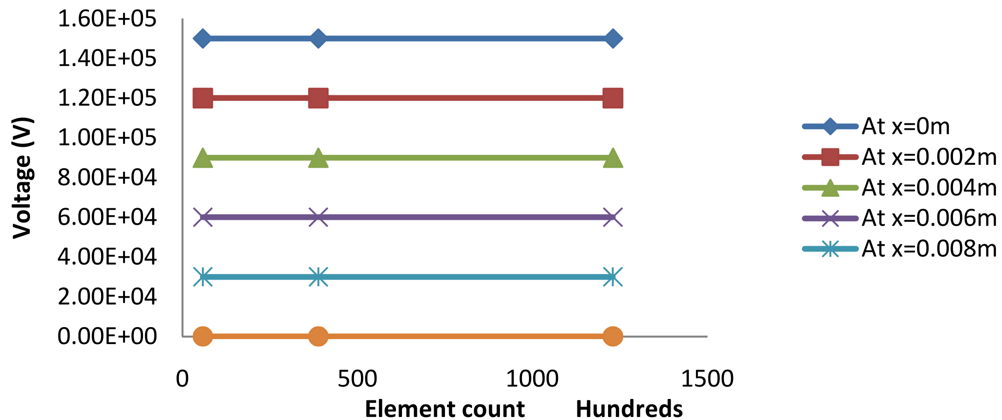

Figure 147: Infinite Slab, Numerical Solution Mesh Convergence for Voltage

The discretized temperature through thickness curve does not necessarily contain a node at the maximum temperature, and as such, the maximum temperature through the slab does change as the element count increases. This has been shown in **Figure 148.**

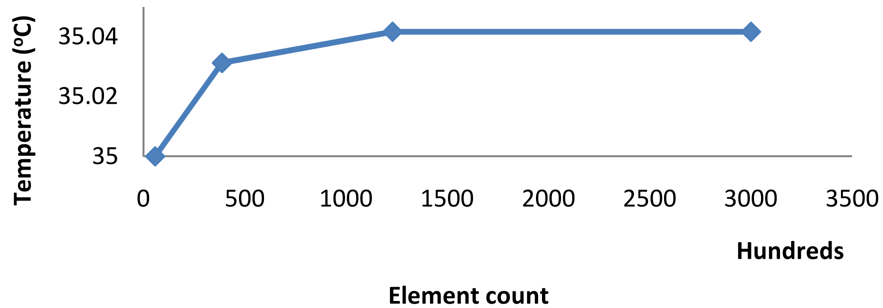

Figure 148: Infinite Slab, Numerical Solution Mesh Refinement Maximum Temperature

The asymptotic behavior of **Figure 148** demonstrates less than 0.05^{o}C movement which is lower than any design consideration. The information from the second to last point on the above curve was used for the comparison in **C** .3.3 **Analytical and Numerical comparison** because it provides accurate results without using a high element count (translates into high computing time).

Screen shots of the entire temperature distribution have been placed in as **Figure 149** and **Figure 150**.

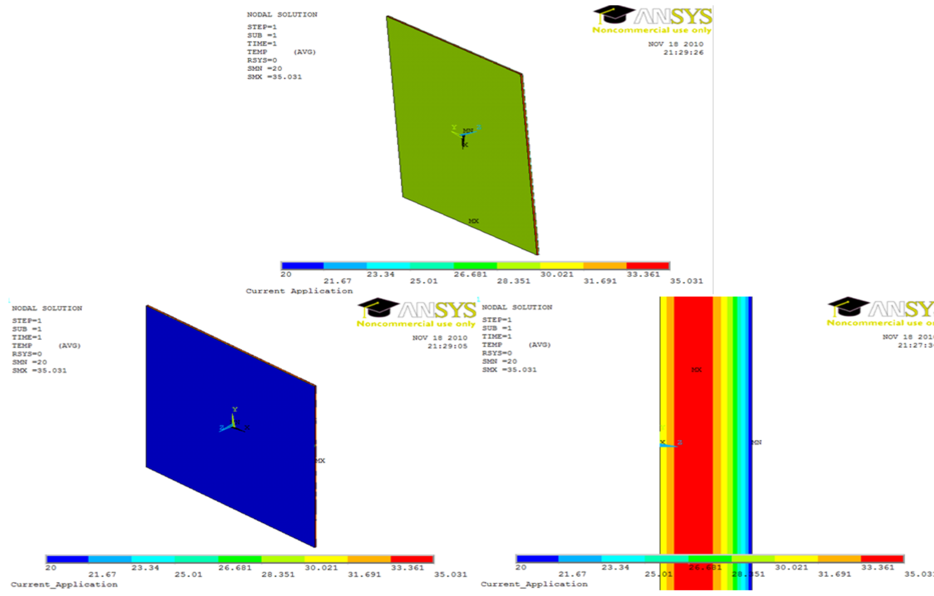

Figure 149: Infinite Slab, Numerical Solution Temperature Distribution

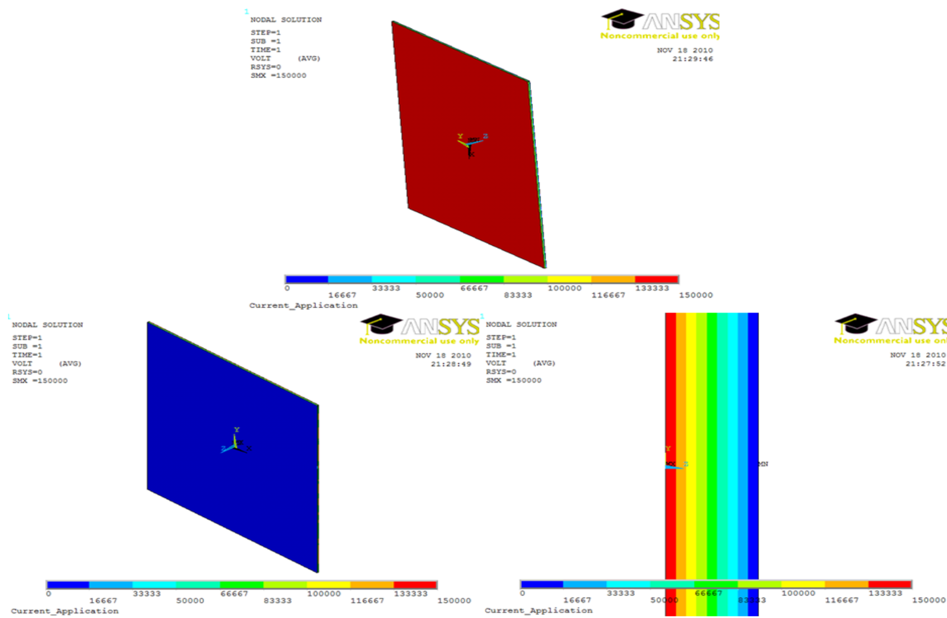

Figure 150: Infinite Slab, Numerical Solution Voltage Distribution

C .3.3 Analytical and Numerical comparison

Following the prescribed procedures for both the analytical and numerical solution, results were calculated and compared in **Table 18** and **Table 19**.

Table 18: Infinite Slab, Temperature Comparison

	Analytical	Numerical	Difference
Temp at x=0m (^{o}C)	30.00	30.00	0.00
Temp at x=0.002m (^{o}C)	34.00	34.00	0.00
Temp at x=0.004m (^{o}C)	35.00	35.00	0.00
Temp at x=0.006m (^{o}C)	33.00	33.00	0.00
Temp at x=0.008m (^{o}C)	28.00	28.00	0.00
Temp at x=0.01m (^{o}C)	20.00	20.00	0.00
Max Temp (^{o}C)	35.042	35.042	0.00
q'''(W/m^3)	4.5e7	4.5e7	0.00

Table 19: Infinite Slab, Voltage Comparison

	Analytical	Numerical	Difference
At x=0m	1.50E+05	1.50E+05	0.00E+00
At x=0.002m	1.20E+05	1.20E+05	0.00E+00
At x=0.004m	9.00E+04	9.00E+04	0.00E+00
At x=0.006m	6.00E+04	6.00E+04	0.00E+00
At x=0.008m	3.00E+04	3.00E+04	0.00E+00

As shown above by the "Difference" quantities, the numerical and analytical methods show the same information for the infinite slab.

The temperature and voltage distributions are compared in **Figure 151** and **Figure 152** respectively.

Analytical and Numerical Comparison of Slab Temperature Distribution

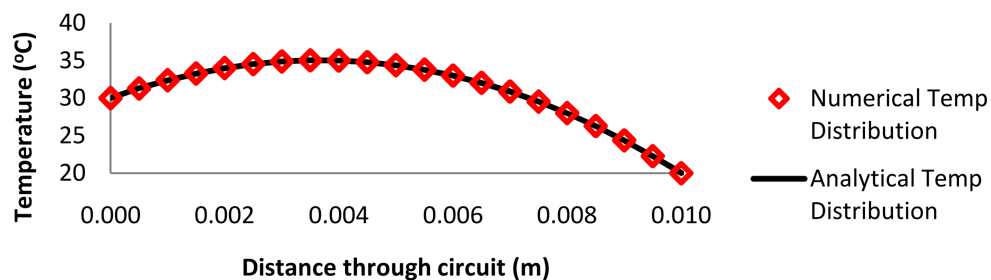

Figure 151: Infinite Slab, Temperature Distribution comparison

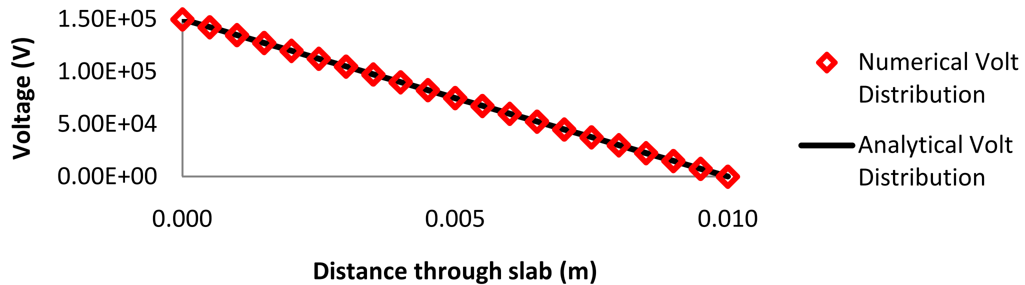

Figure 152: Infinite Slab, Voltage Distribution comparison

The above figure demonstrates that the through thickness numerical information is exactly what the analytical trend predicted. This information, along with **Table 18** and **Table 19**, shows the FEM (and more specifically ANSYS12.0) numerical thermal-electrical model with Joule Heating as a coupling effect to be valid.

C.4 Thermal-Electrical Model with Joule Heating and the Peltier Effect

The thermal and electrical models are coupled with the Joule heating and the Peltier effect. This allows for thermoelectric devices to be analyzed. A one leg cooler was analyzed and shown in **Figure 153**.

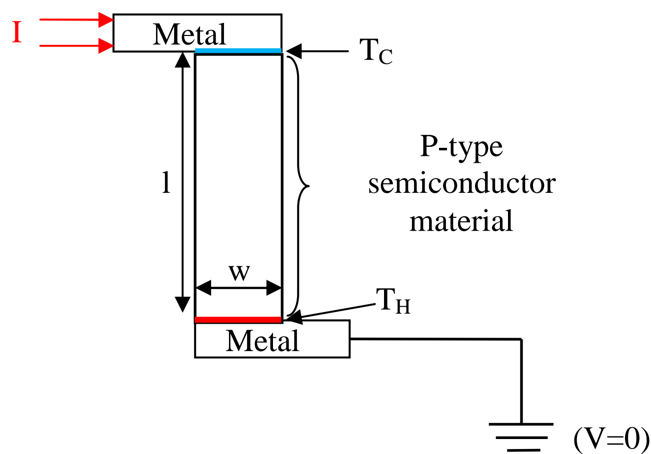

Figure 153: One Leg Thermoelectric Cooler example

The above figure contains many properties that have been listed in **Table 20**.

Table 20: One Leg Thermoelectric Cooler (TEC) Properties

	Thermal Conductivity (W/mK)	Electrical Resistivity (Ω m)	Seebeck Coefficient (V/K)	Temperature (^oC)	Current (A)	Distance (m)	Cross Section Area (m^2)
P Type Leg	1.2	0.98e-5	210e-6	-	-	-	-
Metal	400	1.7e-8	-	-	-	-	-
T_h	-	-	-	40	-	-	-
I	-	-	-	-	10	-	-
l	-	-	-	-	-	1e-2	-
w	-	-	-	-	-	1e-2	-
A_c	-	-	-	-	-	-	1e-2

The variable tested was ΔT, which following the below equation, consequently varies T_c.

$\Delta T = T_h - T_c$

The metrics for the validation are shown in **Table 21.**

Table 21: One Leg Thermoelectric Cooler (TEC) Metrics

	Net Cooling (W)	Power (W)	Coefficient of Performance
Q_c	?	-	-
P	-	?	-
COP	-	-	?

C .4.1 **Analytical Solution**

The analytical solution to the one leg thermoelectric cooler beings with determining the net cooling power described in equation **2-15** for only one leg. This produces equation **C- 9.**

$$Q_{\,Net\ Cooling} = ST_C I - \frac{1}{2} I^2 R_e - K\Delta T \qquad \textbf{C- 9}$$

$where$:

$S = Seebeck\ Coefficient\ (\frac{V}{K})$

$T_c = Absolute\ Cold\ Jucntion\ Temperature\ (K)$
$I = Current(A)$
$\Delta T = T_H - T_C\ (K)$
$R_e = Electrical\ Resistance\ (\Omega) = \rho \frac{l}{A_c}$
$K = Conductance \left(\frac{W}{m^2 K}\right) = k \frac{l}{A_c}$

The other metrics of interest are the Power and the Coefficient of performance. These general equalities are equation **2-14** and **2-16** respectively. After the one leg simplification, they turn into equation **C- 10** and **C- 11**.

$$Power_{TEC} = IS\Delta T + I^2 R_e \quad \textbf{C- 10}$$

$$COP_{TEC} = \frac{Q_{\ Net\ Cooling}}{Power_{TEC}} = \frac{ST_C I - \frac{1}{2} I^2 R_e - K\Delta T}{IS\Delta T + I^2 R_e} \quad \textbf{C- 11}$$

Equations **C- 9** through **C- 11** were computed for each ΔT and compared to numerical values. These results have been shown in **C** .4.3 **Analytical and Numerical Comparison**.

C .4.2 **Numerical Solution**

The numerical solution of the thermoelectric cooler (TEC) is developed in ANSYS 12.0 using the thermal-electrical element Solid226 (50) with Joule heating and the Peltier effect enabled. **Figure 154** shows the numerical simulation geometry.

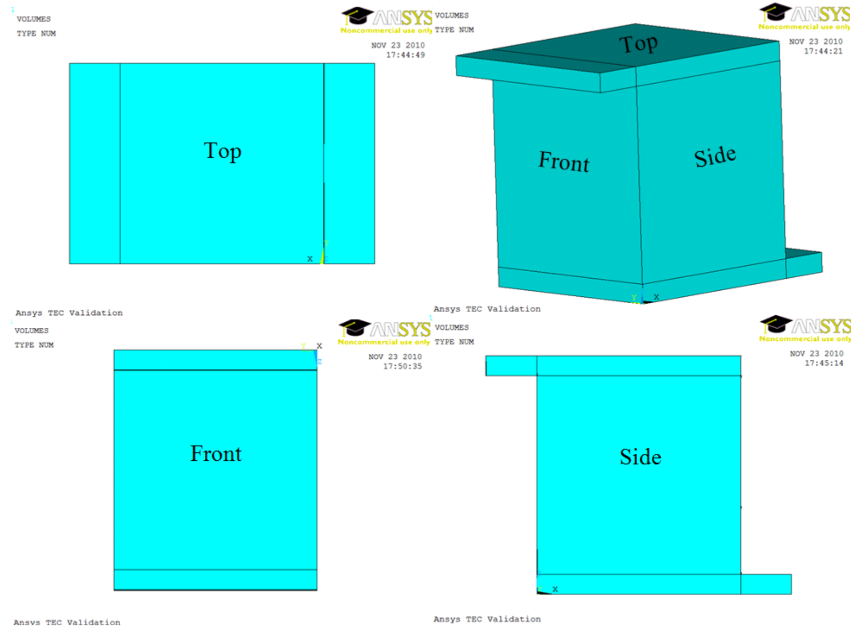

Figure 154: One Leg Thermoelectric Cooler (TEC), Numerical Geometry

The nature of numerical simulations requires that a mesh refinement be conducted to distinguish and ultimately eliminate mesh dependent solutions. Thus the metrics, Q_c, Power, and COP, are computed every 10 ΔT as a function of element count. These curves are shown in **Figure 155**, **Figure 156**, and **Figure 157**. They show no dependence on element count.

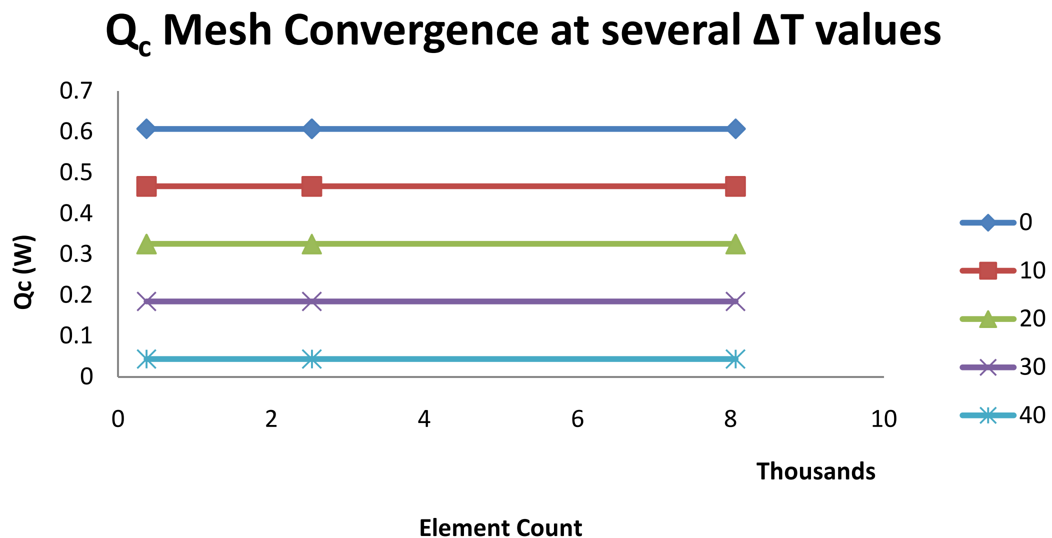

Figure 155: One Leg Thermoelectric Cooler (TEC), Net Cooling Mesh Convergence

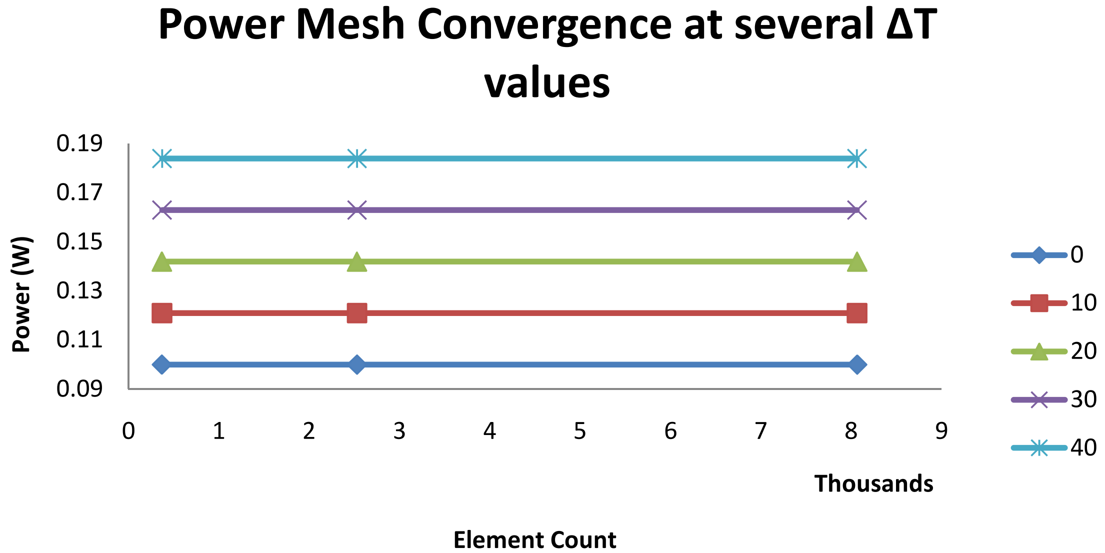

Figure 156: One Leg Thermoelectric Cooler (TEC), Power Mesh Convergence

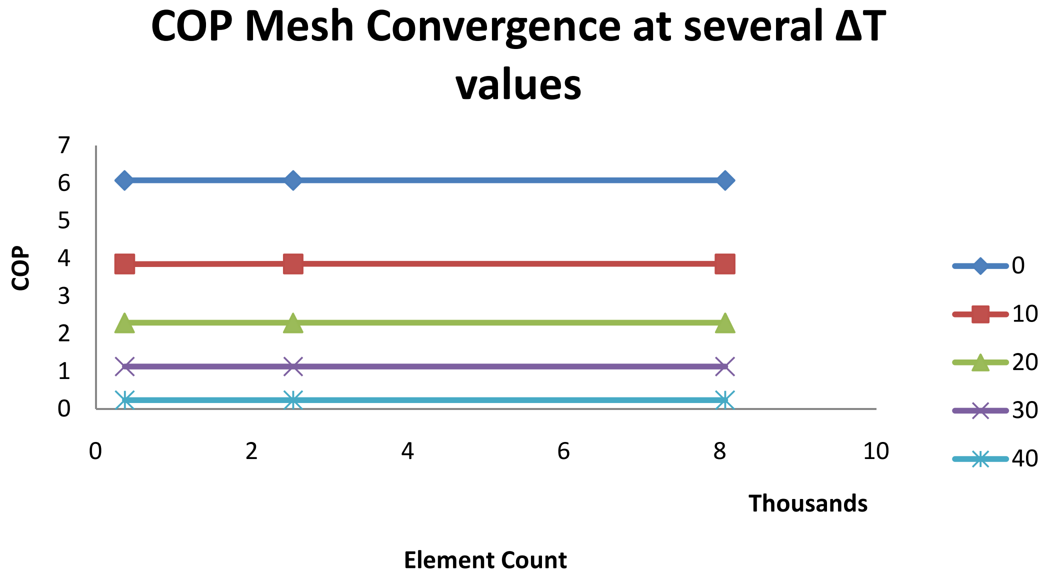

Figure 157: One Leg Thermoelectric Cooler (TEC), COP Mesh Convergence

Screen shots of the entire and voltage distribution (the degrees of freedom for the model) distribution are shown in **Figure 158** and **Figure 159** respectively for the case of ΔT equal to 42°C.

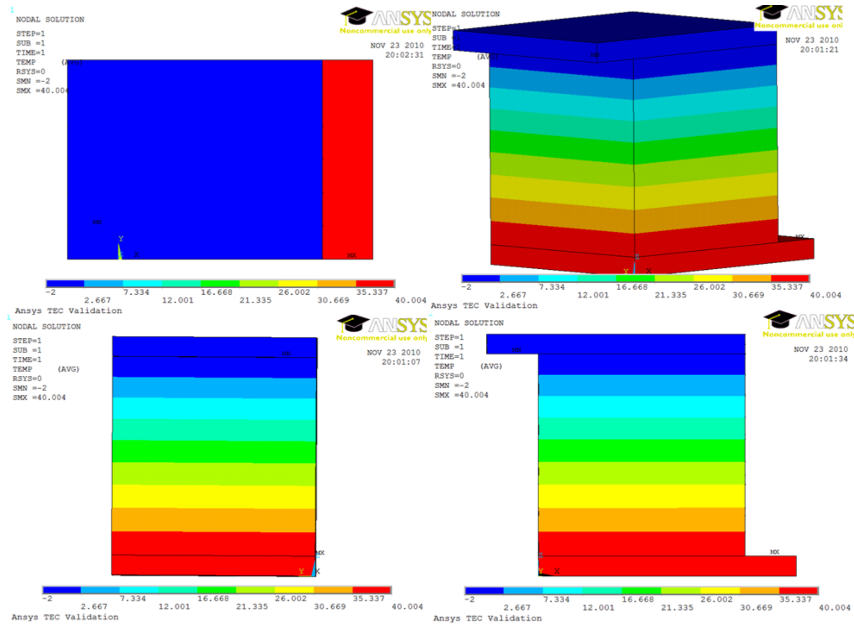

Figure 158: One Leg Thermoelectric Cooler (TEC), Temperature Screenshot for ΔT=42

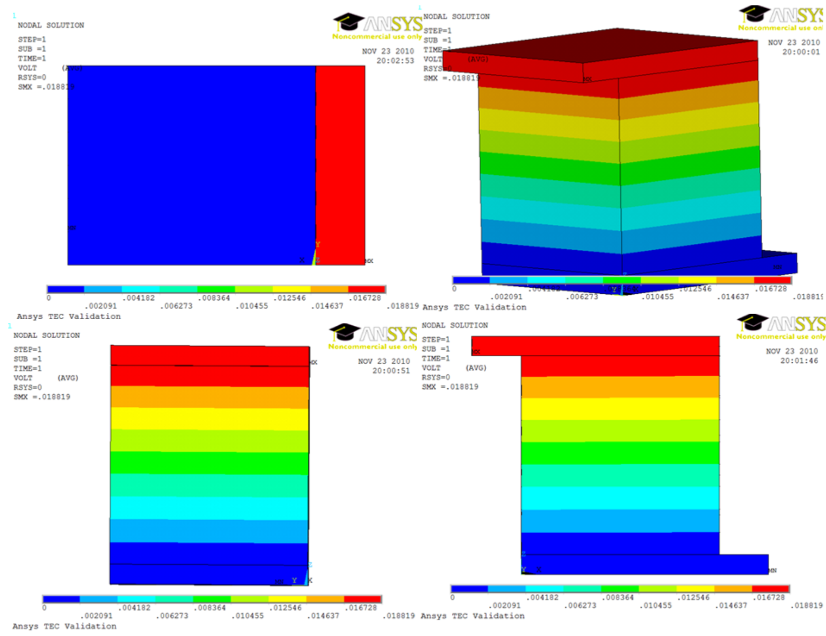

Figure 159: One Leg Thermoelectric Cooler (TEC), Electrical Potential Screenshot for ΔT=42

C .4.3 **Analytical and Numerical Comparison**

The analytical and numerical solutions for the metrics of the one leg thermoelectric cooler (TEC) are compared. The percent error over a ΔT range (0°C to 40°C) is shown in **Figure 160**.

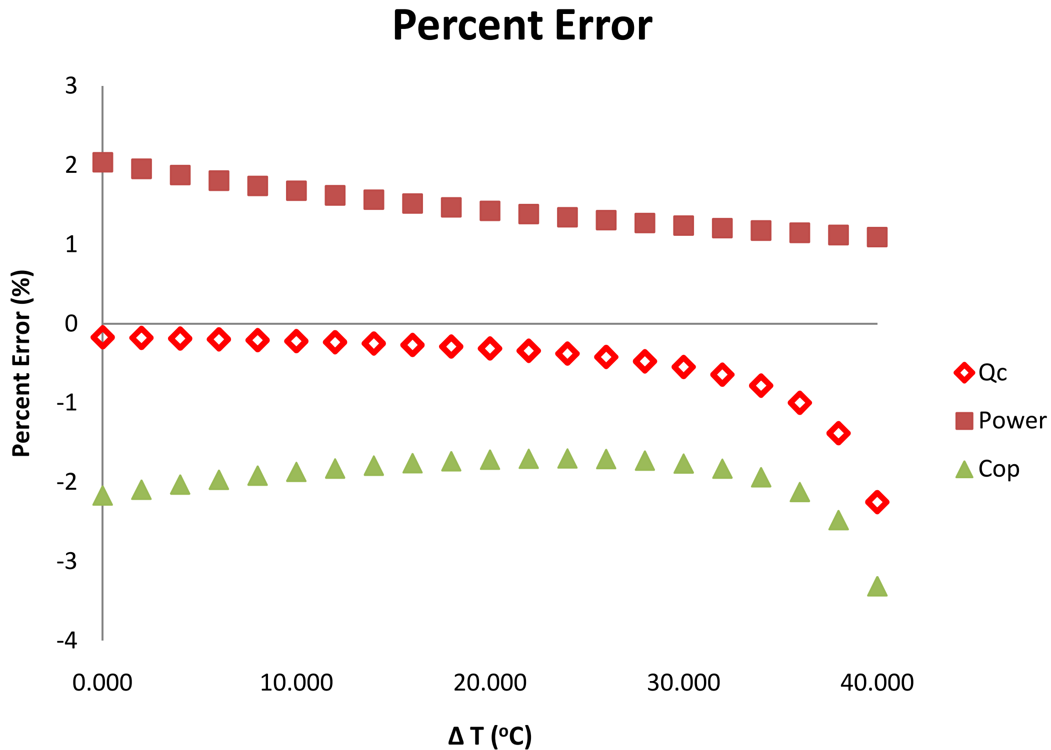

Figure 160: One Leg Thermoelectric Cooler (TEC), Percent Error for metrics

The above shows less than three percent difference between the two solution methods with the highest error found in the COP comparison. The COP is the quotient of the net cooling and power (see equation **C- 11**), and as such, its error is the composition of the other metrics.

Curves of ΔT as a function net cooling (Q_c), Power, and Coefficient of Performance (COP) are placed in **Figure 161** through **Figure 163**.

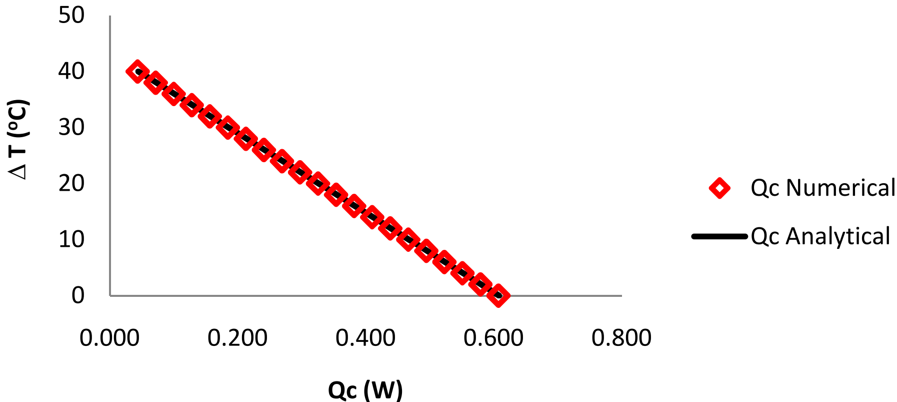

Figure 161: One Leg Thermoelectric Cooler (TEC), Net Cooling Comparison

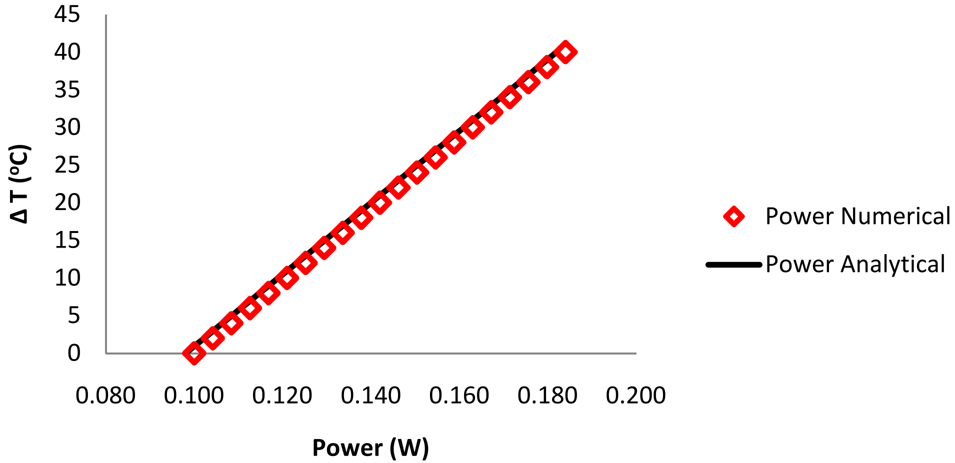

Figure 162: One Leg Thermoelectric Cooler (TEC), Power Comparison

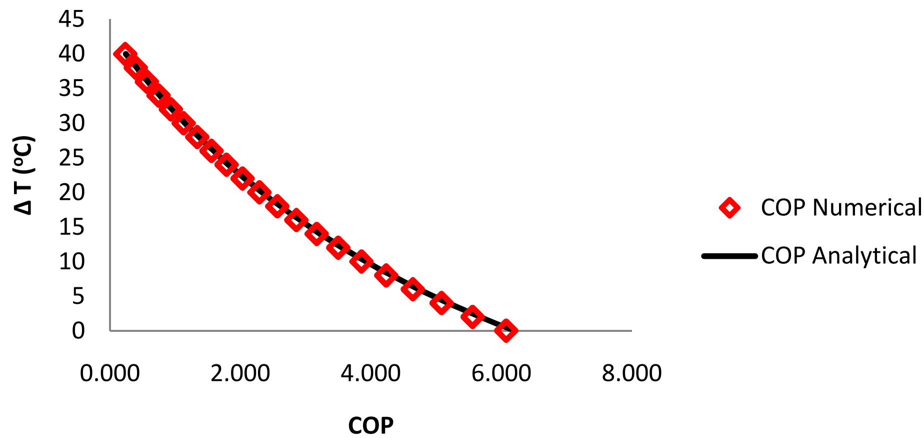

Figure 163: One Leg Thermoelectric Cooler (TEC), COP Comparison

The above figures demonstrate that all the three metrics of concern are numerically modeled with little deviation (less than 3% for all metrics) from the analytical equations. Thus, the FEM (and more specifically ANSYS12.0) numerical thermal-electrical model with both coupling effects (Joule Heating and the Peltier effect) is valid. This provides confidence in thermoelectric device analysis through ANSYS12.0.

C.5 Thermal and Electrical Model Validation Summary

Four numerical (ANSYS 12.0) models are validated using classical analytical examples. The models are the thermal, electrical, and the coupled thermal-electrical model. The validation begins with the thermal and electrical models alone to ensure they work properly. Then the coupling between the models is added to ensure correct thermoelectric device analysis.

The Thermal model is validated using the residential wall example discussed in **Appendix** A **FEM Phases**. The comparison of the temperature distributions between the

solution methods shows no difference. The electrical model is validated in a similar manner using resistors connected in series. The comparison of the voltage distributions between the analytical and numerical solutions shows no difference and thus the FEM (and more specifically ANSYS12.0) numerical thermal and electrical models are valid. This provides confidence in the models that allows their couplings to be studied.

The thermal-electrical model with Joule heating coupling is validated using an infinite slab with uniform current running through it. There is no difference between the two solution methods. The last step in the validation is proving accurate Peltier Effect coupling. This is accomplished using a conventional one leg thermoelectric cooler. Analytical and numerical solutions require Joule heating coupling effect since the Peltier effect occurs simultaneously with it. The comparison between the analytical and numerical solutions shows little difference. Thus the numerical (and more specifically ANSYS 12.0) thermal-electrical model with Joule Heating and the Peltier effect coupling is valid.

Bibliography

1. **Litvinovitch, Viatcheslav.** *Masters Thesis: Miniature Thermoelectric Coolers for On chip Hot Spots.* College Park : Department of Mechanical Engineering, 2009.
2. **ITRS.** The International Technology Roadmap for Semiconductors. [Online] 2005. http://www.ITRSnemi.org.
3. *Thermal modeling, analysis, and management in.* **Pedram, M., and Nazarian, S.** 8, 2006 : IEEE, Vol. 94, pp. 1487-1518.
4. **Wang, Peng.** *On-Chip Thermoelectric Cooling of Semiconductor Hot Spot.* College Park : University of Maryland, 2007.
5. *Electromigration - A brief survey and some recent results.* **Black, J. R.** s.l. : IEEE Transactions on Electron Devices,, 1969, Vols. ED-16, pp. 338-347.
6. *Thermal performance challenges from silicon to systems.* **Viswannath, R., Wakharkar, V., Watwe, A., and Lebonheur, V.** 3, s.l. : Intel Journal of Technology, 2000, Vol. 5, pp. 1-16.
7. **iNEMI.** *Electronics Manufacturing Initiative Technology Roadmap.* s.l. : iNEMI, 2004.
8. *Cooling a microprocessor chip.* **Mahajan, R., Chiu, C., and Chrysler, G.** 8, s.l. : IEEE, Vol. 94, pp. 1476-1486.
9. **Incropera, DeWitt, Bergman, Lavine.** *Fundamentals of Heat and Mass Transfe, 6th Edition.* Hoboken : John Wiley & Sons, 2007. *978-0471-45728-2.
10. *Quantum dot.* **Harman, T. C., Taylor, P. J., Walsh, M. P., LaForge, B. E.** 5590, s.l. : Science,, 2002, Vol. 297, pp. 2229-2232,.
11. *Thin-film thermoelectric devices with high room-temperature figures of merit.* **Venkatasubramanian, R., Siivola, E., Colpitts, T., and O'Quinn, B.** 6856, London : Nature, 2001, Vol. 413, pp. 597-602.
12. *SiGeC/Si superlattice micro-coolers.* **Fan, X., Zeng, G., LaBounty, C., Bowers, J., Croke, E., Ahn, C., Huxtable, S., Majumdar, A.** 11, s.l. : Applied Physics Letters, 2001, Vol. 78, pp. 1580-1600.
13. **Chen, C., Yang, B., Liu, W. L.** Engineering nanostructures for energy conversion. *Heat Transfer and Fluid Flow in Microscale and Nanoscale Structures.* s.l. : WIT Press, 2004, pp. 45-91.
14. *Simultaneous measurements of Seebeck coefficient and thermal conductivity across superlattice.* **Yang, B., Liu, W. L., Wang, K. L., and Chen, G.** 10, s.l. : Applied Physics Letters, Vol. 80, pp. 1758-1760.
15. *"Superlattice microrefrigerators fusion bonded with optoelectronic devices.* **Zhang, Y., Zeng, G. H., Piprek, J., Bar-Cohen, A., and Shakouri, A.** 4, s.l. : IEEE Transactions on Components and Packaging Technologies, 2005, Vol. 28, pp. 658-666.
16. *"An assessment of module cooling enhancement with thermoelectric coolers.* **Simons, R. E., Ellsworth, M. J., Chu, R., C.** 1, s.l. : Journal of Heat Transfer, 2005, Vol. 127, pp. 76-84.
17. *High-power-density spot cooling using bulk thermoelectrics.* **Zhang, Y., Shakouri, A., and Zeng, G.** 14, s.l. : Applied Physics Letters,, 2004, Vol. 85, pp. 2977-2979.
18. *Analytical modeling of silicon thermoelectric microcooler.* **Peng Wang, Avram Bar-Cohen, Bao Yang,Gary L. Solbrekken, Ali Shakouri.** 014501, s.l. : Journal Of Applied Physics, 2006, Vol. 100. 10.1063/1.2211328.

19. *On Chip Hot Spot Cooling using Siliocn Thermoelectric Microcooler.* **Peng, Wang and A., Bar-Cohen.** 3, s.l. : Journal of Applied Physics, 2007, Vol. 102, pp. 034503-034503-11.
20. *THERMOELECTRIC SELF-COOLING ON GERMANIUM CHIP.* **Peng Wang, Avram Bar-Cohen.** Washington D.C : 14th International Heat Transfer Conference, 2010. 14th International Heat Transfer Conference. pp. IHTC14-23312,1-8. 23312.
21. **Allan D. Kraus, Avram Bar-Cohen.** Thermoelectric coolers. *Thermal Analysis and Control of Electronic Equipment.* New York : Hemisphere Publishing Corporation, 1983, pp. 435-465.
22. **Decher, R.** *Direct Energy conversion.* New York : Oxford University Press, 1997. 978-0195095722.
23. **Lian-Tuu Yeh, Richard C. Chu.** *Thermal Management of Microelectronic equipment.* New York : ASME Pres, 2002. 978-0791801680.
24. **Kraus, Allan D.** *Circuit Analysis.* New York : West Publishiing Company, 1991. 0-314-79500-6.
25. **Cenge, Yunus A and Boles, Michael A.** *Thermodynamics An Engineering Approach.* New York : McGraw Hill, 2002. 0-07-238332-1.
26. **Ulrick, K. Richard and Brown, Willian.** *Advanced Electronic Packaging.* Hoboken : John Wiley & Sons, 2006. 10 0-471-46609-3.
27. *Peltier effect in a coevaporated.* **Zhou, H., Rowe, D. M., and Williams, S.,G.,W.** 1, s.l. : Thin Solid Films, 2002, Vol. 1, pp. 270–274.
28. *Micropelt miniaturized thermoelectric devices: small size, high cooling power densities, short response time.* **Bottner, H.** s.l. : 24th International Conference on Thermoelectrics, 2005. pp. 1-8.
29. *"Bi2Te3 thick thermoelectric films obtained by electrodeposition from hydrochloric acid solutions.* **Nedelcu, M., Sima, M., Visan, T., Pascu, T., Franga, I., and Craciuniou, F.** s.l. : 20th International Conference on Thermoelectrics, 2001. pp. 322-326,.
30. **Pandey, R.K., Sahu, S.N., and Chandra, S.** *Handbook of Semiconductor.* 1996 : CRC Press, New York. 978-0824797010.
31. **Ioffe, A. F.** *Semiconductor Thermoelements and Thermoelectric Ccooling.* London : Infosearch Ltd.,, 1957.
32. *A new n-type and improved p-type pseudo-ternary (Bi2Te3)(Sb2Te3)(Sb2Se3) alloy for Peltier cooling.* **Ettenberg, M. H., Jesser, M. A., and Rosi, E., D.,.** s.l. : 15th International Conference on Thermoelectrics, 1996. pp. 52-56.
33. *Bismuth telluride compounds.* **Yamashita, O., Tomiyoshi, S., and Makita, K.** 1, s.l. : Journal of Applied Physics, 2003, Vol. 93, pp. 368-374.
34. *Effect of Annealing on Thermoelectric.* **Yamashita, O., and Tomiyoshi, S.** 2A, s.l. : Japan Journal of Applied Physics, 2003, Vol. 42, pp. 492-500.
35. *High performance n-type bismuth telluride.* **Yamashita, O., and Tomiyoshi, S.** 11, s.l. : Journal of Applied Physics, 2004, Vol. 95, pp. 6277–6283.
36. *Transport properties of.* **Volklein, F., Baier, V., Dillner, U., and Kessler, E.** s.l. : Thin Solid, 1990, Vol. 187, pp. 253-262.
37. *Thermoelectric microdevice fabricated by a MEMS-like electrochemical process.* **Snyder, G. J., Lim, J. R., Huang, C., and Fleurial, J.-P.** 8, s.l. : Nature Materials,, 2003, Vol. 2, pp. 528-531.

38. *Miniature thermoelectric coolers for semiconductor lasers.* **Semenyuk, V. et al.** s.l. : 13th International Conference on Thermoelectrics, 1994. pp. 150-153,.
39. **Semenyuk, V.** *Ph.D. Dissertation.* Odessa, USSR : Odessa Technological Institute of Food and, 1967.
40. *Miniature thermoelectric modules with increased cooling power.* **Semenyuk, V.et al,.** s.l. : 25th International Conference on Thermoelectrics, 2006. pp. 322-326.
41. *Novel High Performance Thermoelectric Microcoolers with Diamond Substrates.* **Semenyuk, V. et al.** s.l. : 16th International Conference on Thermoelectrics, 1997. pp. 683-686.
42. *Finite Elements for Thermoelectric Device Analysis in ANSYS.* **Antonova, Elena E. and Looman, David C.** Vienna, Austria : IEEE, 2005. pp. 215 - 218. 0-7803-9552-2.
43. **Pijush, Kundu K. and Cohen, Ira M.** Carteisan Tensors. [book auth.] Kundu K. Pijish and Cohen Ira M. *Fluid Mechanics.* New York : Academic Press, 2008.
44. **ANSYS, Inc.** *Theory Reference for Mechanical APDL and Mechanical Applications.* Canonsburg,PA : ANSYS,Inc., 2009.
45. **Silvester, P. P. and Ferrari, R. L.** *Finite Elements for Electrical Engineers, 3rd Edition.* Cambridge : University Press, 1996. 9780521445054.
46. **Hambley, Allan R.** *Electrical Engineering, Principles and Applications, Fourth Edition.* Upper saddle River : Pearson Education, Inc., 2008. 978-0131989221.
47. **Moaveni, Saeed.** Finite Element Analysis: Theory and Application with ANSYS. *Moaveni, Saeed.* Upper Saddle River : Pearson Eduction, Inc., 2008, pp. 20-29.
48. *Pulsed laser.* **Raghuveer, S., Makala, K., Jagannadham, A., and Sales, B.,C.** 6, s.l. : ournal of Applied Physics, 2003, Vol. 94, pp. 3907-3918.
49. *Thermoelectric properties of the bismuth–antimony–telluride and the antimony–telluride films processed by electrodeposition for micro-device applications.* **Su-Kyum Lim, Min-Young Kim, Tae-Sung Oh.** 14, s.l. : Thin Solid Films, 2009, Vol. 517, pp. 4199-4203.